



Measurement of toughness in high strength steels sheets to improve material selection in cold forming and crash-resistant components

(TOUGH-SHEET)

FINAL REPORT

Measurement of toughness in high strength steels sheets to improve material selection in cold forming and crash-resistant components (TOUGH-SHEET)

European Commission

Directorate-General for Research and Innovation

Directorate D - Industrial Technologies

Unit D.4 — Coal and Steel

Contact Hervé Martin

E-mail RTD-PUBLICATIONS@ec.europa.eu

European Commission

B-1049 Brussels

Manuscript completed in 2019.

This document has been prepared for the European Commission however it reflects the views only of the authors, and the Commission cannot be held responsible for any use which may be made of the information contained therein.

More information on the European Union is available on the internet (<http://europa.eu>).

Luxembourg: Publications Office of the European Union, 2019

PDF

ISBN 978-92-79-98317-7

ISSN 1831-9424

doi: 10.2777/124159

KI-NA-29-531-EN-N

© European Union, 2019.

Reuse is authorised provided the source is acknowledged. The reuse policy of European Commission documents is regulated by Decision 2011/833/EU (OJ L 330, 14.12.2011, p. 39).

For any use or reproduction of photos or other material that is not under the EU copyright, permission must be sought directly from the copyright holders.

All pictures, figures and graphs © Fundació CTM Centre Tecnològic (CTM), RFSR-CT-2014-00015 TOUGH-SHEET

European Commission

Research Fund for Coal and Steel

Measurement of toughness in high strength steels sheets to improve material selection in cold forming and crash-resistant components (TOUGH-SHEET)

D. Casellas, A. Lara, S. Molas, D. Frómeta, R. Hernández, M. Baldayo

Fundació CTM Centre Tecnològic (CTM)

Plaça de la Ciència 2, 08243 Manresa, Spain.

C.Suppan, J.Rehrl

voestalpine Stahl GmbH (VAS)

Voestalpine-Straße, 3 A-4020 Linz, Austria.

M.Tedesco

Centro Ricerche Fiat SCPA (CRF)

Strada Torino 50, IT-10043 Orbassano (TO), Italia.

J.Salvat, E.Martín, M.Vives

IDIADA automotive technology

L'Albornar, PO Box 20, E-43710 Santa Oliva, Spain.

Grant Agreement RFSR-CT-2014-00015
01/07/14 - 01/07/17

Final report

Directorate-General for Research and Innovation

TABLE OF CONTENTS

1. Final summary	5
1.1 Objectives	5
1.2 Main results	5
1.3 Conclusions	13
1.4 Applications	14
2. Scientific and technical description of the results.....	15
2.1 Objectives of the project	15
2.2 Description of activities and discussion.....	15
2.2.1. <i>WP1. Mechanical characterization of AHSS</i>	15
2.2.2. <i>WP2. Toughness characterization by means of EWF</i>	33
2.2.3. <i>WP3. Crashworthiness assessed by EWF</i>	50
2.2.4. <i>WP4. Sheet formability assessed by EWF</i>	65
2.2.5. <i>WP5. Effect of microstructure on fracture toughness</i>	81
2.2.6. <i>WP6. Implementation of a cracking criterion for crash</i>	89
2.2.7. <i>WP7. Implementation of a sheet forming failure criterion</i>	98
2.2.8. <i>WP8. Management, dissemination and reporting</i>	111
2.3 Conclusions	112
2.4 Exploitation and impact of the research results	116
3. List of figures	119
4. List of tables	123
5. List of acronyms and abbreviations	125
6. References.....	127

1. FINAL SUMMARY

Project objectives, main results and conclusions obtained during the Tough-sheet project are summarized in this section.

1.1 Objectives

The main objectives of the Tough-Sheet project were the following:

- Measure the fracture toughness of thin AHSS sheets through the application of the Essential Work of Fracture (EWF) methodology.
- Develop a failure criterion based on fracture toughness to predict cracking during forming and crash, aimed at improving performance of industrial sheet components.
- Prove the suitability of the fracture toughness as a material property to select high strength steel grades with high formability and crash performance.
- Understand the microstructural effects on the cracking resistance of AHSS, aimed at developing new high strength steel grades with improved fracture resistance.

The project was divided in 8 Work packages (WP) as illustrated in Figure 1.

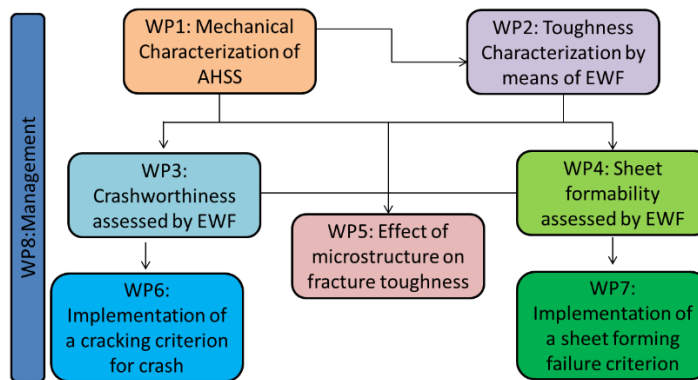


Figure 1. Distribution of project Work Packages.

1.2 Main results

WP1: Mechanical Characterization of AHSS

In this WP the mechanical characterization of the different AHSS was carried out in terms of tensile properties, formability and crash resistance. The material preparation for all the tests was also addressed in this WP.

Task 1.1. Materials and samples preparation

Nine industrially produced AHSS grades in the range of thickness of 1.4-1.6 mm were investigated in the project. Eight grades were supplied by voestalpine (VAS) and one grade by Centre Richerche Fiat (CRF). These steels are:

- 3 commercially available first generation AHSS cold forming grades (DP1000, CP1000 and CP1200)
- 3 new developments of 3rd generation AHSS: 1 TBF steel (bainitic ferrite matrix with retained austenite), 1 Q&P steel (tempered martensite matrix with retained austenite), and 1 mixed TBF/Q&P microstructure.
- 2 microstructures of hot stamped boron steel: one in the press hardened condition (strength of about 1500 MPa) and the other with an additional tempering treatment (strength of about 1000 MPa).
- 1 TWIP (Twinning Induced Plasticity) steel with a fully austenitic microstructure. This steel grade was supplied by CRF.

The blanks of the different materials were prepared and shipped to the partners to perform the corresponding tests.

Task 1.2. Mechanical characterization

Conventional tensile tests and bulge tests were carried out by VAS to characterize the mechanical behaviour of the investigated steels. Digital Image Correlation (DIC)-assisted tensile tests were performed at CTM in order to complete the mechanical characterization. Such tests allow to monitor and determine the strain during the entire test and to calculate the deformation during necking. The strain levels within the necking zone are much greater than the obtained by extensometers and better define the local ductility than conventional strain at fracture, normally obtained from an initial gauge length of 50 or 80 mm (A_{50} , A_{80}).

Tensile properties were determined for all the steel grades at transverse orientation respect to the rolling direction. Results from DIC-assisted tensile tests show that elongation at fracture from conventional tensile tests underestimates significantly the local post uniform ductility. Steels with poorer elongation at fracture can show greater local strain at fracture and vice versa. Bulge tests provide greater deformation before necking or fracture than tensile tests and are a good alternative to characterize the material behaviour when the material is formed in multiaxial directions. The strains at failure determined in bulge tests follow the same trend that the observed in DIC-assisted tensile tests.

Task 1.3. Laboratory impact resistance tests

Axial and bending impact tests

The crash behaviour of the studied steel grades was assessed through laboratory axial and bending impact resistance tests. The axial and bending impact tests were performed at VAS facilities. Such tests give information about the crash failure behaviour of the investigated steel grades. Impact tests were evaluated in terms of deformation, cracking and the overall appearance of the samples after crashing. A crash index (CI) was assigned to quantify the damage of every single crashed specimen according to [LAR10 and LAR15]. In order to obtain detailed information about damage initiation and damage evolution during the deformation of the crashed samples, several experiments were carried out with different load mass speeds. A thorough inspection of the crashed specimens was performed aimed at identifying the damage location and the length of cracks appeared.

A new parameter to describe the evolution of damage in crash tests was introduced, the Crash Index Decreasing Rate (CIDR), which evaluates how the CI diminishes in function of the intrusion level. The CIDR is related to the evolution of a cracking pattern and quantifies the crash resistance of the steels; the lower the CIDR the better crash behaviour. The parameter showed to be suitable to rank the crashworthiness of the investigated steel grades in axial crash tests. No significant differences in CIDR were found in bending tests.

Dynamic tensile tests

The effect of strain rate on tensile properties was evaluated in this task by means of dynamic tensile tests. Tensile tests were performed by CRF at three different strain rates: 5 s^{-1} , 50 s^{-1} and 500 s^{-1} in order to assess the strain rate sensitivity of the different AHSS grades studied. Low and medium strain rate tests ($5-50\text{ s}^{-1}$) were performed in a hydropneumatic machine. For high strain rate tests (500 s^{-1}) a Hopkinson bar machine was used.

Task 1.4. Laboratory forming tests

Laboratory forming tests were performed by CRF in order to obtain the Forming Limit Curves (FLC) of the different AHSS. These curves represent the maximum and minimum strain that the sheet may withstand without necking or failure at different deformation modes. The FLCs were determined according to the ISO12004:2008 by means of Nakajima and Marciak stretching tests. Such tests are suitable to evaluate the formability of AHSS under general deformation modes (uniaxial strain, biaxial strain, plane strain...), where the fracture is preceded by a very localized necking. However, for shearing or edge stretching the fracture occurs before considerable necking and FLC strongly overestimates the strain level at fracture. For this reason, additional tests are required to evaluate the stretch flangeability of AHSS. Stretch-flangeability has become an important formability parameter in addition to FLD and tensile properties, particularly for complicated auto body parts or

parts under heavy deformation conditions. Stretch-flangeability was evaluated by CTM through Hole Expansion Tests (HET). HET were performed following the guidelines established in the ISO16630 standard. The value obtained in this test is the Hole Expansion Ratio (HER), which indicates the maximum diametrical expansion that a circular punched hole can reach when a conical tool is forced into it until a crack in the hole edge extends through the full sheet thickness. HER has shown to be suitable to evaluate the stretch flangeability and the edge cracking sensitivity of AHSS.

WP2: Toughness characterization by means of EWF

The main objectives of this WP were to evaluate the suitability of the EWF methodology to measure the fracture toughness of thin AHSS sheets and set the bases for the development of an energy-based model for fracture modelling. The EWF tests were simulated in Abaqus software by means of *J-integral* computations and compared to the experimental values.

Task 2.1. Evaluation of EWF in AHSS

EWF tests were performed at CTM according to the protocol established by the European Structural Integrity Society (ESIS) [CLU03]. Double Edge Notched Tensile (DENT) specimens with different ligament lengths were tested up to fracture to evaluate the EWF. In order to investigate the effect of notch radius two different notch radii were studied: Notch radius of 150 µm, obtained by electric discharge machining (EDM) and notch radius lower than 0,1 µm obtained by nucleating a fatigue crack from the notch. It was proved that the notch radius has a strong influence on fracture toughness. Thus, when considering the fracture toughness as a material property the values from specimens with the minimum possible radius, i.e. a fatigue crack, should be taken.

The fulfillment of the EWF constraints was assessed through optical strain measurements and the validity of the measurements was checked. The EWF methodology has shown to be suitable to readily measure the fracture toughness of thin AHSS sheets. The obtained toughness value, the specific essential work of fracture (w_e), is an energy value that quantifies the energy dissipated during the ductile tearing process. Additionally, the methodology permits to easily separate energetic contributions from crack initiation and propagation, which is very useful to understand the whole fracture process. A fracture toughness value for cracking initiation, equivalent to the plastic fracture mechanics value J_c was also determined, the specific work of fracture at initiation (w_e'). Experimental *J-integral* measurements were performed aimed at corroborating such equivalence.

Task 2.2. Simulation of EWF tests

The EWF tests were simulated in Abaqus software. *J-integral* values were obtained by FEM simulation of DENT specimens and compared to w_e . The materials studied were DP1000, TBF, Q&P. The results of the simulations of the *J-integral* showed a good correlation with the experimental EWF results of DP1000 and TBF. However, a poor correlation was observed for Q&P steel grade.

WP3: Crashworthiness assessed by EWF

WP3 was focused on the application of the EWF as a tool to understand the crash resistance of AHSS. Experimental and modelling tasks were performed aimed at correlating fracture toughness, in terms of EWF, and crash behaviour. Different damage models were investigated and the first steps for the implementation of EWF as a failure criterion in crash modelling were taken. Moreover, the effect of strain rate on EWF was experimentally assessed.

Task 3.1. Material selection according to impact and EWF results

From the results observed in laboratory impact resistance tests performed in WP1, 3 AHSS grades were selected in this task to perform the corresponding investigations. The selected steels were:

- 2 1000 MPa steel grades: DP1000, TBF
- 1 1200 MPa steel grade: Q&P

The three steels presented significant cracking during axial and bending impact tests, which was essential to investigate the evolution of crack propagation during crash. All the investigations carried out in WP3 were focused in these 3 steels.

Task 3.2. Effect of strain rate on EWF in AHSS

Crash situations involve a wide range of strain rates. Thus, it is important to quantify the effect of strain rate on mechanical properties. In this task the effect of strain rate on fracture toughness was evaluated by means of EWF at different cross-head speeds ranging from 1 mm/min to 500 mm/s. Results showed that, apparently, the EWF tends to increase with the strain-rate. However, the experimental difficulties to determine the final fracture at medium and high strain rates can lead to some uncertainties that compromise the reliability of results.

Task 3.3 Simulation of laboratory impact resistance tests

Laboratory impact resistance tests were simulated by FEM, using LS-Dyna. The capabilities of the constitutive models present in LS-Dyna were tested. The elastoplastic part of the material constitutive law was extracted from tensile data. A plastic damage evolution model was designed to reproduce the material behaviour after necking. Damage laws were designed to dissipate the energy introduced by the fracture toughness as a combination of the necking and the crack growth. Damage-evolution laws were designed in the total strain field, and later they were adapted to the LS-Dyna model formulation, which refers damage to the plastic strain evolution. Damage laws were adapted to the introduced plastic law, in order to ensure proper energy dissipation.

From EWF tests, the degradation by damage of the mechanical properties was defined, assuming several formulations: for the models in which the material properties can be introduced in the tabular form, a linear and a bilinear evolution of the stress with the strain were tested. In models using other formulations implemented in LS-Dyna, a linear evolution of the damage with the strain was introduced.

The impact tests were modelled and simulated, with the application of different impact speeds, corresponding to the experimental tests, and under axial and side loading conditions. 3 different material laws were implemented: two series of simulations were performed in order to check the effect of the experimental values of EWF (2 conditions: notched and fatigue pre-cracked specimens) and a third one, introducing a failure envelope on the material.

The application of EWF value with fatigue pre-cracked specimens resulted in a good correlation in axial impact tests at low impact velocities, where a small amount of damage was observed. At higher speeds, an underestimation of the force returned to the impactor was observed after the onset of damage. On the other hand, the application of EWF values with notched specimens showed an underestimation of the strength in axial tests. The proposed bilinear law showed a small influence over the axial tests, improving the correlation at the final stage of the displacement. In general, an improvement of the specimen behaviour under side-impact loading was observed.

In the third material law, the FLD envelope extracted from the experimental tests was used to compute an equivalent Johnson-Cook criterion, which has a definition of failure depending on load directions. Results of this third series of simulations showed a good level of correlation on the side-impact test simulations, but a loss of correlation on the axial-impact related simulations. Results showed a significant dependency on the mesh refinement, especially after damage is onset.

After the evaluation of the capabilities of the constitutive models in the LS-Dyna material formulations, it was concluded that there is not available any constitutive model considering the three effects that can be relevant in the impact-related simulations:

- Strain-rate related effect
- Inclusion of a failure envelope
- Definition of complex damage evolution laws.
- Implementation of the smeared methodology, in order to reduce the dependency of the results with the mesh-refinement.

In order to account with all of these effects, a new material model definition as a user subroutine in LS-Dyna should be implemented.

Task 3.4 Correlation of fracture toughness evaluated by means of EWF with crash resistance

The investigations on the experimental correlation between EWF results and laboratory impact tests, showed good agreement between crashworthiness and fracture toughness. It was observed that materials presenting higher EWF values exhibit greater crash resistance. A direct correlation between EWF and the CIDR was found in axial crash tests. Such almost linear correlation was not so clear in bending impact tests. However, it was determined a threshold w_e value from which no cracks were observed in impact tested specimens.

Such results highlight the importance of fracture toughness on crashworthiness of AHSS and show the need to implement new failure models that consider the energy dissipated in crack propagation.

A first attempt to introduce fracture toughness values in crash simulations was made in this project. EWF values showed to be valid for the magnitude of energy dissipated during the damage evolution in the material, but not to be accurate enough for the prediction of the damage initiation and propagation for all the different loading cases studied. Different constitutive models for isotropic materials were tested in LS-Dyna. However, none of them showed to be capable of considering all the effects combined: failure criteria, user-defined damage law, strain rate effects, etc. A damage evolution law based on EWF was developed in Abaqus/Explicit software. The law defines the evolution of damage after the fracture is onset and it was implemented in WP7, aimed at improving the accuracy of crash modelling.

WP4: Sheet formability assessed by EWF

An energetic fracture criterion based on EWF was developed in WP4 aimed at implementing it in forming simulations. It is expected that the new damage model, in combination with conventional failure criteria, improve the fracture prediction in cold forming. The effect of pre-straining on EWF was assessed and cracks origin in cold forming was investigated.

Task 4.1 Materials selection according to the formability and EWF results

Three cold forming AHSS grades were selected in this task according to forming tests performed in WP1 and EWF results:

- 1 bending grade: CP1000. This grade presents high fracture toughness, stretch flangeability and bendability, which makes it suitable for bending operations with small bending radii. On the other hand, the deep drawing of this steel is moderate.
- 2 deep-drawing grades: TBF and DP1000. These two steel grades, show lower fracture toughness and stretch flangeability, but their high n-value and elongation make them more suitable for deep-drawing operations.

Task 4.2 Effect of pre-straining on EWF in AHSS

Usually, different forming steps are present in cold forming before reach the final part geometry. The material is strained at different levels and following different strain paths. Thus, cracks can nucleate from pre-strained areas. Aimed at evaluating the pre-straining effect on fracture toughness, EWF tests were performed with pre-strained specimens at different strain levels and deformation modes (uniaxial, plane strain and biaxial). Results showed that pre-straining has not a great influence on w_e , independently of the strain path.

Task 4.3 Fracture origin characteristics in cold forming

The main objective of this task was to investigate the origin of fracture in cold forming. SEM investigations were performed on the fracture area of Marciniak stretched specimens and the punched area of HET specimens in order to assess the damage induced during punching. Fracture origin in an industrial component was investigated and the influence of edge quality was assessed. Different damage mechanisms were observed in function of the initial condition of the material. It was observed that during punching or shearing operations the material is severely damaged. The analysis of punched fracture surfaces revealed a large quantity of defects (microcracks, voids, fractures, etc.), which can act as fracture initiation sites in subsequent cold forming operations. Hence, fracture of sheared or punched areas is mainly governed by the damage introduced during

shearing and the material crack propagation resistance. On the other hand, it was observed that in absence of defects, fracture occurs at much higher deformation levels, due to localized necking.

Task 4.4 Simulation of forming tests

Nakajima tests performed in task 1.4 were simulated in Abaqus software, in order to obtain the energy at failure (following FLC criteria) and compare it with the measured fracture toughness values in task 2.1. The obtained failure energy is the product of the maximum principal plastic strain, maximum principal stress, and element length. It was observed that the estimated values from FLD simulation do not represent the fracture energies involved in sheet ductile fracture. Moreover, the experimental uncertainties in the definition of necking and crack initiation in FLD make the comparison even more difficult. It was concluded that finer mesh (more accuracy in simulation) and better failure detection at FLD is needed to allow proper comparison between estimated fracture energy in FLD and values from fracture toughness.

Task 4.5 Correlation of fracture toughness evaluated by means of EWF with sheet forming tests

Conventional failure approaches, such as tensile tests, FLD's and classic FEM models are generally suitable to predict necking instability during cold forming in general deformation modes, where failure is caused by localized necking. However, for shearing or edge stretching, a poor correlation is obtained and FLC fails to predict the fracture. One of the weak points of the FEM simulations is the prediction of edge cracking, where the fracture occurs at strain levels much lower than predicted.

Edge cracking is one of the main problems in AHSS sheets cold forming. As observed in task 4.3 cracks can be triggered from trimmed or punched areas, where the material is damaged and the existence of defects is more probable (surface irregularities, microcracks, etc.). Thus, this type of fractures are controlled by the crack propagation resistance of the material, i.e. the fracture toughness [GUT13, TAK12].

It has been observed that conventional failure approaches, such as tensile tests, FLD's and classic FEM models do not properly work to predict edge cracking in AHSS and additional tests are required to assess their edge crack sensitivity. Stretch flangeability, measured in terms of Hole Expansion Ratio (HER), has shown to be a good indicator of the edge cracking sensitivity and has become an important parameter to consider in AHSS sheets forming. The correlation between fracture toughness and stretch flangeability, measured in terms of HER, was performed for the Tough-sheet AHSS grades. A quite good correlation was found between both parameters; the higher fracture toughness the higher HER.

Hence, it can be assumed that fracture toughness, in terms of EWF, is a suitable tool to rationalize edge cracking and it can help to predict this type of fractures, improving conventional FEM models, implementing an energetic failure criterion.

The software requirements (elements, mesh, material properties, etc.) for the implementation of EWF in forming simulations were analysed in this task. Different parameters of the material properties were adjusted in Abaqus FEM software. These parameters were the fracture strain and the damage evolution, where it is possible to specify the damage in terms of fracture energy or in a tabular form; apart from the properties of elasticity, density and plasticity. An energetic criterion based on EWF tests was introduced.

WP5: Effects of microstructure on fracture toughness

The correlation between microstructural features and fracture toughness was evaluated in this WP, aimed at understanding the parameters that mainly affect toughness, crashworthiness and formability. Additionally, the effect of sheet thickness and plastic anisotropy on fracture toughness was also evaluated. The knowledge on the relationship microstructure-toughness is the key to develop new AHSS grades with improved crash resistance and formability.

Task 5.1 Effect of sheet thickness in EWF

Plane stress fracture toughness has an important energetic contribution from necking. It is thickness dependent and the toughness value evaluated by means of the EWF should be considered not an intrinsic material property but a property for the evaluated sheet thickness. The effect of the sheet

thickness on EWF was evaluated in CP1000 steel grade with 4 different thicknesses: 1, 1.4, 2 and 2.2 mm. As expected, a linear increase of EWF with the sheet thickness was observed in the investigated steel.

Task 5.2 Effect of plastic anisotropy in EWF

The effect of plastic anisotropy on EWF was evaluated in DP1000 and CP1000. EWF tests were performed at three orientations respect to the rolling direction: longitudinal, diagonal and transverse. CP1000 showed very low anisotropy with similar toughness values in all the orientations. However, DP1000 presented a slight scattering in toughness values for different orientations. Such effects of anisotropy are in good agreement with the observed in tensile tests and can be explained by the microstructural differences between the two steels. The homogeneous microstructure of CP1000 contributes to exhibit a more isotropic behaviour. On the other hand, DP1000 has a more inhomogeneous microstructure and a significant amount of retained austenite, whose stability is probably directional.

Task 5.3 Evaluation of microstructural features

In this task SEM investigations were carried out paying special attention to crack initiation and propagation. Aimed at investigating the Transformation Induced Plasticity (TRIP) effect on crack propagation resistance, the behaviour of retained austenite during crack initiation and propagation was examined by means of EBSD. EBSD measurements were conducted on EWF samples in the plastic zone and at the crack tip at different displacements for TBF, Q&P and TBF/Q&P grade. Generally, very low content of retained austenite was measured in comparison to magnetic measurements. However, measurements verified that further austenite transformation takes place in front of the crack tip during crack propagation. Retained austenite in the plastic zone seems to be consumed during crack propagation.

WP6: Implementation of a cracking criterion for crash

The main objective of WP6 was to implement the EWF-based fracture criterion in crash simulations, aimed at improving their accuracy. A crash subsystem was designed and tested and the material models using the damage laws developed in WP3 were introduced in the simulations of these crash subsystem tests.

Task 6.1 Design and fabrication of crash subsystems

A crash subsystem test was designed in order to achieve a better representation of the impact-related load case in a real environment. For that purpose, an existing automotive component, currently in production was selected. The chosen component was a Fiat 500L anti-intrusion door beam, produced usually by DP1200 steel.

Task 6.2 Material selection according to the component and crash requirements

Taking the results of the experimental tests, three different materials were selected for the component impact tests: TBF, DP1000 and CP1000. The selection was made considering the amount of damage achieved in the impact tests and other aspects of interest, as the formability or the manufacturing feasibility.

Task 6.3 Crash tests and comparisons with simulations

With the purpose of testing different load cases, three different setups were proposed for the subsystem crash tests. In the first setup, the component was fixed by two rigid supports and bolted on each side. The fixation of the component is similar to the real situation in the car, but the whole system becomes stiffer, since the deformation of the whole door is not reproduced. In this case, interferences on the test due to the presence of other components are avoided. In this setup the highest damage value observed in simulations was achieved in the fixture zone instead of the center of the component. The low intrusion level allowed by the bolt connection lead to a tearing damage in this zone, causing high strains and consequently a local zone of high damage. In the experimental tests, some specimens showed an unstable deformation caused by this tearing effect. The

deformation of the specimen due to this damage lead to a misalignment in the load, leading to an unstable progression of the test.

In order to avoid damage onset influenced by the specimen fixations, as well as the misalignment of the impactor displacement after damage is onset, further impact tests were performed using a different setup with a pendulum impactor. In the second setup the fixtures of the specimen were improved, including clamps and bolts at both ends of the beam in order to diminish the stress supported in this zone. The pendulum was cylindrical and impacted completely vertical to the component. The fixtures of the pendulum do not allow a vertical deviation of the impactor after damage is onset, as occurred in the last setup.

In order to obtain damage in the centre of the component, but not influenced by fixtures, a third setup was proposed and tested. The central part of the beam was weakened introducing machined notches. By means of this, it is possible to ensure that the maximum damage was reached in that section, away from the supports. This last proposal was tested using the same pendulum equipment as in the second setup.

Task 6.4 Improvement of crash simulations accuracy by means of EWF

The damage evolution law developed in WP3 was implemented in crash simulations. The results with this new damage law in Abaqus adjusted with the EWF tests offered a better correlation in both axial and side impact cases when it is scaled taking into account the mesh influence.

WP7: Implementation of a sheet forming failure criterion

The implementation of the damage model based on EWF previously developed in WP4 was carried in this WP. Such failure criterion is based on the evolution of damage during the ductile fracture and it was used to improve the accuracy of the simulations performed with conventional FLC fracture criteria. Simulations and experimental results were compared in order to check the failure criterion accuracy.

Task 7.1 Material selection according to the components and forming requirements

The materials chosen for this WP were the steel grades selected in WP4 for formability investigations: DP1000, CP1000 and TBF. The manufactured component was the internal reinforcement of sill side for the model Alfa Romeo Stelvio, which in serial production is made from low alloyed steel: LAC340 with 1.5mm of thickness.

Task 7.2 Forming processes and comparison with simulations

In this task the component chosen in task 7.1, the side sill internal reinforcement, was formed by deep drawing in a hydraulic press. Two different cutting conditions were used to obtain the blanks, aimed at evaluating the effect of the edge quality on sheet forming: laser cutting and shearing. In order to investigate the crack initiation and further propagation, the components were formed up to different levels of press stroke. The apparition of cracks for each stroke was examined and results were compared with simulations. It was observed that edge quality has a great effect on the formability of the investigated AHSS grades. For laser cutting condition the three steel grades showed fractures caused by localized necking and no edge cracking was observed. The behaviour of the three steels was in accordance with their FLCs and tensile properties but not with fracture toughness results. On the other hand, in sheared components edge cracks appeared at much lower stroke levels with hardly noticeable necking. The behaviour of the steels in this case was more related to their fracture toughness values.

The simulation of the forming process predicted accurately the zones where fracture appears. However, it was observed that the criterion is too conservative in predicting formability, i.e. fracture is predicted before it appears. This is typically observed in forming simulation of AHSS grades.

Task 7.3 Improvement of forming simulations accuracy by means of EWF

In order to improve the forming simulation, the energetic damage evolution model developed in task 4.5 was implemented in combination with FLC criteria. EWF based criterion was applied in the edges and FLC in the inner part, where the material is subjected to global deformation modes. This

combination of fracture criteria improved the accuracy of simulations, showing the edge points where the fracture starts and a better correlation of fractures in the inner part of the component.

WP8: Management, dissemination and reporting

The objectives of WP8 were to plan and coordinate between all partners the tasks to perform in different work packages, and to follow up the project outcomes vs. the plans. The coordinator of the project, CTM, was the responsible for the project management.

Task 8.1 Coordination, management, reporting and meetings

CTM was the responsible to ensure the accomplishment of the defined milestones and deliverables and the financial administration of the project as agreed in the proposal

The project progress was closely followed by periodic technical progress meetings. Eight progress meetings were held along the project: 3 online and 5 face-to-face.

Task 8.2 Dissemination, including website, workshops and publications

A project website was created to facilitate the exchange of information between all partners, the organization of the meetings and to keep all the participants updated with the latest project's news. The dissemination of the results obtained in the project was carried out by the participation of the partners in diverse conferences and the publication of papers in scientific journals. A list of contributions presented in conferences and published papers is detailed in section 5.5.

1.3 Conclusions

From the results obtained during the Tough-sheet project the following conclusions can be drawn:

- The EWF methodology has shown to be suitable to readily measure the fracture toughness of thin AHSS sheets.
- The EWF values at crack initiation (w_e) have shown to be equivalent to the elastoplastic fracture mechanics toughness value, J_c . In contrast, the EWF for the whole fracture (w_e) has an energetic contribution from crack propagation and it is a good measure of the energy dissipated during the ductile tearing process.
- The simulation of DENT specimens shows a good correlation with experimental test only up to fracture initiation. Thus, it was not possible to simulate the EWF for the final fracture.
- In general, the EWF tends to increase with strain rate.
- AHSS crashworthiness can be ranked according to a cracking pattern, considering crack initiation and propagation events. The CIDR is a suitable parameter to describe the evolution of damage in impact resistance tests and to quantify the crash resistance of AHSS grades. The total energy absorption capacity of the AHSS is inversely proportional to this parameter.
- Fracture toughness, measured in terms of EWF, has shown to be a suitable material property to assess AHSS crashworthiness.
- It has been observed that the EWF is not significantly influenced by pre-straining conditions
- FLCs are suitable to predict sheet fracture under determined deformation modes. However, they fail to predict edge cracking or stretch-flangeability and additional tests are necessary.
- The HER is a good measure of the stretch flangeability of AHSS and is an important parameter to consider in AHSS cold forming.
- The correlation between EWF and HER shows that fracture toughness is useful to rationalize AHSS edge cracking resistance
- Under plane stress conditions the fracture toughness is thickness dependent. In the range of thickness investigated 1-2.2 mm the fracture toughness increased linearly with the sheet thickness in a CP steel.
- The effect of anisotropy on EWF is dependent on the microstructure. However, no large anisotropic effects were found in the investigated steels.
- The application of a damage evolution model based on EWF in forming simulations in combination with conventional FLC criteria has shown an improvement of simulation accuracy.
- Further work is necessary to implement an energy based fracture criterion in crash simulation, able to take into account the energy dissipated in crack propagation.

1.4 Applications

The experimental application of the EWF will be a useful tool to not only select commercially available steel grades with high crashworthiness and edge cracking resistance but also will help to the development of new AHSS with enhanced fracture resistance. The methodology may be implemented as an additional quality criterion for forming and crash applications.

The developed ductile damage evolution models based on the EWF will help to improve the accuracy of forming simulations, especially in areas where FLCs fail to predict the fracture, such as stretched edges, expanded holes, etc.

2. SCIENTIFIC AND TECHNICAL DESCRIPTION OF THE RESULTS

2.1 Objectives of the project

The main objective of Tough-sheet was to measure the fracture toughness of thin AHSS sheets by means of the essential work of fracture (EWF) methodology, aimed at providing a new mechanical property able to define their cracking resistance and improve material selection in cold forming and crash applications. Other secondary objectives were: a) to develop a new fracture criterion based on EWF, aimed at enhancing sheet failure prediction and b) to check the usefulness of fracture toughness as a suitable material property to develop new high strength steel grades with improved formability and crash performance.

2.2 Description of activities and discussion

This section describes, task per task, all the work performed during the Tough-sheet project and the main results and conclusions obtained from the investigations.

2.2.1. WP1. Mechanical characterization of AHSS

The main objective of WP1 was to characterize the mechanical behaviour of the investigated AHSS grades and to prepare the blanks for the rest of investigations carried out in the project.

The tasks corresponding to this WP are listed in Table 1.

Table 1. Tasks of the WP1

Task	Name of the task
Task 1.1	Material and samples preparation
Task 1.2	Mechanical characterization
Task 1.3	Laboratory impact resistance tests
Task 1.4	Laboratory forming tests

Task 1.1 Materials and samples preparation

Nine industrially produced AHSS grades were investigated in the project. Eight grades have been supplied by voestalpine and one grade by CRF. These steels are:

- 3 commercially available first generation AHSS cold forming grades (DP1000, CP1000 and CP1200)
- 3 new developments of 3rd generation AHSS: 1 TBF steel (bainitic ferrite matrix with retained austenite), 1 Q&P steel (tempered martensite matrix with retained austenite), and 1 mixed TBF/Q&P microstructure.
- 2 microstructures of hot stamped boron steel: one in the press hardened condition (strength of about 1500 MPa) and the other with an additional tempering treatment (strength of about 1000 MPa).
- 1 TWIP (Twining Induced Plasticity) steel with a fully austenitic microstructure.

Table 2. Steels investigated. UC=uncoated, Z=zinc coated

Steel grade	Cold rolled thickness [mm]	Coating
TWIP	1.4	UC
CP1000	1.0, 1.4, 2.0, 2.2	UC, Z
DP1000	1.4	UC
CP1200	1.6	UC
TBF	1.5	UC
Q&P	1.4	UC
TBF/Q&P mixed	1.4	UC
PHS1500	1.5	Z
PHS1000		

The thickness of the grades is shown in Table 2. Annealing of the CP1000, DP1000, CP1200, TBF, Q&P and mixed steel grade was conducted on the continuous annealing line (CAL) in VAS. For the

investigations on the influence of sheet thickness on the fracture toughness, three CP1000 grades with thickness 1.0, 2.0 and 2.2 mm were produced via the hot dip galvanizing line (HDGL). PHS grades were annealed and galvanized on the hot dip galvanizing line, too. Press hardening and tempering of the PHS grades was performed after the HDG route. From the finished grades, samples for the investigations were taken at an inspection line and sent to the project partners. For both PHS grades, press hardening was performed on sheets with size 590x600 mm² by heating them up to 870 °C. After annealing the samples for 45 s, the sheets were cooled with >30 K/s by placing them between water cooled press-hardening cooling plates. For the tempered PHS1000, the hardened samples were heat treated in a furnace at 475 °C for 900 s. The TWIP steel was provided by CRF and shipped to the project partners in the form of blanks with a size of 1000x1025 mm².

The rough chemical composition of these steels is shown in Table 3.

Table 3. Chemical composition of the industrial produced grades [mass%]

Steel grade	C	Si	Mn	Cr	B	Al
CP1000	~0,1					
DP1000	~0,15	<0,5	1,8-2,2			
CP1200	~0,15					
TBF	~0,2					
Q&P	~0,1	0,5-1,0	2,2-2,6			
TBF/Q&P mixed	~0,1					
PHS1500				<0,7		
PHS1000					~0,003	-
TWIP	~0,5	0,10-0,15	~15	~0,1	-	~1,0

Task 1.2 Mechanical characterization

Microstructure

A basic microstructural investigation was performed with the different AHSS grades. Table 4 shows the main constituents of the microstructure of the grades investigated. The retained austenite content was measured with the saturation magnetization method. Additionally, the microstructures were examined by LOM and SEM. SEM images (magnification 20000x) after electro-polishing of the samples are shown in Figure 2 to Figure 4.

Table 4. Characterized steel grades, main constituents of microstructure and retained austenite content

Steel grade	Microstructure	Retained austenite content V _y [%]
CP1000	bainite/tempered martensite B/TM	1.3
DP1000	ferrite/bainitic ferrite F/BF; martensite M; bainite/tempered martensite	4.3
CP1200	bainite/tempered martensite	1.4
TBF	ferrite/bainitic ferrite; bainite/tempered martensite; martensite; martensite/retained austenite M/RA	11.2
Q&P	bainite/tempered martensite	6.0
TBF/Q&P mixed	bainite/tempered martensite; retained austenite	8.4
PHS1500	martensite	3.3
PHS1000	tempered martensite AM	2.3

CP-like grades (CP1000, CP1200, mixed) as well as the Q&P grade show a homogeneous matrix of bainite/tempered martensite. In DP1000 grade and TBF grade the matrix consists of a mixture of ferrite, bainitic ferrite, bainite/tempered martensite and martensite. TBF and the mixed grade show the highest amount of retained austenite. PHS1500 consists of a homogeneous martensitic matrix, which is slightly auto-tempered during cooling. The tempering treatment for PHS1000 basically leads

to relaxation of the tetragonal martensite lattice by formation of carbides, which can be observed as white lines and spots in Figure 4.

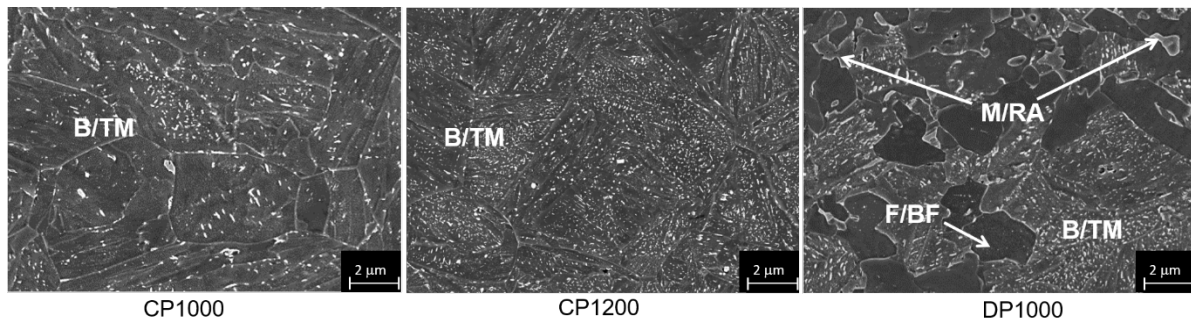


Figure 2. SEM microstructure of CP1000, CP1200 and DP1000 grade

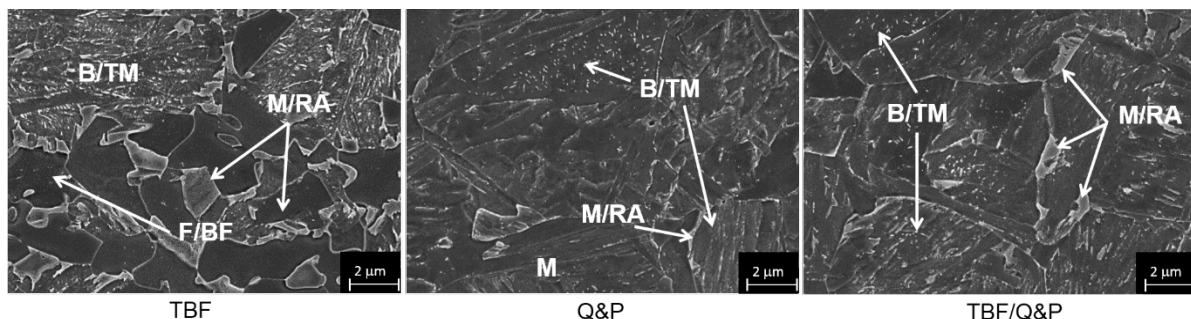


Figure 3. SEM microstructure of TBF, Q&P and TBF/Q&P grade

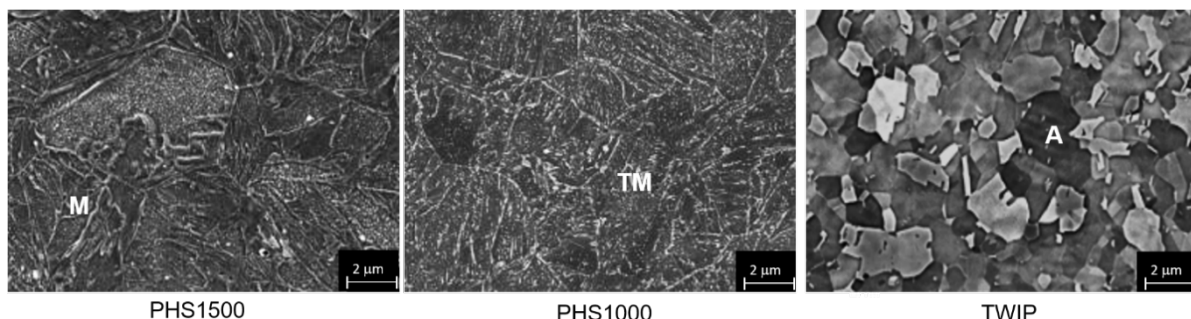


Figure 4. SEM microstructure of PHS1500, PHS100 and TWIP grade

Tensile tests

Conventional tensile tests were performed according to DIN EN ISO 6892-1 for 0°, 45° and 90° to the rolling direction. Table 5 shows the results of conventional tensile tests transverse to the rolling direction. Corresponding tensile curves are plotted in Figure 5 and Figure 6. In general, AHS steel grades with lower tensile strength exhibit higher uniform and ultimate elongations. Within each class of strength, elongations are controlled by strain hardening, which is increased by high hardness differences between phases (e.g. untempered martensite - ferrite) and transformation of retained austenite. Therefore, DP1000 shows higher elongation than CP1000 and for all grades, higher retained austenite content increases uniform and ultimate elongations. TBF reaches the highest elongation of the AHS steel grades. High strain hardening also increases the specific energy absorbed during uniaxial tension $R_m^*A_{80}$. DP-type microstructures with bainitic ferrite and martensite lead to the lowest yield strength (DP1000, TBF), whereas microstructures with homogeneous bainitic/tempered martensite matrix cause higher yield strength in uniaxial tension (CP1000, CP1200, Q&P, mixed). PHS1500 reveals the highest tensile strength but the lowest elongation at fracture. However, strain hardening is lowest for the PHS1000. TWIP steel has the lowest yield strength of all investigated steel grades. Strain hardening decreases little with increasing strain, which leads to the very high uniform elongation of 55 percent. In comparison to its uniform elongation, the post-uniform elongation ($A_{80}-A_g$) is quite small.

Table 5. Tensile parameters of grades transverse to rolling direction

	Rp0.2	Rm	Ag	A80	n2-4	Rm*A80
	MPa	MPa	%	%	-	MPa*%
CP1000	908	1002	4.5	8.1	0.05	8152
DP1000	738	1027	6.9	10.3	0.10	10547
CP1200	1041	1218	3.4	6.0	-	7265
TBF	725	1019	10.1	14.7	0.12	15018
Q&P	909	1209	4.7	7.4	0.09	8944
mixed	876	1026	7.5	11.3	0.09	11598
PHS1500	1075	1552	3.7	5.2	0.08	8070
PHS1000	988	1007	4.9	7.3	0.05	7351
TWIP	530	969	55.0	59.5	0.11	57632

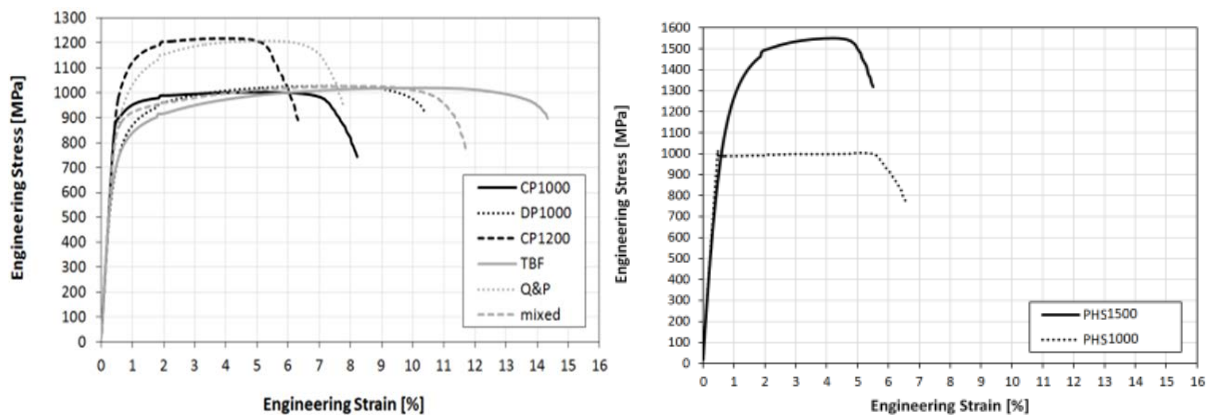


Figure 5. Uniaxial tensile curves of CP1000, DP1000, CP1200, TBF, Q&P, mixed, PHS1500 and PHS1000 grade transverse to rolling direction

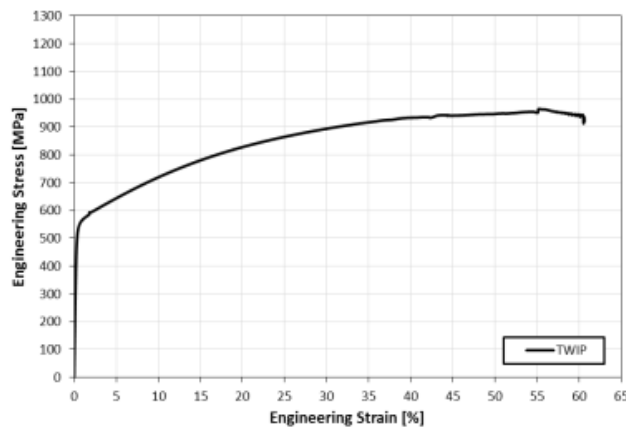


Figure 6. Uniaxial tensile curve of TWIP grade transverse to rolling direction

DIC-assisted tensile tests

Conventional tensile tests using a Digital Image Correlation (DIC) equipment were performed in this task. The DIC system permits to monitor and determine the strain during the whole test. Thus, it allows to measure local strains within the necking area. The local strain level after necking are greater than the obtained by conventional extensometry and it better defines the local ductility potential of the material. The curves obtained from the strain determined in the necking area are shown in Figure 7. The values of local strain at fracture for the investigated steel grades are summarized in Table 6.

Results from DIC-assisted tensile tests show that elongation at fracture from conventional tensile tests totally underestimates the local post uniform ductility of the investigated AHSS and steels with poorer elongation at fracture can show greater local strain at fracture and vice versa. In all cases, the values of local strain at fracture are much greater than conventional A₈₀. CP1000 presents one

of the highest local strain at fracture, in contrast to the relatively low elongation from conventional tensile tests. The opposite case is shown by DP1000 and TBF, which present a great elongation A80 but the poorest local fracture strains together with PHS1500. In general, CP-like grades (CP1000, CP1200, mixed and Q&P) show greater local fracture strain than DP-like (DP1000 and TBF) and martensitic (PHS1500) steels. TWIP steel shows the greatest local ductility.

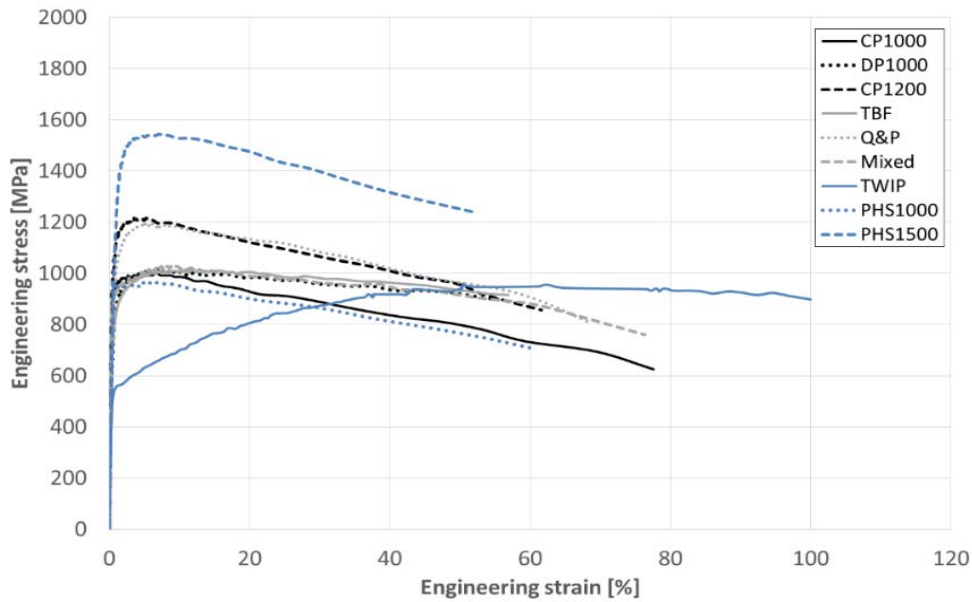


Figure 7. Local engineering stress-strain curves obtained from DIC

Table 6. Local strain at fracture values obtained from DIC-assisted tensile tests

	ϵ_f Local
	%
CP1000	77.6
DP1000	56.4
CP1200	61.6
TBF	56.9
Q&P	68.7
mixed	76.4
PHS1500	52.1
PHS1000	60.1
TWIP	99.9

Bulge tests

For the bulge tests, a round blank was biaxially stretched by hydrostatic pressure. Strain was measured by ARAMIS optical system. Sample thickness, local curvature and oil pressure was used to calculate the true stress and true strain. Obtained flow curves can be seen in Figure 8. It was not possible to perform the bulge test for PHS1500 grade due to the high strength of PHS1500. When comparing CP1000, DP1000, CP1200, TBF, Q&P and mixed grade, the above described correlations between microstructure and strain hardening in tensile tests are also valid for the flow curves of bulge tests. The three materials with higher retained austenite content exhibit higher strain hardening and higher failure strain than those with less retained austenite content when compared at similar microstructure matrix and strength level (TBF- DP1000, Q&P-CP1200, mixed-CP1000). PHS1000 shows the lowest strain hardening. TWIP steel shows the highest strain hardening, failure stress and failure strain in bulge test. It is interesting that although DP1000 and TBF show higher strain hardening in biaxial tension and higher uniform elongation in uniaxial tension than CP1000, they exhibit the lowest failure strains of all six grades in biaxial tension. The mixed grade reaches high failure strain, although its hardening capacity is comparable to DP1000 and TBF. The values of strain at fracture are similar to the obtained in DIC-assisted tensile tests.

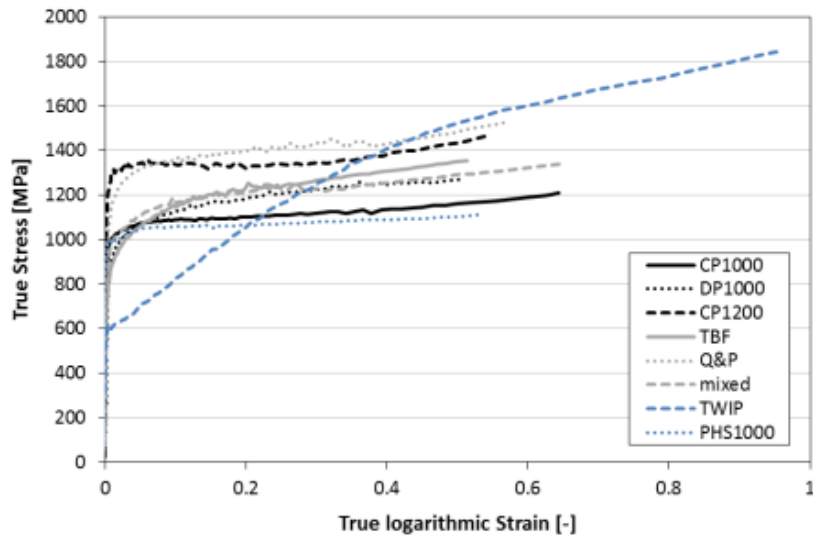


Figure 8. Flow curves of the investigated steel grades from bulge tests

Task 1.3 Laboratory impact resistance tests

In this task, laboratory axial and bending impact resistance tests were conducted for each steel grade. The simulator for impact resistance tests at voestalpine works with a load mass of 283 kg, whose speed can be varied between 10 and 40 km/h. In order to obtain detailed information about damage initiation and damage growth during the deformation of the crash samples, experiments were carried out with a number of different load mass speeds. Hat profile samples of cold forming grades for axial and bending impact tests were formed by die bending (Figure 9). PHS hat profile samples for both axial and bending impact tests were produced by indirect press hardening (preforming at room temperature, subsequent austenitization and press hardening similar to the blank material). PHS1000 crash samples were spot-welded to the closing blanks in hardened condition before tempering in a chamber furnace. Axial hat profiles were spot-welded to a closing blank of the same steel type as the profile itself. Also at the front and back, closing blanks were welded to the profile. For bending impact test samples, a microalloyed steel grade was used as closing blank of the hat profile.

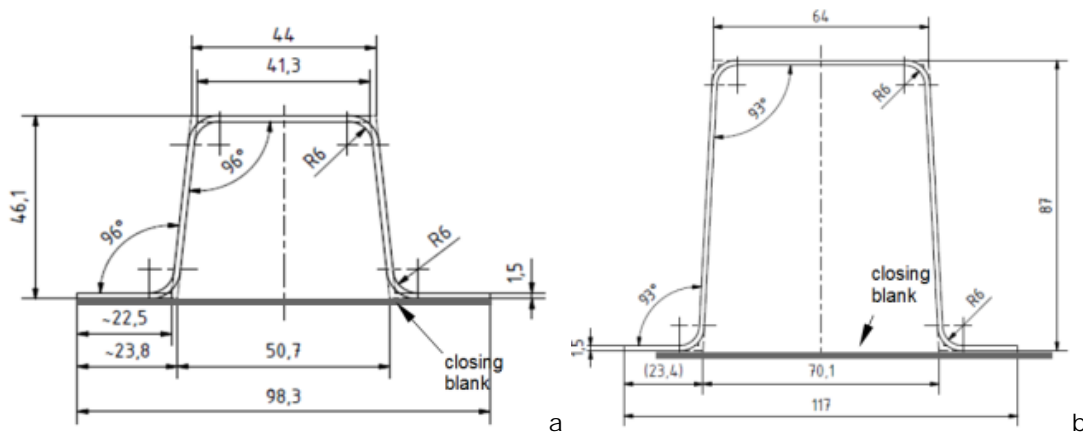


Figure 9. a) geometry of axial (length=300 mm) and b) bending (length=900 mm) crash samples.

Results - axial impact resistance tests

Axial impact tests were evaluated by determination of an overall crash index (CI) for each deformed crash sample (definition in Table 7). However, CI gives no information about location or cause of crack initiation. Crack initiation can result from failure of the bulk material due to the emerging fold geometry, as well as damage induced at the welding spot. Intrusions of axial impact tests in the following content include only plastic deformation and were determined by the difference in length of unloaded and crashed samples.

Table 7. Definition of the CI [LAR10]

Crash index	Damage
100	no cracks
>75	crack length < 10 mm
50-75	10 mm < crack length < 25 mm
25-50	crack length > 25 mm
<25	"splitting and curling"; multiple breaks

Evaluation of crash index as a function of intrusion shows differences in first initiation of cracks and in the slope in decrease of crash index (see Figure 10 to Figure 12). Best resistance is achieved for CP1000, PHS1000 and TWIP, which maintain a very good crash index up to high intrusions. TBF and mixed steel grades reach a crash index of 40 or more up to intrusions of 100 mm and higher. This means that cracks have not propagated through the whole fold. Crash indices of DP1000, CP1200, Q&P and PHS1500 rapidly decrease with increasing intrusion.

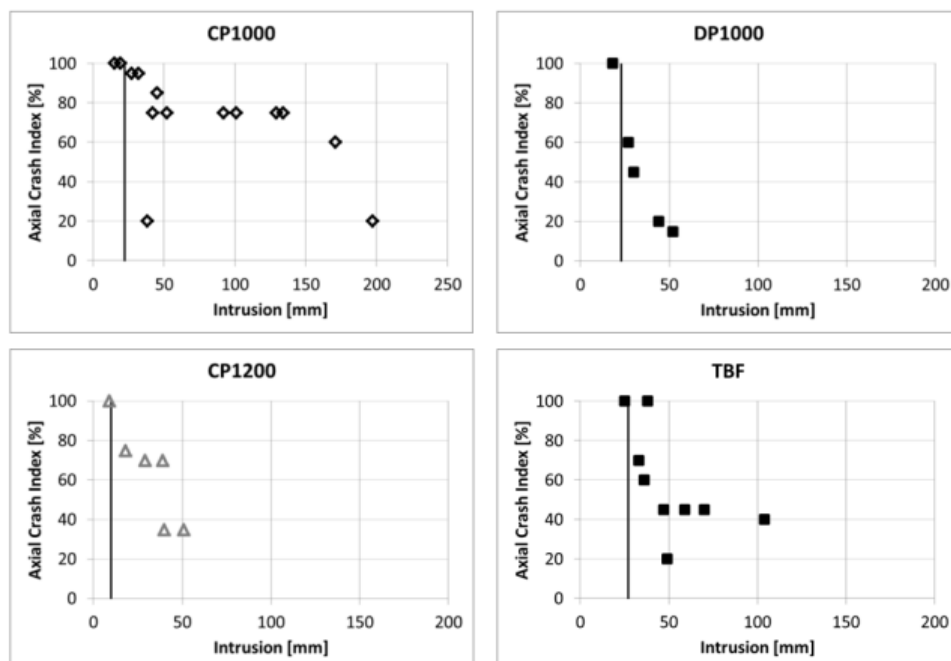


Figure 10. Crash index vs. Intrusion at axial impact tests for investigated steel grades.

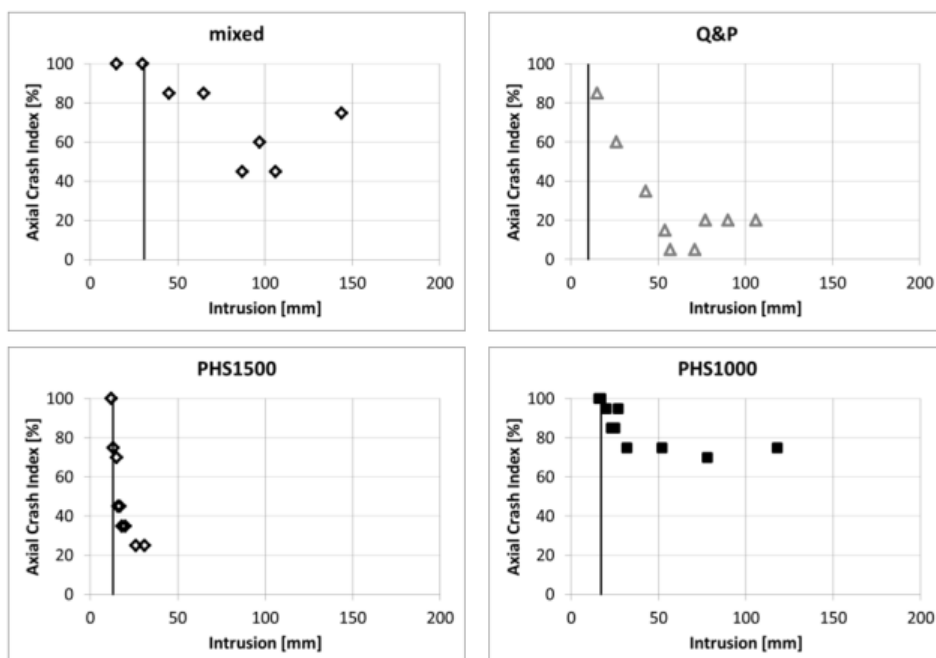


Figure 11. Crash index vs. intrusion at axial impact tests for investigated steel grades.

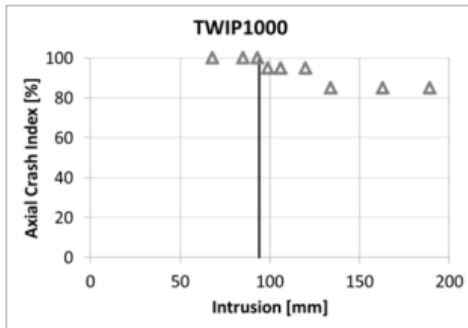


Figure 12. Crash index vs. intrusion at axial impact tests for TWIP steel.

Results - bending impact resistance tests

During bending impact tests, crash samples were bent between bearings with a distance of 700 mm by a fin with radius of 125 mm. Load mass was 86 kg. Cracks initiated at the same location for all investigated steel grades during bending impact test. The set up for the bending impact tests is shown in Figure 13. The high radius of the fin triggers localized bending deformation in the middle of the sample and cracking at this very position. Crash index of bending impact samples was derived from the occurring crack length and calculated according to [LAR15]. The formula for calculation the crash index is shown in Figure 13. The deformation process during the bending impact test was recorded with a high-speed camera and analysed to determine the elasto-plastic intrusions of the samples. Intrusions of bending impact tests in the following content include plastic and elastic deformation. Bending impact samples do not show any welding spot failure, which means that the corresponding results characterize the sole behaviour of the base material.

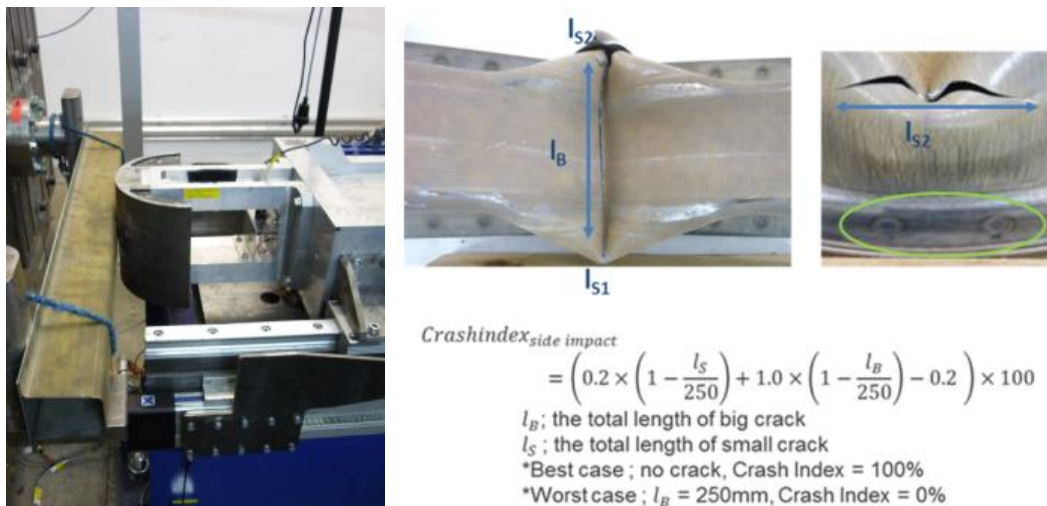


Figure 13. Crash index vs. intrusion for TWIP steel.

Evaluation of crash index as a function of intrusion is shown in Figure 14 to Figure 16 for the steel grades investigated. Due to the limited maximum intrusion (211 mm), it was not possible to trigger crack formation in all investigated steel grades. In case that no damage was observed, at least 3 samples were crashed to the maximum possible intrusion, as for CP1000, mixed, PHS1000 and TWIP. For the other steel grades, crack initiation took place at different critical intrusions, and crack length with increasing intrusion was documented in terms of crash index. In contrast to axial impact tests, there is no large difference in crash index vs. intrusion curve slope between the investigated steel grades with formed cracks.

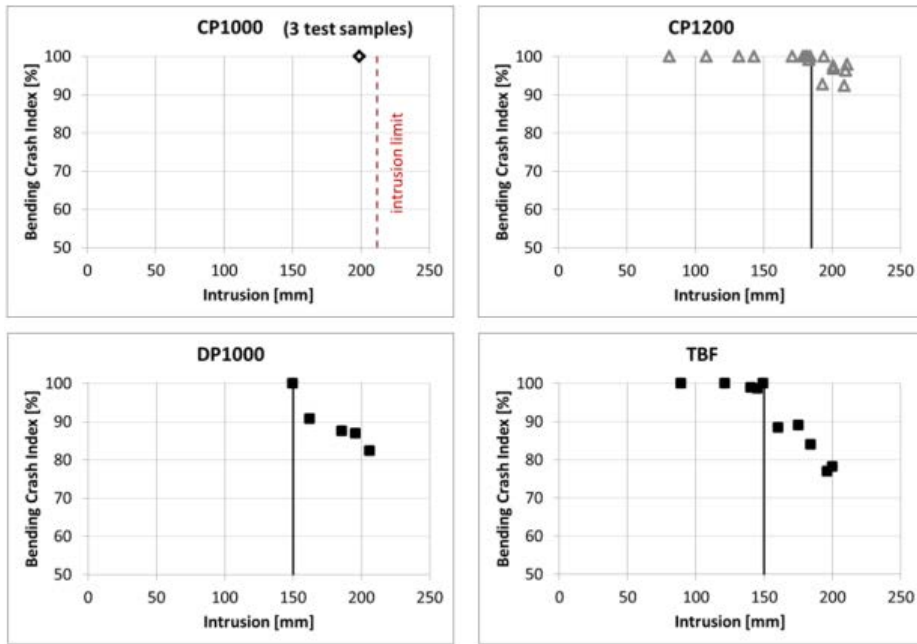


Figure 14. Crash index vs. intrusion at bending impact tests for investigated steel grades.

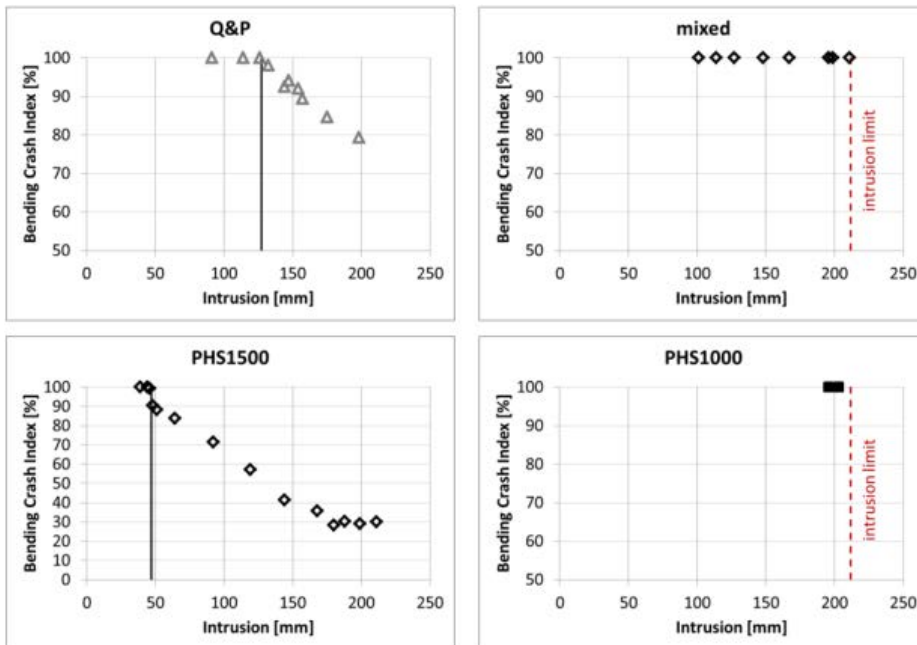


Figure 15. Crash index vs. intrusion at bending impact tests for investigated steel grades.

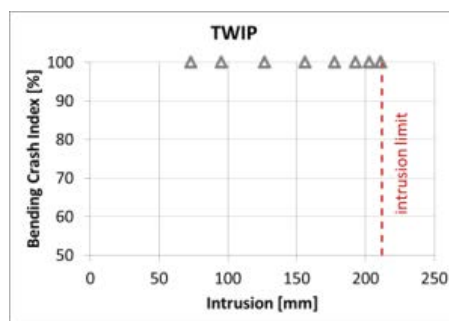


Figure 16. Crash index vs. intrusion at bending impact tests for investigated steel grades.

Dynamic tensile tests

In order to assess the effect of strain rate on tensile properties and quantify the strain rate sensitivity of the investigated AHSS grades, dynamic tensile tests at different strain rates were performed:

- Low strain rate: 5 s^{-1}
- Medium strain rate: 50 s^{-1}
- High strain rate: 500 s^{-1}

Low and medium strain rate tests ($5-50 \text{ s}^{-1}$) were performed in a hydropneumatic machine. Strain measurements were carried out by means of a DIC equipment. For high strain rate (500 s^{-1}) tensile tests a Modified Hopkinson Bar (MHB) machine was used (Figure 17). The operation of MHB is described below.

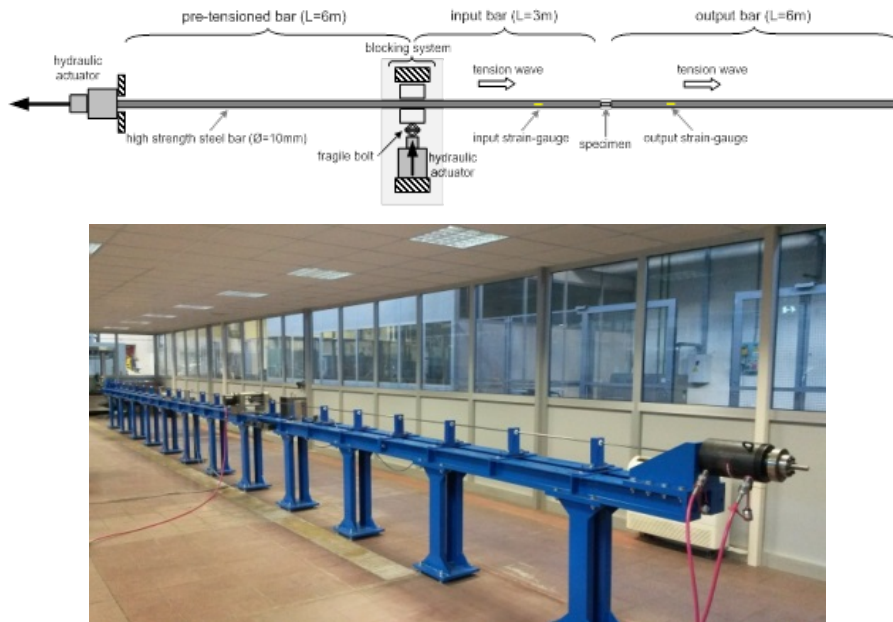


Figure 17. Schematic representation of the MHB machine (top) and image of the MHB machine at CRF.

The tensile load pulse is generated by releasing a certain amount of elastic mechanical energy stored in a portion of the input bar (pre-tensioned bar) through static tensioning, up to a maximum stress value lower than its yield stress. For this purpose, a mechanical clamp is used to grip the incident bar. The section of the incident bar between the clamp and the hydraulic actuator carries a static tensile load. The remainder of the input bar (to the right of the clamp) is unloaded. When the elastic mechanical energy is stored in the pre-tensioned bar and the specimen is inserted between the input and output bar, a notched bolt in the clamp is broken using a second hydraulic actuator, and an elastic tensile pulse is generated, propagating down the incident bar from the clamp toward the specimen. This pulse has a duration that is the double of the elastic wave travel time to move from the clamped section toward the free end of the input bar, and an amplitude that is half of the initial stored tensile pulse. As the wave reaches the input bar-specimen interface, a part of the pulse is reflected as a compression wave into the input bar and the remaining part is transmitted through the specimen. When the wave transmitted into the specimen arrives at the specimen-output bar interface, it is partially transmitted into the output bar and partially reflected into the specimen. If the specimen length is short so that the time taken by the wave to propagate through the specimen is short compared to the total time of the test, many reflections inside the specimen are created, allowing an homogenous stress and strain distribution along the specimen gauge length until fracture.

In this case the total length of the input bar is 9m, the portion of it that is pre-tensioned during the test is 6m, and the output bar length is 6m; both bars have a diameter of 10mm and are made in high strength steel. This configuration permits to achieve tensile pulse duration of 2.4ms, allowing the deformation at constant high strain rate until fracture of high ductility specimens.

The semi-conductor strain-gage station is glued on the input bar at 750mm from the specimen, in order to record the deformation ε_I of the bar generated by the incident tension pulse during the propagation toward the specimen and the deformation ε_R , caused by the part of the incident tension pulse reflected at the interface incident bar-specimen. Such reflection is correlated with the deformation of the specimen. Another strain-gage is glued on the output bar at the same distance from the specimen as

the strain-gauge on the incident bar. This second strain-gauge is used to record the deformation ϵ_T provoked on the bar by the part of the incident pulse which was sustained by the specimen and was, therefore, transmitted to the output bar. The transmitted pulse is proportional to the engineering stress in the specimen. A third strain-gauge station is bonded in the pre-tensioned bar to check the preload.

On the basis of the recorded signals ϵ_I , ϵ_R and ϵ_T , and applying the one-dimensional elastic plane stress wave propagation theory to the input bar-specimen-output bar system, it is possible to calculate the stress, strain and strain-rate in the specimen. With the described apparatus it is possible to test a wide range of materials at high strain rate, in the range of 500-1500s⁻¹.

The obtained true stress-strain curves from the tensile tests at different strain rates are shown in

Figure 18 and Figure 19.

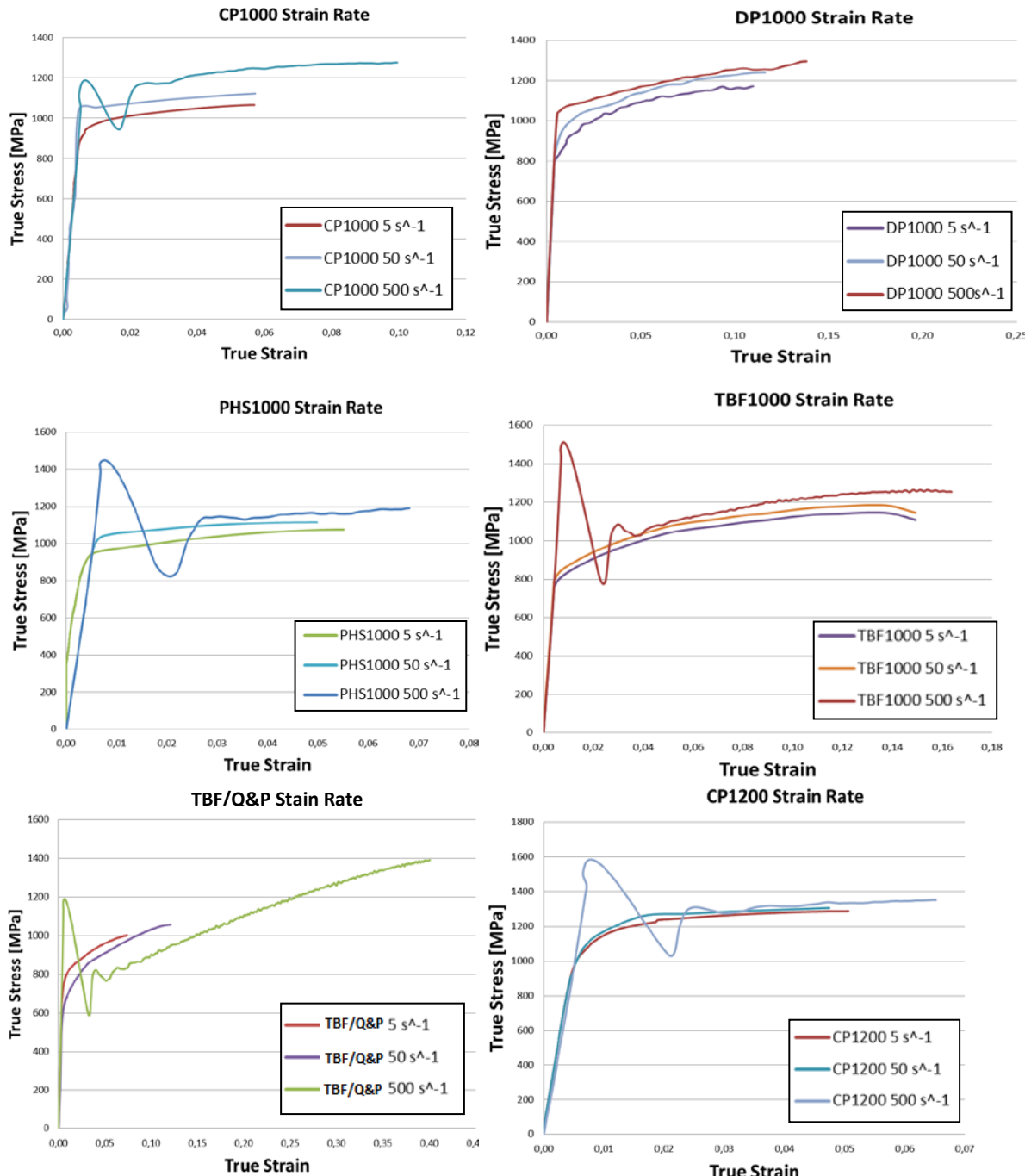


Figure 18. True stress-strain curves from dynamic tensile tests for CP1000, DP1000, PHS1000, TBF, TBF/Q&P and CP1200

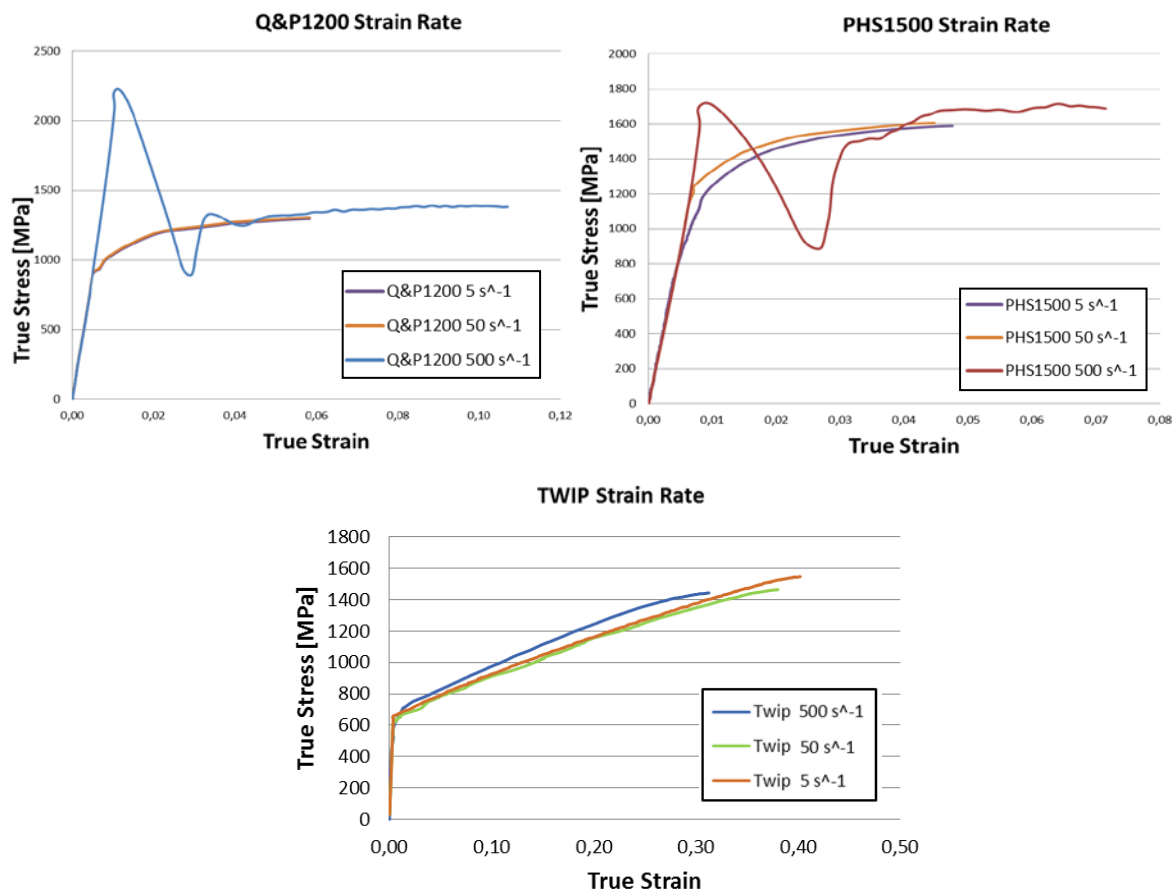


Figure 19. True stress-strain curves from dynamic tensile tests for Q&P, PHS1500 and TWIP

No significant effect on tensile properties was observed at medium strain rates (50 s^{-1}) in any of the investigated AHSS grades. Some steel grades showed a slight increase of yield strength and maximum strength (CP1000, PHS1000 and DP1000), but no noticeable differences were found regarding the elongation at fracture. At high strain rates (500 s^{-1}) such differences were more remarkable, especially in elongation values. Most of the steel grades studied showed much higher elongation at fracture at high strain rates, except DP1000, TBF and TWIP. In general, it was observed an increase of mechanical properties at high strain rates. TWIP steel was the only grade that showed a moderated negative strain rate effect. CP1000 and mixed grades presented the highest strain rate sensitivity. The latter exhibited a marked softening effect, especially at high strain rate.

Task 1.4 Laboratory forming tests

The formability of the investigated steel grades was assessed through Forming Limit Diagrams (FLD) and Hole Expansion Tests (HET). The FLD together with the Forming Limit Curves (FLC) provides a method for determining process limitations in sheet metal forming and are used to assess the stamping characteristics of sheet metal materials. Usually, they are used in method planning, tool manufacturing and in tool workshops to optimize stamping tools and their geometries. The comparison of deformations on stamped metal sheets with the FLC leads to a security estimation of the stamping process and provides a reliable assessment of sheet metal forming processes.

The FLC is based on the assumption that for forming purposes, the maximum deformation is limited by the initiation of unstable deformation, e.g. necking. When forming metal sheets the material is subjected to different strains and strain paths, which have been found to have different maximum allowable deformations. Hence, these curves represent the maximum and minimum strain that the sheet may withstand without necking or failure at different deformation modes. The FLCs were determined for cold forming steel grades (this excludes PHS grades) according to the ISO12004:2008 by means of Nakajima and Marciniak stretching tests.

Nakajima tests

The most common method for measuring sheet forming limits is the Nakajima test, which uses a hemispherical punch and a circular grid for the analysis and measurement of strains. The main

advantages of the Nakajima test consist, on one hand, in the fact that the forming tool is very simple, and on the other hand, it allows the determining of the FLC on the whole usual domain of the strains. Also, the geometry of the test samples is a very simple one. The main disadvantages reside in the possibility that a wrinkling of the test sample occurs during the forming process, in the appearance of measurement errors due to the punch's curvature and in the necessity to use various lubricants. In the test, the specimen geometry determines the strain path. Figure 20 is a schematic representation of the Nakajima test.

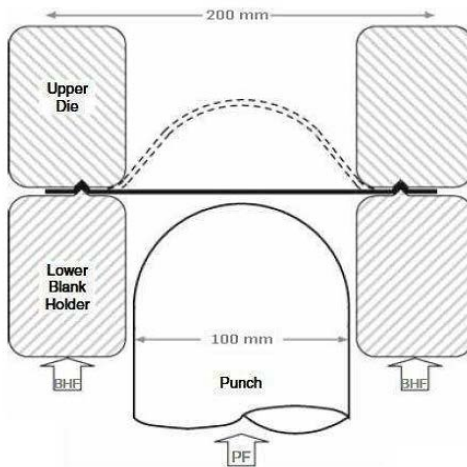


Figure 20. Nakajima test

For the Nakajima test, CRF forming tests laboratory generally use the following machine parameters, reported in Table 8. Grease, Teflon and polyurethane disk were inserted between the punch and the sample, in order to reduce at the minimum the friction between the two parts. Six different geometries were used to construct the FLC (Figure 21, the complete disk is not depicted). The difference between each specimen geometry was the shaft width; changing that dimension it is possible to obtain different stress-strain conditions:

- 20 mm geometry, pure shear
- 60 mm geometry, uniaxial stress
- 100 mm geometry, plain strain condition
- 140-170 mm geometries, intermediate condition between plain strain and plane stress condition
- 215 mm geometry, biaxial tension condition.

Plane strain FLC₀ values for each steel grade are reported in Table 9.

Table 8. Equipment parameters for Nakajima test

Blank Holder Force [kN]	Punch Speed [mm/min]
600	90

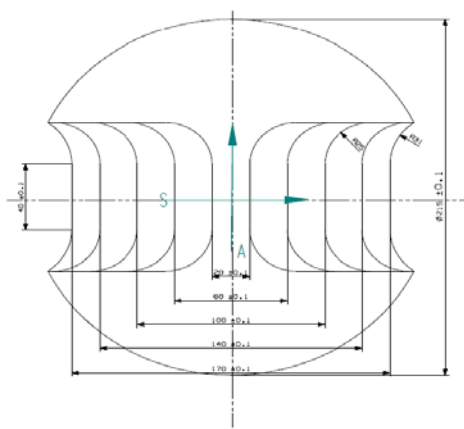


Figure 21. Nakajima and Marcinia sample geometries

The FLCs obtained from Nakajima tests are shown in Figure 22 and Figure 23.

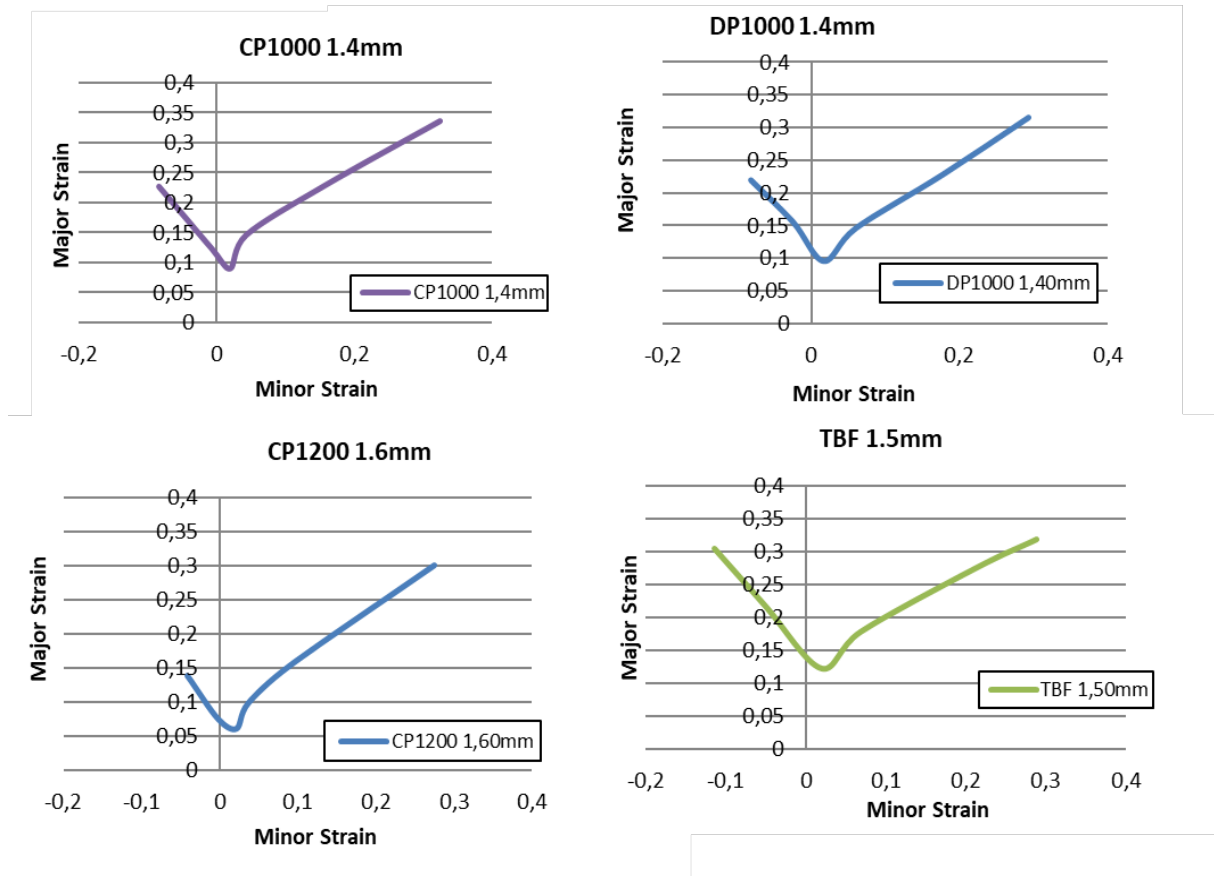


Figure 22. FLCs obtained from Nakajima tests for CP1000, DP1000, CP1200 and TBF.

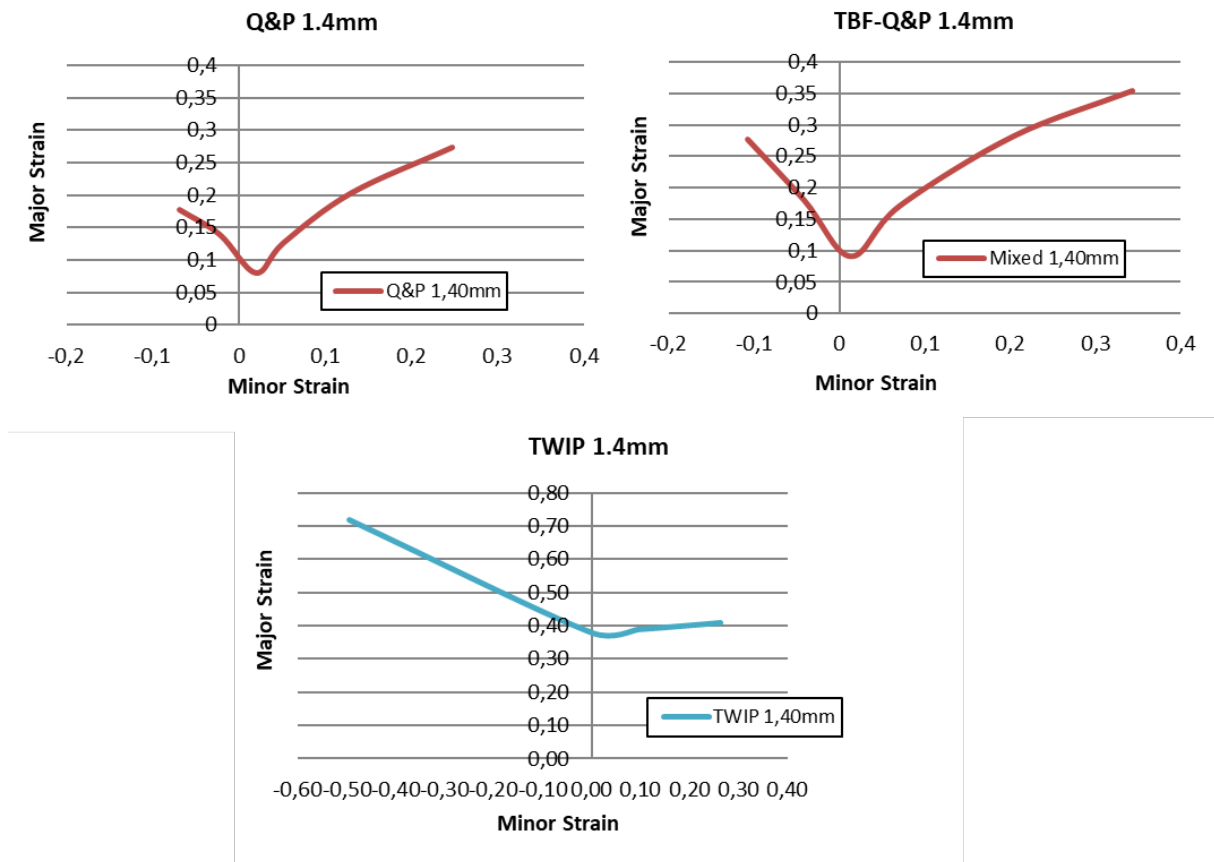


Figure 23. FLCs obtained from Nakajima tests for Q&P, TBF/Q&P and TWIP.

Table 9. FLC_0 for each steel grade in Nakajima test.

Material	FLC_0
CP1200	0.0617
DP1000	0.0957
Mixed 1000	0.0912
Q&P 1200	0.0798
TBF 1000	0.122
CP1000	0.09
TWIP 1000	0.39

The results showed that the FLC_0 for 1000 MPa grades is around 0.1, on the contrary for 1200 MPa grades the major strain in plane strain condition is lower, around 0.05. TBF and TBF/Q&P steel grades exhibited better formability, especially in uniaxial strain paths (left side of the FLD). The strain levels in biaxial deformation modes (right side of the FLD) were very similar for all the steel grades, except for TWIP steel. TWIP steel showed greater formability properties, with an FLC_0 of 0.4 and higher major and minor strains in all cases.

Marciniak tests

The Marciniak method has higher experimental complexity than the Nakajima one. However, strains in the Nakajima experiment are not completely proportional. The initial strain is always bi-axial. Then the strain path gradually changes towards the final path imposed by the sample geometry and material properties. Such bi-axial pre-strain causes that FLC_0 is not centered in the x-axis ($\varepsilon_2=0$), but it is moved to the right side of the FLD. The specimen geometry is the same as the one used for the Nakajima test.

The main difference between the Nakajima and the Marciniak tests is the punch geometry (Figure 24). The Marciniak test uses a flat punch; furthermore an additional sheet metal with a hole in the centre, called carrier blank (Figure 24), was used to prevent the contact between the punch and the tested blank. It prevents failure of the blank outside the region of interest and localizes necking in the center of the planar zone of the blank. The machine parameters for Marciniak formability tests are described in

Table 10.

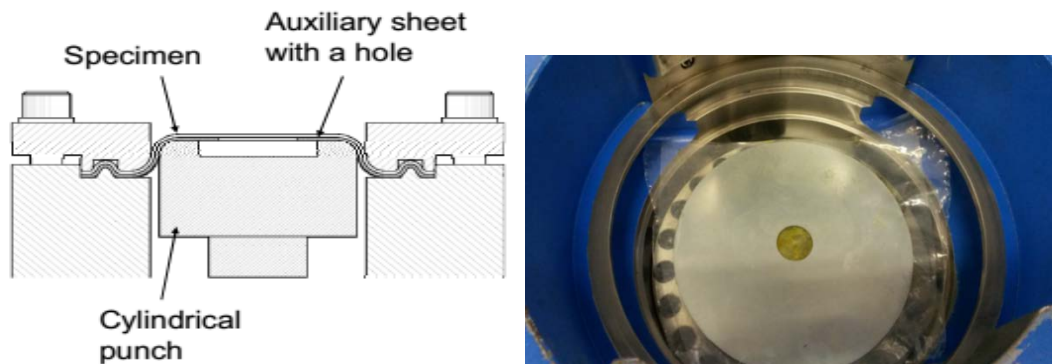


Figure 24. Marciniak test (left) and image of the carrier blank (right).

Table 10. Equipment parameters for Marciniak test

Blank Holder Force [kN]	Punch Speed [mm/min]
600	67

Results of Marciniak formability tests are shown in Figure 25. The data points are compared to the FLC obtained with Nakajima tests. The FLC_0 values obtained with Marciniak tests are summarized in Table 11. In general, it was observed that the strain values are lower than the observed with

Nakajima tests, especially in plane strain FLC₀ and uniaxial deformation modes. This effect is less pronounced in biaxial deformation modes and it was negligible in most steel grades.

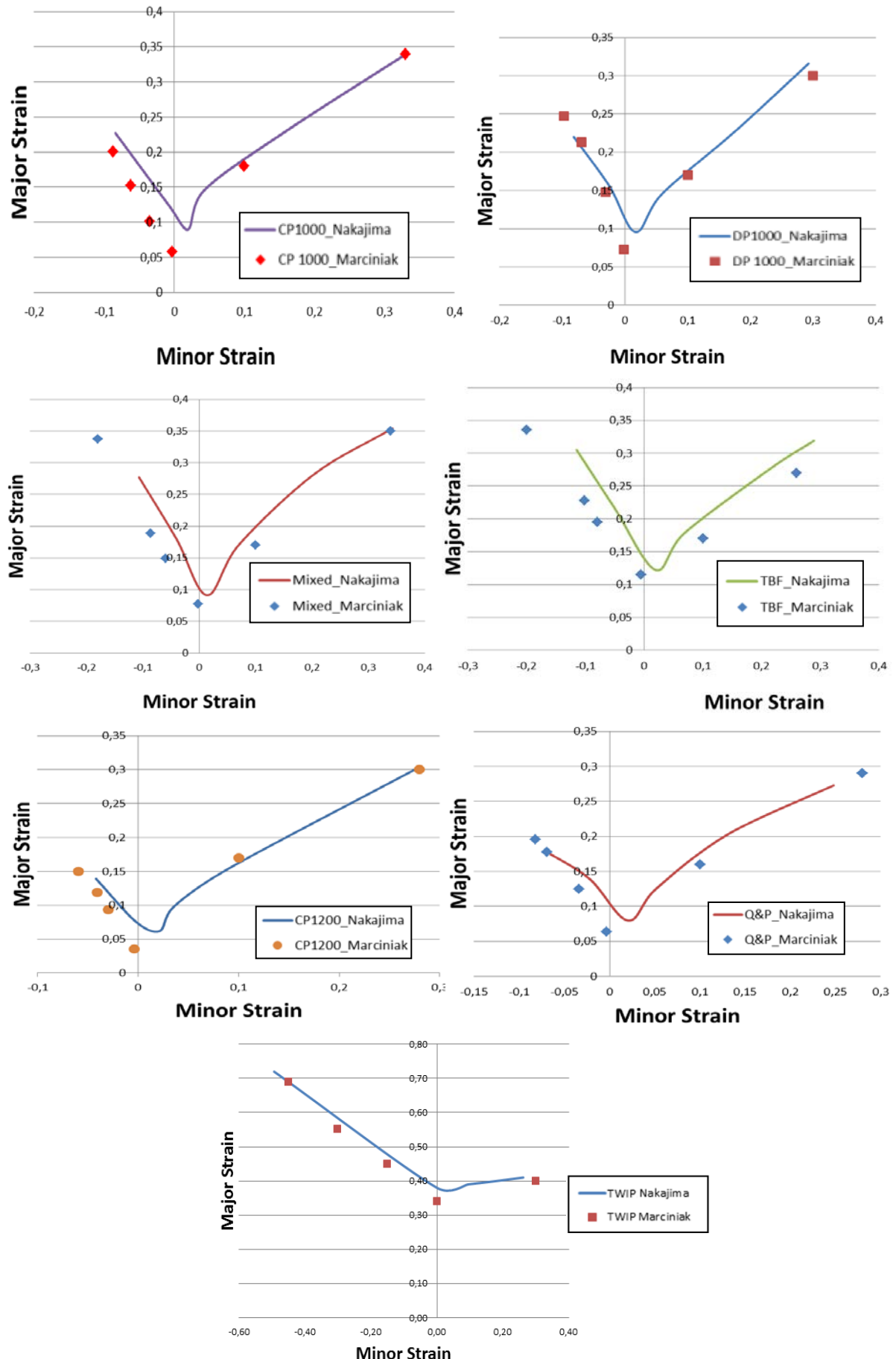


Figure 25. Results of Marciniak tests compared to the FLCs obtained with Nakajima tests.

Table 11. FLC₀ for each steel grade in Marciniaik test.

Material	FLC ₀
CP1200	0.0355
DP1000	0.0731
Mixed	0.077
Q&P	0.0636
TBF	0.115
CP1000	0.0584
TWIP	0.324

Hole Expansion Tests (HET)

FLCs are suitable to evaluate the formability of AHSS under general deformation modes (uniaxial strain, biaxial strain, plane strain...), where the fracture is preceded by a very localized necking. However, for shearing or edge stretching the fracture occurs before considerable necking and FLC strongly overestimates the strain level at fracture. For this reason, additional tests are required to evaluate the stretch flangeability of AHSS. Stretch-flangeability has become an important formability parameter in addition to FLD and tensile properties, particularly for complicated auto body parts or parts under heavy deformation conditions. Stretch-flangeability is usually evaluated through Hole Expansion Tests (HET). The HET closely resembles the forming operations starting with die-cut or punched holes and it is the most used method to evaluate the suitability of the sheet steel for forming such flanges. HET were performed at CTM following the guidelines established in the ISO16630 standard. The value obtained in this test is the Hole Expansion Ratio (HER), which is calculated using the initial hole diameter D_0 and the diameter at first through thickness crack apparition D_h as follows:

$$HER[\%] \text{ or } \lambda = \left[\frac{D_h - D_0}{D_0} \right] \cdot 100 \quad \text{Equation 1}$$

The HER indicates the maximum diametrical expansion that a circular punched hole can reach when a conical tool is forced into it until a crack in the hole edge extends through the full sheet thickness. HER has shown to be suitable to evaluate the stretch flangeability and the edge cracking sensitivity of AHSS.

The HET consists of forcing a conical expansion tool into a pre-punched hole until anyone crack extends through the test piece thickness of the metallic sheet. The conical punch was stopped as soon as cracks were detected. The followed punching and flanging processes are shown in Figure 26 and Figure 27. Three samples from each steel were tested. During the HET the extension of cracks were detected by a digital image correlation equipment (DIC) located below the tool as shown in Figure 28. Obtained HER values are summarized in Table 12.

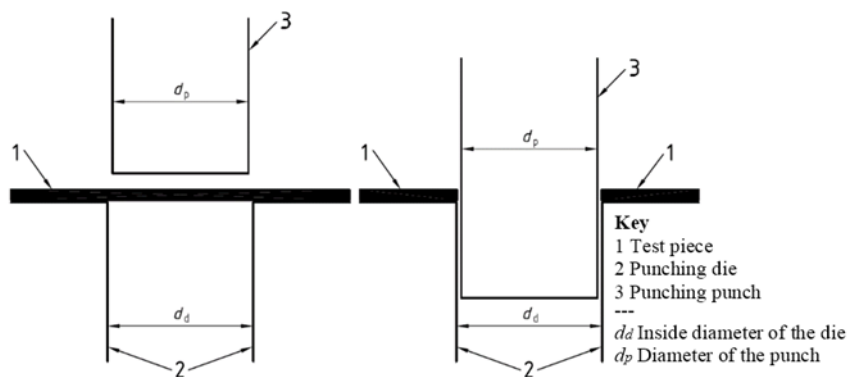


Figure 26. Hole punching procedure.

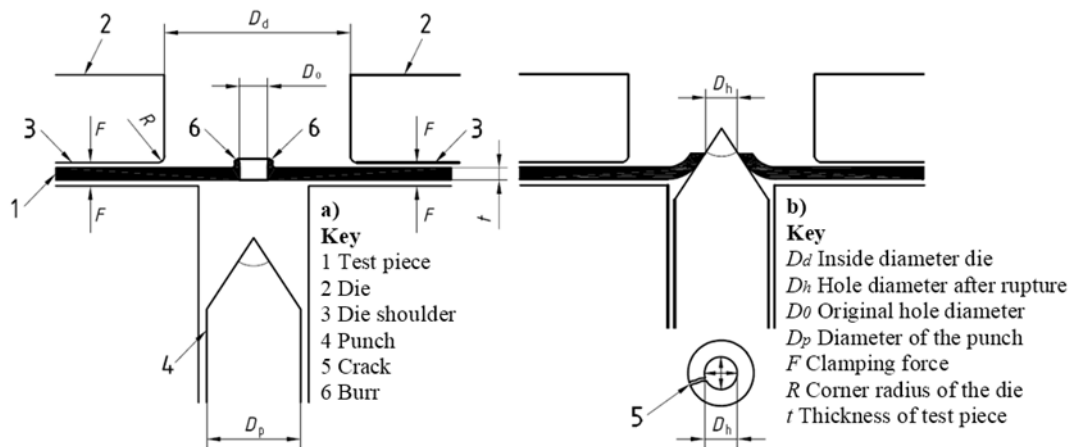


Figure 27. Hole expansion procedure.



Figure 28. Tool setup with DIC system.

Table 12. Hole Expansion Ratio for the investigated steels

Steel grade	HER, λ [%]	
	Mean	Deviation
CP1000	85	4
DP1000	27	11
CP1200	53	15
TBF	30	1
Q&P	55	8
TBF/Q&P mixed	42	10
PHS1500	28	2
PHS1000	33	27
TWIP	34	7

2.2.2. WP2. Toughness characterization by means of EWF

The main objective of this WP was to evaluate the suitability of the EWF methodology to measure the fracture toughness of thin AHSS sheets. Additionally, *J-integral* measurements according to ASTM E1820 were performed in two different steel grades. The EWF and *J-integral* tests were simulated by FEM and compared with experimental results.

The tasks corresponding to this WP are listed in Table 13.

Table 13. Tasks of WP2.

Task	Name of the task
Task 2.1	Evaluation of EWF in AHSS
Task 2.2	Simulation of EWF tests

Task 2.1 Evaluation of EWF in AHSS

Essential Work of Fracture

The fracture toughness of different AHSS sheets were evaluated by means of Essential Work of Fracture (EWF) methodology. The experimental procedure is described in detail in some works developed by CTM [CAS17, FRO17, CAS15, GUT12]. The EWF is based on the idea that in the ductile fracture the energy can be separated in two terms; one related to the plastic work and other related to the fracture. The EWF allows to separate the energy spent by the plastic deformation in the front of the crack tip and the energy spent by the crack grow processes.

The area in the front of the crack tip where a new surface is created is called Fracture Process Zone (Figure 29). In brittle materials this energy is totally elastic and allows the KI_c evaluation, but in the ductile materials exists a necking before the fracture.

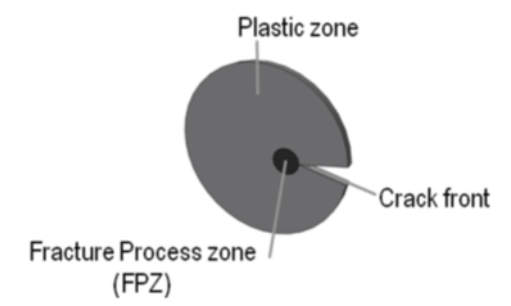


Figure 29. Definition of the Fracture Process Zone, FPZ

In the ductile fracture, the FPZ is surrounded by a large plastic area. The necking and the creation of surfaces contributes to the crack propagation resistance in the FPZ. The energy necessary for overcome both terms, W_e , can be considered as the toughness. Since W_p depends on the sample size and geometry, as well as on load mode, it can't be considered as a material property and must be separated from the total work of fracture to obtain the essential work of fracture carried out in the FPZ.

Cotterell and Redell developed a method for quantify the energy spent per unit area in the formation of two fracture surfaces in metal sheets [COT77]. This energy, w_e (W_e divided by the cross section area) is an essential work of fracture. This work is not completely essential since it contains an energy contribution from necking. As the necking is strongly influenced by stress triaxillity, in thin metal sheets, the essential work of fracture also depends on the sheet thickness and it must be considered as a sheet property, not an intrinsic material property.

Hence, the sheet thickness used in the tests must be the same thickness that for the industrial parts.

The method developed by Cotterell and Reddel allows to separate the total fracture energy (W_f) in two terms: 1) the essential work of fracture (w_e) and 2) non-essential plastic work (w_p) due to the plastic deformation.

If the ligament is completely yielded and the plastic zone is limited by the ligament, with a diameter equal to the ligament length, then the work performed in the FPZ is proportional to the ligament

length. The total work of fracture can be written like the summation of the essential work, W_e , and the plastic work W_p as indicates Equation 2.

$$W_f = w_e l t + w_p \beta l^2 t \quad \text{Equation 2}$$

Where β is a shape factor that depends on the shape of the plastic zone, t is the sheet thickness and l is the ligament length between the two notches.

The essential work of fracture is considered a material property for a determined sheet thickness and independent of the sample geometry. On the other hand, the non-essential work depends on the shape of the plastic zone that surrounds the crack and it's related to the dissipation of the plastic work per volume unit w_p . Normalizing the previous equation by cross section area (lt), allows the experimental determination of the EWF shown below:

$$\frac{w_f}{lt} = w_f = w_e + w_p \beta l \quad \text{Equation 3}$$

If the w_f is plotted against the ligament length l , a straight line with a positive intercept, which is the specific essential work of fracture, is obtained (Figure 30).

The total work of fracture (W_f) is measured by loading DENT samples with different ligament lengths. The displacement is measured with a video extensometer with gauge length of 50 mm. The specific total work of fracture (w_f) is obtained by integrating each load-displacement curves and rating by the initial ligament area and thickness (lt). A plot is shown in Figure 30 as an example.

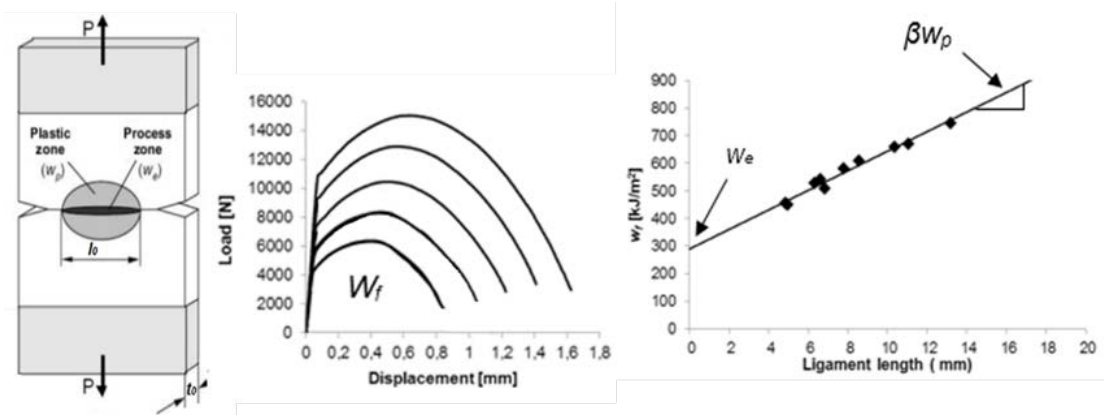


Figure 30. Schematic representation of the EWF experimental procedure

Tests were performed at CTM following the European Structural Integrity Society (ESIS) protocol [CLU01]. The protocol provides the guidelines to accomplish the necessary conditions to use equation (2): the ligament area must be completely yielded before crack initiation and the ligament must be in a plane stress state [COT77]. To accomplish these restrictions, the lower ligament length should be 3 to 5 times the thickness of the sheet, ($3t < l_{min} < 5t$) (1). The upper limit should not be larger than the 1/3 times the width of the specimen ($W/3$) or 2 times the radius of the plastic zone in plane stress at the crack tip r_p [MAR96a, MAR96b].

$$r_p = \frac{1}{2\pi} \left(\frac{K}{\sigma_y} \right)^2 \quad \text{Equation 4}$$

where K is the applied stress intensity factor and σ_y is the yield strength of the material.

The results obtained by CTM in AHSS grades with strength up to 1200 MPa fulfilled these constraints.

For the evaluation of EWF, rectangular Double Edge Notched Tensile (DENT) specimens of 240 x 55 with different ligament lengths ranging from 6 to 16 mm were used (Figure 31a). In order to evaluate the effect of the notch root radius, two different notch root radii were studied: Notch radius of 150 μm , obtained by electric discharge machining (Figure 31b) and notch radius lower than 0,1 μm obtained by nucleating a fatigue pre-crack from the notch (Figure 31c). EWF with no propagated notches (NP specimens) evaluate the crack nucleation and propagation resistance of the material , whereas EWF with fatigue pre-cracked specimens (P specimens) measure the material resistance to propagate a pre-existent crack.

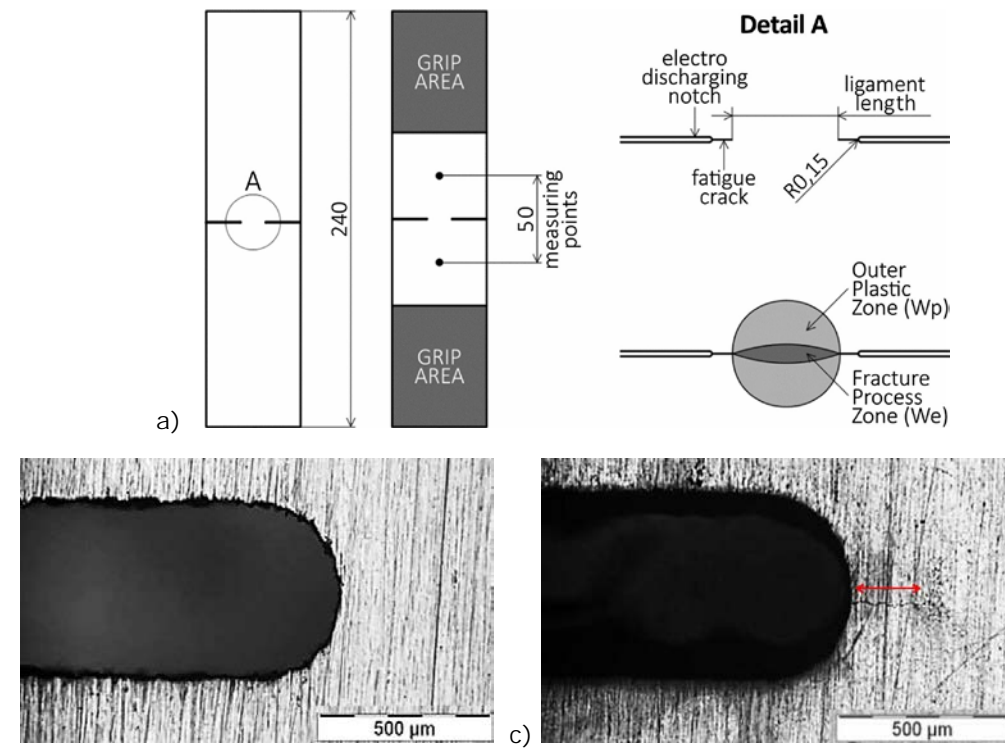


Figure 31. a) DENT geometry and detail of the ligament area. b) Notch radius of $150 \mu\text{m}$ and c) Notch radius of $0.1 \mu\text{m}$ (fatigue pre-crack).

The tensile tests of DENT specimens were performed at a 250 KN INSTRON 5585H tensile machine, equipped with a video extensometer. A Digital Image Correlation (DIC) software was used to check the yielding behaviour in the ligament area to assess that EWF constraints are met. Uniaxial tensile tests are performed using the DIC system to determine the Mises strain when the material is completely yielded (above yield strength). Data from PHS1500 is shown in Figure 32 as an example.

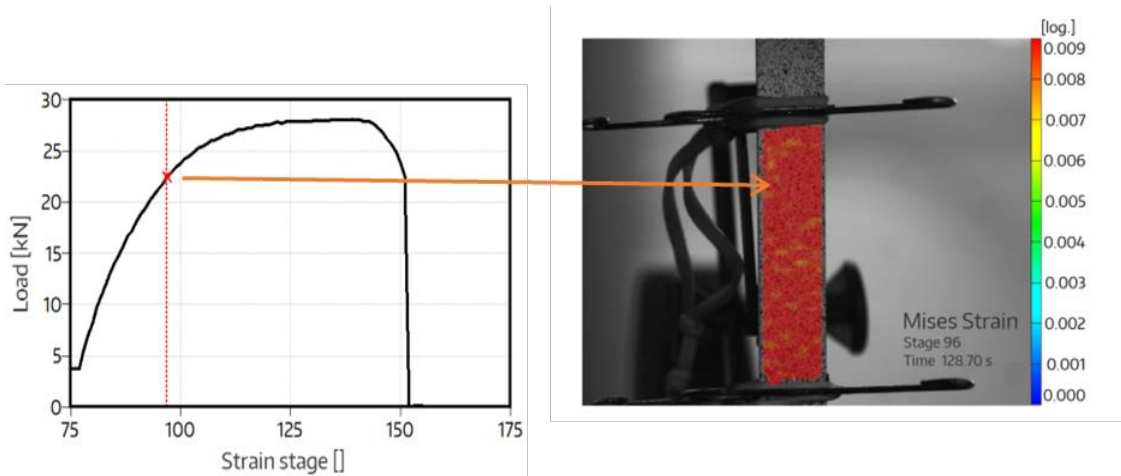


Figure 32. Images taken from the DIC system for the PHS1500 steel

According to Figure 32, the specimen was completely yielded when Mises strain is greater than 0,009 in logarithmic scale. The strain level was checked during EWF tests. Figure 33 shows the Mises strain level in the DENT specimen just before the fracture initiation. It was observed that the ligament area was fully yielded before the fracture and, thus, the application of EWF was validated. This validation was performed for all the AHSS grades and it was concluded that all of them fulfilled the EWF constraints.

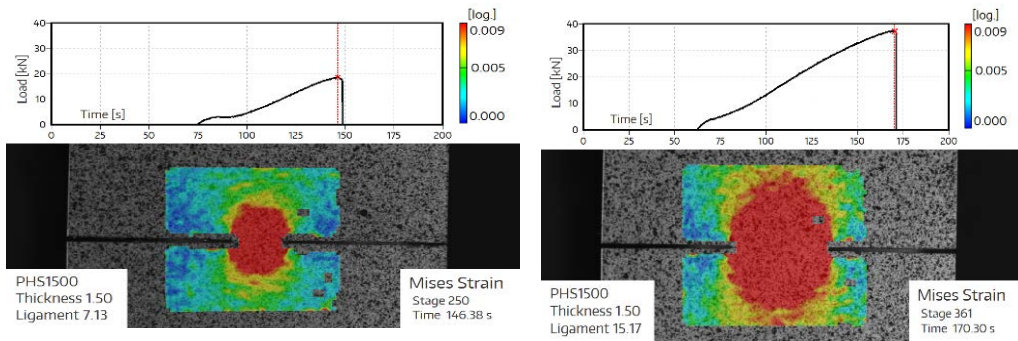


Figure 33. Checking of Mises strain at Pmax before fracture initiation in the shortest (left) and the largest ligament (right). Measurements in PHS1500 specimens.

EWF results for NP specimens ($\rho=150 \mu\text{m}$)

Figure 34 and Figure 35 show obtained w_f values in function of the ligament lengths for all the investigated steel grades. The intercept (w_e), the slope (βw_p) and the correlation coefficient R^2 are also indicated. EWF results are summarized in Table 14 and Figure 36.

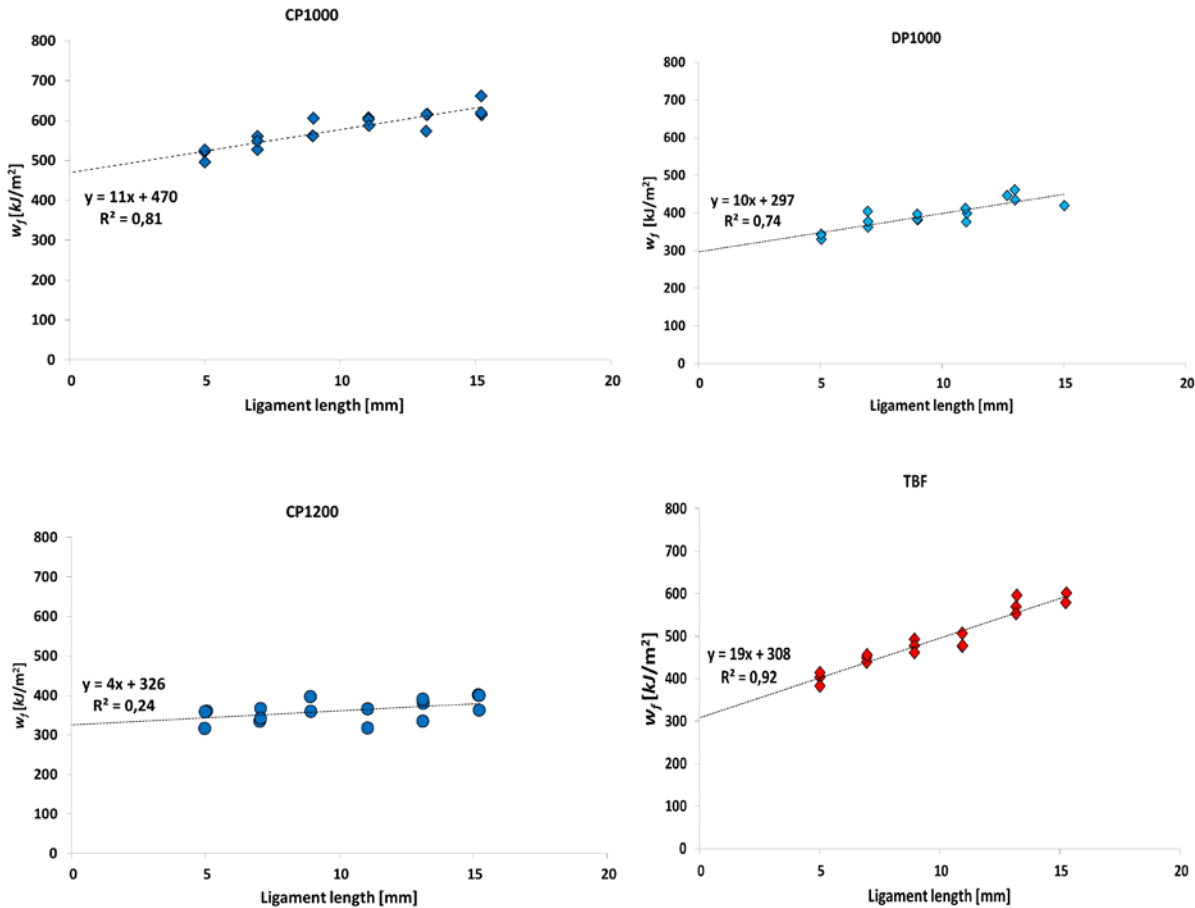


Figure 34. NP specimens. w_f values in function of the ligament length for CP1000, DP1000, CP1200 and TBF steel grades.

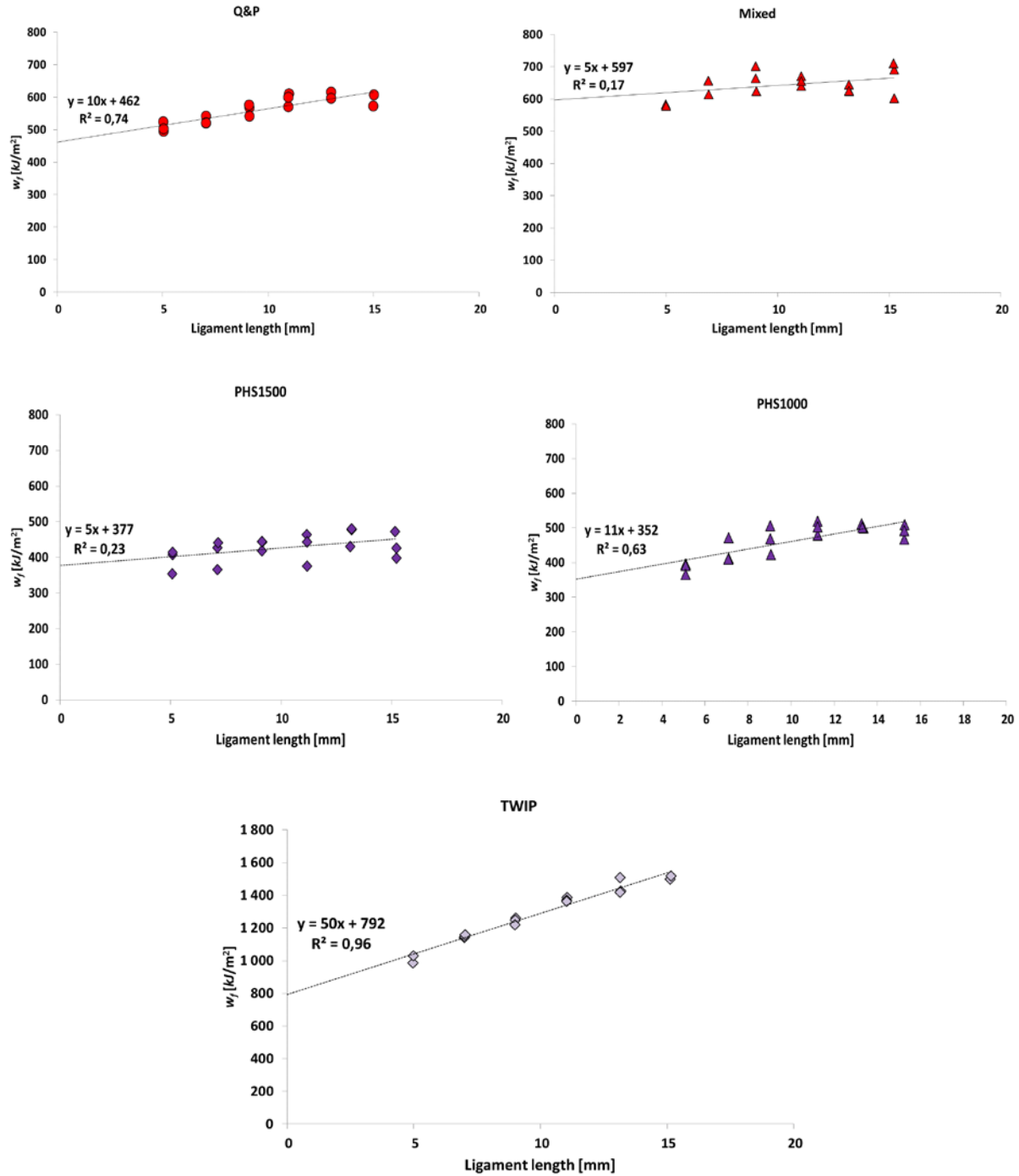


Figure 35. NP specimens. w_f values in function of the ligament length for Q&P, Mixed, PHS1500, PHS1000 and TWIP steel grades.

Table 14. EWF results for NP specimens

Steel grade	Thickness (mm)	w_e (kJ/m ²)	βw_d (MJ/m ³)
CP1000	1.4	470 ± 14	11 ± 1
DP1000	1.4	297 ± 16	10 ± 2
CP1200	1.6	326 ± 18	4 ± 2
TBF	1.5	308 ± 15	19 ± 1
Q&P	1.4	462 ± 16	10 ± 2
mixed	1.4	597 ± 28	5 ± 3
PHS1500	1.5	377 ± 24	5 ± 2
PHS1000	1.5	352 ± 22	11 ± 2
TWIP	1.4	792 ± 27	50 ± 3

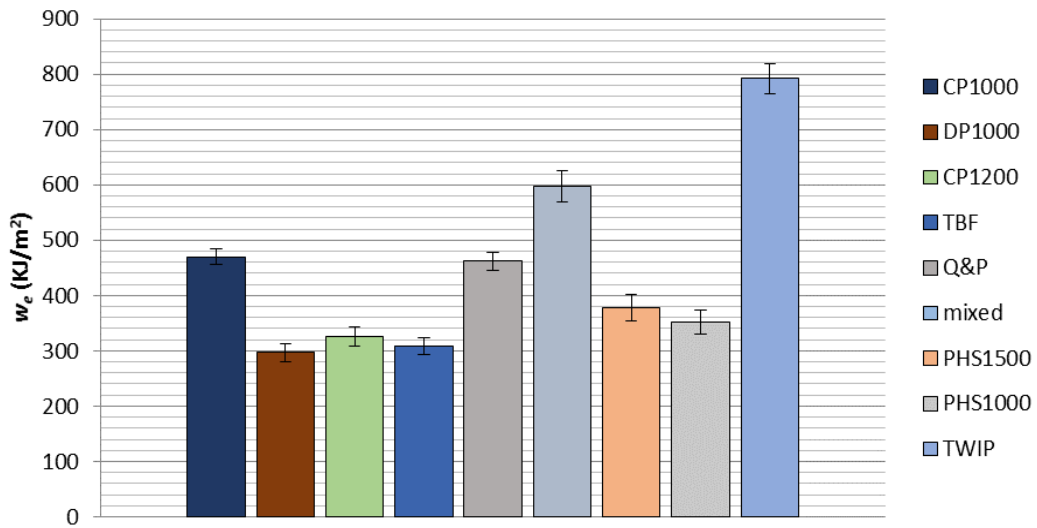


Figure 36. EWF results for NP specimens

EWF results for P specimens ($\rho=0.1 \mu\text{m}$)

Figure 37 and Figure 38 show the obtained w_f values obtained with fatigue pre-cracked specimens in function of the ligament length. The intercept (w_0), the slope (βw_p) and the correlation coefficient R^2 are also indicated. EWF values for P specimens are summarized in Table 15 and Figure 39.

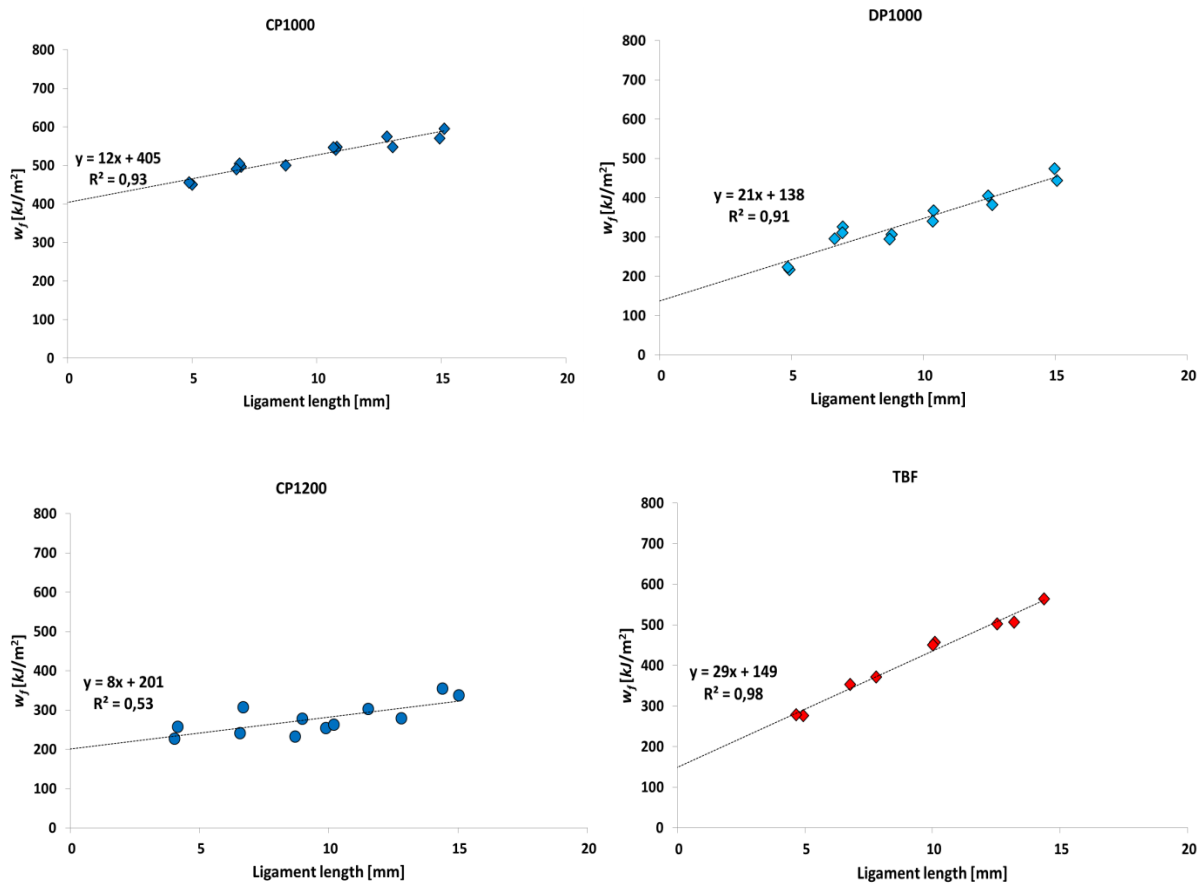


Figure 37. P specimens. w_f values in function of the ligament length for CP1000, DP1000, CP1200 and TBF.

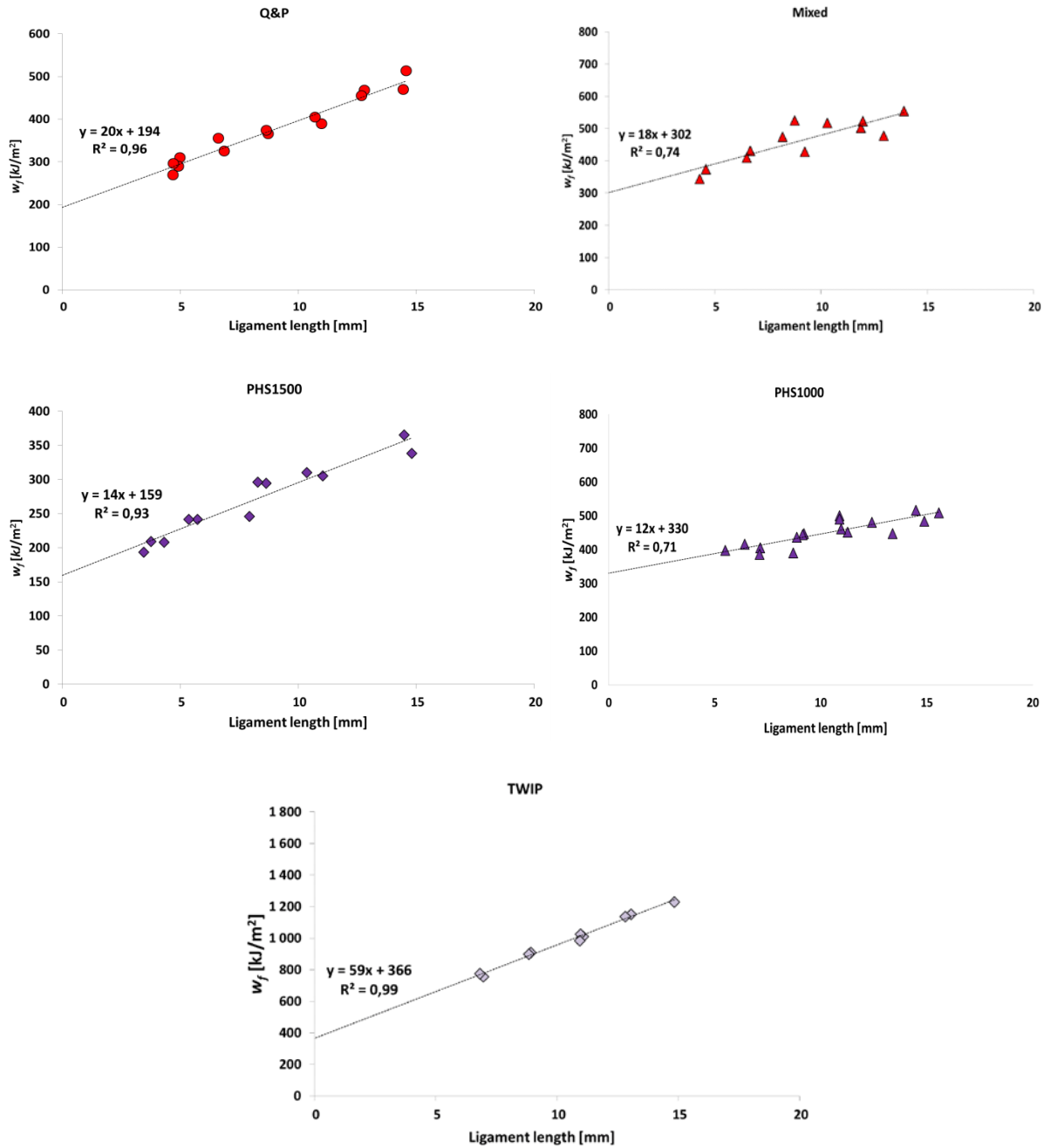


Figure 38. P specimens. w_f values in function of the ligament length for Q&P, Mixed, PHS1500, PHS1000 and TWIP steel grades.

Table 15. EWF results for fatigue pre-cracked specimens

Steel grade	Thickness (mm)	w_e (kJ/m ²)	βw_p (MJ/m ³)
CP1000	1.4	405 ± 11	12 ± 1
DP1000	1.4	138 ± 20	21 ± 2
CP1200	1.6	201 ± 24	8 ± 2
TBF	1.5	149 ± 13	28 ± 1
Q&P	1.4	194 ± 12	20 ± 1
mixed	1.4	302 ± 32	18 ± 3
PHS1500	1.5	159 ± 11	14 ± 1
PHS1000	1.5	330 ± 21	15 ± 3
TWIP	1.4	366 ± 24	65 ± 2

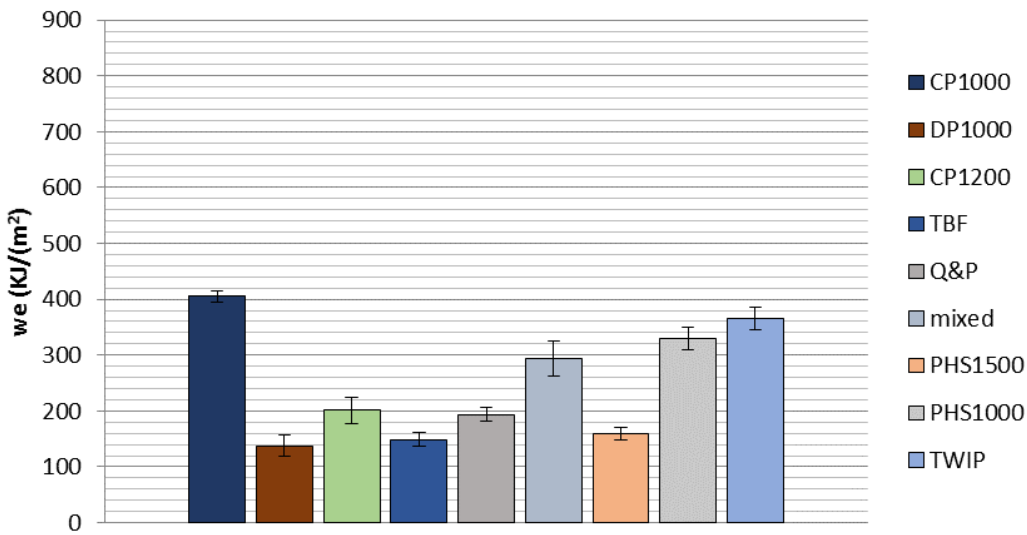


Figure 39. EWF results for specimens with fatigue pre-cracked specimens

For no propagated notches ($\rho=150 \mu\text{m}$) TWIP steel showed the highest EWF values, followed by mixed, CP1000 and Q&P grades. On the other hand, the lowest toughness values are shown by DP1000, TBF and CP1200. PHS1000 and PHS1500 exhibit slightly higher EWF. No clear correlation is observed between EWF with no propagated notches and mechanical properties or microstructural features. It can be noticed that this toughness values drop dramatically (approx. 50%) in most cases when a fatigue pre-crack is introduced, except for CP1000 and PHS1000, which showed a low notch radius sensitivity. This demonstrates that the notch radius has a strong influence on fracture toughness and the values from specimens with the minimum possible radius, i.e. a fatigue crack, should be taken to consider it a material property.

In case of the fatigue pre-cracked specimens, three ranges of values can be discerned: high (CP1000, TWIP, PHS1000 and mixed), medium (CP1200 and Q&P) and low (DP1000, TBF and PHS1500) toughness values. It is especially significant the low EWF value of PHS1500, which for no propagated specimens showed higher toughness than PHS1000 and CP1200. It is also noticeable that CP1000 presented the highest EWF, when it showed similar toughness to Q&P steel with no propagated notches.

Specific work for fracture initiation

The EWF methodology also permits to separate the energetic contributions from crack initiation and propagation. As described by Mai and Cotterell [MAI86], a cracking initiation value (w_e') can be obtained, calculating the work of fracture up to the onset of crack propagation (w_{fi} , Figure 40). The specific work for fracture initiation (w_f'), on the contrary to w_f , is constant and independent of the ligament length [MAI86]. The load at which the crack nucleates was determined by means of a high-resolution video extensometer synchronized with the testing machine. Results of toughness values for cracking initiation are summarized in Table 16 and Table 17. EWF at crack initiation forTable 17 for no propagated and fatigue pre-cracked specimens, respectively. Since w_f' does not depend on the ligament length, only mean values are reported.

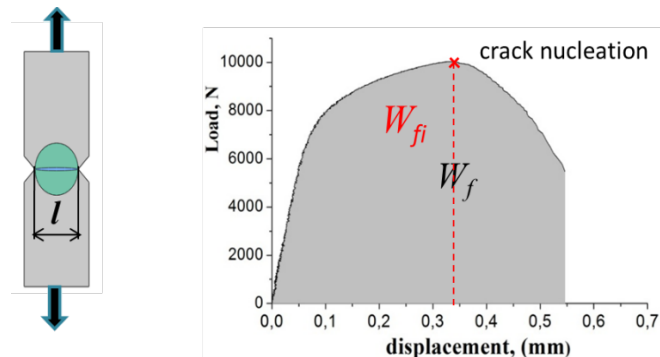


Figure 40. Determination of the work for fracture initiation (w_f')

Cracking initiation results for no propagated notches ($p=150 \mu\text{m}$)

Toughness values for cracking initiation (w_e^i) in NP specimens are shown in Table 16. Figure 41 summarizes the obtained toughness values for the investigated steel grades with NP specimens, in terms of w_e and w_e^i . It is observed that the values of fracture toughness at initiation follow a similar trend than toughness for the complete fracture. In general, no large differences are observed between w_e and w_e^i , except for mixed steel grade, which shows a significant increase of fracture resistance after crack initiation. TWIP and TBF shows identical w_e and w_e^i values. It indicates that all the fracture energy in NP specimens is dissipated in crack nucleation. However, it is important to note that for some materials it was difficult to determine the crack initiation in NP specimens due to the large plastic deformation near the notch tip, which probably masks the onset of the fracture. For this reason, no clear conclusions can be reached from the results for fracture initiation (w_e^i) with NP specimens and further investigations are suggested. CTM is working in an acoustic emission based method, aimed at improving the accuracy of crack initiation detection.

Table 16. EWF at crack initiation for NP specimens

Steel grade	Thickness (mm)	w_e^i (kJ/m ²)
CP1000	1.4	376 ± 6
DP1000	1.4	201 ± 8
CP1200	1.6	221 ± 20
TBF	1.5	308 ± 13
Q&P	1.4	378 ± 16
mixed	1.4	394 ± 10
PHS1500	1.5	297 ± 17
PHS1000	1.5	281 ± 9
TWIP	1.4	776 ± 17

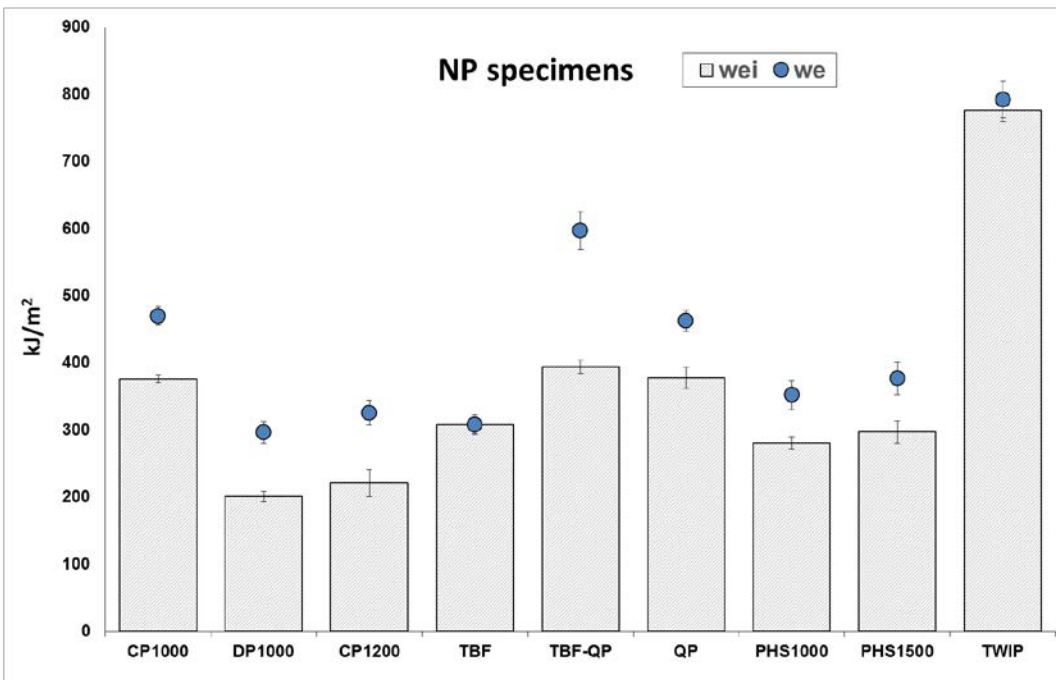


Figure 41. NP specimens. Summary of w_e^i and w_e values for the investigated AHSS grades.

Cracking initiation results for propagated notches ($p=0.1 \mu\text{m}$)

w_e^i values obtained with fatigue pre-cracked specimens are shown in Table 17. Figure 42 shows w_e^i and w_e values obtained for the investigated AHSS grades. The most remarkable thing is that work for fracture initiation of most of steel grades was very similar, in contrast to the large differences observed in their overall toughness values, w_e . Most of steels presented cracking initiation values ranging from 140 to 170 kJ/m² approximately, except DP1000 and TBF, which showed again the lowest toughness values (113 ± 5 kJ/m² and 108 kJ/m², respectively) and TWIP, with significant

higher w_e^i (286 ± 11 kJ/m²). It is observed that CP1000, mixed and PHS1000 showed a large difference between w_e^i and w_e , which indicates a significant increase of crack propagation resistance after the initiation. On the other hand, small differences were found between both values in the rest of steel grades, especially in DP1000, Q&P and PHS1500. In general, a high reproducibility of the results was observed with fatigue pre-cracked specimens, which enhance the reliability of the evaluated toughness values at cracking initiation.

Table 17. EWF at crack initiation for fatigue pre-cracked specimens

Steel grade	Thickness (mm)	w_e^i (kJ/m ²)
CP1000	1.4	151 ± 8
DP1000	1.4	113 ± 5
CP1200	1.6	129 ± 8
TBF	1.5	108 ± 9
Q&P	1.4	171 ± 15
mixed	1.4	154 ± 6
PHS1500	1.5	141 ± 10
PHS1000	1.5	160 ± 20
TWIP	1.4	286 ± 11

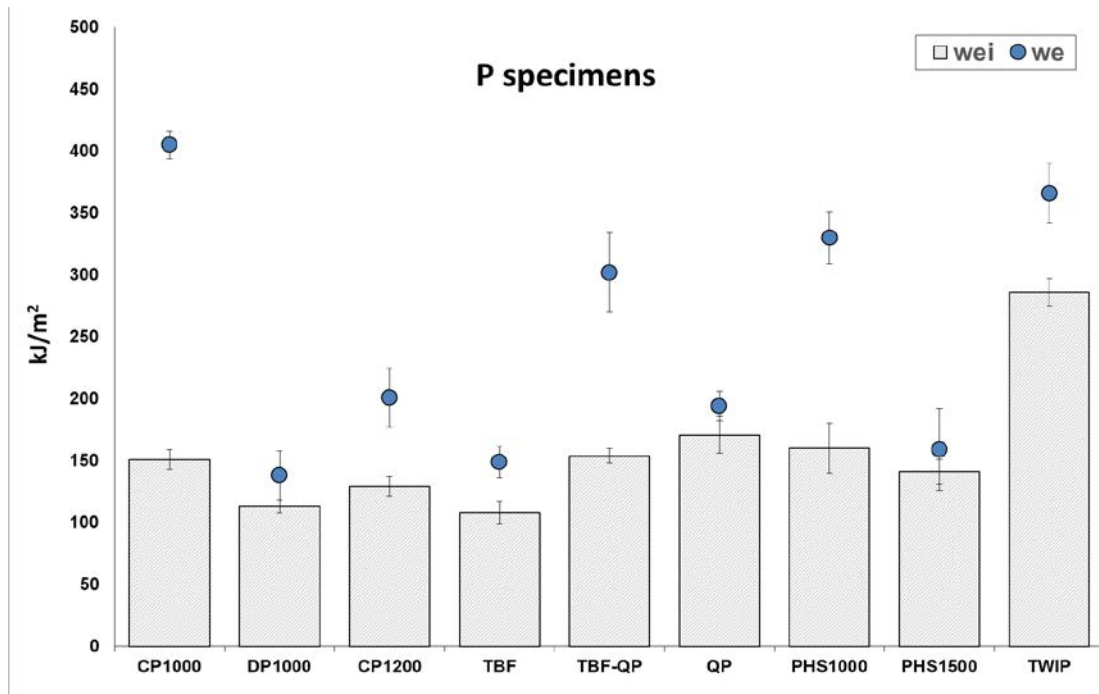


Figure 42. P specimens. Summary of w_e^i and w_e values for the investigated AHSS grades.

J-Integral measurements

In order to compare the fracture toughness values obtained by means of the EWF methodology with conventional Elastic-Plastic Fracture Mechanics (EPFM) procedures, *J-integral* measurements were performed according to ASTM E 1820 in two different steel grades: CP1000 and PHS1500.

ASTM E 1820 describes two procedures to evaluate the fracture toughness of ductile materials:

a) Basic test procedure

The basic procedure consists of loading multiple specimens up to a determined displacement level and determining the amount of crack extension that occurred during loading. This procedure is focused on obtain a single fracture toughness value, J_c .

b) Resistance curve procedure

The resistance curve method uses an elastic unloading compliance or equivalent procedure to obtain a J- or CTOD-based resistance curve from a single specimen.

As observed in EWF tests, AHSS grades can show a significant increase of crack propagation resistance after crack initiation, such as the case of CP1000, Mixed and PHS1000. According to this, a single cracking initiation resistance value is not enough to describe their overall fracture toughness and a J-Resistance curve should be used. With this purpose, the resistance curve procedure described in ASTM E1820 was followed to construct a J-based resistance curve.

Compact Tension (CT) specimens were used for *J-integral* measurements (Figure 43). Note that the specimen geometry was designed according to the standard ASTM E 647, which is less restrictive regarding the specimen proportions respect to the thickness ($W/20 \leq B \geq W/4$). ASTM E1820 is not directed to thin sheets and specimen proportions are too limitative ($B=W/2$). Thus, considering ASTM E1820 constraints, W should be equal to 2.8 or 3 mm, which would hamper the realization of the experiment. Load-line displacements were measured by means of a clip-on gage (Figure 44).

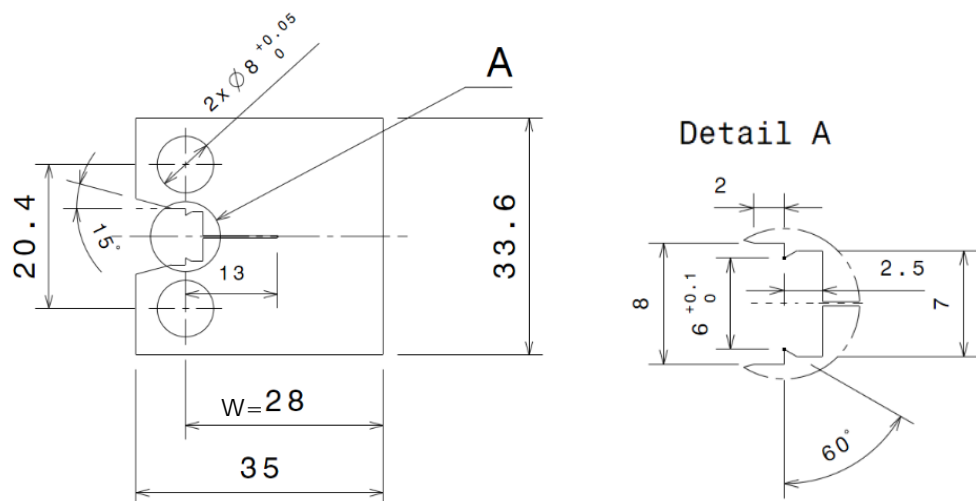


Figure 43. Geometry of the CT specimen used for *J-integral* measurements



Figure 44. Experimental setup of *J-integral* measurements.

The elastic unloading compliance method was used for the construction of the J-resistance curve. The specimen was loaded and subjected to successive partial unloadings. The slopes provide a measure of the elastic stiffness of the specimen, which decreases as the crack grows, and allow to estimate the crack length in different points during the test (Figure 45). The J values were calculated for the different points along the $P-\delta$ curve.

For the evaluation of J is necessary the value of the area A_{pl} . Such area represents the area under the load vs displacement curve for the load and unload of a hypothetical crack length $a=a_i+\Delta a$. Where

a_i is the initial crack length and Δa the crack extension. Thus, the hypothetic load slope for m_5 is lower than the initial slope m_i . the J value can be determined by:

$$J = J_{el} + J_{pl} \quad \text{Equation 5}$$

$$J_{el} = \frac{K^2(1-\vartheta^2)}{E} \quad \text{Equation 6}$$

$$J_{pl} = \frac{\eta A_{pl}}{B(W-a)} \quad \text{Equation 7}$$

Where $\eta = 2 + \frac{0,522(W-a)}{B}$ for the CT specimen, B and W are the specimen thickness and width respectively and a is the crack size.

The J values determined are plotted against the crack extension, Δa , in order to obtain the J -R curve (Figure 46). A construction line is drawn with slope $2\sigma_y$, where:

$$\sigma_y = \frac{\sigma_{ys} + \sigma_{TS}}{2} \quad \text{Equation 8}$$

Such slope $2\sigma_y$ represents the initial slope caused by the blunting of the crack tip. Two exclusion lines parallel to the construction line are plotted at 0.15 mm and 1.5 mm. The data points lying between these two lines define the J -R curve. The J_Q value, which characterize the fracture toughness at the onset of the crack propagation is determined by the intersection of the J -R curve with a third line, parallel to the exclusion lines, drawn at 0.2 mm. The boundary J_{limit} is given by the smaller of the following:

$$J_{max} = b_0 \sigma_y / 10 \quad \text{Equation 9}$$

$$J_{max} = B \sigma_y / 10 \quad \text{Equation 10}$$

Where b_0 is the distance from the original crack front to the back edge of the specimen, i.e. the initial ligament length and B is the thickness of the specimen. The maximum crack extension capacity for a specimen is:

$$\Delta a_{max} = 0.25 b_0 \quad \text{Equation 11}$$

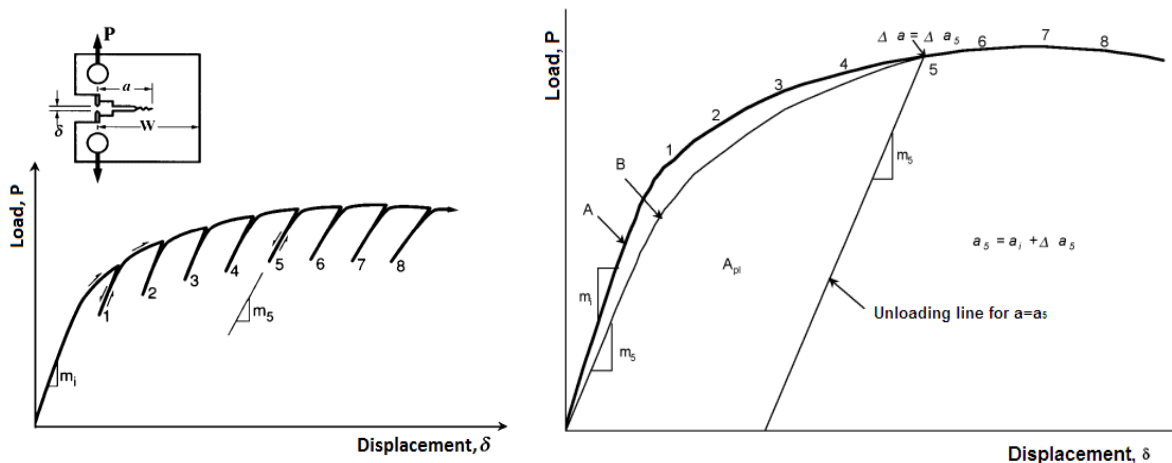


Figure 45. J determination through partial unloadings following the compliance method. Area A_{pl} for the evaluation of J . Curve A is the real P - δ curve registered. Curve B is an hypothetic curve for a crack length = a_5

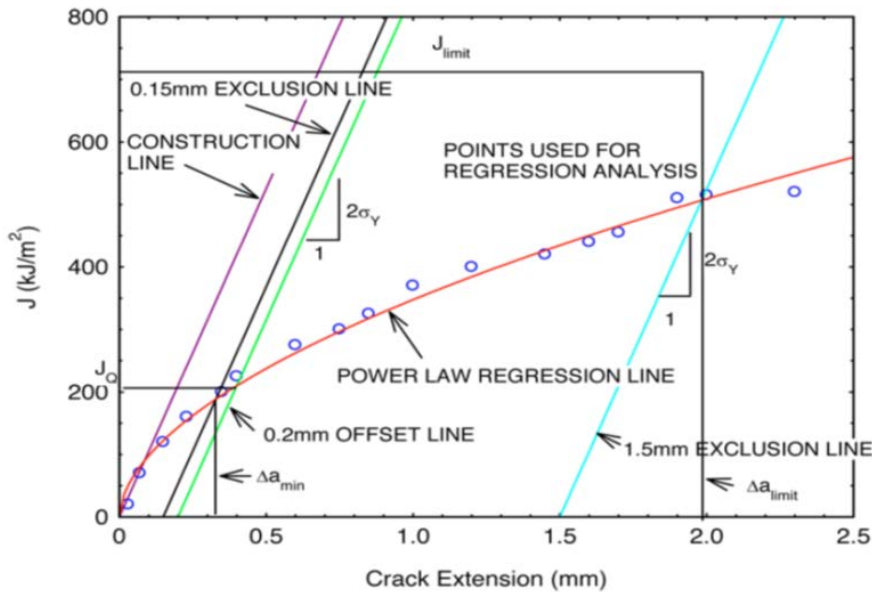


Figure 46. J values against crack extension for the J-R curve determination

The J-R curves obtained for CP1000 and PHS1500 are shown in Figure 47 and Figure 48. For CP1000 a mean J_c value of 318 ± 2 kJ/m² was obtained and a J_{max} of 549 kJ/m². These values are high if compared with the EWF values, w_e^i (151 ± 8 kJ/m²) and w_e (405 ± 11 kJ/m²). However, according to ASTM E1820 the value of J_c is evaluated for a crack growth of 0.2 mm, which probably overestimates the energy for cracking initiation. If the power law regression is made to 0 mm crack extension, a critical J value of ≈ 140 kJ/m² would be obtained, which is in good agreement with w_e^i . On the other hand, PHS1500 showed a mean J_c of 133 ± 2 kJ/m² and a J_{max} of 337 ± 42 kJ/m². In this case, fracture initiation values J_c and w_e^i were more similar (133 vs 141 kJ/m²). It is observed that CP1000 presented a steeper curve than PHS1500, which indicates a higher increase of crack propagation resistance as the crack grows.

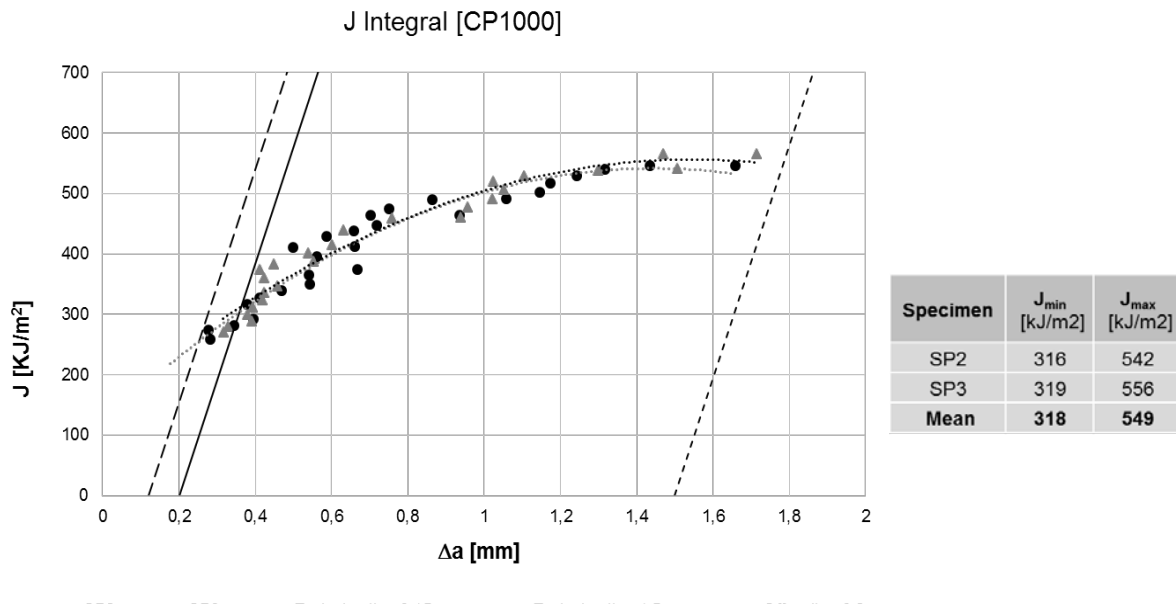


Figure 47. J-R curve for CP1000 obtained by the elastic compliance method

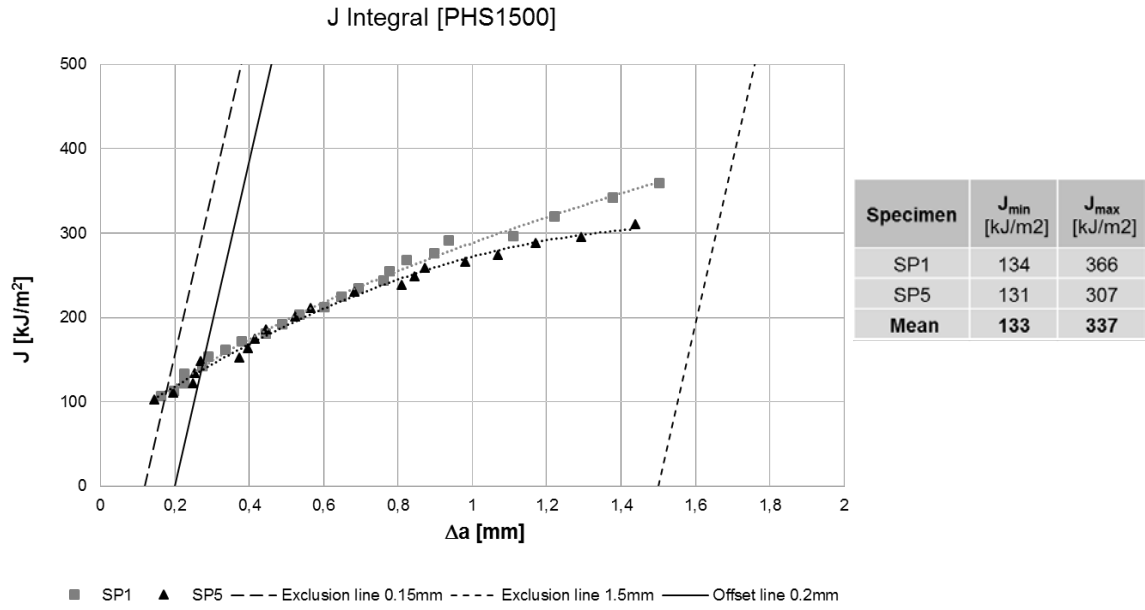


Figure 48. J-R curve for PHS1500 obtained by the elastic compliance method.

The critical CTOD, δ_c also can be used as a measure of fracture initiation toughness when J dominance conditions are fulfilled at initiation of cracking. The relation between $CTOD$ and J is given by:

$$\delta = \frac{J}{m\sigma_y} \quad \text{Equation 12}$$

Where m is a plastic constraint factor. It is an empirical dimensionless parameter and is defined in the ASTM E1820 according to:

$$m = A_0 - A_1 \left(\frac{\sigma_{ys}}{\sigma_{TS}} \right) + A_2 \left(\frac{\sigma_{ys}}{\sigma_{TS}} \right)^2 - A_3 \left(\frac{\sigma_{ys}}{\sigma_{TS}} \right)^3 \quad \text{Equation 13}$$

Where σ_{ys} is the yield strength, σ_{TS} the ultimate tensile strength and $A_0 = 3.62$, $A_1 = 4.21$, $A_2 = 4.33$ and $A_3 = 2.00$ for the CT specimen.

A DIC equipment was used to measure the CTOD in CP1000 and PHS1500 specimens (Figure 49 and Figure 50). A critical CTOD at cracking initiation, δ_c of 0.088 mm was obtained for CP1000 and 0.060 mm for PHS1500. The associated J_c values for these CTOD were 158 kJ/m² for CP1000 (Figure 49) and 168 kJ/m² for PHS1500 (Figure 50). As observed, the toughness values at cracking initiation measured from CTOD are more conservative than the obtained from the J-resistance curve at 0.2 mm of crack extension and are similar to the works for fracture initiation (w_e) evaluated by means of the EWF methodology.

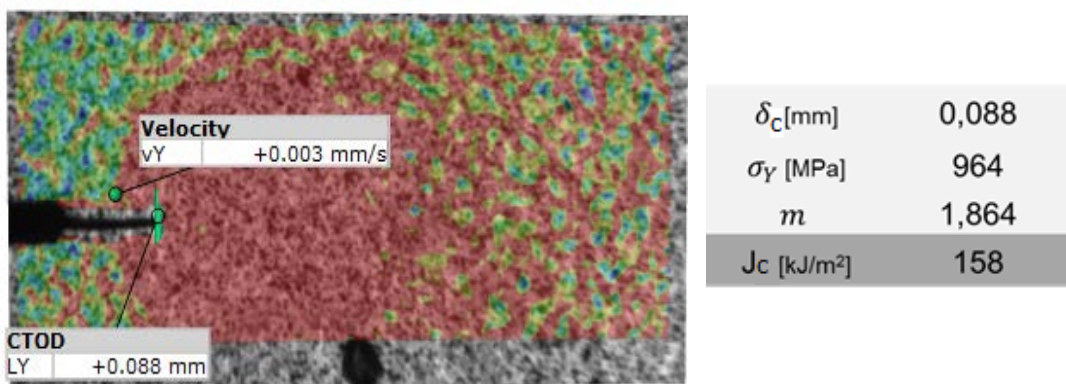


Figure 49. Measurement of the CTOD by means of DIC and J_c value obtained for CP1000

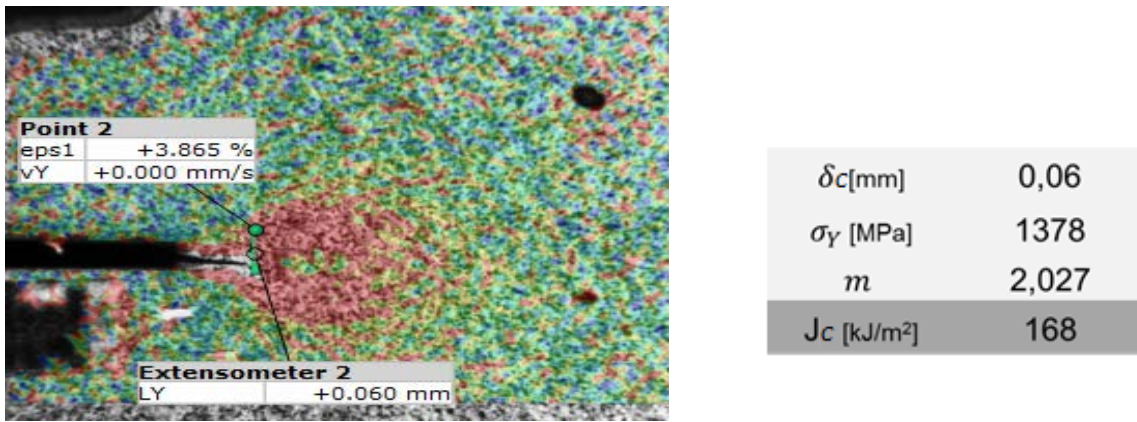


Figure 50. Measurement of the CTOD by means of DIC and J_c value obtained for PHS1500

Therefore, after investigate different fracture toughness measurement methodologies, it can be concluded that w_e' is equivalent to EPFM toughness value J_c . However, in some cases the extra energy associated to the 0.2 mm of crack extension in J-Resistance curves can overestimate the cracking initiation resistance, as observed for CP1000. On the other hand, w_e is an average resistance value for the complete fracture containing energetic contributions from crack initiation and propagation and it is a suitable parameter to describe the overall toughness resistance. The main advantage of the EWF methodology is the relative easiness of the procedure if compared to standard methods.

Task 2.2 Simulation of EWF tests

The aim of this task is to model the EWF tests and perform *J-Integral* calculations following currently available models in commercial FEM software.

Simulation of EWF test

The model was based on the specimens used in experimental EWF tests, and was modelled using ABAQUS. Only 1/8 of the specimen was reproduced due to the symmetry with respect to the 3 axes. A 3D deformable solid was built trough extrusion. The true stress/true strain (PEEQ) measured on the tensile test were used as the material input to reproduce the plastic behaviour. The whole model was defined as homogeneous. The simulation was validated by comparing force-displacement data with the experimental curves for various ligaments of DP1000. The simulation curves were trimmed at the average displacement value for the maximum force points of same ligament tests. As seen in the following graphs (Figure 51), the force displacement simulation results adjust well to the experimental force displacement curves.

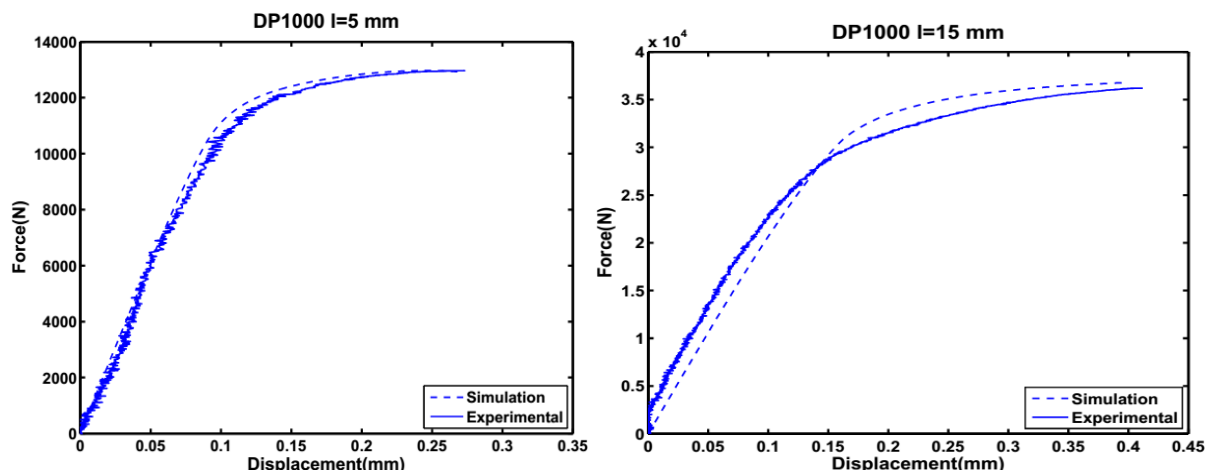


Figure 51. Comparison between experimental and simulation force-displacement curves for some ligaments of DP1000.

Simulation of *J*-integral

The simulation of *J-Integral* measurements was performed following the work published by Simula in the Abaqus Technology Brief TB-04-FMCAE-1(2007). The main objective was to identify the best meshing technique for the evaluation of the integral of the contour, mainly size and element type. As shown in Figure 52, different mesh size was used to study its influence in the results accuracy.

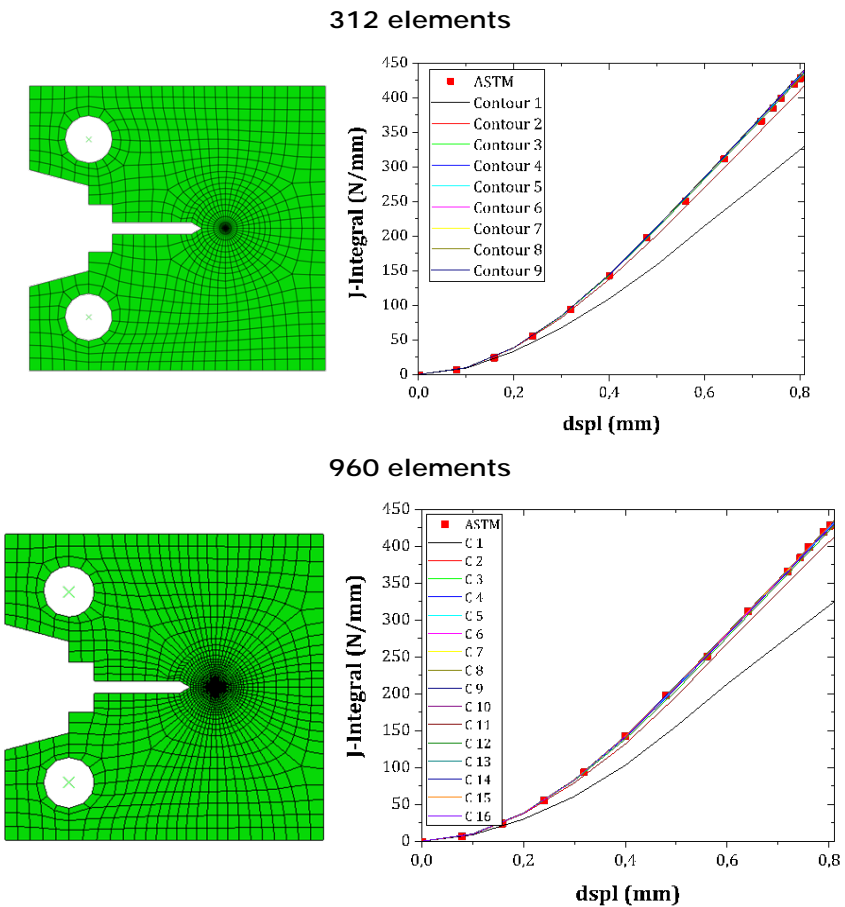


Figure 52. Comparison between experimental and FEM analysis results with different mesh size

In a mesh with quadrilateral elements, at the crack tip the element sides are collapsed with single-node-type degenerate element control. The circular partitioned areas are meshed using the “swept meshing” technique; this method allows the mesh to be regular and focused. The inclusion of the seam and singularity definition causes Abaqus/CAE to create automatically collapsed elements with correct connectivity definitions. The remaining portion of the model is free meshed. As observed in Figure 53, the circular partition works much better than squared partition.

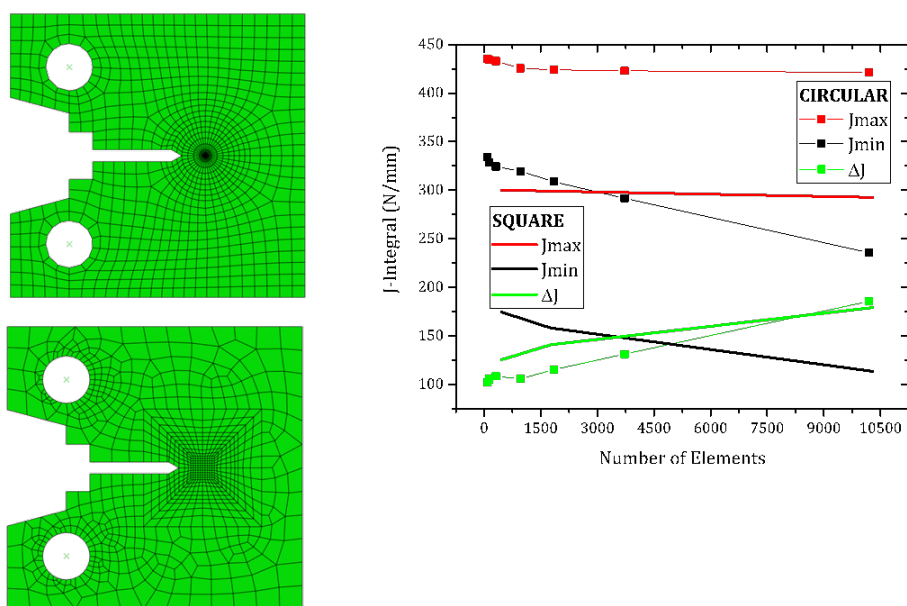


Figure 53. Comparison between different mesh type analyses.

This approach was used to calculate the *J-integral* of DENT specimens. The model for the DENT specimen previously designed was used but using shell elements. The analysis was done with three

different materials: DP1000, TBF and Q&P. Meshing strategy is the same as in the previous example (Figure 54)

Figure 54). Correlation between experimental results and simulation for material behaviour was checked successfully in a tensile test (Figure 55)

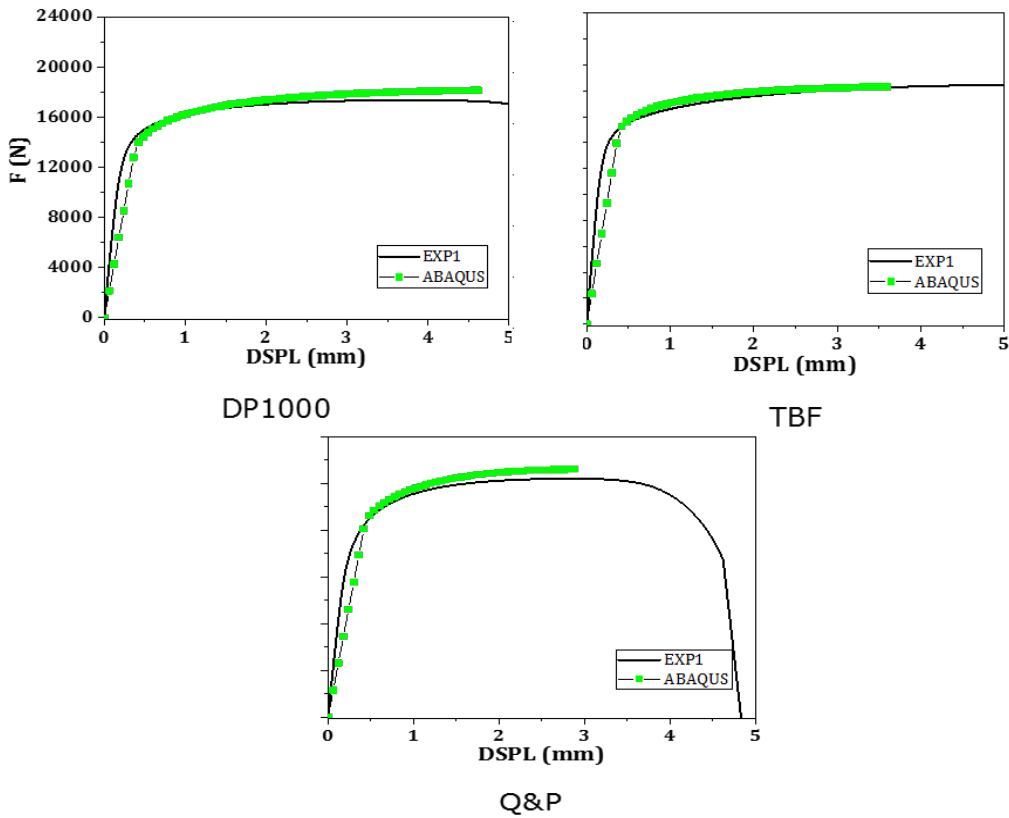


Figure 55). The best correlation is observed for TBF specimen, whereas Q&P showed not so good fitting. *J-Integral* was evaluated for different ligament length and compared with the total work of fracture (w_f) values obtained in EWF experiments (Figure 56Figure 56). Values obtained for DP1000 and TBF show quite good agreement, whereas Q&P shows some discrepancies between experimental values and simulations. These results show the need of accurate models to obtain reliable *J-integral* values for DENT specimens.

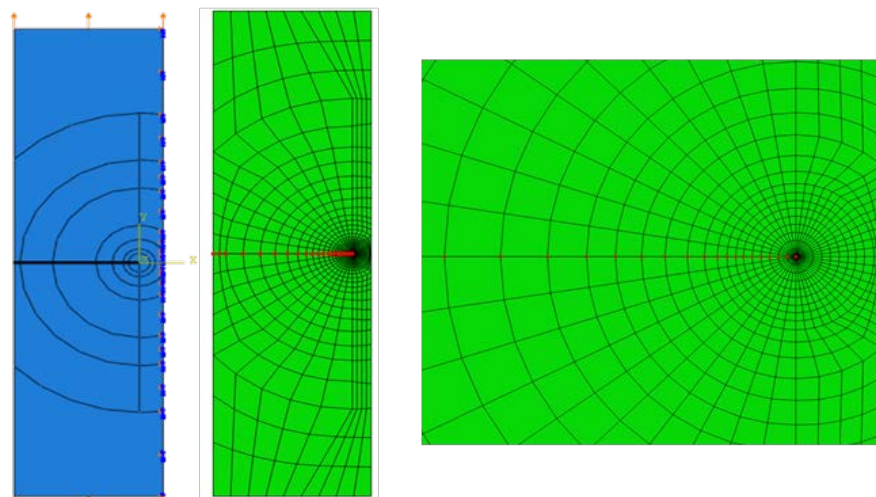


Figure 54. Simulation model and mesh of the DENT specimen.

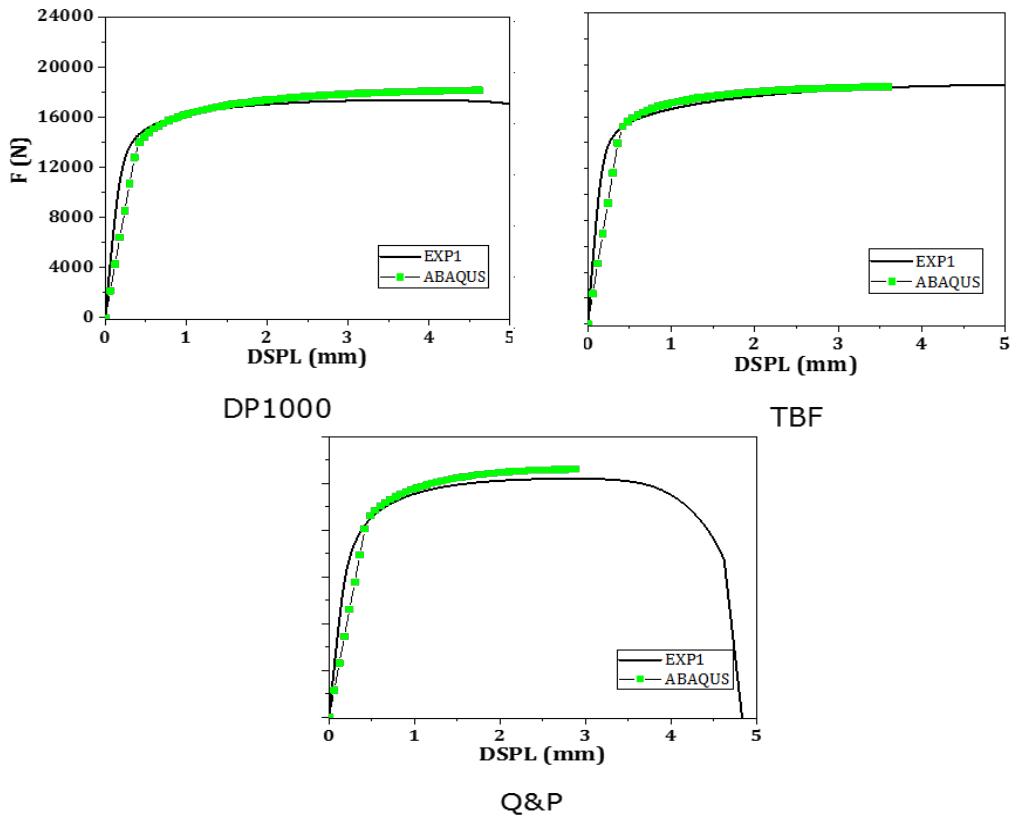


Figure 55. Correlation between experimental tension test and simulation.

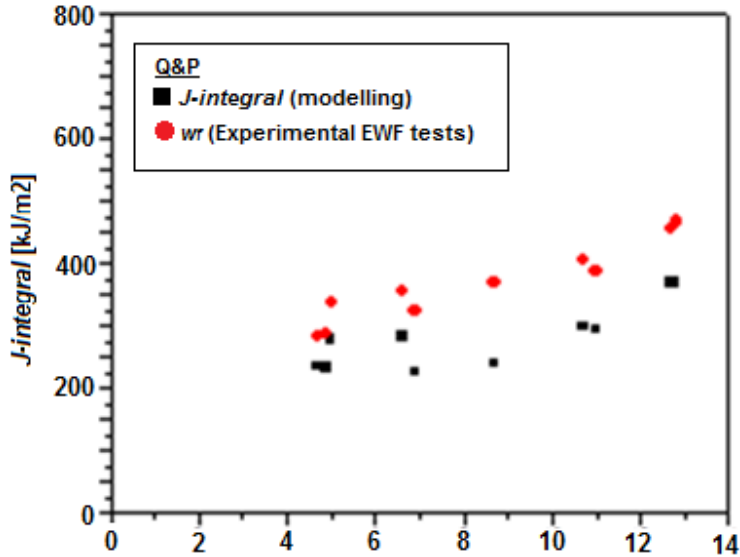


Figure 56. Correlation between experimental values of w_f and J -Integral values of simulation.

2.2.3. WP3. Crashworthiness assessed by EWF

The main objective of WP 3 was to assess the applicability of the EWF as a tool to understand the crash resistance of AHSS. Experimental investigations on the correlation between fracture toughness and crash worthiness were carried out in this WP. Different damage models were investigated in FEM simulations and the first steps for the implementation of EWF as a failure criterion in crash modelling were taken. Additionally, other influencing aspects on fracture toughness such as the effect of strain rate on EWF were experimentally assessed. Table 18 shows the tasks corresponding to the WP3.

Table 18. Tasks of WP 3

Task	Name of the task
Task 3.1	Material selection according to impact and EWF results
Task 3.2	Effect of strain rate on EWF in AHSS
Task 3.3	Simulation of laboratory impact resistance tests
Task 3.4	Correlation of fracture toughness evaluated by means of EWF with crash resistance

Task 3.1 Material selection according to impact and EWF results

From the results observed in laboratory impact resistance tests performed in WP1, 3 AHSS grades were selected in this task to perform the corresponding investigations. The selected steels were:

- 2 1000 MPa steel grades: DP1000, TBF
- 1 1200 MPa steel grade: Q&P

The three steels presented significant cracking during axial and bending impact tests, which was essential to investigate the evolution of crack propagation during crash and correlate it with fracture toughness results. All the investigations carried out in WP3 were focused in these 3 steels.

Task 3.2 Effect of strain rate on EWF in AHSS

The fracture toughness of all the AHSS grades studied in Tough-sheet project was evaluated by means of the EWF methodology in task 2.1 at quasi-static loading conditions, but during crash situations the components are subjected to high strain rates and the dynamic effects can influence on the material behaviour. As observed in Task 1.3 Laboratory impact resistance tests, the mechanical properties of the AHSS, such as yield strength and total elongation, can be affected by the strain rate. Therefore, the crack propagation resistance is also probably affected. Thus, the aim of this task was to evaluate and quantify the influence of strain rate on the fracture toughness (measured in terms of EWF). For this purpose, EWF tests were conducted at different strain rates: low ($3 \cdot 10^{-4} \text{ s}^{-1}$), medium (0.1 s^{-1}) and high (30 s^{-1}) with steel grades selected in task 3.1: DP1000, TBF and Q&P.

EWF tests at low strain rate (Task 2.1: Evaluation of EWF in AHSS) were conducted at a constant cross-head speed of 1 mm/min with a gauge length of 50mm. The strain rate was calculated from the following expression [DIE61]:

$$\dot{\epsilon}(t) = \frac{de}{dt} = \frac{d(L-L_0)/L_0}{dt} = \frac{1}{L_0} \frac{dL}{dt} = \frac{v}{L_0} \quad \text{Equation 14}$$

According to Equation 14, the strain rate obtained was $3 \cdot 10^{-4} \text{ s}^{-1}$. Figure 57 shows the EWF at low strain rate for the selected steel grades (DP1000, TBF and Q&P). TBF and DP1000 showed very similar EWF values ($150 \pm 13 \text{ KJ/m}^2$ and $138 \pm 20 \text{ KJ/m}^2$, respectively). Q&P grade showed a higher value ($194 \pm 12 \text{ KJ/m}^2$).

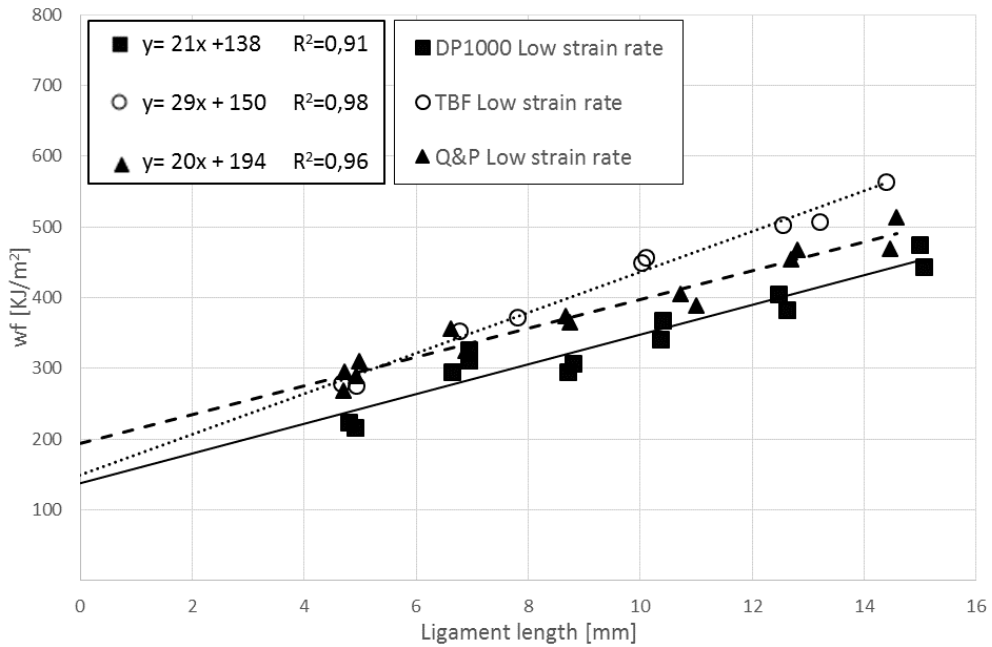


Figure 57. EWF results at low strain rate

Medium strain rate tests were performed using the same equipment and specimen geometry used at low strain rate tests (see task 2.1). The methodology was similar but with some modifications. In this case, the cross-head speed was set in 300 mm/min and the strain rate obtained was 0.1 s^{-1} for a gauge length of 40 mm. The fixture system was modified in order to achieve homogeneous speed, avoiding the initial cross-head acceleration. The tests were recorded by an external high speed camera and the displacement was measured in ARAMIS software. The specimens were painted with a stochastic pattern to perform such measurements. DIC measurements were also used to check that the ligament area was fully yielded prior to fracture and, therefore, to ensure the validity of the EWF measurements.

Figure 58 shows the EWF values at medium strain rate for the selected steel grades (DP1000, TBF and Q&P). It can be observed that the EWF values are very similar for all the steel grades:

- **DP1000:** $212 \pm 23 \text{ KJ/m}^2$
- **TBF:** $210 \pm 36 \text{ KJ/m}^2$
- **Q&P:** $189 \pm 16 \text{ KJ/m}^2$

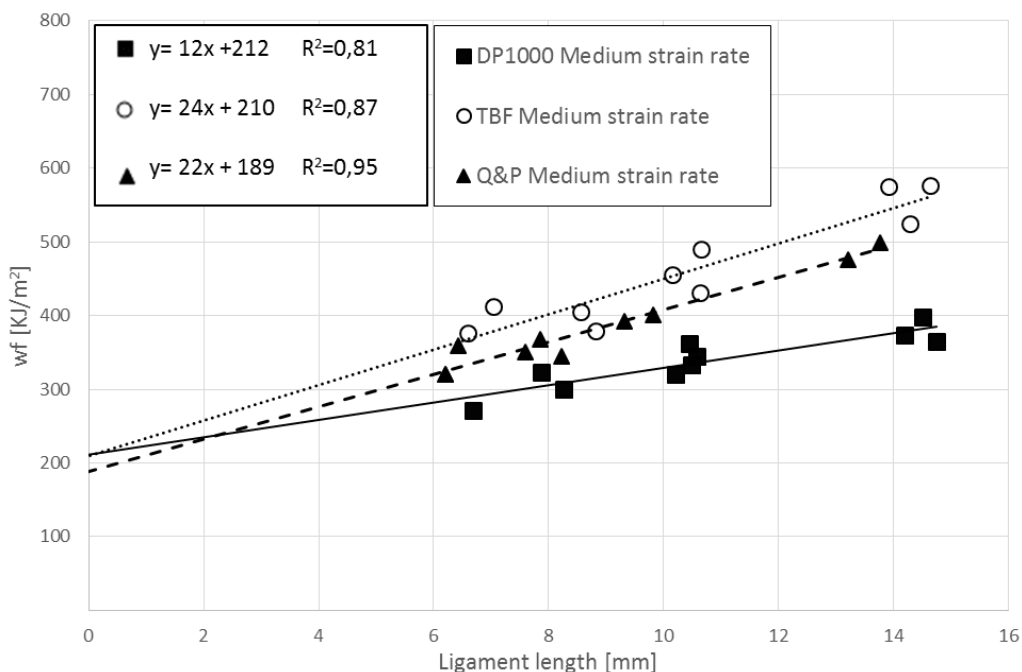


Figure 58. EWF results at medium strain rate

EWF tests at high strain rates were performed in a high speed tensile machine, an INSTRON High Strain Rate VHS system, which utilizes advanced servo-hydraulic and control technologies designed for a wide range of high strain rate and high-speed test requirements. The system is dimensioned for loads up to 100kN and velocities up to 25m/s. An operating pressure of 280 bar results in high acceleration velocity and load performance. The cross-head speed was set in 0.5 m/s and the initial gauge length was 16 mm, obtaining a strain rate of 30 s^{-1} . It must be noted that the strain rate at the vicinity of the crack tip is much higher [NOD15].

It was necessary to adapt the geometry of specimens in order to fit them properly in the high speed tensile machine. Figure 59 shows the specimen geometry designed for the high strain rate tests. The specimen is fixed in the lower clamp of the machine by a bolt. The length of the specimen (300 mm) is necessary to accelerate the cross-head before the specimen is gripped in the upper clamp.

Images for DIC measurements were taken by a Phantom v1610 high-speed camera and imported in ARAMIS software.

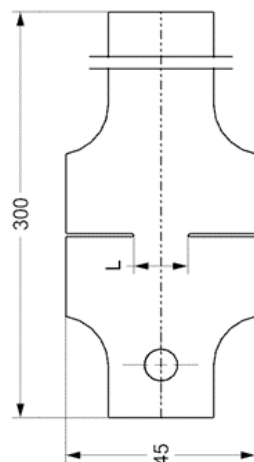


Figure 59. Specimen geometry for high strain rate EWF tests

The results of EWF measurements at high strain rates are shown in Figure 60. Again the EWF values are very similar for the three steel grades:

- **DP1000:** $297 \pm 25 \text{ KJ/m}^2$
- **TBF:** $281 \pm 64 \text{ KJ/m}^2$
- **Q&P:** $291 \pm 13 \text{ KJ/m}^2$

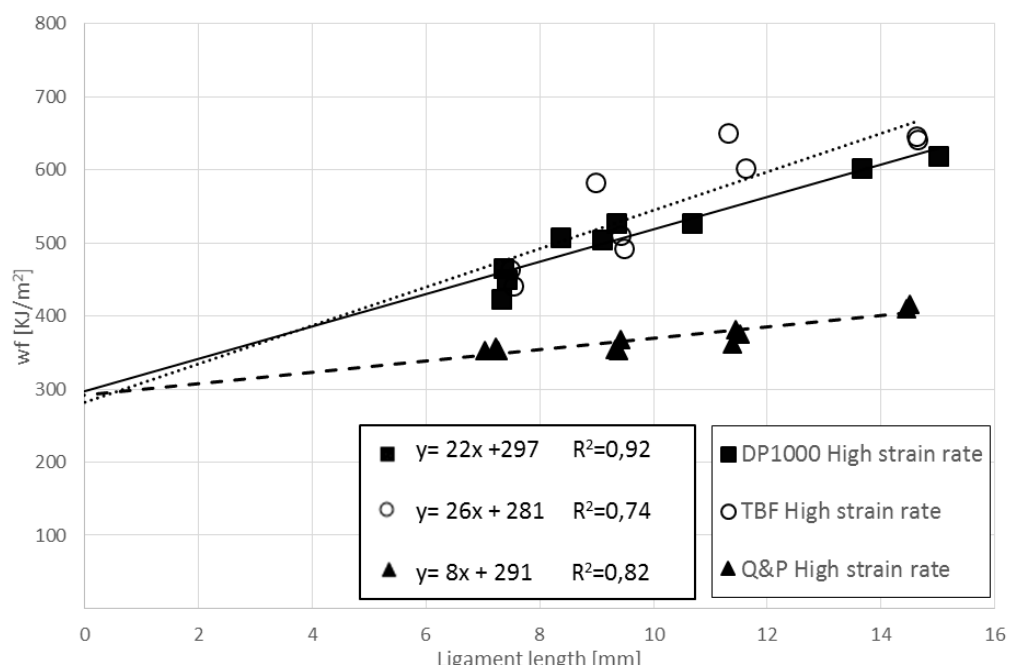


Figure 60. EWF tests at high strain rate

EWF results at different strain rates are summarized in Figure 61. It was observed that EWF increases with the strain rate in all cases, except for Q&P, whose EWF is higher at high strain rate (HSR), but it showed similar EWF values at low and medium strain rates. TBF and DP1000 showed higher strain rate sensitivity than Q&P. Respect to the EWF values at low strain rate, TBF showed an increase of 40% at medium strain rate (MSR) and 80% in HSR. DP1000 also showed a significant increase of EWF at medium and high strain rates (54 % and 115 % respectively), respect to the low strain rate (LSR) values. Finally, Q&P showed the lowest sensitivity with no increase at MSR and an increase of 47% at HSR. It can be noted that, at LSR TBF and DP1000 showed similar values while Q&P presents a significantly higher EWF value. At medium and high strain rates these differences were not observed and the fracture behaviour of the three steel grades was very similar. It is worth noting that, in some cases, it was difficult to detect the exact point for the complete fracture in medium and high strain rates. The selection of displacement at fracture is critical and affect significantly the results. Hence, these difficulties can lead to some uncertainties in the evaluation of the EWF at high speeds. Nevertheless, the obtained EWF results are in good agreement with dynamic tensile tests performed in task 1.3 (Figure 18 and Figure 19). Most of steels evaluated in such task presented similar or slightly higher mechanical properties at MSR, whereas a remarkable better performance was observed at HSR (especially greater elongation).

The works for fracture initiation (w_e^i) were also evaluated for EWF at HSR. The values were compared to the obtained at LSR in Table 19. In this case, it was observed the same trend for both loading conditions. Q&P steel grade showed higher cracking initiation values than DP1000 and TBF, which show similar w_e^i .

Hence, results showed that, in general the EWF tends to increase with the strain rate, especially at high strain rates. These results were in good agreement with the mechanical behaviour observed in dynamic tensile tests (task 1.3). However, the uncertainties observed at medium and high strain rates related to the detection of the final fracture can affect significantly the reliability of the results. Further investigations are suggested aimed at reducing such uncertainties and improve the accuracy of EWF measurements at medium and high strain rates.

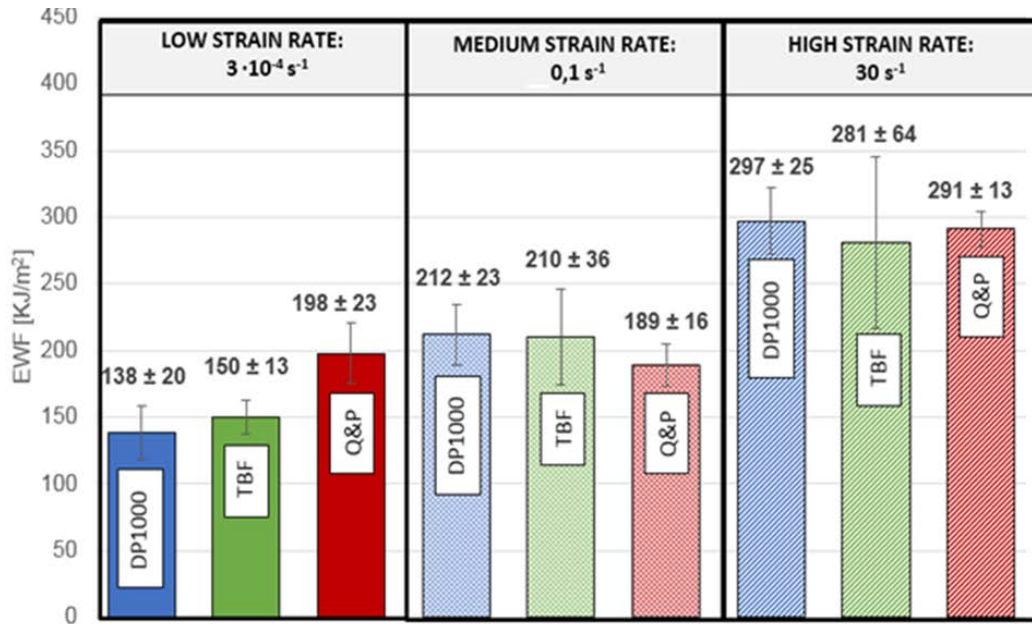


Figure 61. Summary of EWF results at different stain rates

Table 19. w_e^i values at LSR and HSR

Steel grade	w_e^i [kJ/m²]	
	LSR ($3 \cdot 10^{-4} \text{ s}^{-1}$)	HSR (30 s^{-1})
DP1000	113 ± 5	202 ± 26
TBF	108 ± 9	218 ± 31
Q&P	171 ± 5	288 ± 29

Task 3.3 Simulation of laboratory impact resistance tests

From the tensile test, the data for the definition of the elastoplastic part of the material constitutive law was extracted. From the point of necking onset (maximum load point in the true strain-stress curve), the plastic evolution was designed for the Finite Element model to reproduce such necking behaviour.

Damage laws were designed to dissipate the introduced fracture toughness as a combination of the necking and the crack growth. For this purpose, damage-evolution laws were designed in the total strain field, and later they were adapted to the LS-Dyna model formulation, which refers damage to the plastic strain evolution. Damage laws were adapted to the introduced plastic law, in order to ensure proper energy dissipation.

From the EWF values, a definition of the degradation of mechanical properties by damage was completed, assuming several formulations: for the models in which the material properties can be introduced in the tabular form, a linear and a bilinear evolution of the stress with the strain was tested (Figure 62). In models using other formulations implemented in LS-Dyna, a linear evolution of the damage with the strain was introduced.

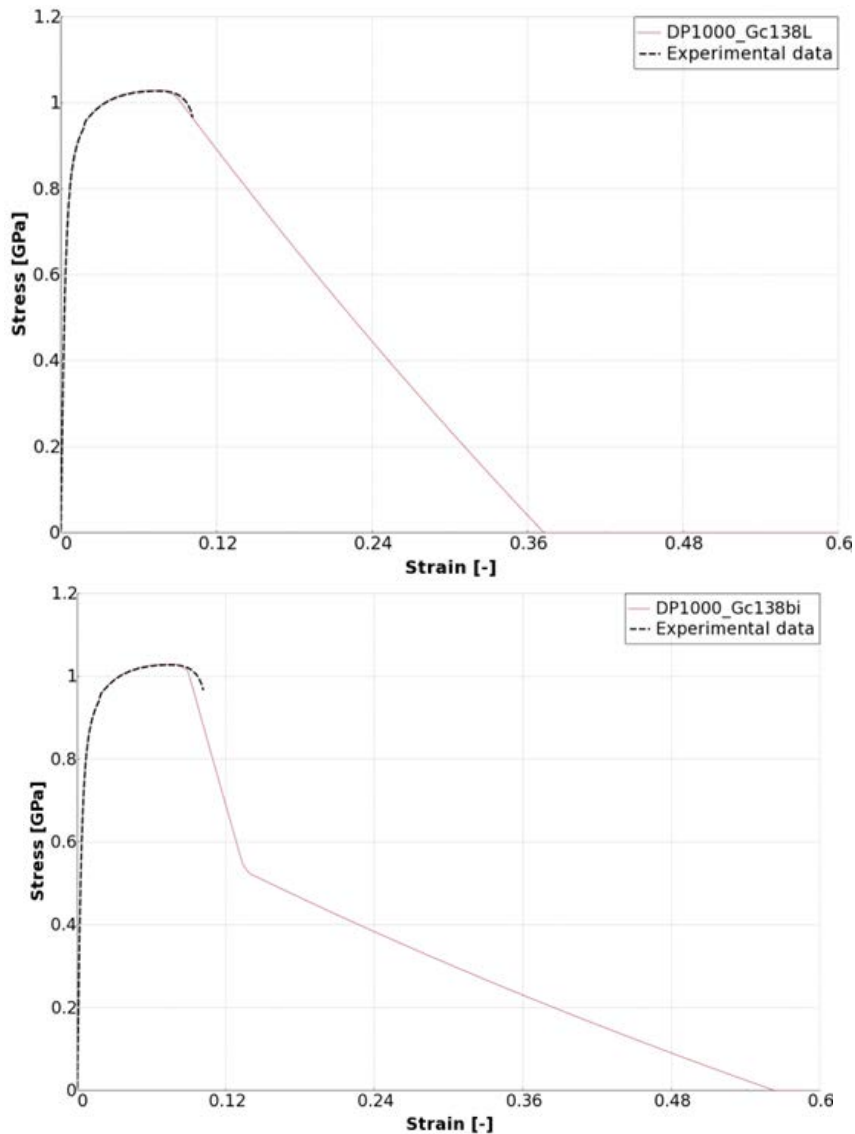


Figure 62. DP1000 with linear (upper) and bilinear (lower) damage definition, Gc 138 kJ/m²

The impact tests were modelled and simulated at different impact speeds, corresponding to the experimental tests. Axial and side loading conditions were considered. In the starting phase of the project, two series of simulations were performed in order to check effect of the values of both fracture toughness provided by the experimental EWF tests (from propagated and no-propagated specimens), and a third one, taking into account a brittle failure on the material.

The materials law used for these simulations was the material 24 (Piecewise Linear Plasticity) from the LS-Dyna material libraries. Damage and plasticity were introduced in a tabular form and no

failure criteria were considered. A good correlation level was achieved for the initial stiffness and the peak of initial load previous to damage. The correlation in the degradation phase, but, showed that neither of the tested laws is capable of providing a satisfactory solution for all the cases.

A second material law was evaluated from the LS-Dyna material libraries: the material 81 (plasticity with damage). This material is able to account with strain rates and allows the damage definition in the tabular form. The addition of the strain-rate effects, but, seems not to take influence in the range of strain rates observed in the models in this work. Thus, the correlation level remains similar than in the previous models, being improved only in the case of the Q&P material. Results obtained with this material law are shown in Figure 63 and Figure 64. A linear and a bilinear damage law was used and the different fracture toughness (G_c) values obtained in the EWF tests were applied (the low fracture toughness value corresponds to the propagated samples and the higher value corresponds to the not propagated samples).

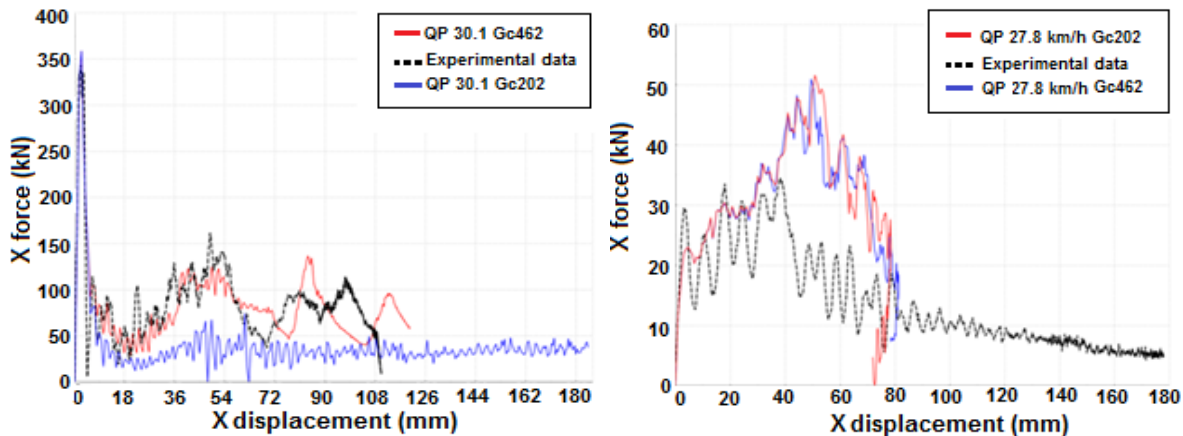


Figure 63. Force-displacement curves for QP linear axial impact at 30.1 km/h (left) and side impact at 27.8 km/h (right)

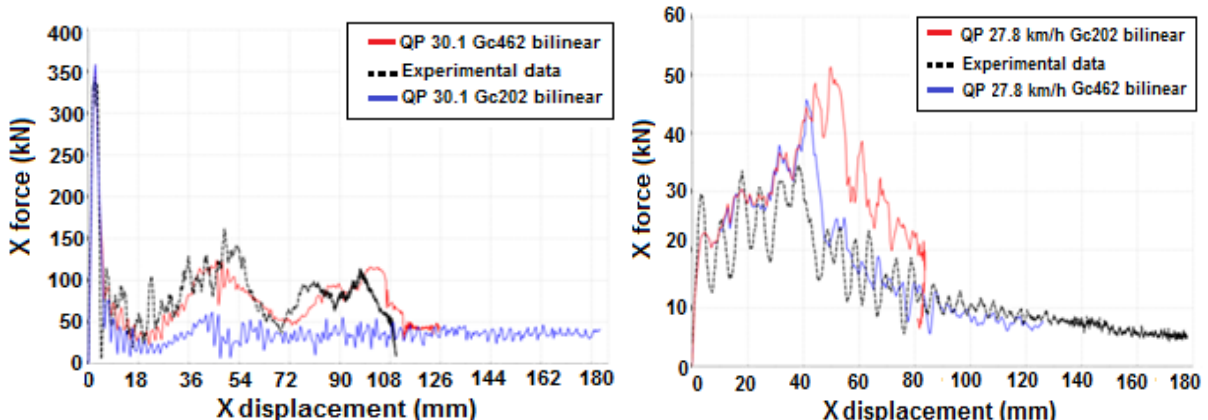


Figure 64. Force-displacement curves for QP bilinear axial impact at 30.1 km/h (left) and side impact at 27.8 km/h (right)

A third material definition was tested for the models in this work, in which the material is modelled as a material 24, as in the first series of simulations, but adding the option (“ADD_EROSION”). With the addition of this card to the material definition, the inclusion of a failure envelope is possible, but the damage must be introduced in linear evolution with the strains, leading to some limitations on the definition of the damage evolution in the material. The FLD envelope extracted from the experimental tests was used to compute an equivalent Johnson-Cook criterion that has a definition of failure dependent of the load directions, by means of one-element simulations.

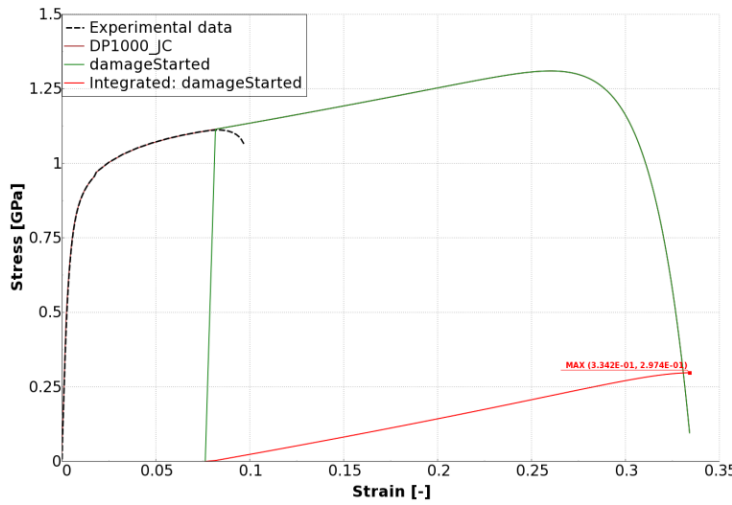


Figure 65. DP1000 mat 24 and MAT_ADD_EROSION, Gc 297 kJ/m²

Results of this third series of simulations (Figure 66, curves in red) showed a good level of correlation on the side-impact test simulations, but a loss of correlation on the axial-impact related simulations.

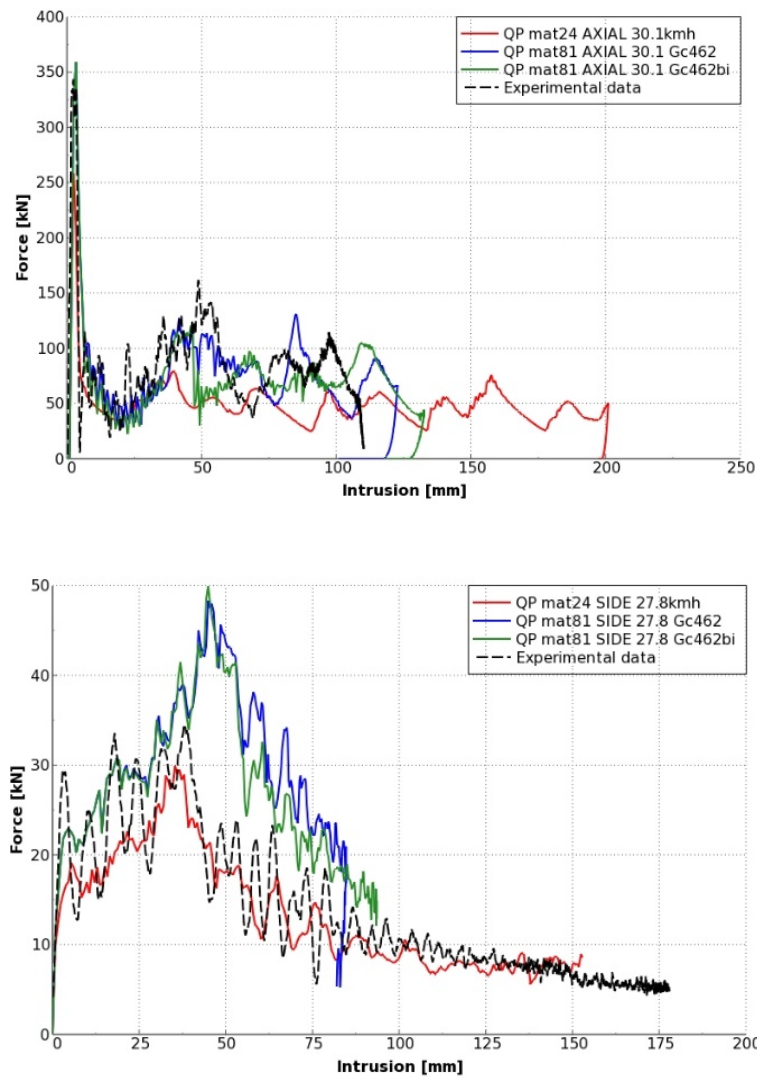


Figure 66. Force-displacement curves for QP mat 24 axial impact at 30.1 km/h (upper) and side impact at 27.8 km/h (lower)

Simulations with two different mesh refinements were solved for some models in this work. Results showed a dependency of the results with the mesh refinement, especially after damage is onset.

After the evaluation of the capabilities of the constitutive models in the LS-Dyna material formulations, there is not available any constitutive model regarding the three effects that can be relevant in the impact-related simulations in this work:

- Strain-rate related effect
- Inclusion of a failure envelope
- Definition of complex damage evolution laws.
- Implementation of the smeared methodology, in order to reduce the dependency of the results with the mesh-refinement.

In order to account with all of these effects, a new material model definition as a user subroutine in LS-Dyna should be implemented.

Task 3.4 Correlation of fracture toughness evaluated by means of EWF with crash resistance

Experimental correlation between EWF and crashworthiness

Aimed at investigating the correlation between fracture toughness and AHSS crashworthiness, the results of laboratory impact resistance tests were compared to EWF values. The impact resistance of the investigated steel grades was assessed according to a CI (definition in Table 7) and the energy absorbed in each deformed crash sample. The energy absorbed during impact tests was calculated by integrating the area under the load vs impactor displacement curves (Figure 67).

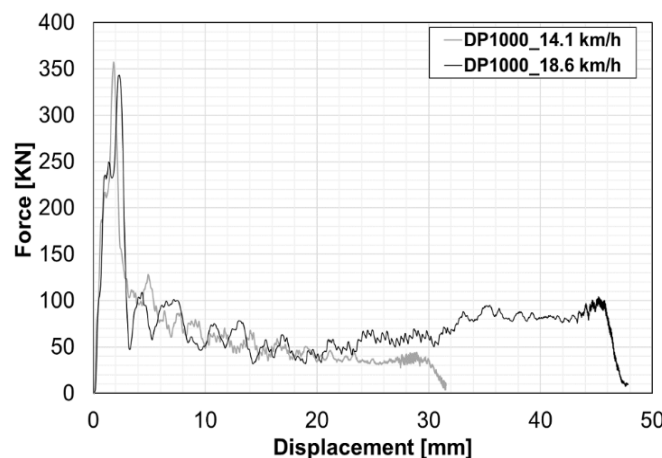


Figure 67. Force vs impactor displacement curves for two axial impact tests with DP1000

The evolution of damage in crash tests was investigated by plotting the values of energy absorbed and CI in function of intrusion level. Figure 68 shows the CI against intrusion and energy absorbed in axial crash tests for CP1000, DP1000 and CP1200. The crash index decreasing rate (CIDR), represented by the slope defined by the decrease of CI as a function of the intrusion level ($-\Delta CI/intrusion$), quantifies the crash resistance of the steel; the lower the slope the better crash performance. In the case of axial impact tests, CIDR is not a result of only base material behaviour because also includes the effect of welds unbuttoning for some steels. Nevertheless, it describes well the growth of existing cracks through the sample under impact loading, independently of their origin. The values of energy at maximum intrusion were used to determine the energy absorption capacity of the steels.

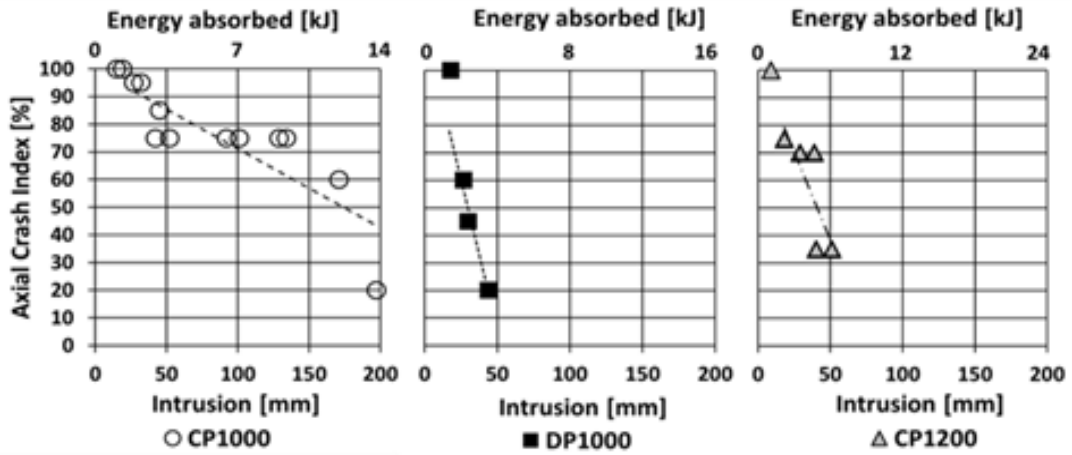


Figure 68. Variation of Crash Index (CI) in function of the intrusion and energy absorbed in axial impact tests for the studied steels. The slopes define the crash resistance of the material.

The axial and bending CIDR of the investigated AHSS grades is plotted against the EWF values in Figure 69 and Figure 70. A good correlation between both parameters was observed in axial crash tests (Figure 69). Results show better crash behaviour (lower CIDR) for tougher materials (higher w_e), following an almost linear relationship [FRO17]. The same investigations were performed on bending crash tests (Figure 70). In this case, no clear correlation was found, but it was defined a threshold w_e value from which no cracks were observed in the tested samples.

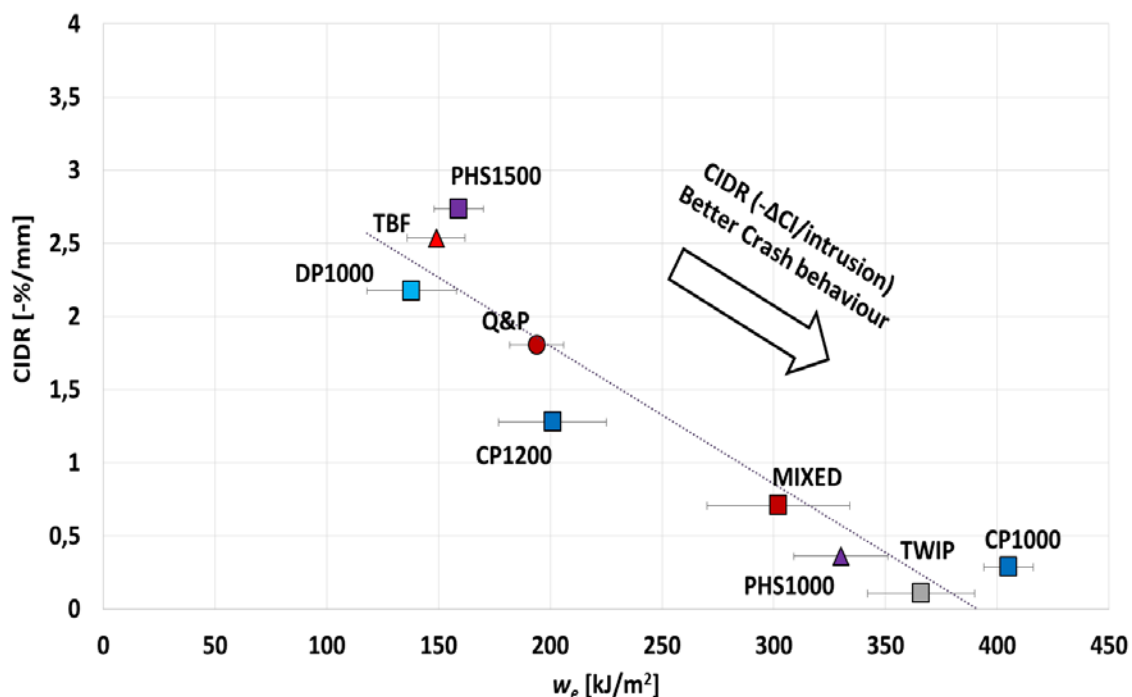


Figure 69. Correlation between w_e and axial CIDR

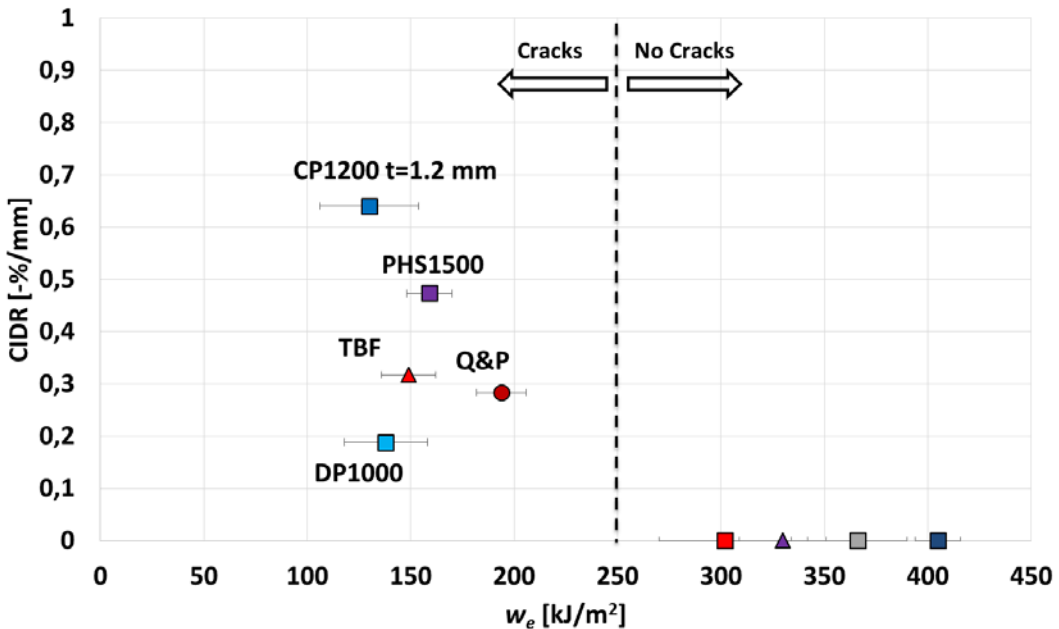


Figure 70. Correlation between w_e and bending CDR

The values of maximum energy absorbed in impact tests were also compared to toughness values in Figure 71 and Figure 72. The plotted energy values correspond to the energy absorbed at the maximum intrusion reached. Dashed arrows in Figure 71 indicate that energy values for some steel grades might be higher, since they did not reach the maximum possible intrusion in crash tests. As expected, a good correlation is observed between fracture toughness and the maximum energy absorption capacity in axial crash tests (Figure 71). However, no correlation was observed in bending impact tests (Figure 72). The values of energy absorbed at maximum intrusion were very similar for all steel grades, since maximum intrusion level was limited by the test equipment configuration (211 mm) and not by the material behaviour.

Such results prove the important role of fracture toughness on AHSS crashworthiness and the EWF is positioned as a suitable material parameter to classify AHSS impact behaviour. Hence, the identification and application of failure criteria based on EWF could be an important step towards the improvement of crash simulations, whose conventional models are based on plastic strain not considering the crack propagation.

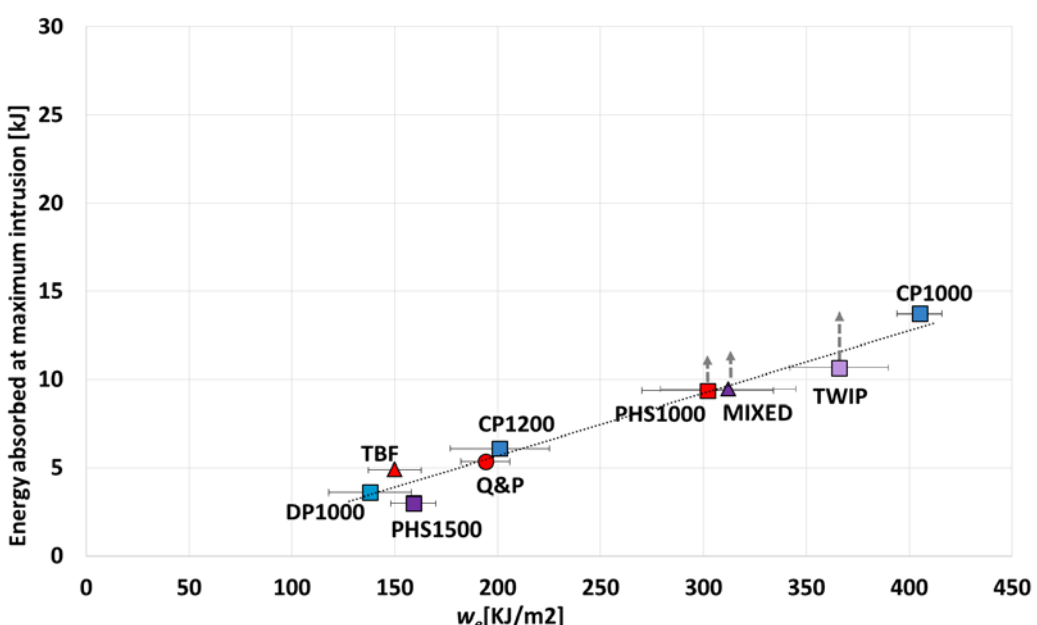


Figure 71. Correlation between w_e and energy absorbed at maximum intrusion in axial crash tests

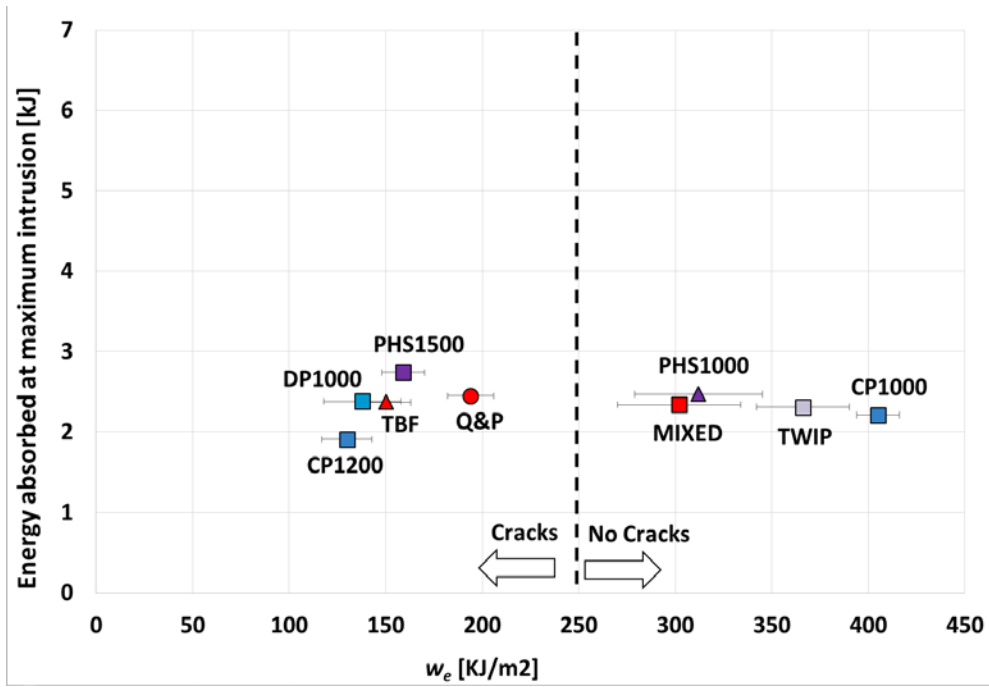


Figure 72. Correlation between w_e and energy absorbed at maximum intrusion in bending crash tests

Implementation of EWF-based criterion in crash simulations

A first attempt to use EWF as energetic fracture criterion in LS-Dyna was carried out in task 3.3. Axial-impact simulations showed a good correlation level with the application of fracture toughness obtained from notched specimens (no pre-cracks) with linear and bilinear strain-stress degradation. The application of the failure criteria and the linear strain-damage evolution, but, leaded to an underestimation of the force returned by the specimen.

The side-impact simulations showed an overestimation of the force returned by the specimen in the linear and bilinear strain-stress degradation, and a good level of correlation in the models where the failure envelope was introduced. The combination of complex damage evolution laws and the failure envelope would lead to the best correlation of both loading cases with the non-propagated fracture toughness. In that case, the side-impact related simulations would be able to consider the effects of complex loading states and the linear or bilinear strain-stress degradation would result in constitutive laws with a strain range large enough for the proper representation of the stress state in the axial-impact related simulations. In conclusion, EWF values showed to be valid for the magnitude of energy dissipated during the damage evolution in the material, but not to be accurate enough for the prediction of the damage initiation and propagation for all the different loading cases studied. Thus, the inclusion of failure criteria when the material works in complex loading states and a proper definition of the damage evolution is necessary to reproduce the behaviour of the materials in the whole range of the crash event.

Different constitutive models for isotropic materials from the LS-Dyna material libraries were tested. However, none of them showed to be capable of considering all the effects combined: failure criteria, user-defined damage law, strain rate effects, etc. The implementation of a user material accounting with all of these effects is recommended in order to improve the level of correlation and to be able to reproduce the behaviour of the material in the different loading cases studied.

In order to take profit of the modular material definition and combination of implicit/explicit simulations, a detailed study of the EWF tests with material DP1000 was performed using ABAQUS/Standard and ABAQUS/Explicit solver.

Two different options are available for the input of the damage evolution: Energy-based evolution and Displacement-based evolution. Both of them offer similar laws (Figure 73). Displacement-based evolution is defined as displacement at failure measured from the damage onset. An equivalent linear damage law can be defined with both methods but the energy-based evolution is less flexible because it is not possible to define it in tabular form. For that reason, the energy-based definition can only take a linear or exponential form.

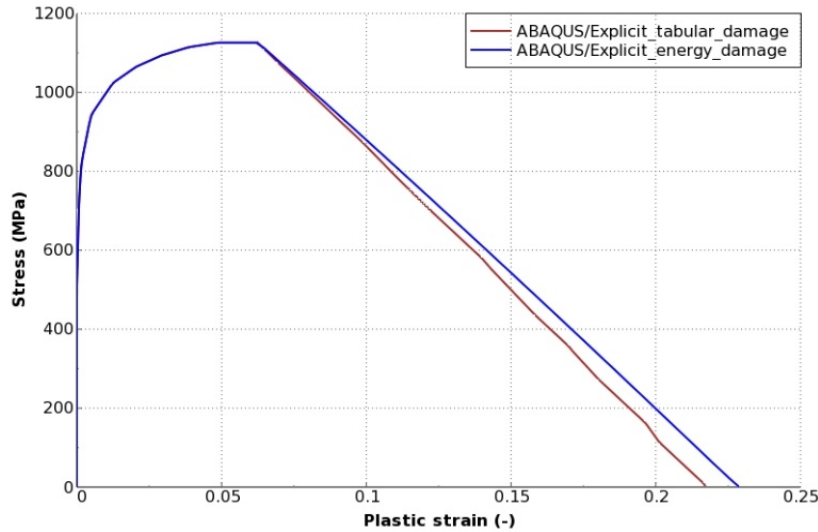


Figure 73. DP1000 1 element tensile test comparing damage inputs

In order to check the influence of the integration methodology, a similar simulation was solved using standard and explicit solver (Figure 74). When comparing both integration methods, it can be observed that the integration scheme leads to small changes in the solution of the simulation, where the explicit method shows a delay in the damage onset and propagation of about 0.02mm.

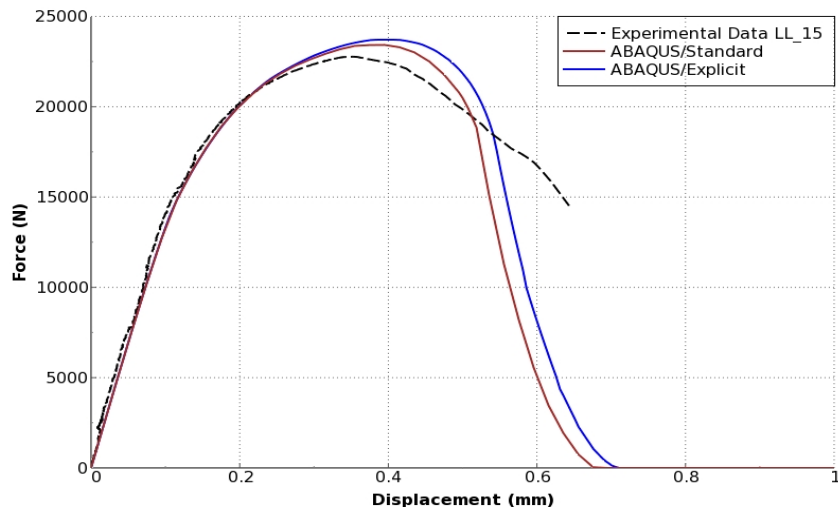


Figure 74. Comparison Implicit vs Explicit solver. Ligament length (LL) = 15 mm

Regarding the mesh influence, results showed a strong dependence with the mesh refinement after damage is onset (Figure 75). Therefore, the damage law was adjusted to 1mm element length, and scaled to different mesh refinements.

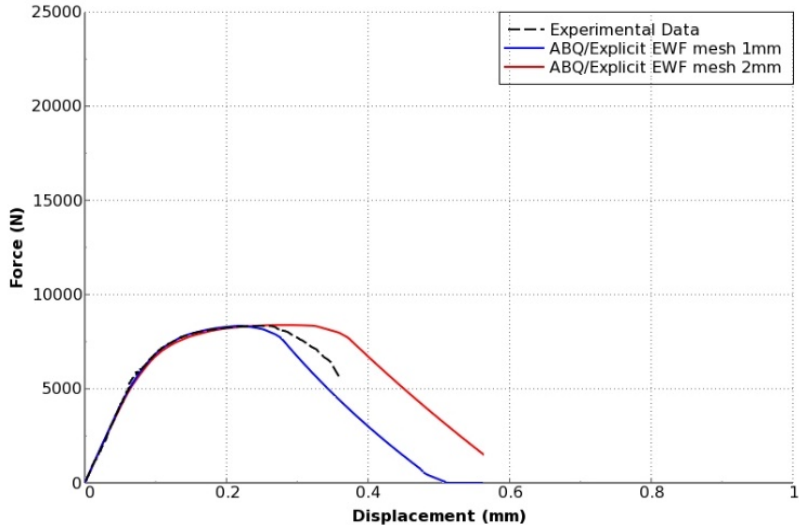


Figure 75. Mesh influence. Ligament length (LL) = 5 mm

The influence of damage evolution parameters was assessed by proposing linear degradation laws with different fracture toughness values. These investigations aimed at obtaining a better correlation of the force in the necking and onset of crack propagation of the experimental tests. Figure 76 shows different damage evolution values proposed for a DP1000 specimen of 15 mm length. It is observed that small values of fracture toughness lead to a brittle damage evolution, not able to capture the progressive loss of stiffness in the experimental test until the brittle failure. For higher values, a better correlation for damage propagation can be achieved, but the overestimation of the maximum force becomes higher and the brittle failure cannot be represented.

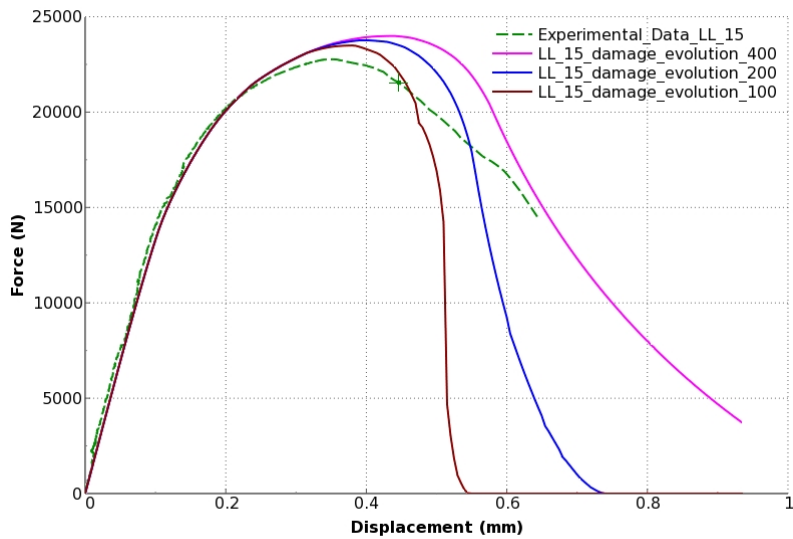


Figure 76. DP1000 EWF test with different damage evolution values

The brittle failure of the specimens was studied, in order to find a damage law that fits well with the experimental behaviour, keeping the damage initiation already defined by plastic deformation and defining the damage evolution in tabular form (displacement-damage). In this case, a complex degradation law was used, where a first degradation slope was defined for the necking process, and a second slope with brittle ending was used to define the crack propagation and specimen failure.

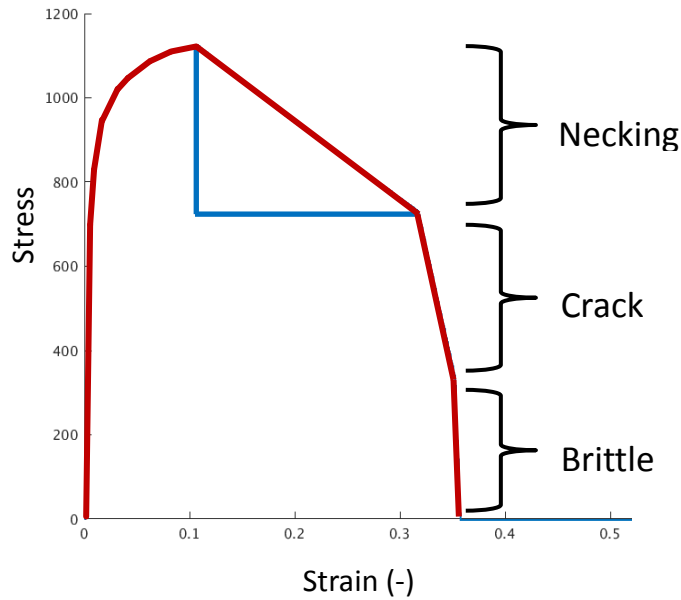


Figure 77. Failure processes modelling

Two new damage law types were proposed (Figure 78), law 1 in blue and law 2 in red. Both laws include different slopes for the necking, while the crack propagation and the brittle failure processes remain equal.

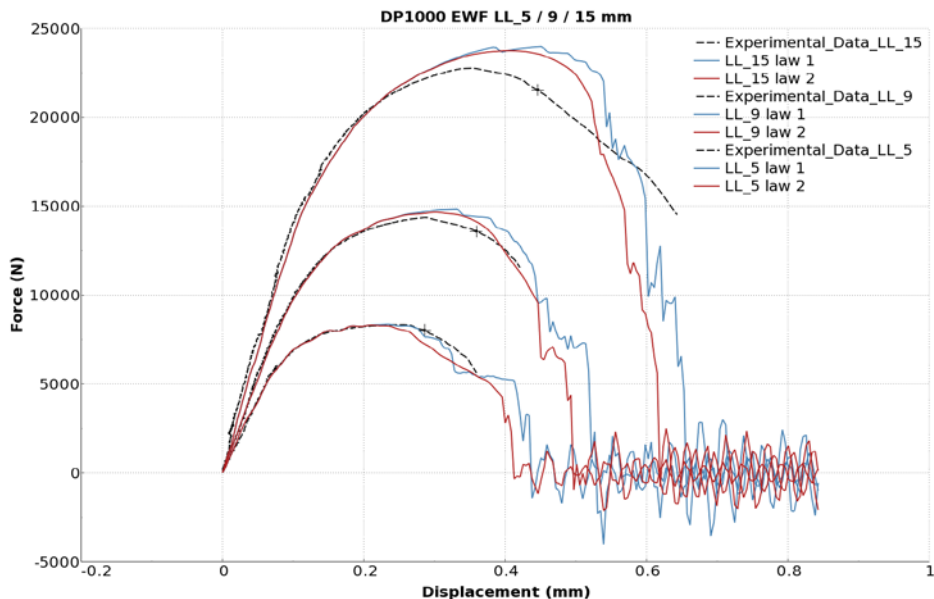


Figure 78. EWF quasistatic DP1000 NP with two new damage laws

The application of the new proposed laws leads to an improvement on the correlation of the specimens from the previously proposed damage laws (Figure 79). The onset of damage at the specimens with larger ligament length remains at the levels of the linear laws, while a good representation of the brittle failure was observed with these damage laws.

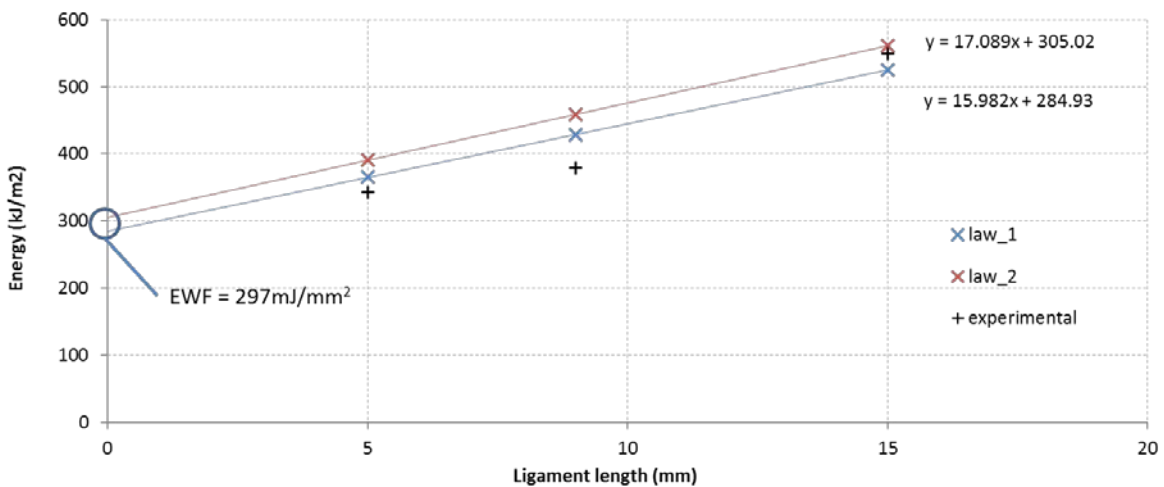


Figure 79. EWF energy with the last two damage laws

The EWF value computed from the numerical simulations (305.02 and 284.93 mJ/mm²) was similar to the provided by the experimental data (297 mJ/mm²).

The damage law that presented a better behaviour is the law 2 because it allows a smoother evolution of the damage. The parameters for this damage law 2 are detailed below.

```

*DAMAGE INITIATION, CRITERION=DUCTILE
** Eq.Str.,      Str.3ax.,   Str.Rat.
    0.100,        0.0,        0.
    0.100,        1.0,        0.

*DAMAGE EVOLUTION, TYPE=DISPLACEMENT, SOFTENING=TABULAR
** Damage.,      displac.,
    0.,          0.,        0.
    0.15,        0.0850,    0.
    0.35,        0.210,     0.
    0.70,        0.2450,    0.
    1.,          0.250,     0.
  
```

This new damage evolution model was used in WP6 in order to improve the accuracy of crash simulations.

2.2.4. WP4. Sheet formability assessed by EWF

The main objective of WP4 was to assess the formability of the different AHSS grades through fracture toughness measurements. An energetic fracture criterion based on EWF was investigated in this WP aimed at implementing it in FE forming simulations. Additionally, some probably influencing parameters on fracture toughness, such as pre-straining conditions were investigated as well as the origin of cracks in cold forming. The laboratory forming tests were simulated by FEM modelling aimed at analyzing the accuracy of the current models and to detect their weak points.

Table 20. Tasks of WP4

Task	Name of the task
Task 4.1	Material selection according to the formability and EWF results
Task 4.2	Effect of pre-straining on EWF in AHSS
Task 4.3	Fracture origin characteristics in cold forming
Task 4.4	Simulation of forming tests
Task 4.5	Correlation of fracture toughness evaluated by means of EWF with sheet forming tests

Task 4.1 Material selection according to the formability and EWF results

3 materials were selected for the formability investigations in WP4, according to the results of WP1 and WP2:

- 1 bending grade: CP1000. This grade presents high fracture toughness, stretch flangeability and bendability, which makes it suitable for bending operations with small bending radii. On the other hand, the deep drawing of this steel is moderate.
- 2 deep-drawing grades: TBF and DP1000. These two steel grades, show lower fracture toughness and stretch flangeability, but their high n-value and elongation make them more suitable for deep-drawing operations.

Task 4.2 Effect of pre-straining on EWF in AHSS

The main objective of this task was to determine the effect of pre-straining on fracture toughness. The EWF tests were carried out with specimens subjected to different pre-straining conditions in order to evaluate the influence of the strain level and the strain path. 3 pre-straining conditions were considered: uniaxial, plane and biaxial pre-strain (Figure 80). For uniaxial pre-straining conditions, the pre-strain level was set in 4% for DP1000 and CP1000 and 8% for TBF. For plane and biaxial pre-straining the pre-strain level was set in 4% for the three steel grades.

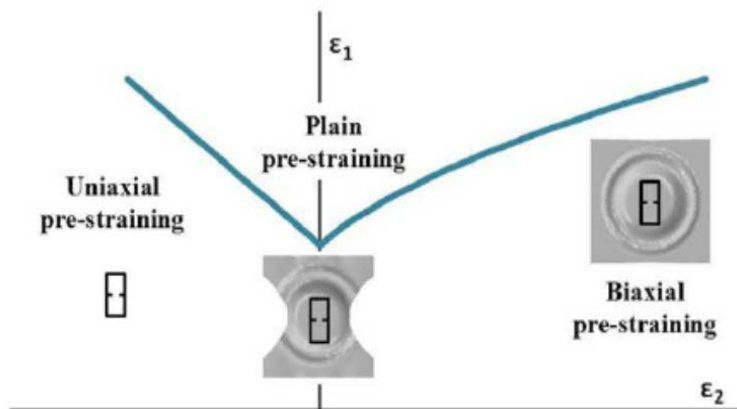


Figure 80. Schematic representation of uniaxial, biaxial and plane pre-straining conditions for fracture toughness measurements

For uniaxial pre-strained condition, rectangular samples of 240x70 mm were deformed up to the above-mentioned strain values. Such strain levels were within the plastic zone and before maximum stress. After pre-deformation, rectangular DENT specimens of 240 x 55 mm (Figure 31a) were extracted from pre-strained samples.

Biaxial and plane pre-strained specimens were pre-deformed by means of Marciak tests. Two different geometries were used to achieve biaxial and plain strain conditions. The pre-strain tests were conducted at the forming test lab by CRF. For each material (DP1000, CP1000 and TBF) 24 samples were pre-strained: 12 in plain strain condition and 12 in biaxial condition. The final pre-strain was set to 4% in the biaxial and plane pre-straining conditions. Strain level was checked in all samples by means of a DIC equipment.

After the pre-straining process, DENT specimens of 140x55 for EWF evaluations were extracted from the flat zone of the stretched samples (Figure 81). It must be noted that the EWF in uniaxial pre-straining condition was evaluated with fatigue pre-cracked specimens. Thus, uniaxial pre-strained EWF was compared with the EWF for propagated specimens (P-type specimens). On the other hand, due to the limitation of the Marciak samples geometry, the DENT specimens obtained were smaller than usually (140 x 55 mm) and the ends were slightly bended, which hampered the proper propagation of the cracks from the notches. For this reason, it was decided to test these specimens without fatigue pre-cracks and compare the results with those reported in task 2.1 for not propagated notches (NP-type specimens). Results of EWF at different pre-straining conditions are summarized in Figure 82 and Figure 83.



Figure 81. Rectangular specimens extracted from pre-strained samples.

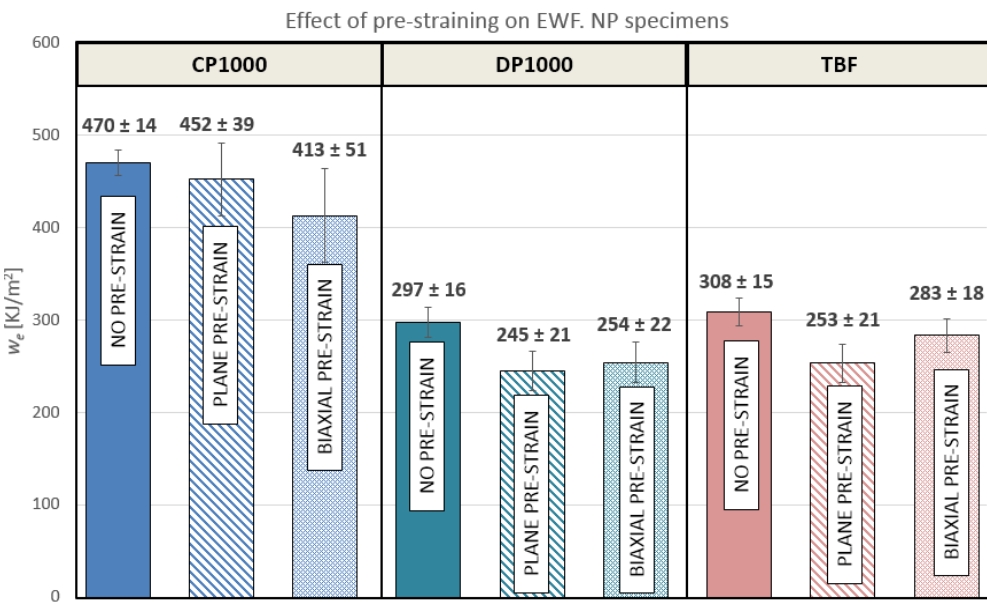


Figure 82. Results of EWF with plane and biaxial pre-strained NP-type specimens. EWF results with no pre-strained NP-type specimens are also shown for comparison.

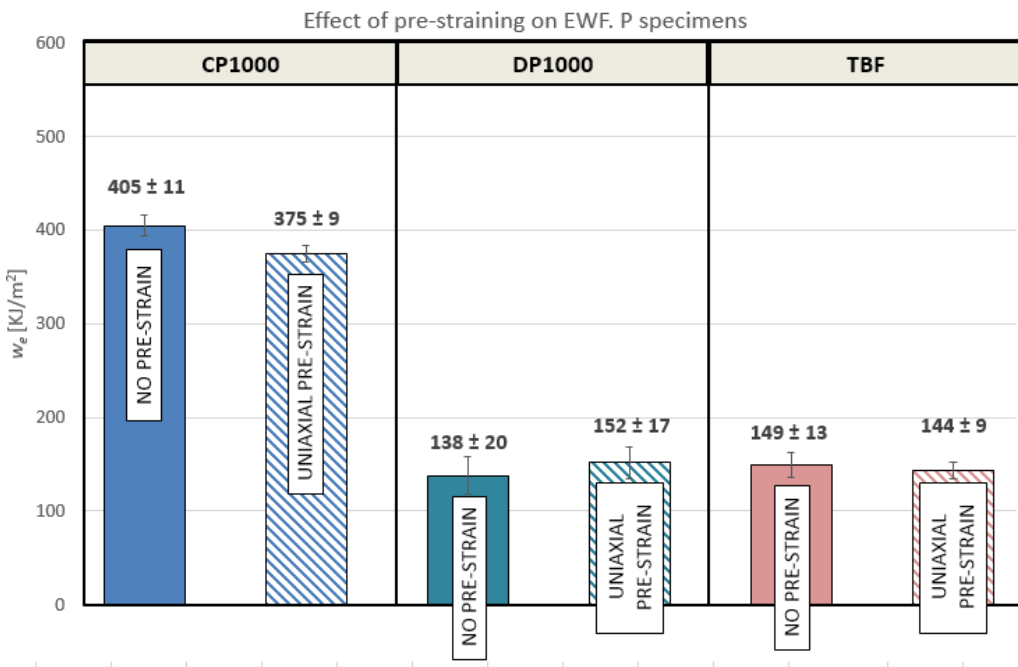


Figure 83. Results of EWF with uniaxial pre-strained P-type specimens. EWF results with no pre-strained P-type specimens are also shown for comparison.

Results show that uniaxial pre-straining has no influence on the EWF in any of the investigated steel grades. For biaxial and plane pre-straining conditions, the influence is not so clear. EWF values are slightly lower than the obtained for the no pre-strained specimens, but it must be considered that the thickness of the pre-strained specimens is lower and this could explain such differences. In the case of NP-type specimens, the influence of specimen thickness is probably greater.

Hence, from the obtained results, it can be assumed that pre-straining conditions did not affect significantly the measured fracture toughness of the studied steel grades.

Task 4.3 Fracture origin characteristics in cold forming

The main objective of this task was to investigate the origin of fracture in cold forming tests (task 1.4). SEM investigations were performed on the fracture area of Marciniaik stretched specimens. Also the punched area of HET specimens was examined in order to assess the damage induced during punching.

Marciniak test specimens

The SEM images of the investigated Marciniaik specimens are shown in Figure 84 and Figure 85. The investigation was focused on searching possible damage initiation sites, such as inclusions or precipitates.

The analysis of the fracture surfaces showed an overall ductile fracture, indicated by the multiple dimples. Some inclusions were found in DP1000 (Figure 85). However, these inclusions (titanium carbides) were located in the middle section of the material thickness, far from the surface and they did not have influence on fracture initiation. In general, the defects observed had no influence on the fracture process.

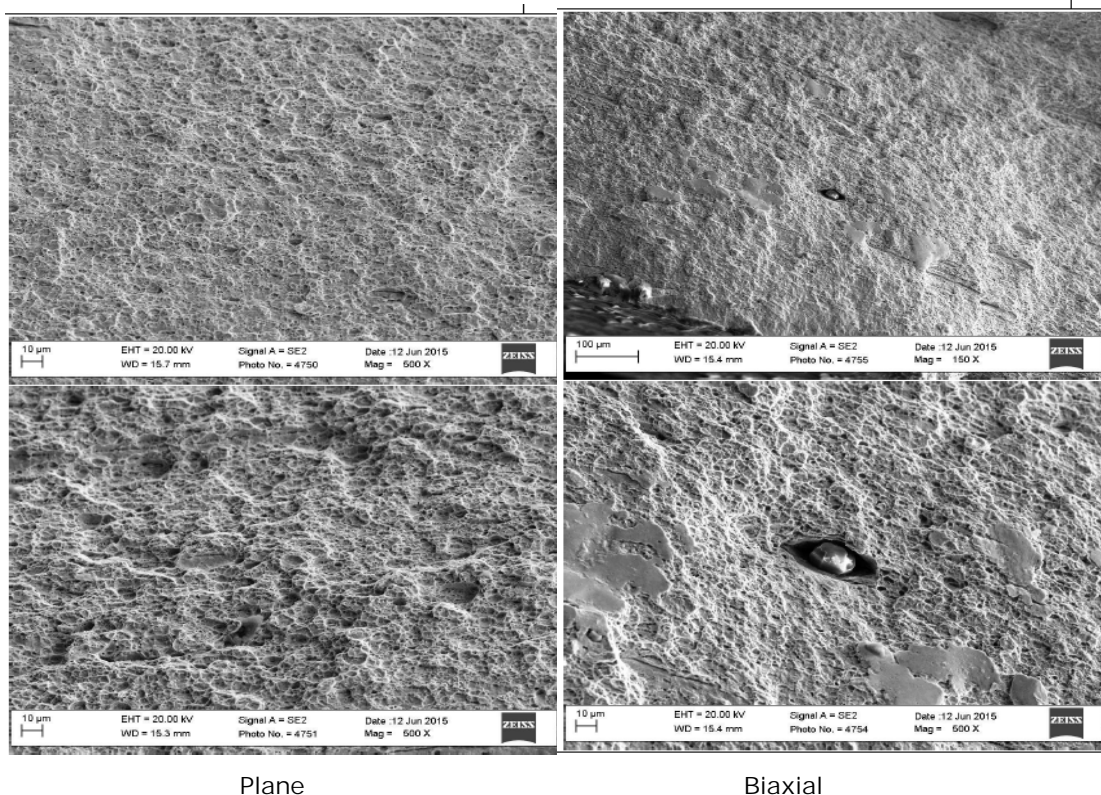
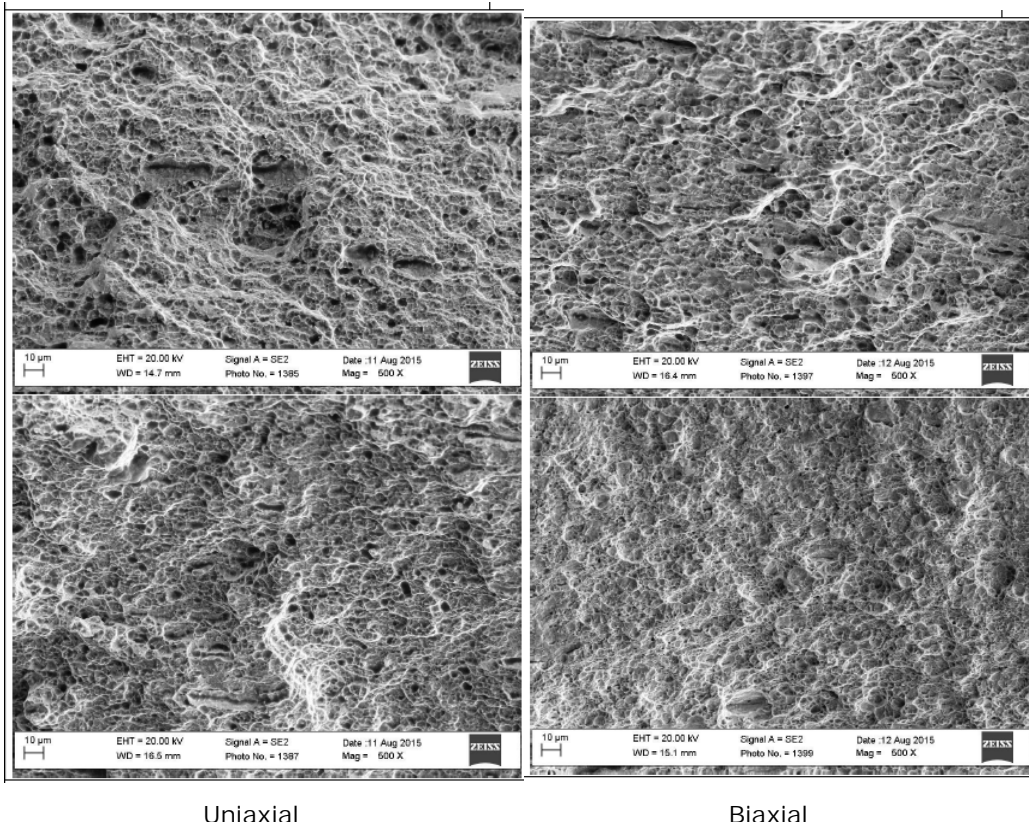


Figure 84. DP1000. SEM images of the fracture surfaces of Marciniaik test specimens at plane and biaxial deformation modes.



Uniaxial

Biaxial

Figure 85. TBF. SEM images of the fracture surfaces of Marcinick test specimens at uniaxial and biaxial deformation modes.

Punched HET specimens

HER has become a useful tool to assess the stretch-flangeability of AHSS grades, since it closely resembles cold forming operations starting from punched holes or trimmed areas such as stretch flanging or hole expansions. AHSS grades, due to their limited ductility are especially sensitive to the damage induced during punching operation.

Aimed at investigating crack origin in HER, the fracture surfaces of punched HET specimens were examined by means of SEM.

Figure 87 to Figure 89 show some SEM images of fracture surfaces of CP1000, DP1000 and TBF punched specimens. Images show a general view of the fracture surface at 45x and details of different areas at various magnifications. In the images can be distinguished the different characteristic zones of sheared fracture surfaces: rollover, burnished zone and fracture zone (

Figure 86). Generally, it is observed that burnished zone is 1/3 or less of the full thickness for the three steel grades. Burnished zone shows typical punch scratching marks (Figure 87a) and some cracks in the case of DP1000 (Figure 88a). The fracture zone presents a rough surface with a large amount of dimples orientated to the shearing direction, which are indicators of ductile fracture. However, also quasi-brittle facets (Figure 87b) and a significant quantity of defects, such as micro-cracks, voids or material ripped out, are present in the three investigated steel grades. Cracks can be also observed in the transition zone burnished-fracture for DP1000 and TBF (Figure 88b and Figure 89b). Such defects can act as fracture initiation sites and trigger crack propagation through the sheet thickness in subsequent cold forming operations [GUT13, TAK09, WU12]. Therefore, AHSS stretch-flangeability and edge fracture is mainly governed by two factors: the edge quality (how much the material is damaged) and the material resistance against the propagation of cracks, i.e. the fracture toughness [CAS17, TAK12, FON11, YOO16].

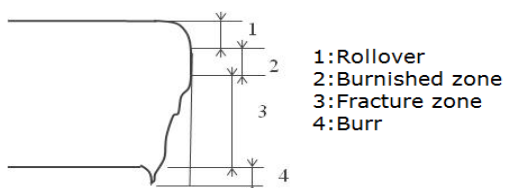


Figure 86. Characteristics of sheared fracture surface

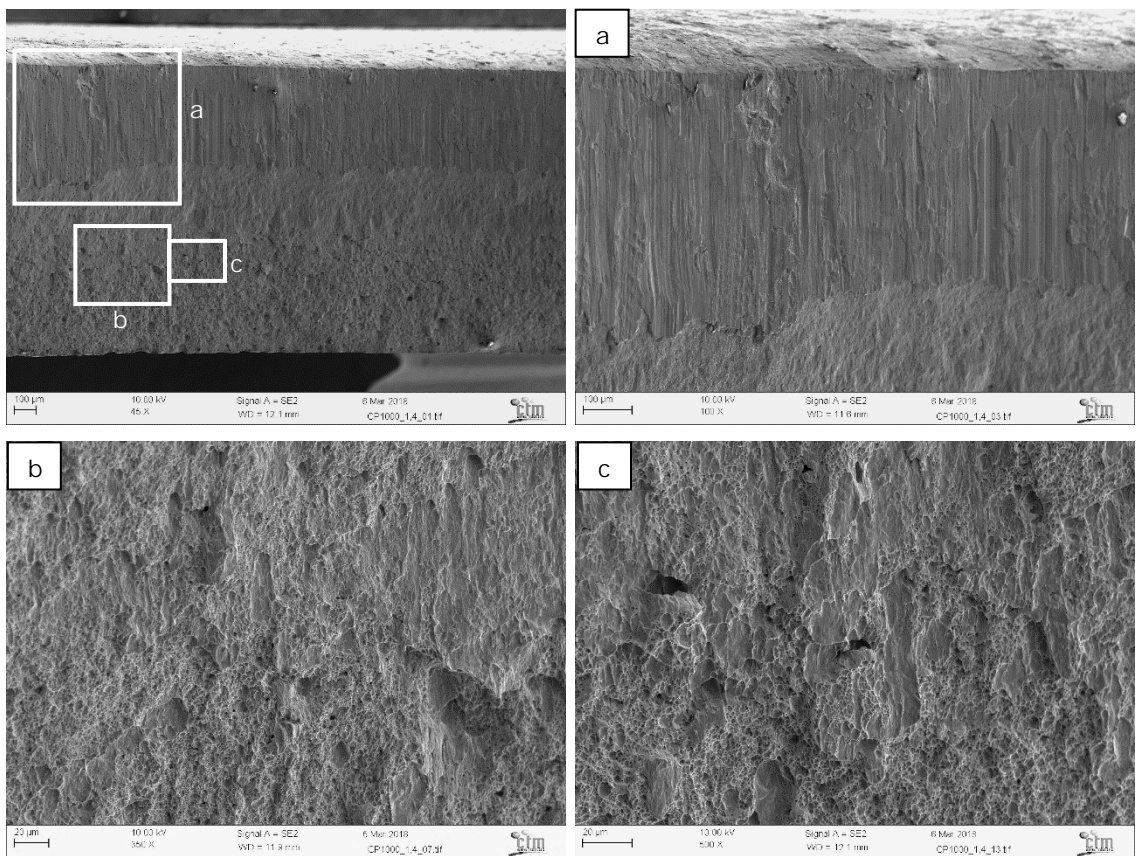


Figure 87. CP1000. Fracture surface of punched area. Top left: General view of the fracture surface at 45x. a) Detail of burnished area (100x), b) Detail of fracture zone (350x) and c) detail of fracture zone (500x).

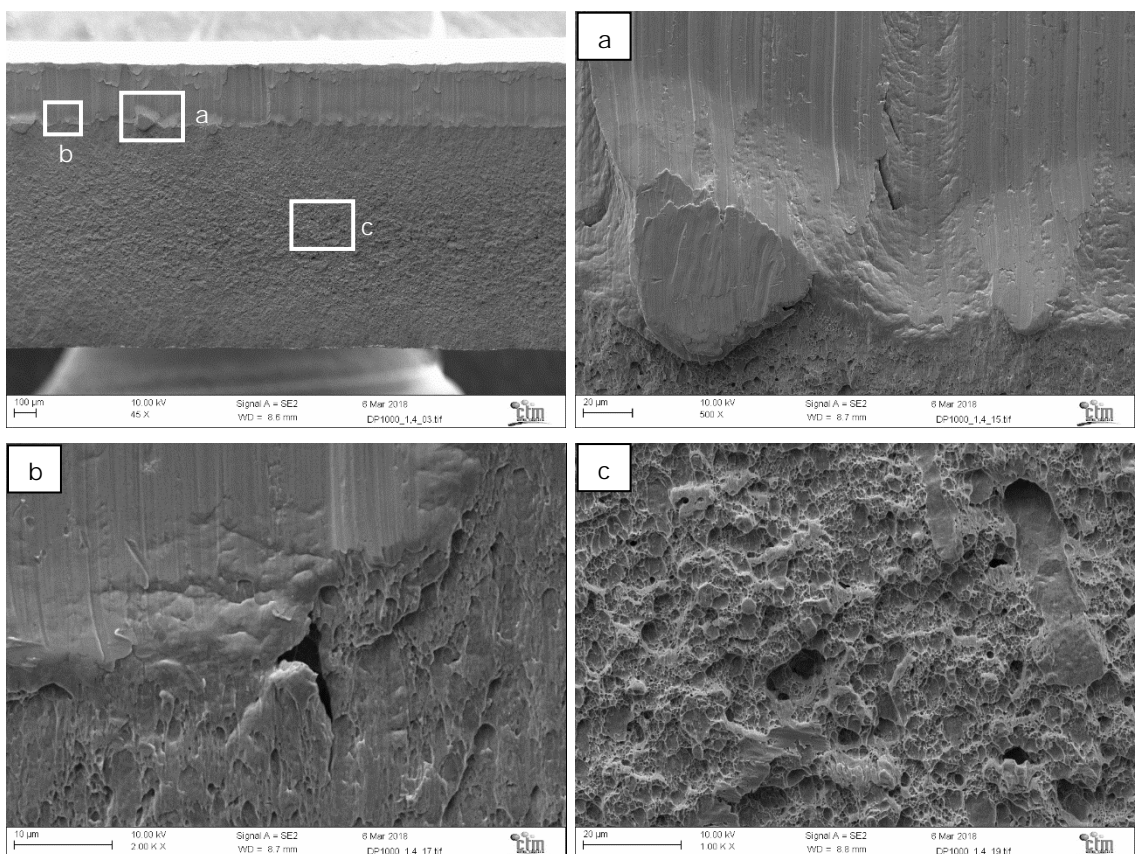


Figure 88. DP1000. Fracture surface of punched area. Top left: General view of the fracture surface at 45x. a) Detail of burnished area (500x), b) Detail of transition burnished-fracture zone (2000x) and c) detail of fracture zone (1000x)

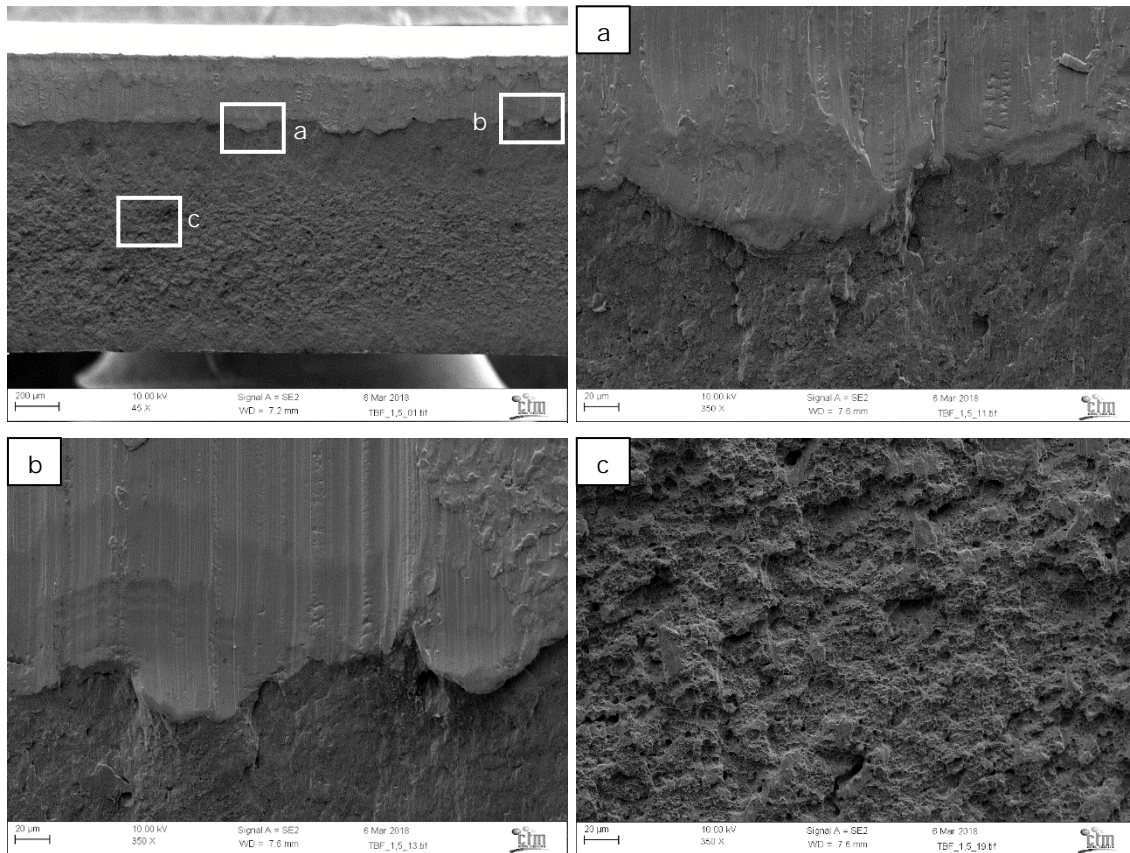


Figure 89. TBF. Fracture surface of punched area. Top left: General view of the fracture surface at 45x. a) Detail of transition burnished-fracture area (350x), b) Detail of transition burnished-fracture zone (350x) and c) detail of fracture zone (350x)

In order to investigate the fracture origin in an automotive part, CRF manufactured a complex geometry component, the inner sill side reinforcement (Figure 90). The component was formed using crash forming methodology with the three steel grades selected in task 4.1: CP1000, DP1000 and TBF. Such component was used in WP7 to investigate the correlation between forming process and simulations. Two different cutting methods were applied, aimed at evaluating the influence of the edge quality on the apparition of cracks: laser cutting and shearing. The forming process was stopped at different levels of press stroke to investigate the crack initiation and propagation. The first cracks appearing in the component were examined by means of SEM.

Figure 91 shows the first cracks appeared in components formed with DP1000, CP1000 and TBF laser cut blanks. Cracks appeared at different strokes for the three materials:

- DP1000: 45 mm of stroke
- CP1000: 45 mm of stroke
- TBF: 50 mm of stroke

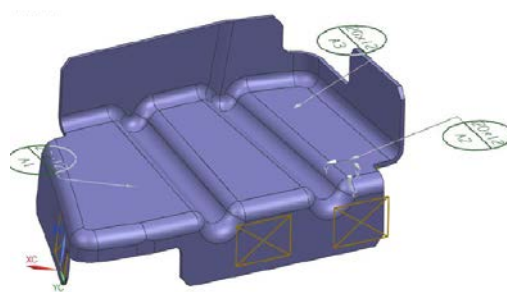


Figure 90. Inner sill side reinforcement.

DP1000

CP1000

TBF



Figure 91. First crack appearance (red circles) in components manufactured with laser cut blanks of DP1000, CP1000 and TBF.

SEM images of the examined fractures are shown in Figure 92 to Figure 94. The fracture analysis indicated that cracks were due to localized necking and not by edge conditions. These type of fractures are related to strain hardening and FLC, whereas edge cracking is more related to fracture toughness and edge quality [CAS17, GUT13, TAK12, THO13, GLA14]. In this case, no significant edge cracking was observed in any of the steel grades. The absence of edge cracks can be explained by the high edge quality obtained by the laser cutting.

Small secondary edge cracks were observed along the fractured area in TBF and DP1000 but not in CP1000. These cracks were triggered by defects present in the damaged area (in this case the fracture surface), no necking took place and the fracture was controlled by the crack propagation resistance of the material. This can explain why cracks are observed in the two steel grades with lower EWF values (TBF and DP1000) and not in CP1000, which shows much higher fracture toughness values. In any case, such secondary edge cracks were not the origin of the component fracture.

Similar investigations were performed in sheared cut blanks. The first observation is that strain level for crack appearance is much lower than the observed with laser cut blanks (Figure 95 to Figure 97). In this case, the first cracks appeared at lower press strokes:

- DP1000: 38 mm
- CP1000: 39 mm
- TBF: 37 mm

SEM images of fractures in shear cut components are shown in Figure 98 to Figure 100. A low strain localization was observed in the fracture. In this case, the fracture is highly influenced by the damage induced in shear cutting and, thus, the fracture is more related to fracture toughness. This relation is also suggested by the stroke levels for cracking appearance, which are in good agreement with fracture toughness results. The results remark the importance of the edge quality on AHSS forming and the role of fracture toughness on sheared edge fracture.

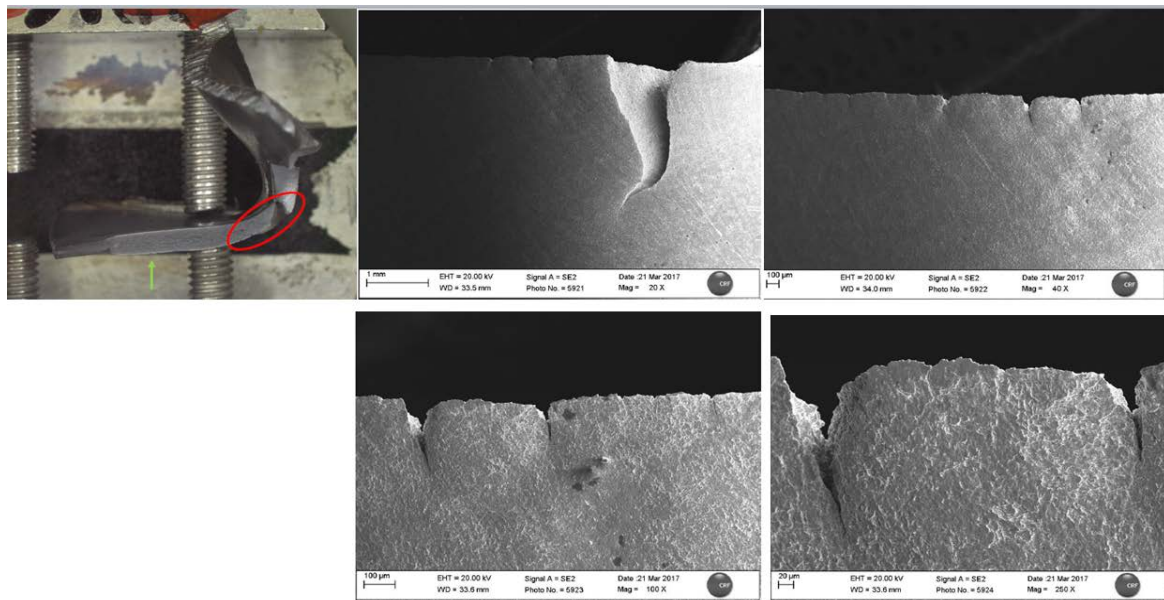


Figure 92. DP1000 SEM analysis. Laser cut blank

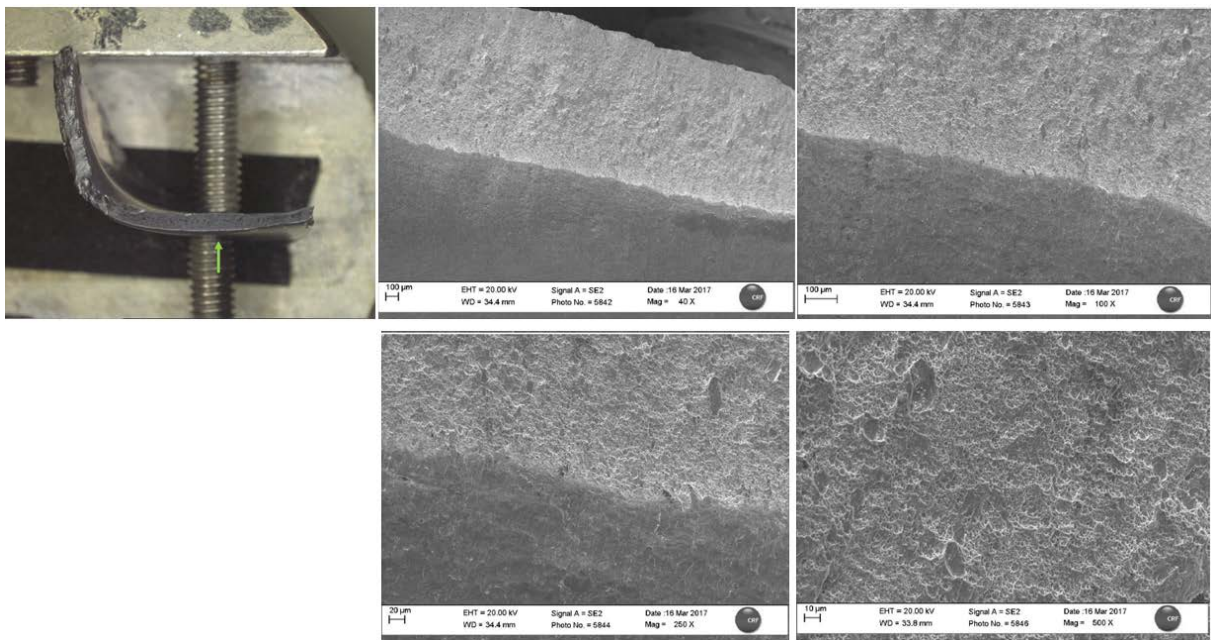


Figure 93. CP1000 SEM analysis. Laser cut blank

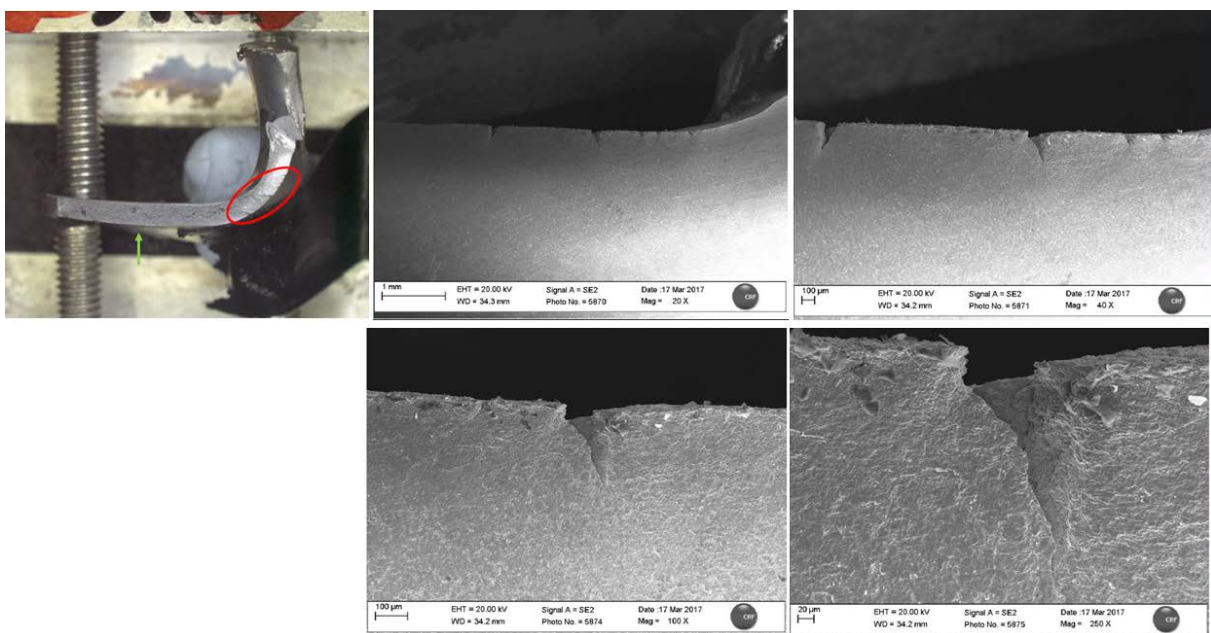


Figure 94. TBF SEM analysis. Laser cut blank



Figure 95. First crack appearance (red circle) in a component manufactured with DP1000 sheared blank.

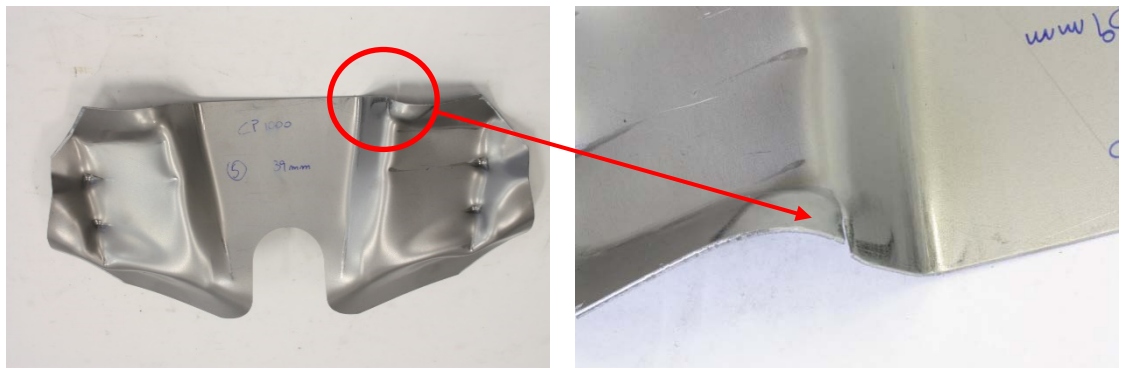


Figure 96. First crack appearance (red circle) in a component manufactured with CP1000 sheared blank



Figure 97. First crack appearance (red circle) in a component manufactured with TBF sheared blank

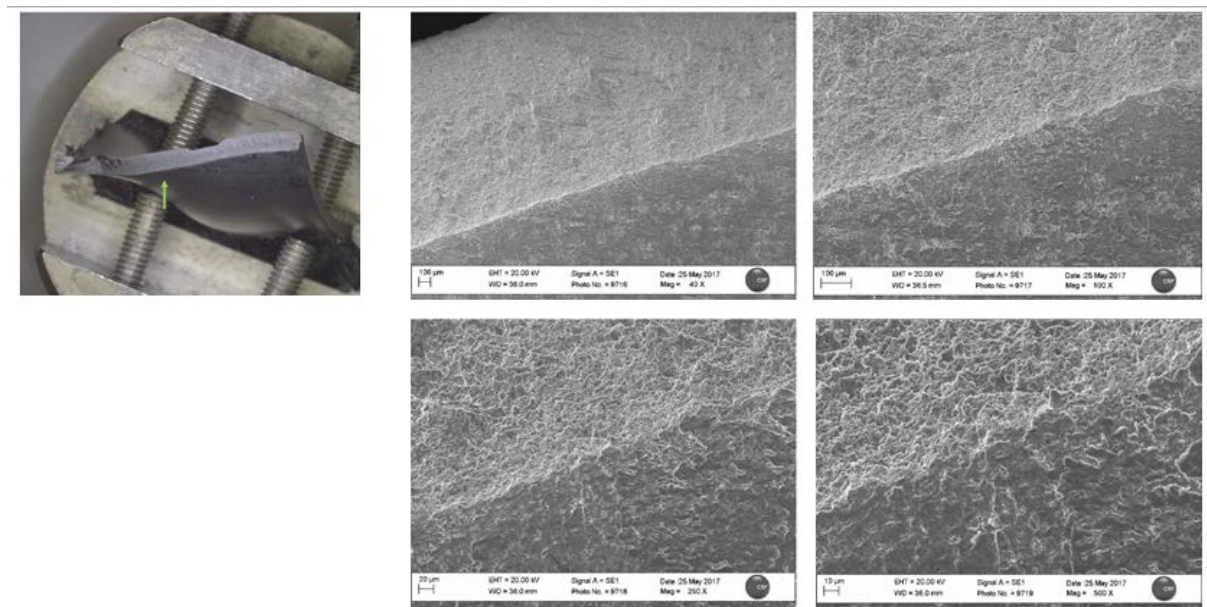


Figure 98. DP1000 SEM analysis. Sheared blank

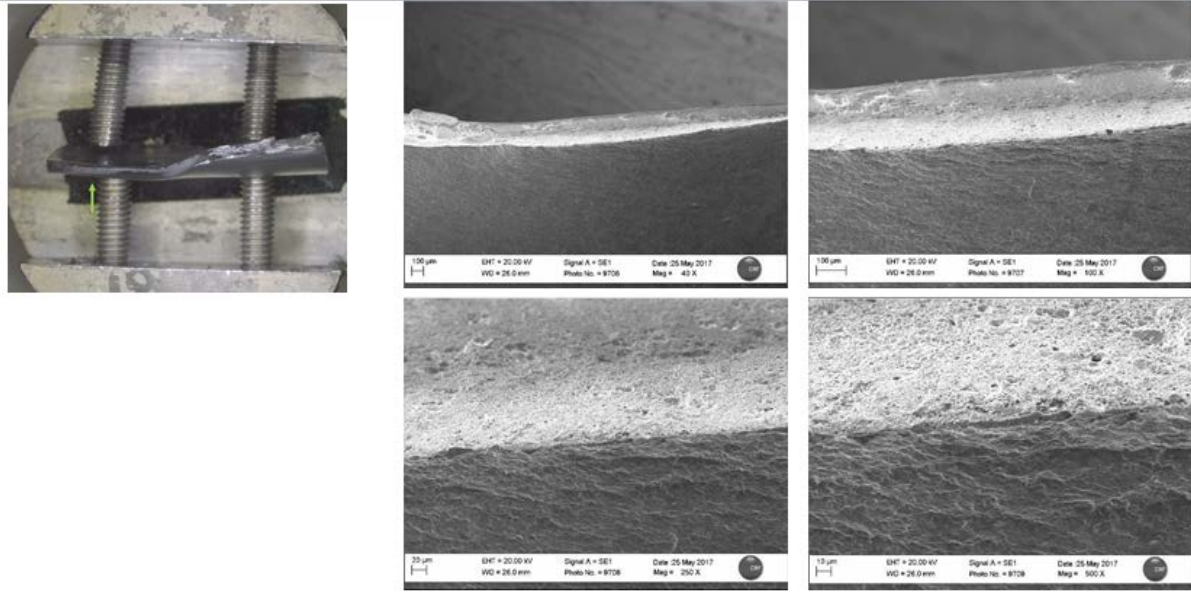


Figure 99. CP1000 SEM analysis. Sheared blank

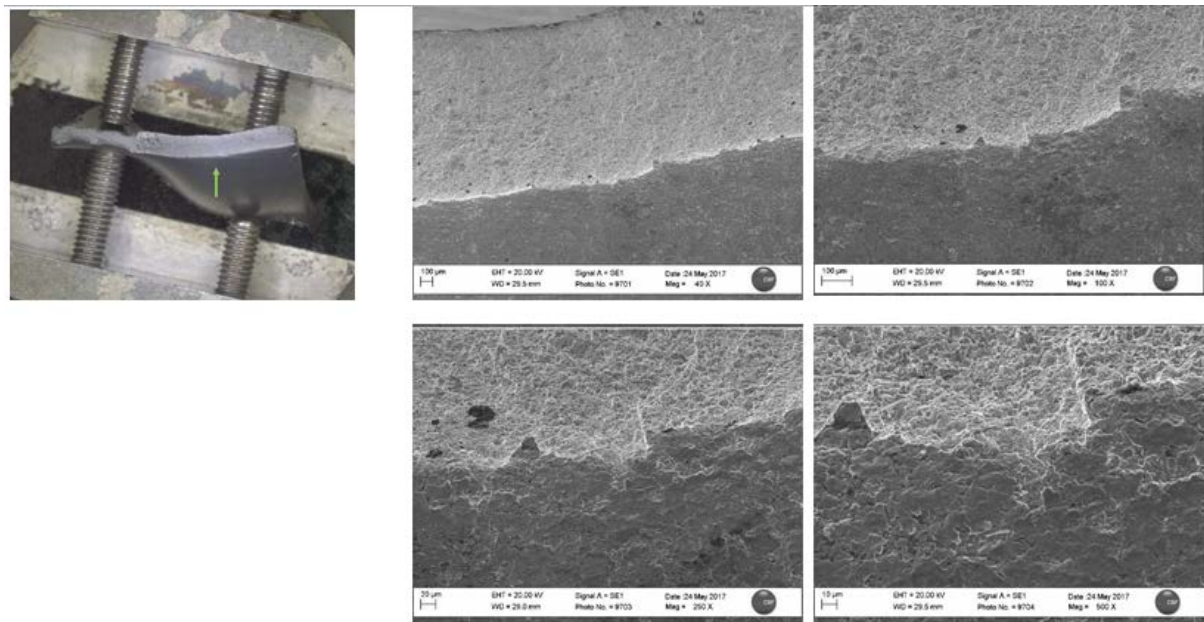


Figure 100. TBF SEM analysis. Sheared blank

Task 4.4 Simulation of forming tests

Simulation of FLDs

Nakajima tests performed in task 1.4 were simulated in Abaqus software, in order to obtain the energy at failure (following FLC criteria) and compare it with the measured fracture toughness values in task 2.1. The model was based on the specimens used in experimental FLC tests. Only 1/4 of the specimen was reproduced due to the symmetry with respect 2 axes. The sketches of the model geometry given by CRF and the specimens to calculate a 3D deformable shell planar with 1.4mm thickness are shown in Figure 101.

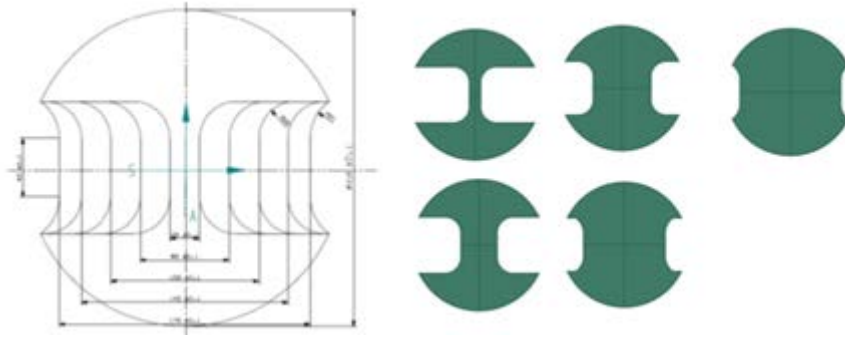


Figure 101. Geometry of experimental FLD specimens and modelled specimens

The model was meshed using an edge seed mesh control to get the right size of each element, 0.5mm for the specimens of 20 and 60 mm and 1mm for the 100,140 and 170 mm specimens, and with the S4R element type provided in ABAQUS. This element is a four-node doubly curved thin or thick shell, reduced integration, hourglass control and finite membrane strains (see Figure 102). An example of strain contour plot is shown in Figure 103.

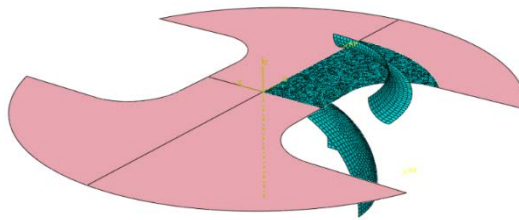


Figure 102. Mesh of the 60 mm specimen.

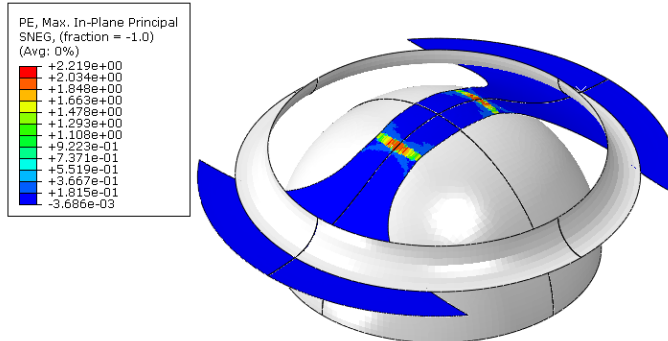


Figure 103. Maximum principal plastic strain in the specimen of 20mm with mirror extended in its symmetry.

Figure 104 to Figure 106 show the results of the FLD simulations and the failure energy estimated for each specimen (different deformation paths). The points of the diagram were extracted from the different elements of the specimens in the simulation step where the strains combination reach the same level that the experimental curve. The highest points define the beginning of necking, according to the experimental curve; therefore, fitting the simulation up to the FLC results allows extracting the failure energy on the most deformed elements. The failure energy (kJ/m^2) is the product of the maximum principal plastic strain, maximum principal stress, and element length. Results from failure energy strongly depends on specimen geometry, and then from deformation path. This behaviour is not expected for an energy value as fracture toughness, that should depend more on loading/deformation mode (fracture Mode I, II or mixed) than on deformation paths. Specimens of 60 and 100 are subjected to Mode I and the values considerably differ among them. Additionally, there is no correlation with fracture toughness at initiation (w_e') or total fracture toughness (w_e) measured by EWF methodology. So, the estimated values from FLD simulation do not represent the fracture energies involved in sheet ductile fracture. Moreover, the experimental uncertainties in the definition of necking and crack initiation in FLD make the comparison even more difficult. It is concluded that finer mesh (more accuracy in simulation) and better failure detection at FLD is needed

to allow proper comparison between estimated fracture energy in FLD and values from fracture toughness.

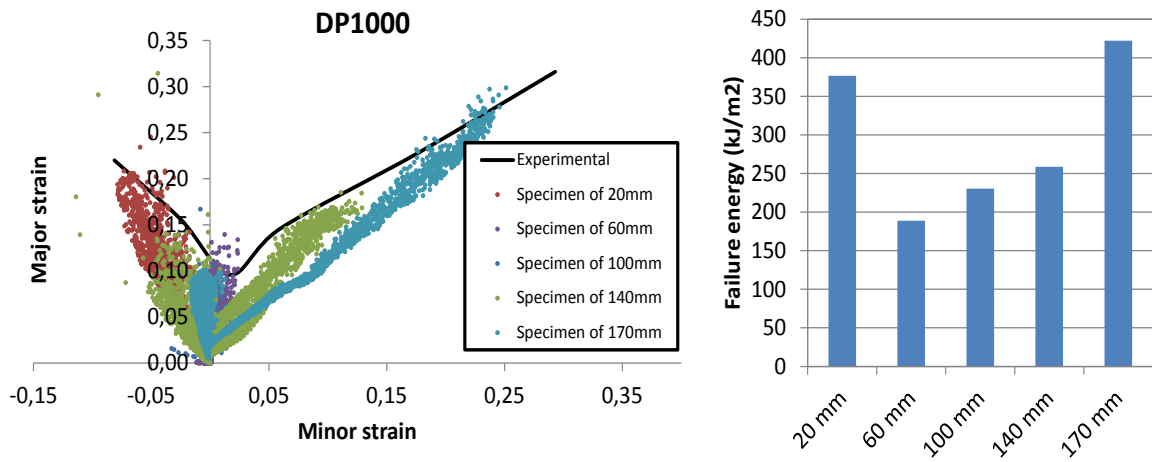


Figure 104. FLC from experimental and simulation results and estimated fracture energy for DP1000

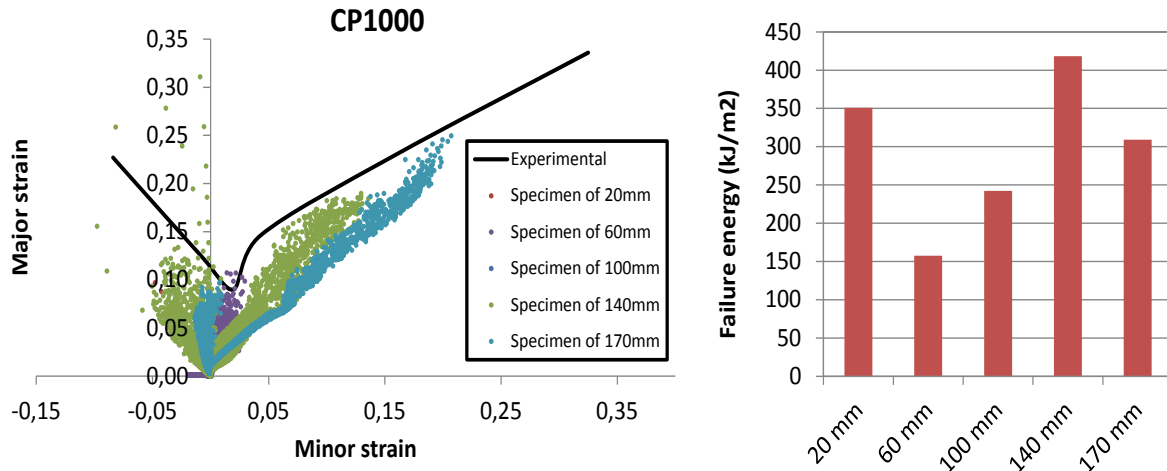


Figure 105. FLC from experimental and simulation results and estimated fracture energy for CP1000.

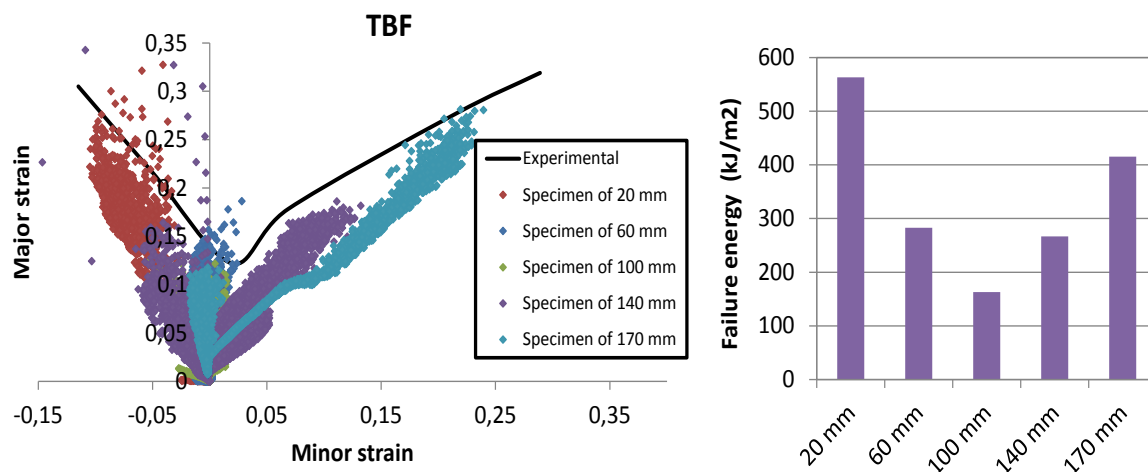


Figure 106. FLC from experimental and simulation results and estimated fracture energy for TBF.

Simulation of edge cracking

Since edge cracking involves the propagation of cracks generated at the edge, the simulation criteria should contain the resistance to crack propagation. The followed strategy was to incorporate the damage model developed at Task 3.4 in the forming simulations. The failure process modelling showed in Figure 77 was parametrized as an exponential law (Figure 107, Equation 15):

$$D = S \cdot e^{t \cdot u_{pl}} \quad \text{Equation 15}$$

Where D is the damage (values from 0: no damage to 1: complete fracture), u_{pl} the plastic displacement and S and t constants for the exponential adjustment.

The damage law was experimentally fitted to obtain the parameters of Equation 16. This approach is based on the assumption that the area under the damage-displacement curve is proportional to the essential work of fracture (Figure 107, Equation 16).

$$\text{Area} \cdot k = \int u_{pl} dD = w_e \quad \text{Equation 16}$$

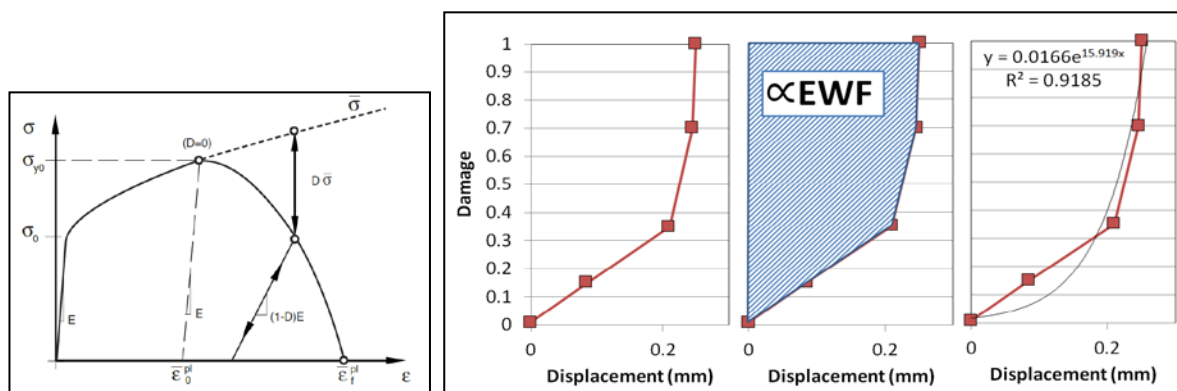


Figure 107. Stress-strain curve with progressive damage degradation and hypothesis about the relationship between the EWF and the evolution of the damage.

From these assumptions, the values for the damage evolution laws of the different materials can be obtained. The damage evolution obtained with these parameters is represented in Figure 108.

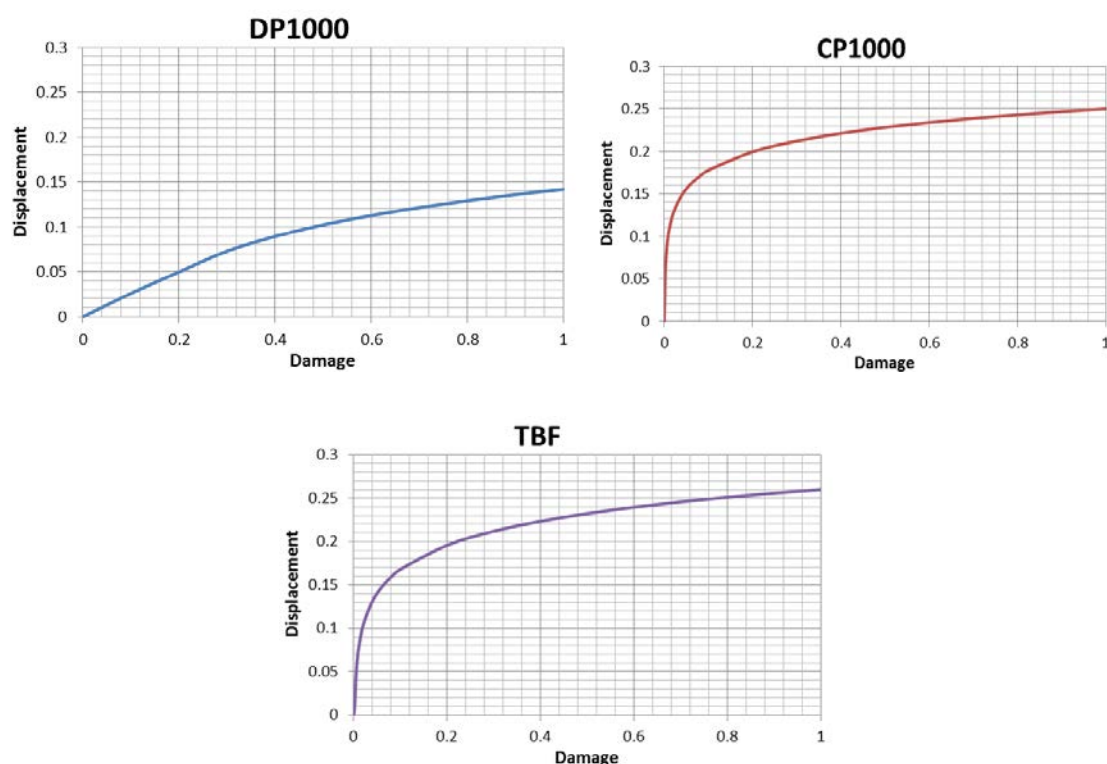


Figure 108. Displacement-damage of TBF.

In order to validate the damage evolution law, the DENT specimens were simulated implementing the model (Figure 109 to Figure 111). When the simulations reach the fracture strain, then the damage is controlled by the proposed damaging law until all the elements in the mesh fail.

Three different ligament lengths were simulated for the three materials. As observed a good correlation was obtained between experimental data and simulations for DP1000 and CP1000. However, a poor correlation was obtained for TBF. Further investigations must be carried out to find the parameters that best define the evolution of damage in TBF steel. This is an example of the complexity that involve the material modeling for these advanced steels. Not only the failure model must be adjusted, but also the elastoplastic stress strain model must be calibrated, taking special care in the extrapolation of the stress strain curves.

The proposed damage evolution laws for the different materials were implemented in WP7 aimed at improving the accuracy of forming simulations.

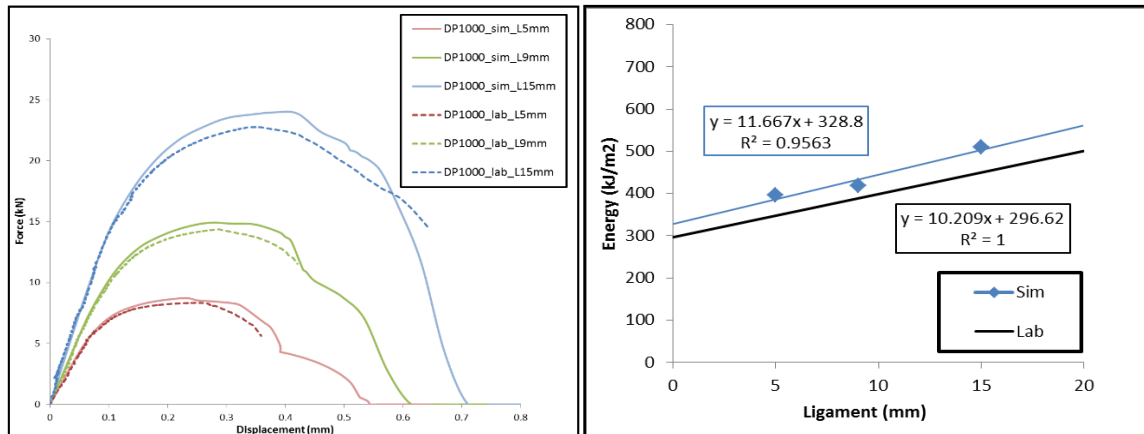


Figure 109. Force-displacement and EWF of DP1000.

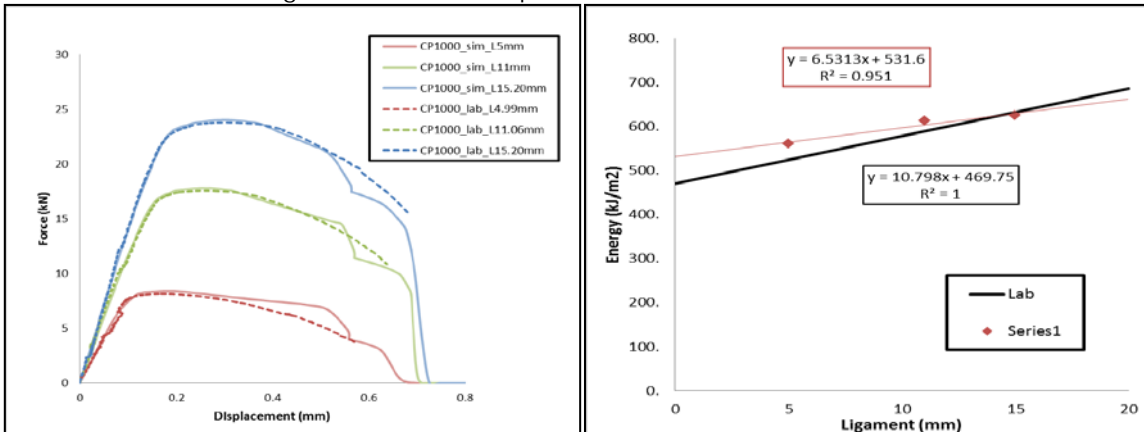


Figure 110. Force-displacement and EWF of CP1000.

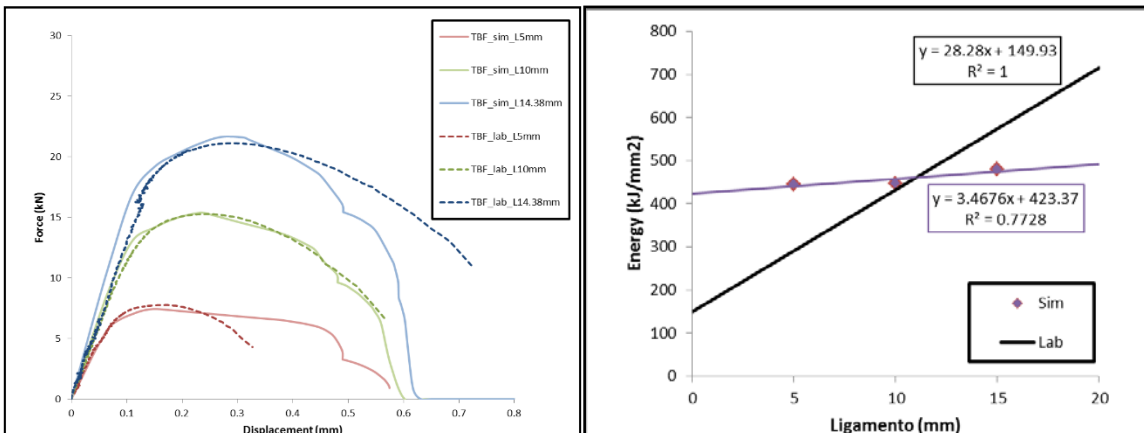


Figure 111. Force-displacement and EWF of TBF.

Task 4.5 Correlation of fracture toughness evaluated by means of EWF with sheet forming tests

Punching produces cracked regions around the flanged area. Such cracks propagate during hole expansion. Thus, HET values are controlled by the material resistance to crack nucleation and propagation, which is the fracture toughness. Some authors also stated that stretch-flangeability is controlled by crack propagation and showed that tougher materials give rise to higher HER values [FON11, TAK12, GUT13]. Aimed at proving the correlation between fracture toughness and stretch flangeability the EWF values obtained in task 2.1 (w_e) are plotted against the HER values from task 1.4. in Figure 112. A good correlation was found between fracture toughness and stretch flangeability; the higher fracture toughness the higher HER. These results allow to postulate that fracture toughness, in terms of w_e , becomes a relevant material property for edge cracking resistance in AHSS and can be used to properly rationalize stretch-flangeability in AHSS sheets.

This good correlation EWF-HER is not apparently followed by TWIP steel, which show lower HER than the expected, according to its high EWF. This may be explained by the considerable deformation suffered in the hole edge during the punching operation, which induces a local change of microstructure around the punched area due to strain induced twinning or phase transformation ($\gamma \rightarrow \alpha'$ or ϵ martensite). Thus, local toughness in this sheared area for TWIP steels would be much lower than that measured for non-transformed TWIP specimens (conventional EWF tests). Aimed at understanding this effect, the punched specimens were cross cut and inspected to determine hardness and edge damage for TWIP and other AHSS grades. As can be seen in Figure 113, hardness is really high in TWIP steel, showing that twinning transformation has been triggered around the hole. For the other AHSS the increase in hardness is as expected. Then, the effect of pre-strain on the EWF values of TWIP steels should be much higher than in other AHSS grades (Figure 83) and the values of toughness should be much lower (move to the left as showed by blue arrow in Figure 114). Pre-strained specimens were prepared and tested. The resulting fracture toughness for pre-strained TWIP decreases to 187 ± 49 KJ/m² (compared to the original of 366 ± 24 KJ/m² measured with pre-cracked DENT specimens). Now, considering this local fracture toughness value for punched TWIP, the steel follows the same trend EWF-HER as other AHSS grades.

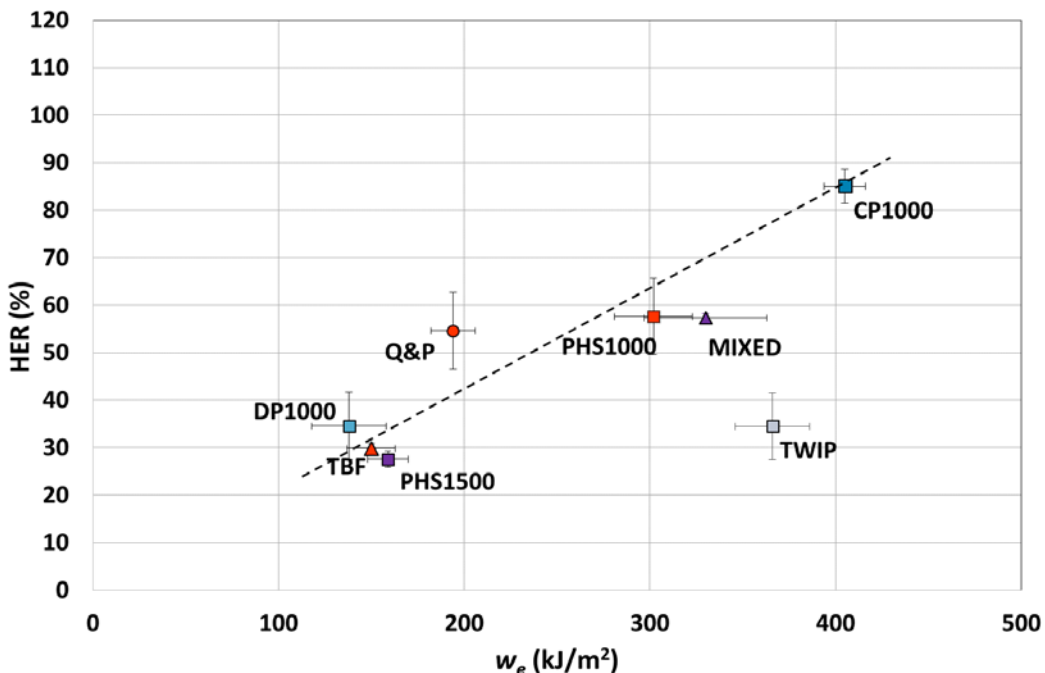


Figure 112. Correlation between w_e and HER.

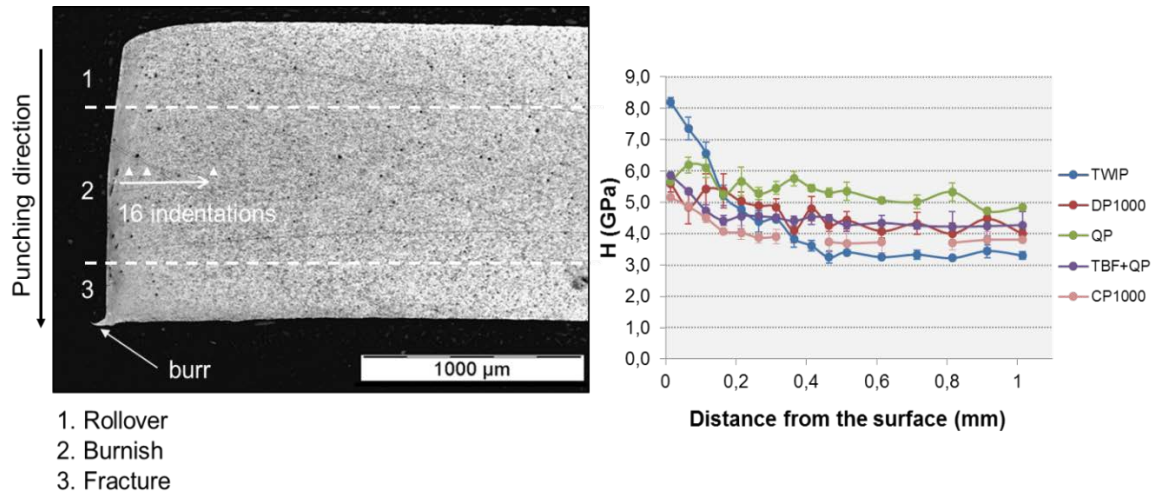


Figure 113. Hardness profiles measured at punched specimens. Note the high increase in hardness for TWIP steel in the sheared area, compared to the moderate increase of the other AHSS grades.

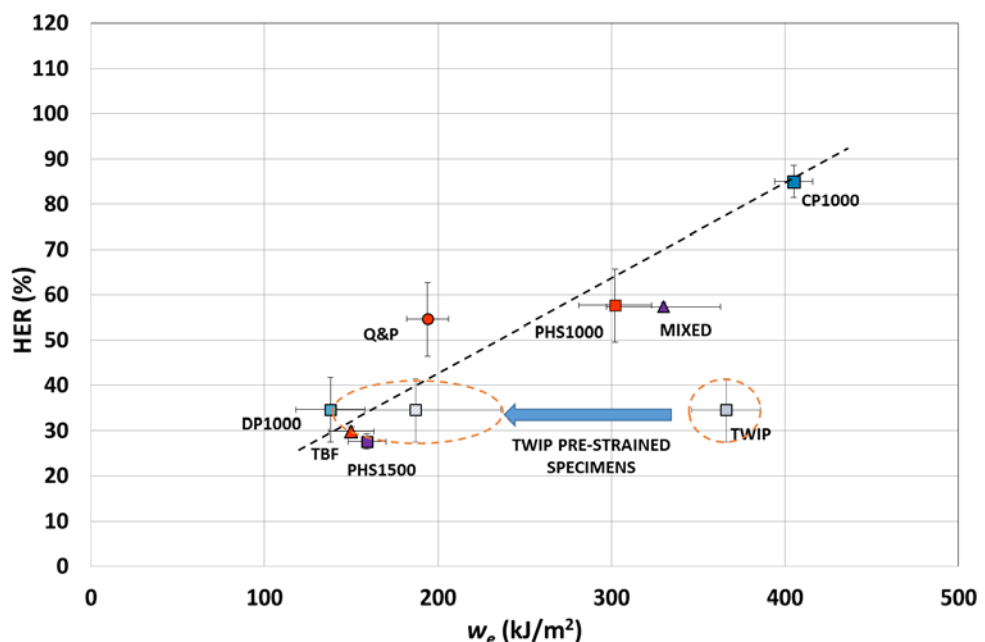


Figure 114. Correlation between w_e and HER with the corrected behaviour of TWIP, considering the 'local' fracture toughness due to the twinning transformation around the punched hole (this effect is much lower for other AHSS grades and has minor effect on EWF-HER relationship).

2.2.5. WP5. Effect of microstructure on fracture toughness

The aim of WP5 was to assess the effect of different microstructural parameters on fracture toughness. The gathered knowledge about the relation microstructure-toughness will be very useful for the development of new AHSS grades with improved formability and crash resistance. Effects of thickness and plastic anisotropy on fracture toughness were also evaluated. The contribution of TRIP-effect to fracture toughness on steel grades with retained austenite was investigated by means of Electron Backscattering diffraction (EBSD) measurements.

Table 21. Tasks of WP5.

Task	Name of the task
Task 5.1	Effect of sheet thickness in EWF
Task 5.2	Effect of plastic anisotropy in EWF
Task 5.3	Evaluation of microstructural features

Task 5.1 Effect of sheet thickness on EWF

The fracture toughness of a material susceptible to deform plastically before fracture, depends on the volume in front of the crack tip. Hence, the material resistance to crack propagation varies with the thickness of the sample (Figure 115). When the sheet is thin ($t = t_0$) the plastic zone developed in the front of the crack tip is large and the toughness show high values (plane stress conditions). On the other hand, when the sheet is thick (t_c) plane strain conditions prevail and fracture toughness values are minimum. From this thickness value, it was found that fracture toughness is independent of thickness.

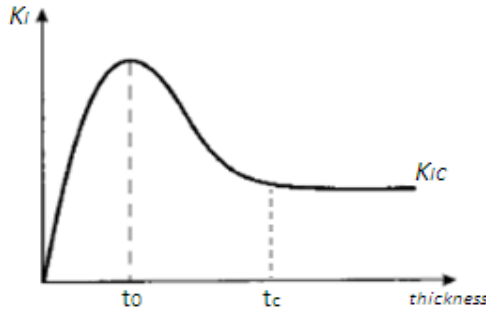


Figure 115. Effect of specimen thickness on toughness

The main use of AHSS is in form of thin sheets (1-3 mm). Due to their limited thickness, AHSS sheets present plane stress conditions and, thus, the fracture toughness is thickness dependent. In order to evaluate such dependence, fracture toughness was evaluated by means of the EWF methodology in CP1000 grade with 4 different thicknesses (1mm, 1.4 mm, 2 mm and 2.2 mm). The evaluation of the EWF was carried out with specimens with no propagated notches (notch radius, $\rho=150 \mu\text{m}$). Figure 116 shows the EWF results obtained for the different thicknesses. It was observed that for CP1000 grade, in the studied range of thicknesses, the EWF increases with the sheet thickness. Such behaviour corresponds to thickness values below t_0 in Figure 115 (pure plane stress). From this critical value (t_0), the transition from plane stress to plane strain takes place and the fracture toughness decreases when increasing thickness.

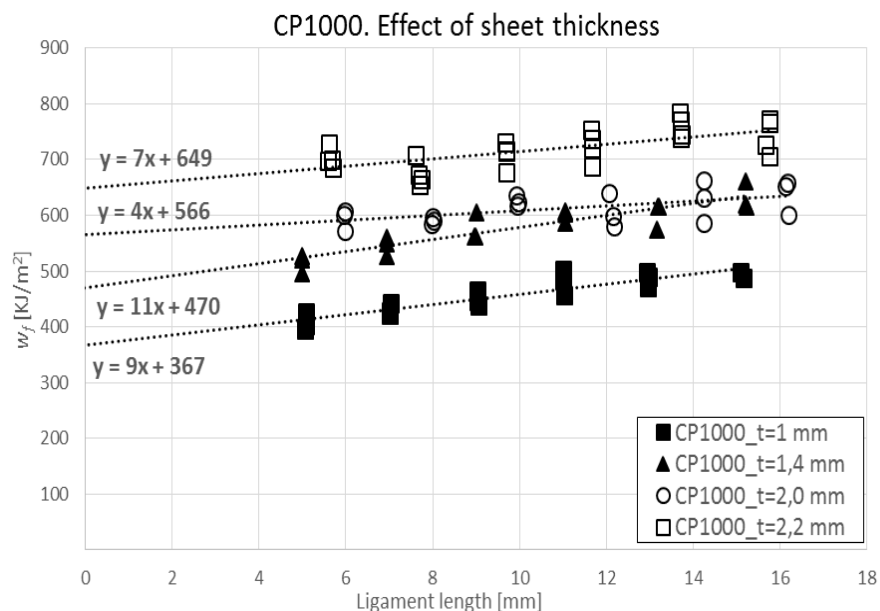


Figure 116. CP1000. EWF values obtained from sheets with different thicknesses.

The variation of EWF with sheet thickness is shown in Figure 117. A linear relation between EWF and thickness was observed, expressed by Equation 17.

$$w_e = 219t + 152 (\pm 21) \text{ kJ/m}^2 \quad \text{Equation 17}$$

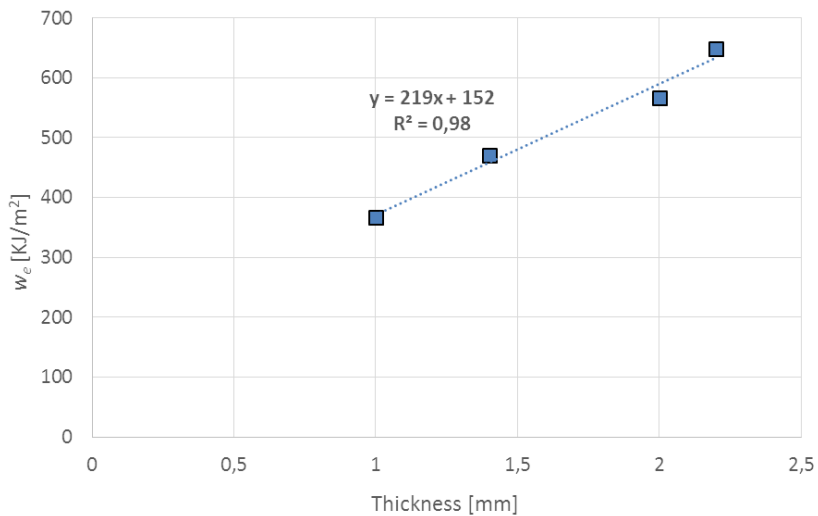


Figure 117. Variation of EWF with sheet thickness for CP1000 steel grade. EWF values obtained from No Propagated specimens.

Task 5.2 Effect of plastic anisotropy in EWF

During the rolling process the grains are aligned in a preferential orientation. Thus, metal sheets can have different properties depending on the testing direction respect to rolling. The effect of plastic anisotropy was evaluated in two AHSS grades: a bending grade (CP1000) and a deep-drawing grade (DP1000). The CP1000 grade has a very homogeneous microstructure and showed isotropic mechanical properties in conventional tensile tests, whereas DP1000 showed a more anisotropic behaviour and has a more inhomogeneous microstructure.

EWF measurements were carried out with specimens machined in three different orientations respect to the rolling direction: 0°, 45° and 90°.

Figure 118 and Figure 119 show the EWF values obtained with CP1000 and DP1000, respectively, at the three different orientations. The behaviour of the materials regarding anisotropy was the expected and in concordance with tensile characterizations (Figure 120). CP1000 showed an isotropic behaviour, obtaining very similar toughness values at the three rolling directions. On the other hand, DP1000 has shown similar values at 0° and 90°, but a lower EWF has been observed at 45°. A large scatter was observed in intermediate ligament lengths at 0°.

The behaviour of DP1000 is more sensitive to the rolling direction. This behaviour could be explained by the inhomogeneity of the microstructure and the retained austenite content, whose morphology and stability are probably directional.

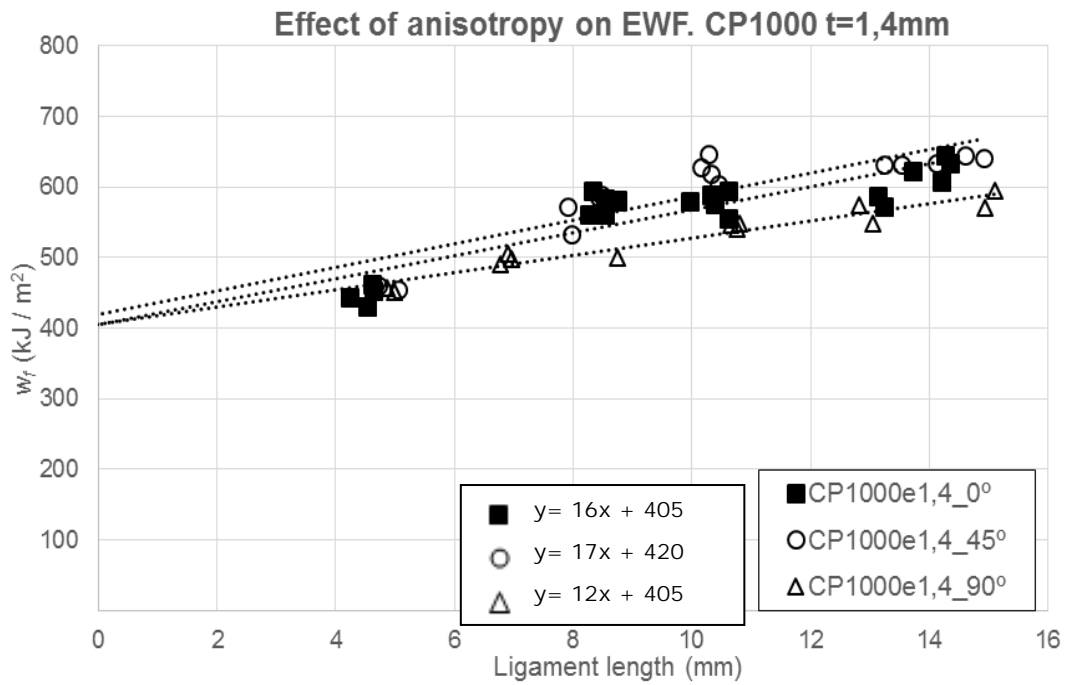


Figure 118. CP1000. EWF values at different orientations respect to the rolling direction

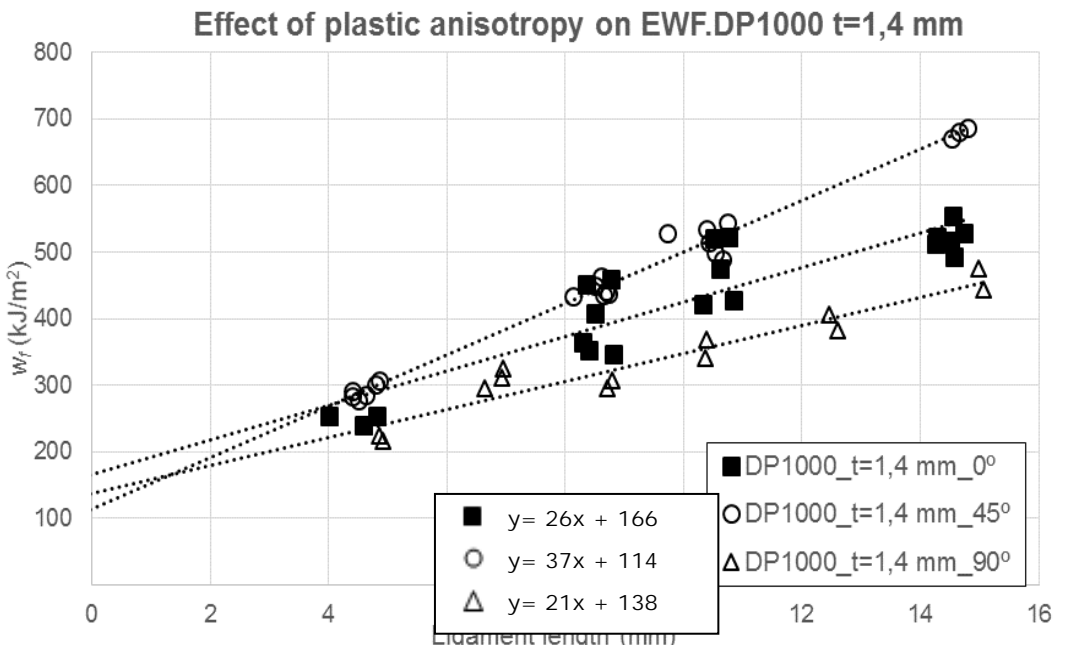


Figure 119. DP1000. EWF values at different orientations respect to the rolling direction

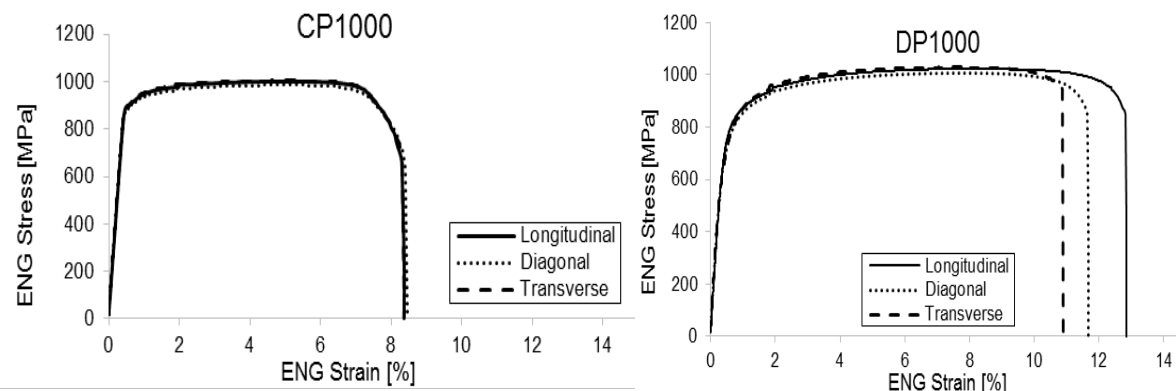


Figure 120. Tensile tests for CP1000 and DP1000 at different rolling directions

Task 5.3 Evaluation of microstructural features

The evaluation of the influence of different microstructural parameters on fracture toughness was addressed in this task. A general relation between microstructure and fracture toughness was observed: DP-like steel grades (mixture of soft-hard microstructural components), such as DP1000 and TBF, exhibited poorer toughness values than CP-like grades (homogeneous bainite/martensite matrix), in contrast to their higher elongation at fracture. Hisker et al. [HIS12] identified the different damage mechanisms in CP and DP steels and differentiated between local and global damage. It was observed that DP-steels are more sensitive to local damage than CP steels. It was found that local damage mechanisms are highly influenced by hardness differences between phases. High hardness differences between microstructural constituents give rise to higher internal stressess during deformation, which contribute to the rapid generation of micro voids or decohesion of the soft/hard phase interfaces. Fracture toughness, just as hole expansion, is very sensitive to local damage. Cracks act as stress concentrators and the deformation is localized in a small zone near to the crack tip. Thus, microvoid coalescence rapidly contribute to the macroscopic failure of the sample. On the other hand, as observed in DP1000 and TBF, tensile tests are less sensitive to such local damage. The large work hardening capacity of these steels around the nucleated voids, impede that void growth lead directly to macroscopic fracture. The more homogeneous matrix of CP steel grades and the lower differences in hardness between the different phases makes them more tolerant to local damage, as indicate their higher toughness values.

The low toughness values of PHS1500 are related to its fully hard martensitic microstructure. However, it is observed that the tempering treatment performed in PHS1000 increases significantly the fracture toughness.

The fracture behaviour of bending impact and DENT specimens was also investigated in this task. The influence of other microstructural constituents, such as retained austenite and the martensitic transformation (TRIP-effect) during crack propagation was investigated in TRIP-assisted steels (TBF, Q&P and TBF/Q&P).

Fracture behaviour for bending impact test samples

LOM investigations were performed for DP1000, TBF and Q&P grade at side impact test samples with crash index of approximately 90%. Therefore, two normal sections (1 and 2 in Figure 121) and the crack surface appearance were investigated at the bending deformation zone (3 in Figure 121) in the middle of the sample.

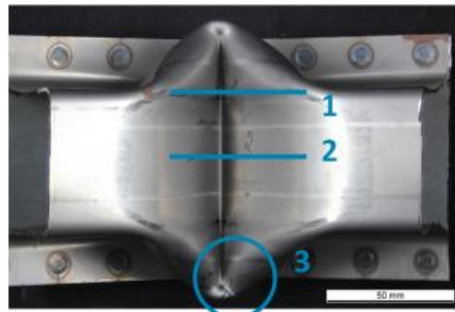


Figure 121. Sections on samples used for LOM. Section 1 is in the upper third and section 2 in the center line of the sample. Circle 3 shows the area for investigations on crack surface appearance.

Light optical microscopy showed that for the high crash index used for investigations, no cracks were found in section 1 for all three materials. In section 2, cracks were only visible for TBF and Q&P. Section 3 is a tridimensional complex-bending zone at the side impact test. At this zone, through-thickness cracks for all three steel grades were detected. Ductile growth of shear cracks inclined 45° to the surface was observed, starting from the most strained, inner surface for Q&P and TBF at section 2 (Figure 122).

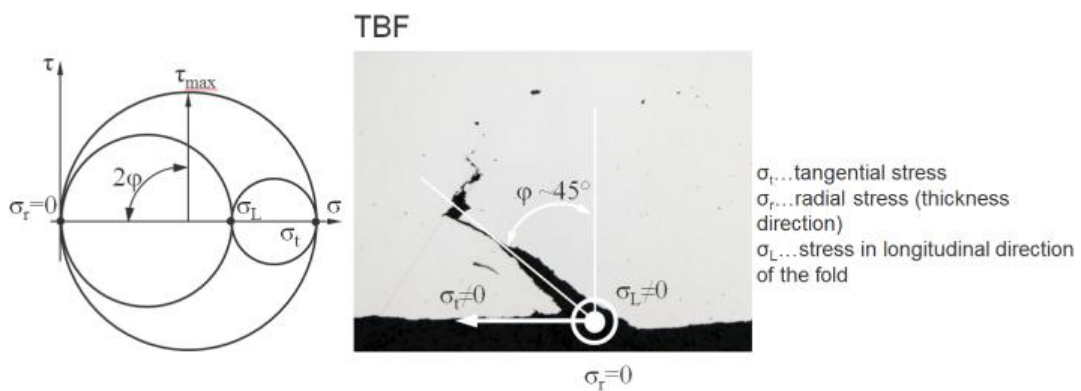


Figure 122. Stress situation on the surface and crack propagation for side impact test samples.

SEM investigations were performed at section 3 of side impact test samples. Therefore, crack-zones were carved-out from the complex-bending site and final ruptured in liquid nitrogen. The fracture zone generated during side impact test showed a homogeneous, ductile fracture surfaces with distended voids and dimples (Figure 123). This appearance confirms a shear-triggered fracture mode also in this complex bending situation. Void initiation at inclusions was often detected, typical for ductile shear fracture. With increasing macroscopic deformation, void growth and coalescence take place resulting in the depicted honeycomb fracture surface. In summary, the investigations showed that damaging during side impact testing corresponds to a fully ductile mode.

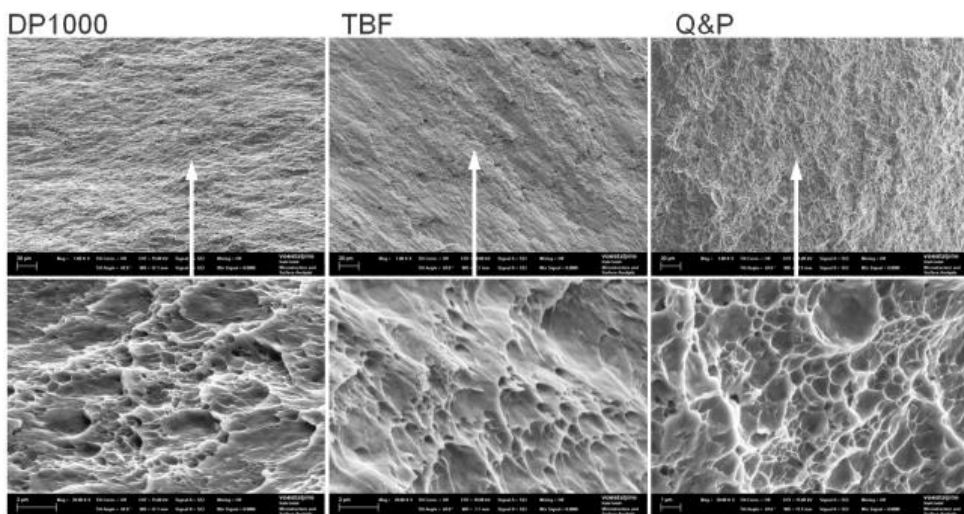


Figure 123. Fracture surfaces generated during the side impact test.

Fracture behaviour for EWF samples

Investigations regarding crack initiation and crack propagation at full cracked EWF samples were performed for TBF and Q&P grade by using SEM. Generally, EWF tests were performed on double edge notched tension (DENT) samples. These samples have spark-eroded notches and fatigue cracks symmetrical to the tensile axis. During EWF-testing, a complex stress state was generated in front of the fatigue cracks, resulting in the observed areas shown in Figure 124.

TBF

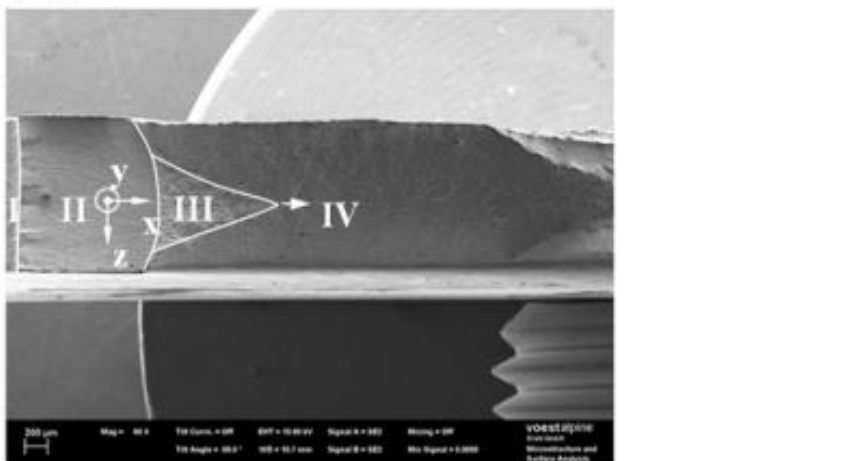


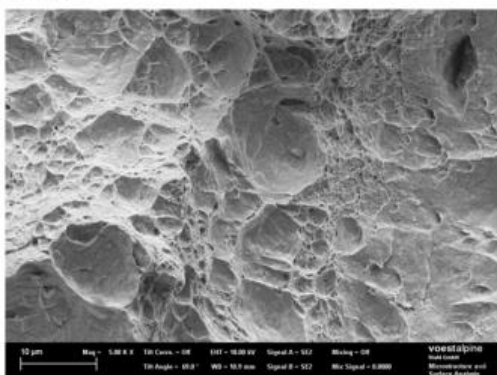
Figure 124. The observed four areas at the fracture zone at EWF samples.

Due to sample preparation and the appearing stress state during EWF-testing, the fracture zones of EWF samples can be divided in four areas (Figure 124):

- I spark-eroded notch
- II fatigue crack
- III principal normal stress induced fracture
- IV shear induced fracture

The fatigue crack areas in zone II showed very small, hardly detectable fatigue striations. These striations commonly depict the crack propagation per load cycle. Zone III is the principal normal stress induced fracture area. In this fracture zone, a stress state with high triaxiality is generated in the center (with respect to sheet thickness) in front of the fatigue crack during EWF-testing. This caused the formation and growth of larger voids and the generation of ductile fracture surface perpendicular to the tensile axis during forced rupture in this zone (see Figure 125).

Q&P



TBF

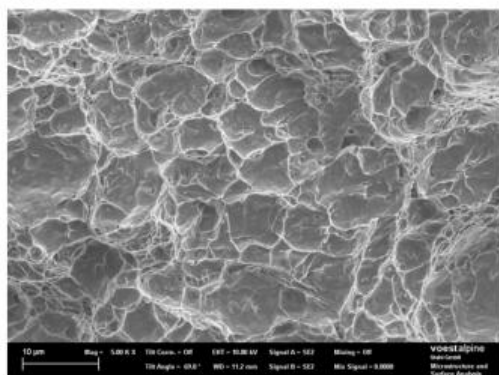
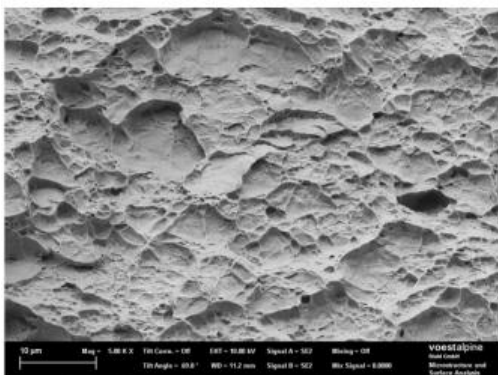


Figure 125. Ductile fracture behaviour in zone III.

For zone IV, shear-induced ductile fracture was observed, which can be explained by the lower triaxiality towards the surface of the steel sample. With increasing distance to the initial fatigue crack, this shear induced fracture forwarded to the centre axis of the DENT sample. Thus, the perpendicular fracture zone was surrounded by a zone of shear induced fracture (zone IV). Zone IV showed a ductile fracture appearance (Figure 126). In contrast to area III, the fracture surface in zone IV consisted of rather homogeneous size distribution. The large voids which were visible in Figure 125 (zone III) are not present in Figure 126 (zone IV) to the same extent. This difference was more pronounced for TBF than for Q&P steel grade.

Q&P



TBF

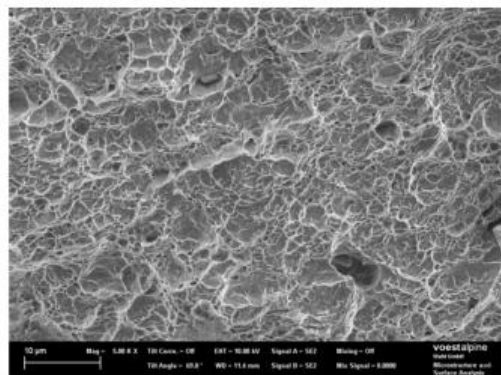


Figure 126. Ductile fracture behaviour in zone IV.

When comparing the ductile fracture areas between the steel grades, Q&P grade revealed coarser voids and dimples than TBF grade. However, both grades have different content of bainite, martensite, tempered martensite, ferrite and retained austenite in the microstructure. For TBF, zone IV had a complete ductile fracture surface appearance. For Q&P, minor areas with partial transcrystalline cleavage fracture were observed. This fracture mode is thought to be triggered by a change in local stress state towards higher tensile and lower shear stresses, caused by microstructural effects. Its area fraction was found to lie below 5 percent in total, but it was observed on both sides of the EWF sample.

EBSM measurements on EWF samples

In order to characterize the amount of body-centered cubic (ferrite, bainite, martensite) and face-centered cubic constituents (retained austenite) at different displacement states, EBSD measurements were carried out. The state at crack initiation was denominated state 3, the state after significant crack propagation was called state 4. For EBSD measurements, samples were mechanically polished first, and afterwards polished with an oxide-containing suspension (one part oxide, two parts distilled water). Electrochemical etching was not performed. Standard step size for EBSD-mapping was 120 nm. Dependent on the steel grade, EBSD measurements were performed in front of the crack tip, in the plastic zone between the both notches/cracks of the EWF samples and in the undeformed area of the respective EWF sample (state 3 / state 4). The results are listed in Table 22.

Table 22. Content of bcc, fcc and zero-solutions for the grades and states investigated.

AHSS grade	state	bcc, %	fcc, %	zero solutions, %
TBF	3, undeformed zone	85.6	1.6	12.8
	3, plastic zone	86.0	1.6	12.4
	4, plastic zone	74.6	0.5	24.9
	4, crack tip	69.1	0.4	30.6
Q&P	4, plastic zone	82.1	0.6	17.3
	4, crack tip	49.0	0.3	50.7

In undeformed TBF, the amount of retained austenite determined by magnetical measurements was 11%, whereas by EBSD-measurement, a value of 1.6% was found (state 3, undeformed zone). Based on these results, the amount of retained austenite detected by EBSD was not much larger than one tenth of the actual amount of retained austenite in the structure. This discrepancy might be caused by either transformation of retained austenite to martensite at the sample surface during preparation (bcc instead of fcc is measured by EBSD), or due to low band contrast of the austenitic areas (leading to zero solutions in the EBSD measurement). Thus, local investigation of retained austenite transformation by EBSD measurements could only be used to draw a qualitative comparison between the states examined.

Generally, near the crack tip lowest amounts of solutions and hence highest amounts of zero solutions were generated with EBSD due to high local deformation. In this area, the amount of retained austenite observed by EBSD is nearly zero. At a larger distance from the crack tip, higher amounts

of retained austenite could be detected. When compared to TBF grade, a considerable higher content on zero solutions was generated in the measurement field in front of the crack tip for Q&P grade.

In the plastic zone, the amount of retained austenite at crack initiation (state 3) is more than three times higher for TBF than the measured amount in the plastic zone after a certain crack growth (state 4). This indicates to some extent, that retained austenite in the plastic zone between the cracks is transformed during crack propagation.

A very small amount of retained austenite is present in the plastic zone of the samples at state 4 after certain crack growth. Figure 127 shows the EBSD-mappings for TBF and Q&P grade. However, fcc-content is higher in the plastic zone than at the crack tip at state 4. Therefore, some influence of retained austenite transformation to martensite on further crack growth within the plastic zone is expected. The amount of zero solutions is significantly lower than near the crack tip, which is assumed to be caused by the higher plastic deformation near the crack tip when compared to the plastic zone of EWF samples.

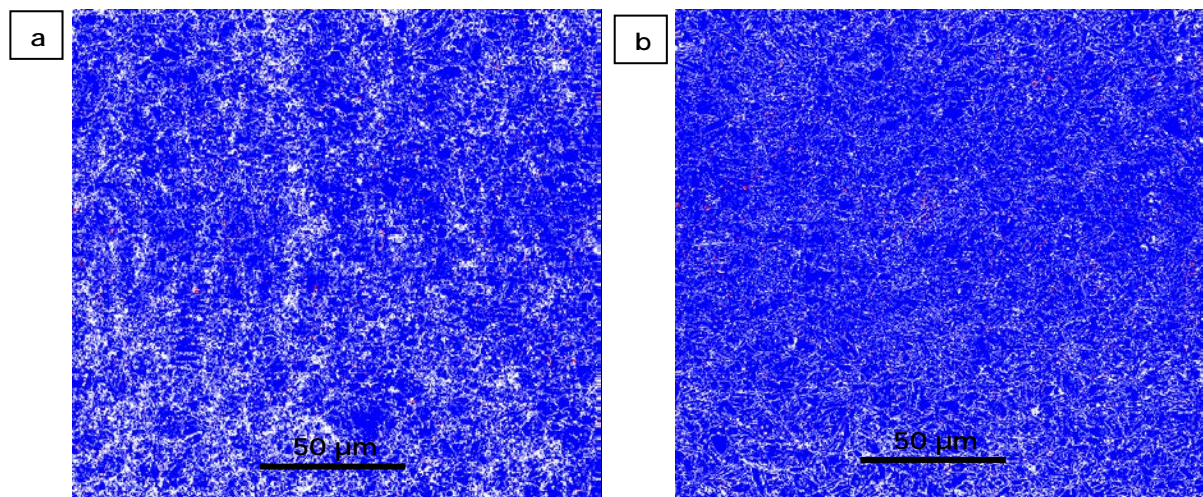


Figure 127. EBSD-mapping at state 4 in the plastic zone between the cracks. (a) TBF grade. (b) Q&P grade. Blue = bcc, red = fcc, white = zero solution.

2.2.6. WP6. Implementation of a cracking criterion for crash

The main objective of WP6 was to design a crash subsystem in order to achieve a better representation of the impact-related load case in a realistic environment. For that purpose, an existing automotive component that is currently in production was selected.

The material models using the damage laws developed in WP3 were tested in the simulations of these crash subsystem tests. Three different setups were designed for these tests.

Finally, a study of the EWF tests was performed using Abaqus/Explicit and a material model using a new damage law has been tested in the side and axial impact tests. The tasks performed in WP6 are listed in Table 23.

Table 23. Tasks of WP6

Task	Name of the task
Task 6.1	Design and fabrication of crash subsystems
Task 6.2	Material selection according to the component and crash requirements
Task 6.3	Crash tests and comparisons with simulations
Task 6.4	Improvement of crash simulations accuracy by means of EWF

Task 6.1 Design and fabrication of crash subsystems

The chosen component for the crash subsystem tests is a Fiat 500L anti-intrusion door beam (Figure 128), usually conformed by DP1200 steel. For this project, the component was produced using the selected materials assessed in the Tough-Sheet project: DP1000, TBF1000 and CP1000.



Figure 128. Component chosen for subsystem evaluation

With the purpose of testing different load cases, three different setups were proposed for the subsystem crash tests.

Setup#1: In the first setup, the impactor was a ball oriented to the centre of the anti-intrusion door beam. The beam was fixed using bolts to two rigid supports on each side. The fixation of the component is similar to the real situation in the car, but the whole system becomes stiffer, since the deformation of the whole door is not reproduced. In this case, interferences on the test due to the presence of other components were avoided. The test configuration is shown in Figure 129.

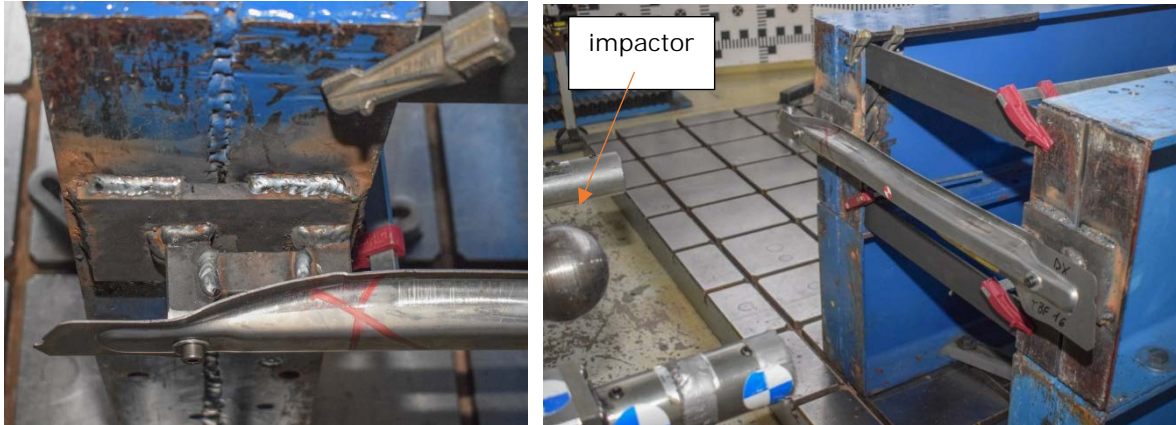


Figure 129. Subsystem test first setup

Previous simulations were solved to determine the proper mass and velocity of the impactor, in order to ensure the damage onset in the component during the test (Figure 130). Results from the simulations showed that an impact energy of 1200 J was adequate for the subsystem test. Taking into account the impactor mass (i.e. 20.145kg), a velocity of 40 km/h would result in the defined levels of impact energy. In this setup, the highest damage value observed in simulations was achieved in the fixtures zones but not in the centre of the beam. The low intrusion level allowed by the bolt connection lead to a tearing damage in this zone, causing high strains and consequently a local zone of high damage. In the experimental tests, some specimens showed an unstable deformation caused by this tearing effect. The deformation of the specimen due to this damage leads to a misalignment in the load, leading to an unstable progression of the test.

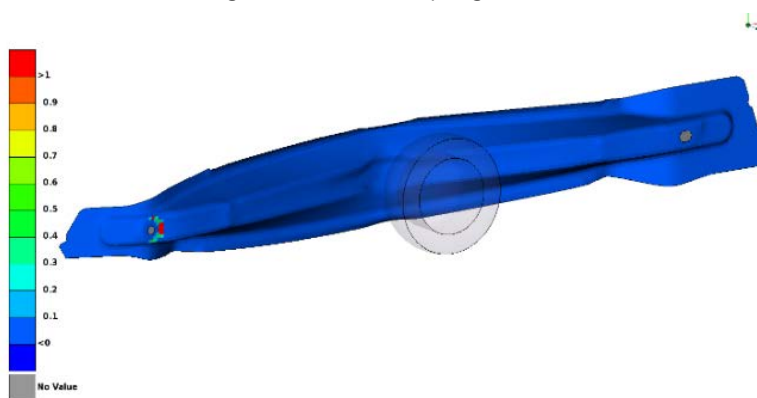


Figure 130. Damage value in first subsystem configuration, impacting with 20kg at 40 km/h

Setup#2: In order to avoid damage onset influenced by the specimen fixations, as well as the misalignment of the impactor displacement after damage is onset, further impact tests were performed using a different setup with a pendulum impactor (Figure 131).

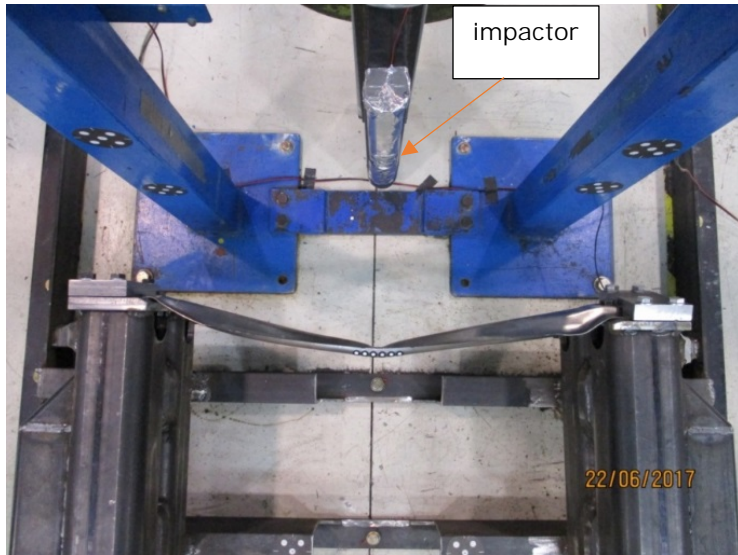


Figure 131. Second experimental setup: pendulum impact

In this second setup the fixtures of the specimen were improved, including clamps and bolts at both ends of the beam in order to diminish the stress supported in this zone. The pendulum was cylindrical and impacted completely vertical to the component. The fixtures of the pendulum do not allow a vertical deviation of the impactor after damage is onset, as occurred in the last setup. In this setup the impactor had a mass of 76.37 kg and the impact was performed at 21 km/h so the kinetic energy to be absorbed (1299 J) was slightly higher than in the first setup (1244 J). The FEM model in LS-Dyna included the supports represented as rigid parts joined by bolts. Bolts were represented by beams with an axial pretension equivalent to the tightening torque applied in the experimental tests (Figure 132). In this second setup there was no problem of vertical deviation because the impactor was cylindrical. However, the maximum damage was still reached in the area near the supports and not in the centre of the component.

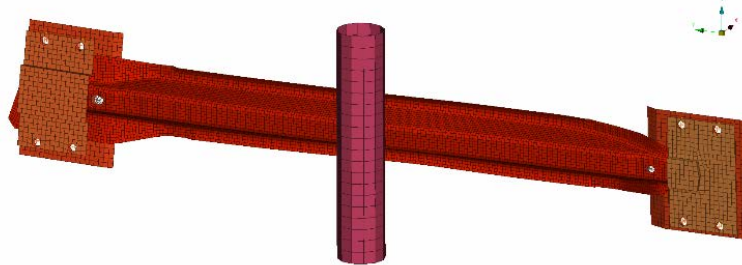


Figure 132. LS-Dyna model for the second setup

Setup#3: In order to obtain damage in the centre of the component, but not influenced by fixtures, a third setup was proposed and tested. In this last setup the central part of the beam was weakened introducing machined notches (Figure 133). This design ensure that the maximum damage was concentrated in that section. This last proposal was tested using the same pendulum equipment as in the second setup. However, the impact velocity was adjusted to provoke a small crack in the central part of the beam that did not break completely the sample. In a second impact at a higher speed in the same sample the crack propagated and completely broke the beam. The impactor mass was 76.37 kg as in setup#2. The first impact was performed at 8 or 10 km/h depending on the material (189 or 295 J respectively). The second impact was performed at 15 km/h (663 J).

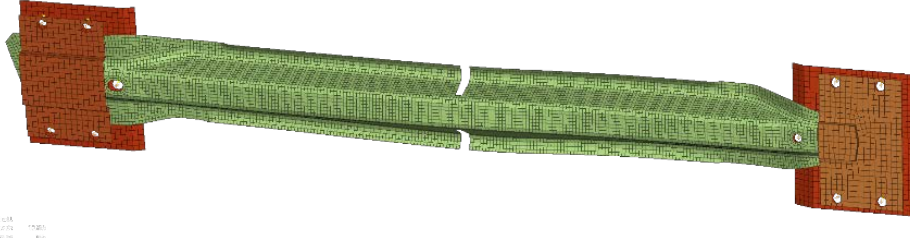


Figure 133. Proposal for the third setup

Task 6.2 Material selection according to the component and crash requirements

Taking the results of the experimental tests, three different materials were selected for the component impact tests: TBF, DP1000 and CP1000. The selection was made considering the amount of damage achieved in the impact tests as other aspects of interest, as the formability or the manufacturing feasibilities.

Task 6.3 Crash tests and comparisons with simulations

Results of the tests for each material with the different experimental setups are presented below. Figure 134 shows the results obtained with the first proposed configuration.

Setup#1

In general, the results of the simulation over the different materials showed a similar behaviour. In Figure 134, the first part of the test (until $t = 4.5\text{ms}$) shows a proper level of correlation when taking into account the damage of the material introduced as a GISSMO model using MAT_ADD_EROSION as described in WP3 (considering the failure envelope). However, the experimental acceleration values showed a softer evolution after their maximum point. Since damage in this set up occurred as tearing near the fixtures, the crack propagation in the constitutive law takes more influence over the general specimen's behaviour, and the limitations on the design of the cohesive law shown by the constitutive model applied become more relevant.

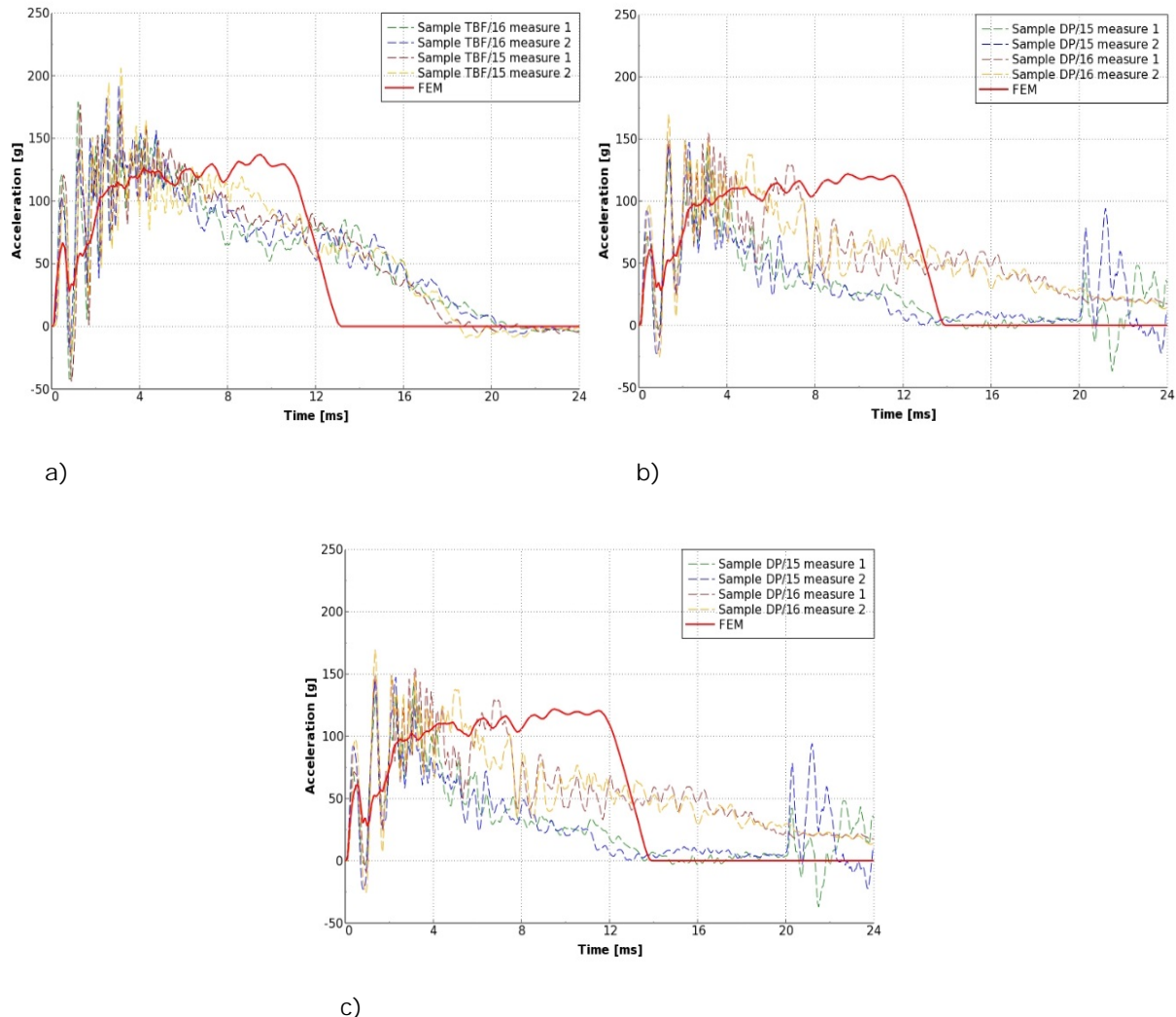


Figure 134. Subsystem first setup correlation for: (a) TBF, (b) DP1000, (c) CP1000

Setup#2

Results of the second setup with the pendulum impact are presented in Figure 135. The samples TBF/2 and TBF/12 reached higher accelerations than TBF/3 because the beam was not achieve a complete fracture in those cases (Figure 135(a)). A good correlation level was obtained until damage is onset. After that, the specimens that was not fail completely showed an overestimation of the acceleration, since a good level of correlation was obtained in the failed test. The sample DP/12 reached a higher acceleration than the other samples because the beam was not achieve a complete fracture (Figure 135(b)). For this material also, a good correlation level was obtained until damage is onset. After that, an overestimation of the acceleration in the experimental tests was observed, especially in the specimen that was not fail completely. This leads to an overestimation of the contact time. Material CP1000 (Figure 135(c)) showed a good level of correlation until $t = 15\text{ms}$. After that, the acceleration was overestimated in the numerical tests.

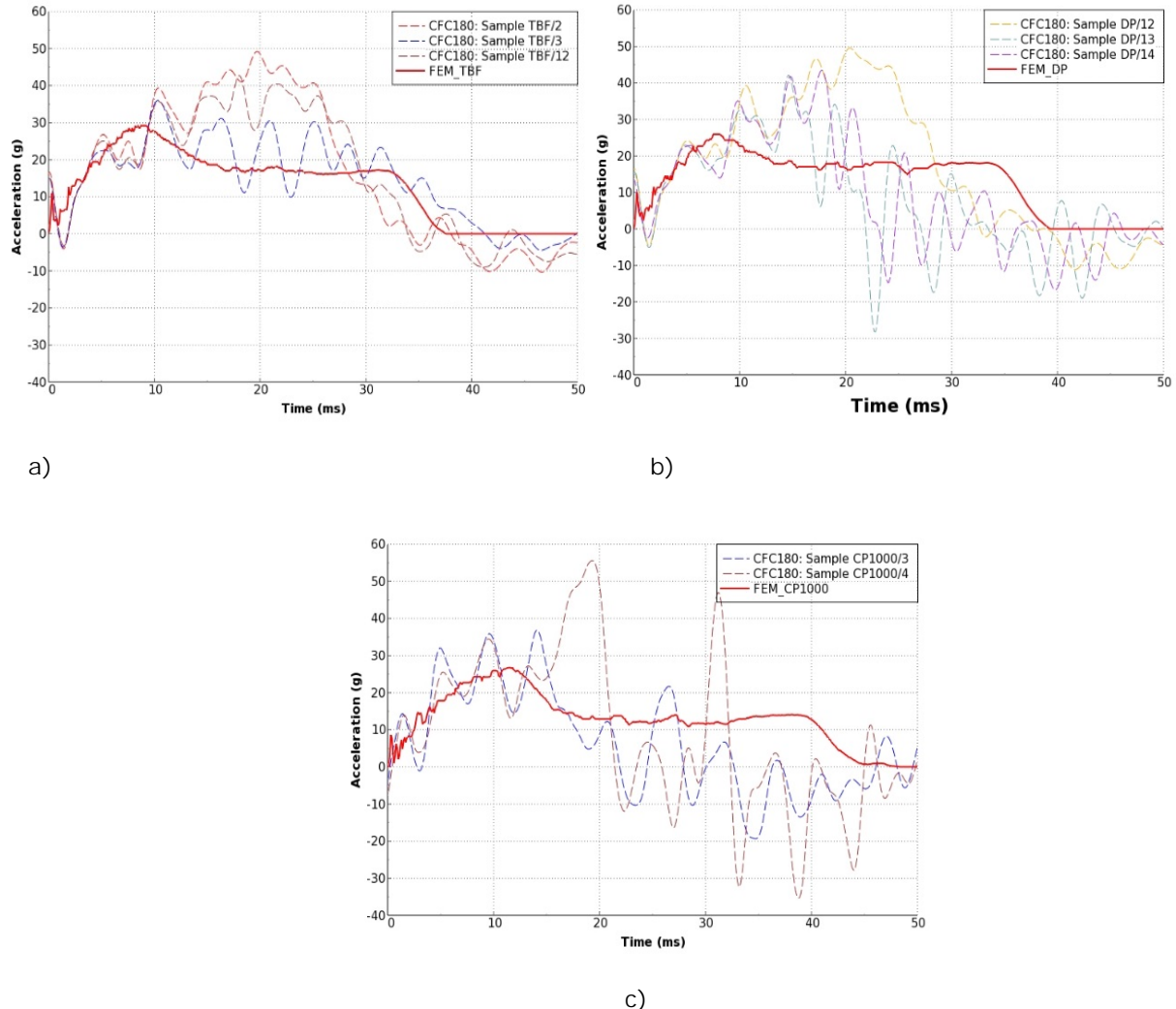


Figure 135. Subsystem second setup correlation for: (a) TBF, (b) DP1000, (c) CP1000

Setup#3

Results are presented in Figure 136(a) shows the results for TBF. The initial part of the test until damage was onset, and the contact time showed a proper level of correlation. However, the maximum value of acceleration was underestimated in the simulation. For DP1000 (Figure 136 (b)) a similar magnitude of the maximum acceleration was observed, but shorter in time for the numerical model. The initial part of the test was well correlated with the CP1000 until damage was onset Figure 136(c). After this, a sudden peak in acceleration was observed around 30ms in the experimental results, due to a certain displacement of the sample fixed in the supports. This displacement could have increased the tensile stress in the specimen, leading to a stiffer behaviour, not reproduced in the simulation.

In this setup, a worse correlation level was observed than in the second one. In addition to the numerical lacks of the material models commented earlier, this could be caused by differences in the experimental tests: The cutting process could have modified the material in this zone, showing different mechanical properties. In addition, due to the cutting process, residual stresses in the manufacturing process were observed, which were not included in simulation.

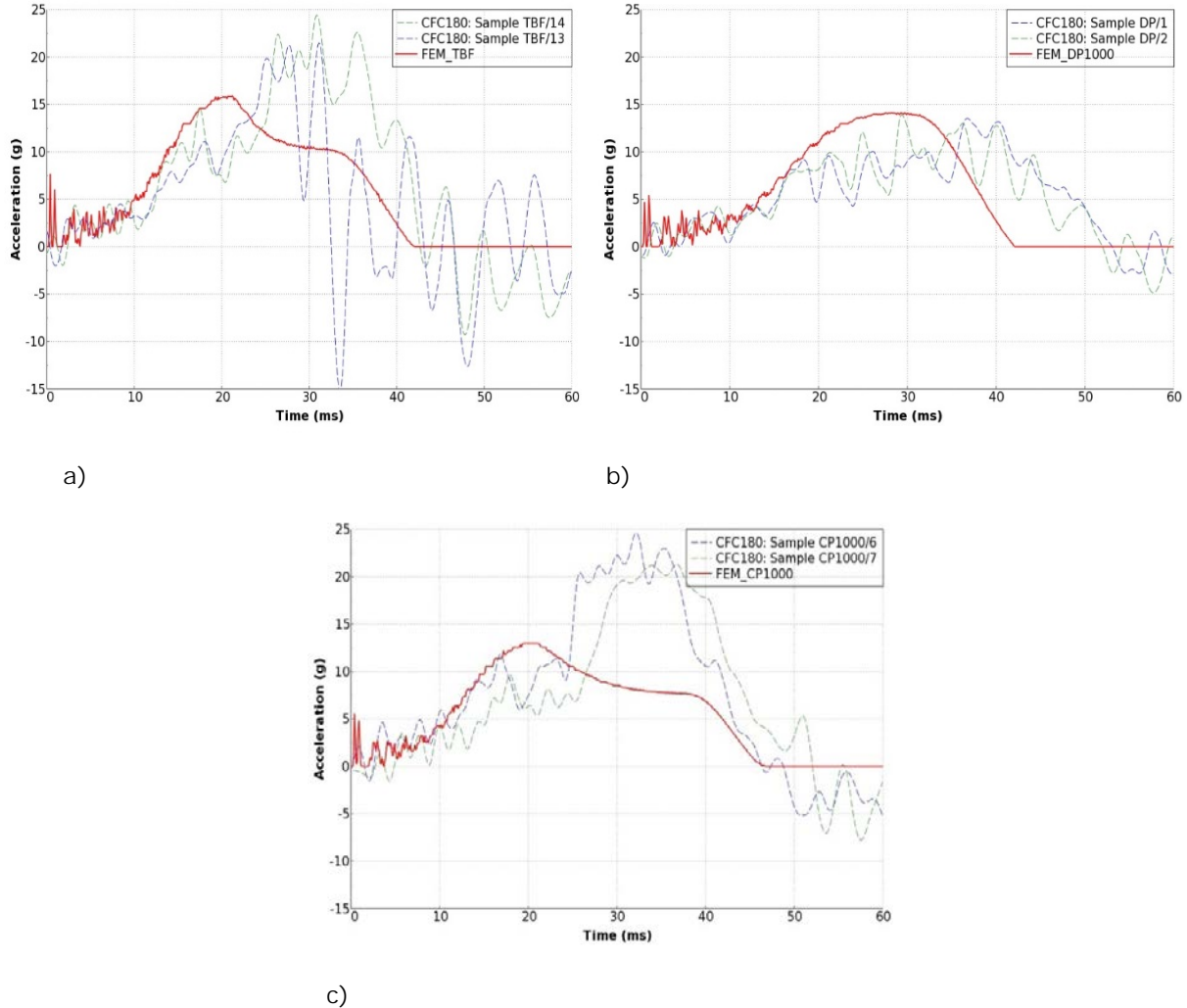


Figure 136. (a) TBF subsystem third setup correlation at 10km/h. (b) DP1000 subsystem third setup correlation at 8km/h. (c) CP1000 subsystem third setup correlation at 10km/h.

Task 6.4 Improvement of crash simulations accuracy by means of EWF

The damage evolution law 2, proposed in task 3.4 was implemented in this task, aimed at improving the accuracy of simulations. Such damage law was tested with different mesh sizes and it was compared with the damage law used in the LS-Dyna models for the impact tests described in WP3.

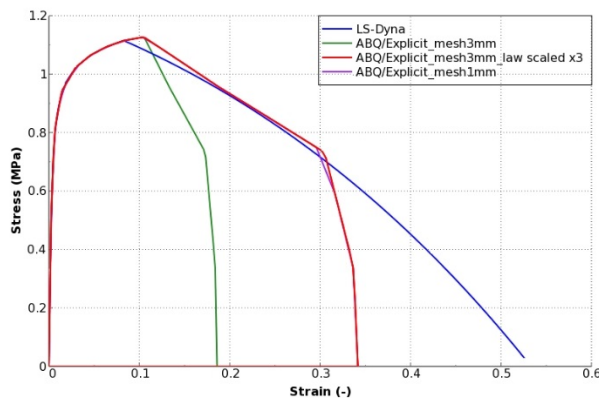


Figure 137. Tensile one-element test in Abaqus and comparison with LS-Dyna

While the model in LS-Dyna (blue curve) is mesh-independent, the Abaqus model (green curve) depends on the element size. Therefore, the damage law must be scaled depending on the mesh size, in order to obtain similar results. For a 3mm element length, the damage evolution must be scaled by 3 (red curve) in order to obtain the same response as the 1mm element (purple curve, on top of red curve). This modified Abaqus damage law was applied in axial (Figure 138) and bending

(Figure 139) impact tests as well as in impactors systems (setups#1,2,3). The results using the scaled damage law with 3mm mesh (red curve) are shown below.

Axial and bending impact specimens

The axial impact behaviour when eliminating elements was not seem accurate because the folds seen in the experimental tests do not appear in this case in the simulation (Figure 138). However, the Force-Intrusion results show a better correlation with the new damage law in Abaqus adjusted with the EWF tests and scaled to take into account the mesh influence. The new damage law in Abaqus offers a better correlation in both axial and side impact cases when it is scaled taking into account the mesh influence.

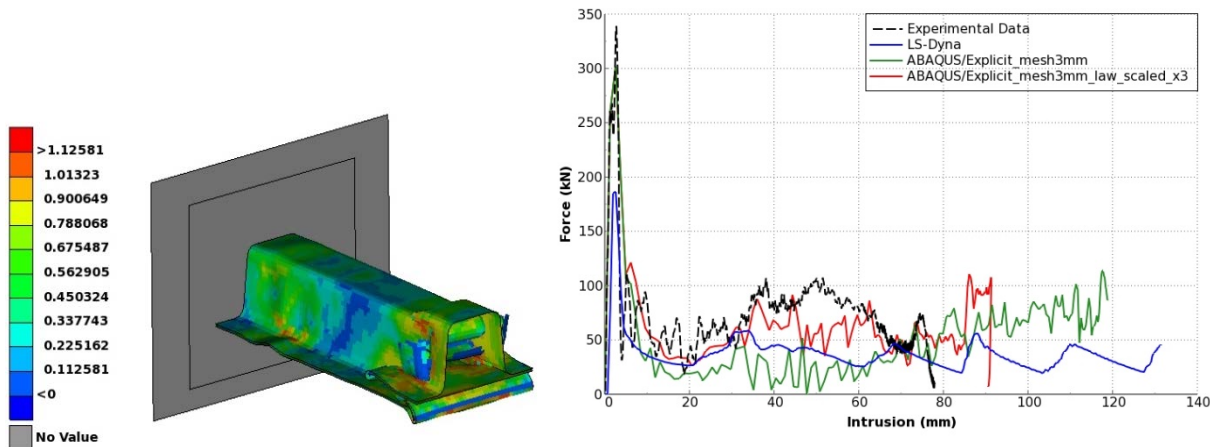


Figure 138. Von Mises Stress [GPa] for DP1000 axial impact at 23.4 km/h in Abaqus with 3mm mesh

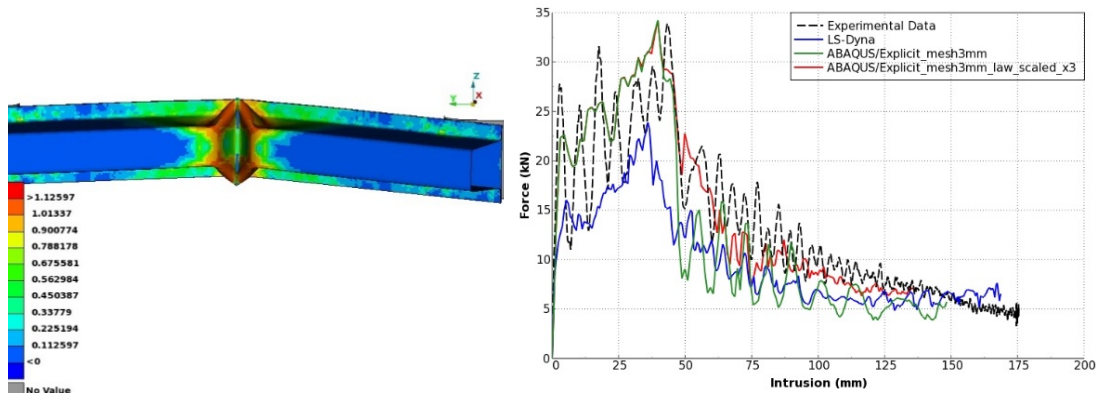


Figure 139. Von Mises Stress [GPa] for DP1000 side impact at 27.4 km/h in Abaqus with 3mm mesh

Setup#1

Figure 140 shows the results of the simulation of the subsystem impact performed in ABAQUS with the new material law proposed and the setup#1. It is observed that the application of the new law results in an overestimation of the acceleration for this configuration.

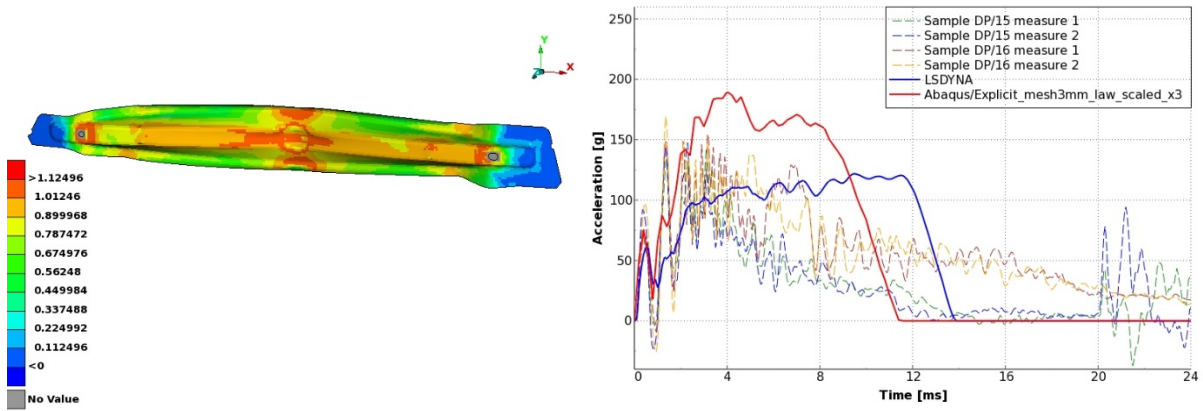


Figure 140. Von Mises Stress [GPa] for DP1000 crash subsystem impact setup#1 at 40 km/h in Abaqus with 3mm mesh

Figure 141 shows the results of the simulation of the subsystem impact performed in ABAQUS with the new material law proposed and the setup#2. In this case, the simulation in ABAQUS shows a stiffer behaviour than the simulation in LS-DYNA and in the experimental tests. After the maximum acceleration, the correlation level gets improved, both in the acceleration level as in the contact time.

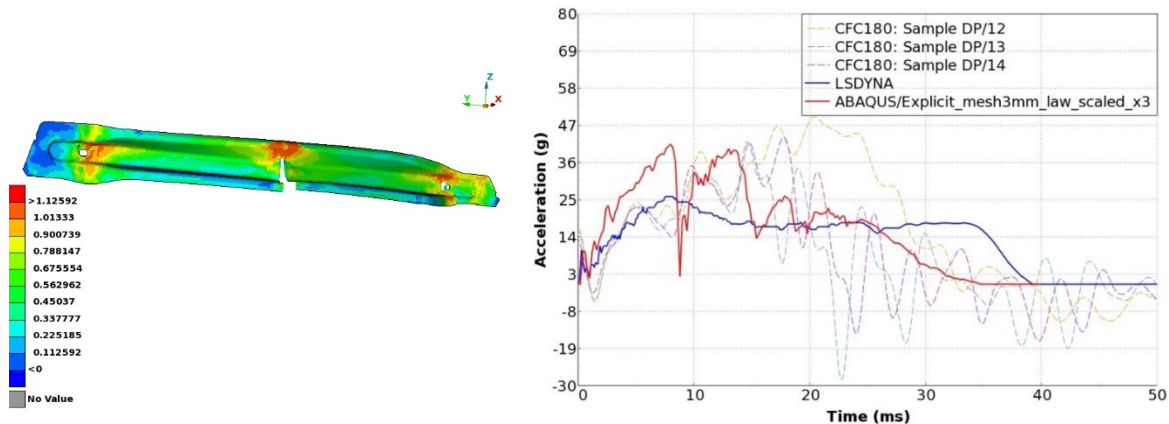


Figure 141. Von Mises Stress [GPa] for DP1000 crash subsystem. Impact setup#2 at 21 km/h in Abaqus with 3mm mesh

The results of the simulation of the subsystem impact performed in ABAQUS with the new material law proposed and the setup#3 are shown in Figure 142. For the setup, the maximum acceleration is overestimated, and thus, the contact time becomes shorter than in the experimental tests.

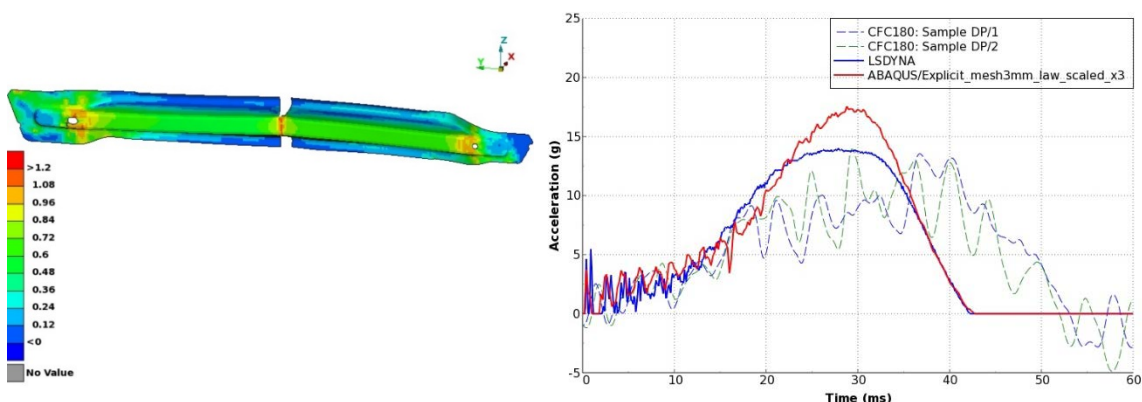


Figure 142. Von Mises Stress [GPa] for DP1000 crash subsystem impact setup#3 at 8 km/h in Abaqus with 3mm mesh

Table 24 summarizes the modelling results for the different tested crash configurations, giving the accuracy of crash simulation results using current LS-DYNA and ABAQUS models and the damage

model developed at Tough-sheet (1- poor correlation, 2- acceptable correlation, 3- good correlation, 4- excellent correlation).

Table 24. Level of correlation in crash simulations with different damage models

Demonstrator	Current FE models	Damage model from Tough-sheet	
		LS-DYNA	ABAQUS
Axial impact specimen (WP1)	2	1	2
Bending impact specimen (WP1)	1	3	4
Crash subsystem setup 1 (WP6)	1	1	1
Crash subsystem setup 2 (WP6)	-	2	2
Crash subsystem setup 3 (WP6)	-	3	2

2.2.7. WP7. Implementation of a sheet forming failure criterion

The main objective of this WP was to implement in the simulation of forming industrial parts the EWF-based failure criterion developed in WP3 and WP4. Such failure criterion is based on the energy released in fracture and it is expected to predict sheet fracture during forming. Simulations and experimental results were compared in order to check the failure criterion accuracy and propose solutions to optimize the simulation methodology. The tasks performed in WP7 are described in Table 25.

Table 25. Tasks of WP7

Task	Name of the task
Task 7.1	Material selection according to the components and forming requirements
Task 7.2	Forming processes and comparison with simulations
Task 7.3	Improvement of forming simulations accuracy by means of EWF
Task 7.1	Material selection according to the components and forming requirements

Task 7.1 Material selection according to the components and forming requirements

The materials chosen for this WP were the steel grades selected in WP4 for formability investigations: DP1000, CP1000 and TBF. The manufactured component was the side sill internal reinforcement of the Alfa Romeo Stelvio model (Figure 90), which in serial production is made from low alloyed steel: LAC340 with 1.5mm of thickness.

Task 7.2 Forming processes and comparison with simulations

Forming process

The side sill internal reinforcement (Figure 90) is formed in only one deep drawing operation with an hydraulic press of 300 tons and the blank is laser cut. Some images of the press are reported in Figure 143.

This component have many flanges where the resistance of edge cracking plays an important role on the deformation process. Two kind of edge qualities were tested: laser cut (good quality), hard cut (low quality).

In order to correlate the crack initiation and propagation with the press stroke, 10 components from laser cut blanks and 6 components from hard cut blanks for each grade were formed at different values of press stroke. Table 26 and Table 27 summarize the forming tests performed with laser cut and hard cut blanks respectively. Figure 144 to Figure 152 show the images of the formed components at different press strokes with DP1000, CP1000 and TBF. In general for all 3 steel grades, cracks appear in the same position of the component.

Table 26. Summary of press stroke levels for manufactured components with laser trimmed edge. In red the stroke level at what the first crack is detected.

DP1000		CP1000		TBF	
Number	Stroke	Number	Stroke	Number	Stroke
n	mm	n	mm	n	mm
1	45	1	45	1	50
2	50	2	50	2	52
3	55	3	55	3	55
4	60	4	60	4	60
5	45	5	45	5	58
6	50	6	50	6	55
7	60	7	48	7	58
8	45	8	55	8	55
9	50	9	45	9	52
10	55	10	50	10	58



Figure 143. Hydraulic press for side sill internal reinforcement of Alfa Romeo Stelvio model production

DP1000: For DP1000 steel grade formed component, cracking started at 45 mm of stroke in different regions of the component (Figure 144). Increasing the stroke value, the cracks propagated and they appeared also in other zones (Figure 145). It is observed that at final stroke the component is severally fractured (Figure 146).



Figure 144. Cracks in DP1000 steel grade (45mm stroke)



Figure 145. Cracks in DP1000 steel grade (50mm stroke)



Figure 146. Cracks in Dual Phase 1000 steel grade (60mm stroke)

CP1000: CP1000 grade showed similar behaviour to Dual Phase 1000, starting to crack for a stroke of 45mm (Figure 147). Multiple cracking is also observed at further press strokes. (Figure 148 and Figure 149).



Figure 147. Cracks in CP1000 grade (45mm stroke)



Figure 148. Cracks in CP1000 grade (50 mm stroke)



Figure 149. Cracks in CP1000 grade (60 mm stroke)

TBF: The TBF grade exhibited better formability properties than CP 1000 and DP 1000. In this case, the component started to cracking at a press stroke of 50 mm (Figure 150). This behaviour could be justified because the thickness of TBF was higher than CP and DP grades (1.5mm instead of 1.4 for DP and CP).



Figure 150. Cracks in TBF grade (50 mm stroke)



Figure 151. Cracks in TBF grade (55 mm stroke)



Figure 152. Cracks in TBF grade (60 mm stroke)

From the fracture analysis it was concluded that cracking was due to strain localization in all three materials. No edge cracks were observed in any of the investigated materials, due to the high edge quality provided by laser cutting.

A second series of forming tests were performed with hard cut blanks in order to evaluate the effect of edge quality in AHSS cold forming. Figure 153 shows the hard cut areas of the blank. In this case, a total of 6 specimens for each steel grade were tested. Special attention was paid to the crack initiation (lower press strokes). The press stroke levels for the different tests with hard cut blanks are summarized in Table 27. In general, cracks appeared at the same position for all the investigated steel grades. Figure 154 to Figure 156 show some images of the cracks appeared in components formed from hard cut blanks

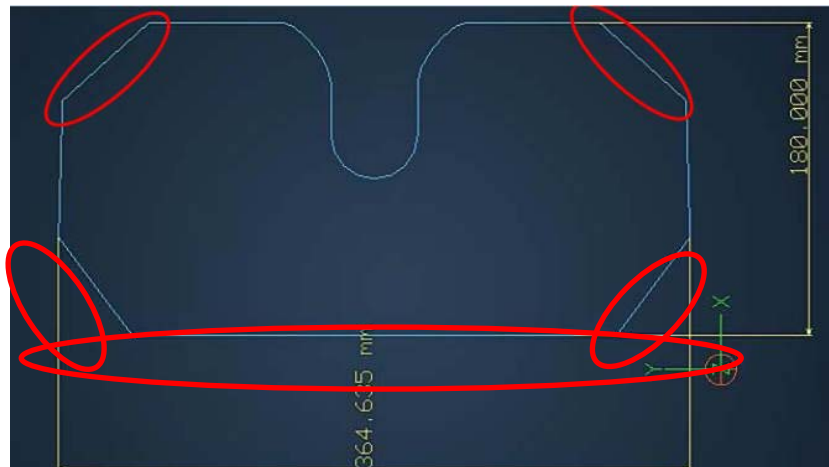


Figure 153. Hard cut area in Stelvio component

Table 27. Different strokes for DP1000, CP1000 and TBF1000 hard cut blanks. In red the stroke level at what the first crack is detected.

DP1000	
Number	Stroke
n	mm
1	35
2	40
3	38
4	39
5	39
6	38

CP1000	
Number	Stroke
n	mm
1	40
2	40
3	35
4	38
5	39
6	39

TBF	
Number	Stroke
n	mm
1	40
2	35
3	38
4	37
5	38
6	37

DP1000: DP1000 grade started to crack for a stroke of 38mm in the right side of component. Figure 154 shows the detail of the crack.



Figure 154. Crack in DP1000 at 38mm

Complex Phase 1000 CP1000 grade started to cracking at 39mm of stroke in the right side of component (Figure 155).

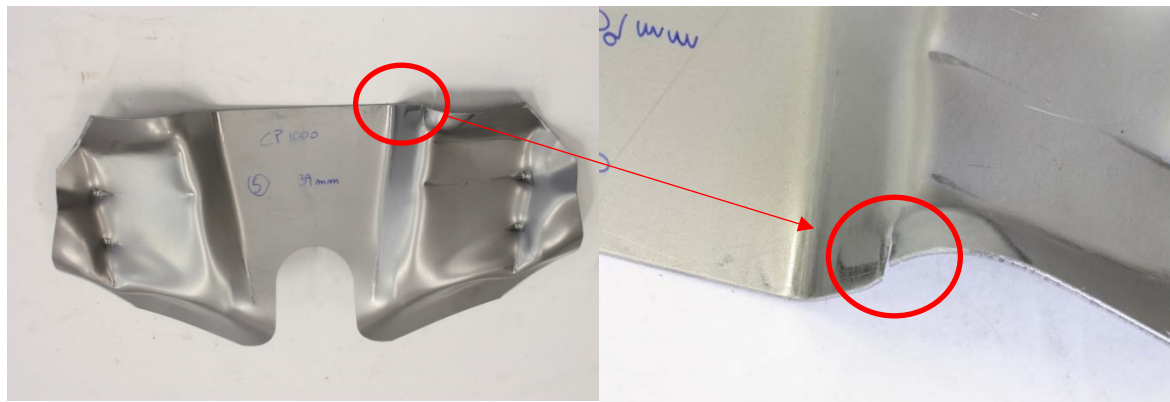


Figure 155. Crack in CP1000 at 39mm

TBF: The first cracks in TBF steel grade were observed at 37mm of stroke. Cracks appeared in the same position observed in the components manufactured with DP1000 and CP1000 (Figure 156).



Figure 156. Crack in TBF1000 at 37mm

The most remarkable difference respect components formed with laser cut blanks is the appearance of cracks at lower press strokes (37-38mm instead of 45-50mm) in all the investigated steel grades. It means that the components start to cracking at lower deformation levels, as observed in Figure 154 to Figure 156. The fracture analysis performed in task 4.3 also revealed a poor strain localization in the fracture area, which indicates that fracture is triggered by edge damage. In this case, even though there is no significant differences between the three steel grades, forming process results are in better agreement with fracture toughness results obtained in WP2. The steels presenting poorer fracture toughness (DP1000 and TBF) start to cracking at lower press strokes (37-38 mm) than steel with superior toughness (CP1000), contrary to the observed in laser cut blanks.

Results highlight the importance of edge quality on AHSS cold forming and the role of fracture toughness on edge fracture. To better rationalize these results the following ideas should be considered:

- Edge-crack nucleation: it could be related to the energy needed for crack initiation, that is the w_e^i calculated for crack-propagated DENT specimens (Table 17). So the higher w_e^i the more resistant the material to edge cracking is. The following table support this idea.

Table 28. Values of stroke at first crack appearance and crack initiation toughness, w_e^i

Material	Stroke for crack initiation (mm)	w_e^i (kJ/m ²)
TBF	37	108 ± 9
DP1000	38	113 ± 5
CP1000	39	151 ± 8

- Edge-crack propagation: it could be related to the energy needed for crack propagation, that is the w_e calculated for crack-propagated DENT specimens (Table 15). So the higher w_e the more resistant the material to the propagation of edge cracks is. The following table support this idea. It is interesting to see that the CP1000, with a high toughness, shows no crack growing.

Table 29. Crack growth for different press strokes and w_e values for the investigated steels.

Material	Crack length at first cracking stroke (mm)	Crack length at last stroke (mm)	Crack growth (mm)	w_e (KJ/m ²)
TBF	1.8	2.1	0.3	149 ± 13
DP1000	1.8	2.0	0.2	138 ± 20
CP1000	1.7	1.7	0	405 ± 11

Simulation of forming process

The simulation of the forming process of the side sill internal reinforcement was carried out in Abaqus with conventional FLC failure criteria. Only one half of the model was reproduced, due to the symmetric conditions of the part. The geometry provided by CRF and the Abaqus model are shown in Figure 157.

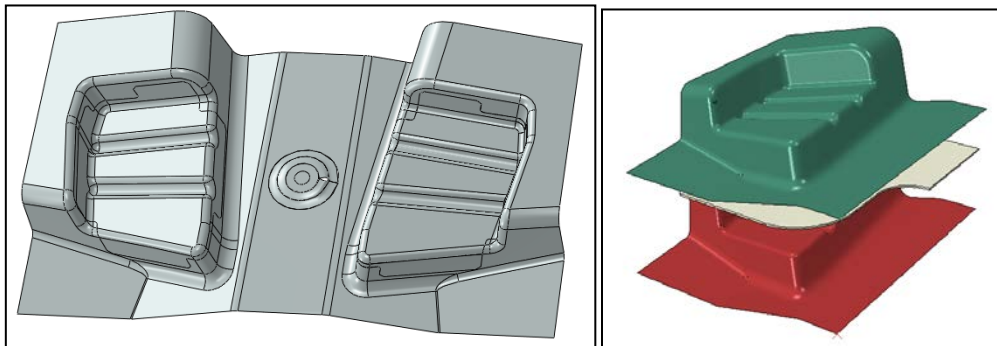


Figure 157. Part geometry provided (left) and model designed for simulations in Abaqus (right).

The forming model was meshed using an edge seed mesh control to get the right size of each element and with the C3D8R an 8-node linear brick, reduced integration, hourglass control .The model has a seed of 1.1 mm and have 24464 elements (Figure 158). Simulation results were analyzed using the FLC to predict the rupture. Simulations were performed with the three steel grades selected in task 7.1: DP1000, CP1000 and TBF.

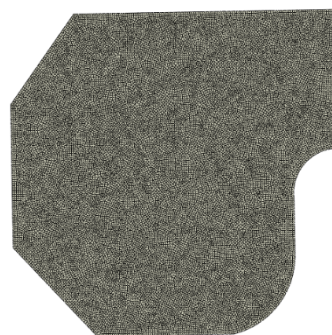


Figure 158. Mesh on the sheet blank.

The contour diagrams of the principal and minimum principal strains are shown in the following figures and they are compared with the limit of forming strains. It is observed that the data points from the simulation lie above experimental FLC for the studied materials and thus failure will occur in the analyzed zones. Therefore, forming simulations using conventional FLD failure criterion

accurately predict the zones where fracture initiates. However, the criterion is too conservative in predicting formability, i.e. fracture is predicted before it appears. This is typically observed in forming simulation of AHSS grades. In addition, FLD criterion does not predict edge cracking in any material. This is solved by combining damage model based on EWF (task 4.5) with FLC criterion. It is detailed on task 7.3.

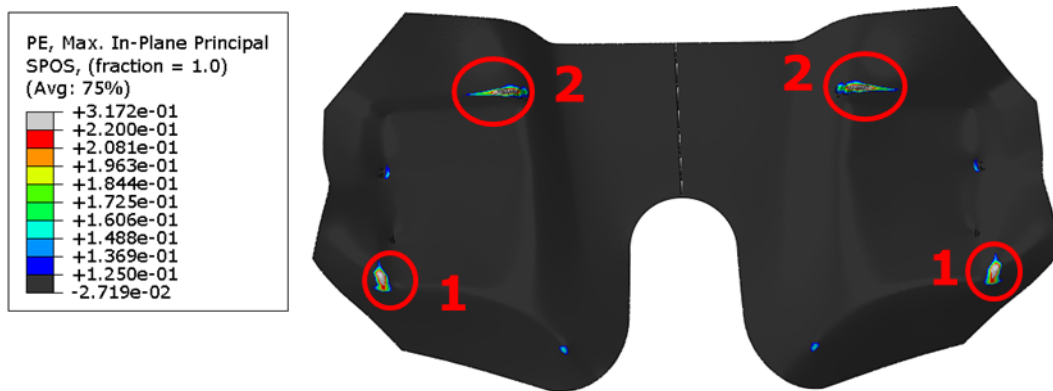


Figure 159. DP1000. Simulations with FLC criterion in Abaqus software. Maximum principal strain.

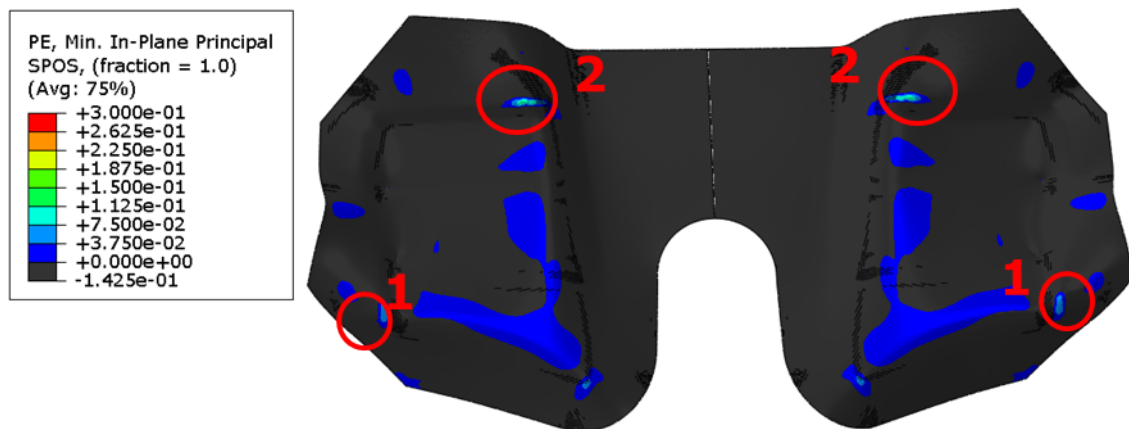


Figure 160. DP1000. Simulations with FLC criterion in Abaqus software. Minimum principal strain

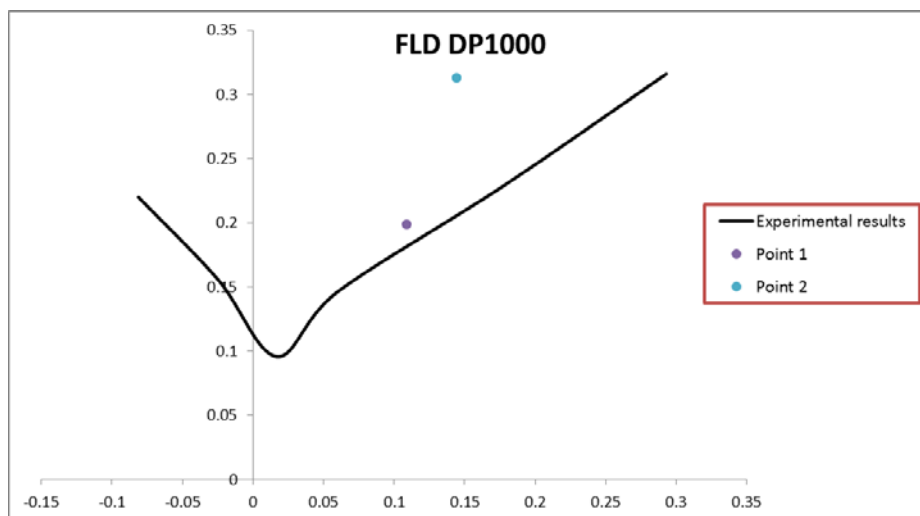


Figure 161. DP1000 FLC with the points of the simulation

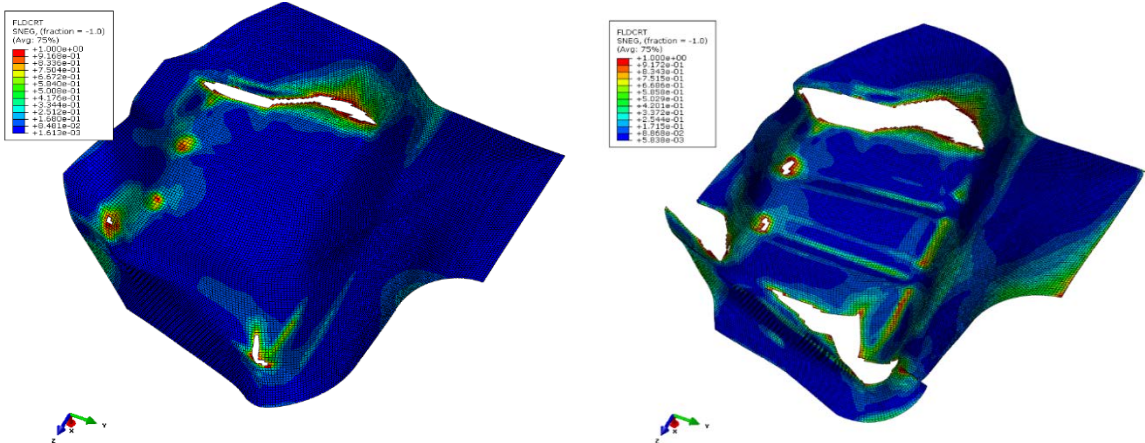


Figure 162. DP1000. Forming simulations with FLC failure criterion at first crack initiation (45 mm of stroke) and 100% (60 mm of stroke) of the forming process.



Figure 163. DP1000. Industrial formed component at 60 mm of stroke

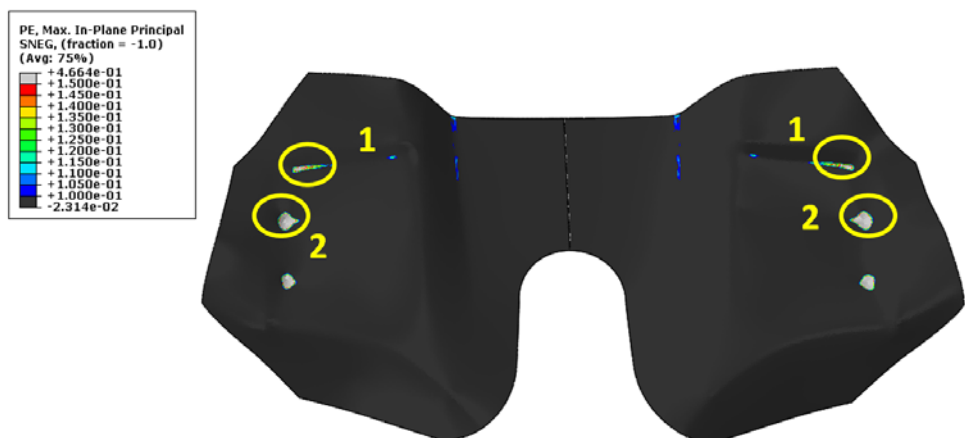


Figure 164. CP1000. Simulations with FLC criterion in Abaqus software. Maximum principal strain.

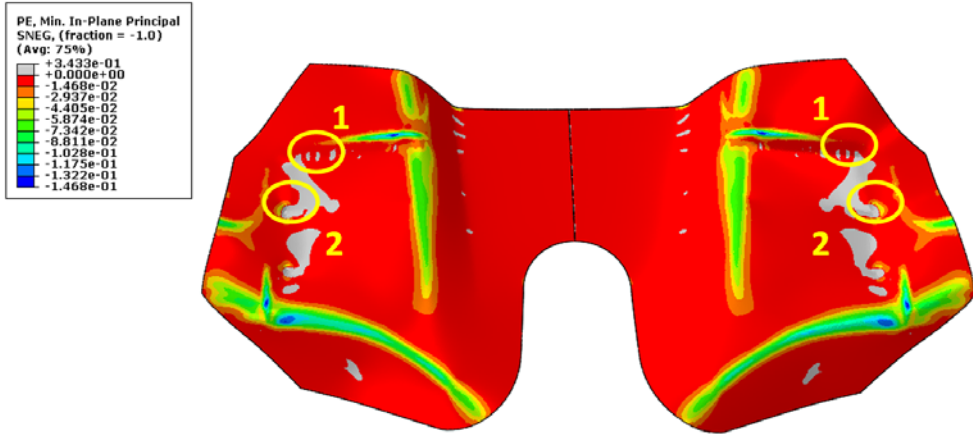


Figure 165. CP1000. Simulations with FLC criterion in Abaqus software. Maximum principal strain.

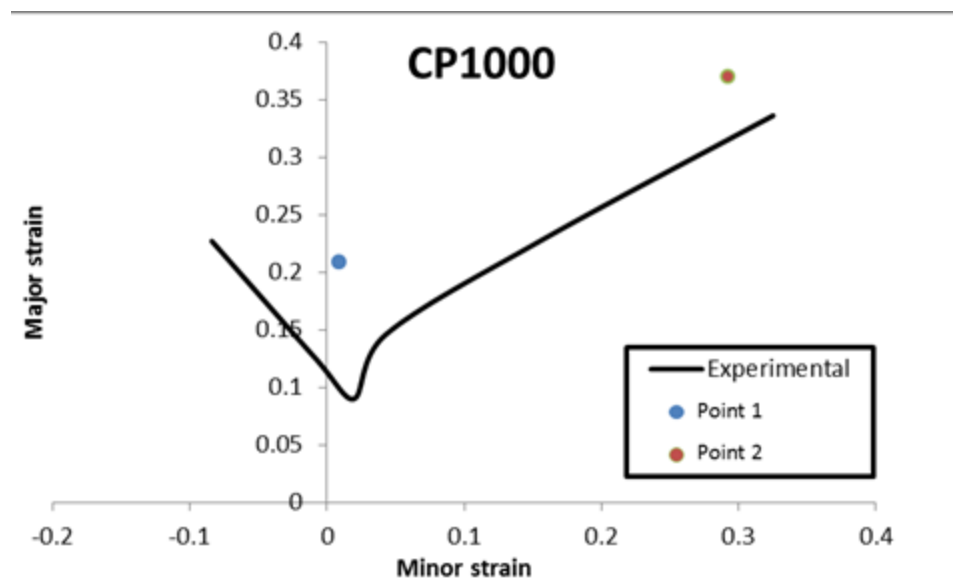


Figure 166. FLC with the points of the simulation for CP1000 steel.

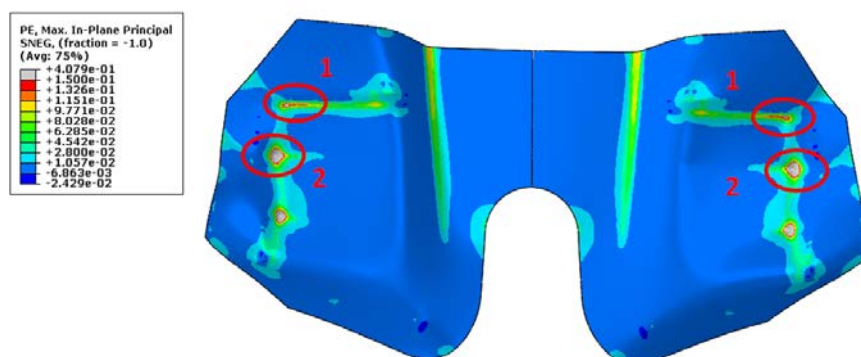


Figure 167. TBF. Simulations with FLC criterion in Abaqus software. Maximum principal strain.

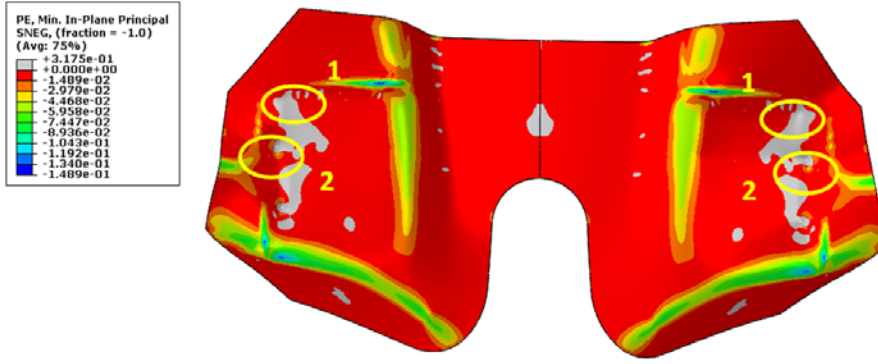


Figure 168. TBF. Simulations with FLC criterion in Abaqus software. Maximum principal strain.

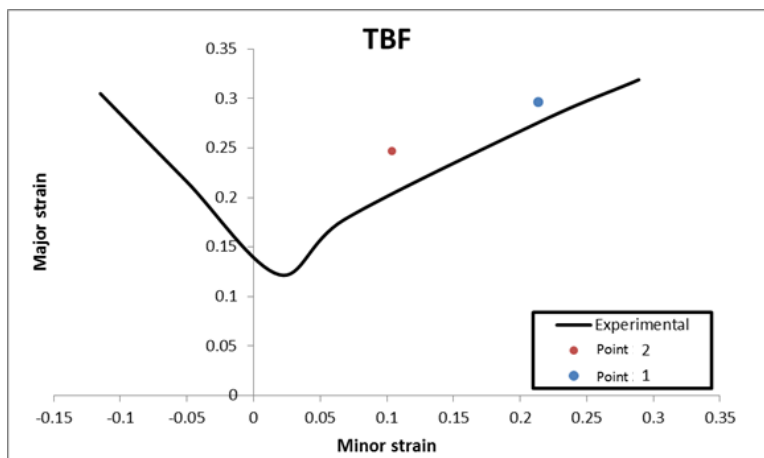


Figure 169. FLC with the points of the simulation for TBF steel.

Task 7.3 Improvement of forming simulations accuracy by means of EWF

In order to improve the accuracy of forming simulations the EWF-based damage evolution law developed in WP4 was implemented in this task in combination with conventional FLC failure criteria.

It was proposed to divide damage criteria in two parts: FLC criteria for bulk material and EWF failure criterion for the external contour (Figure 170). As observed in task 4.5 edge cracking resistance of AHSS grades is closely related to their fracture toughness measured in terms of EWF. For this reason, the damage evolution law based on EWF should better describe the material behaviour in the edges. On the other hand, the areas subjected to general deformation modes (uniaxial, plane strain, biaxial, etc.) should be well represented by FLC failure criterion.

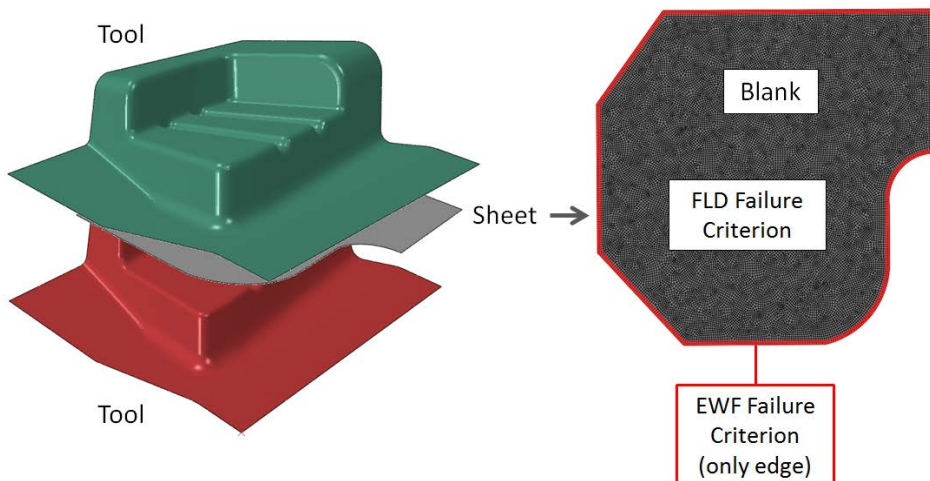


Figure 170. Model for forming simulation.

Figure 171 shows the forming process in the simulation in three steps, one at 70% another at 80% and the last at 100%. The legend shows the level of damage according to FLC criterion. All the elements with damage above 1, are starting to fail or are already damaged and failed. It is remarkable that the model can capture the crack initiation and that edge cracks apparition, not captured in previous simulations (solely based on FLC criteria), are now reproduced.

Figure 172 to Figure 174 show the comparison between the simulations using combined EWF-FLC failure criterion and the experimental forming processes at 60 mm of stroke. Some of the different fractures observed in simulations were numbered from 1 to 5. DP1000 (Figure 172) shows a high correlation level with experimental tests, presenting fractures in the same position and of similar magnitude for both experimental and simulated forming process. CP1000 simulations (Figure 173) also show great similarities with experimental tests (fractures 1,2,3 and 5). The lowest level of correlation is found for TBF steel grade (Figure 174). Only the points 1, 3 and 5 coincide with the experimental component.

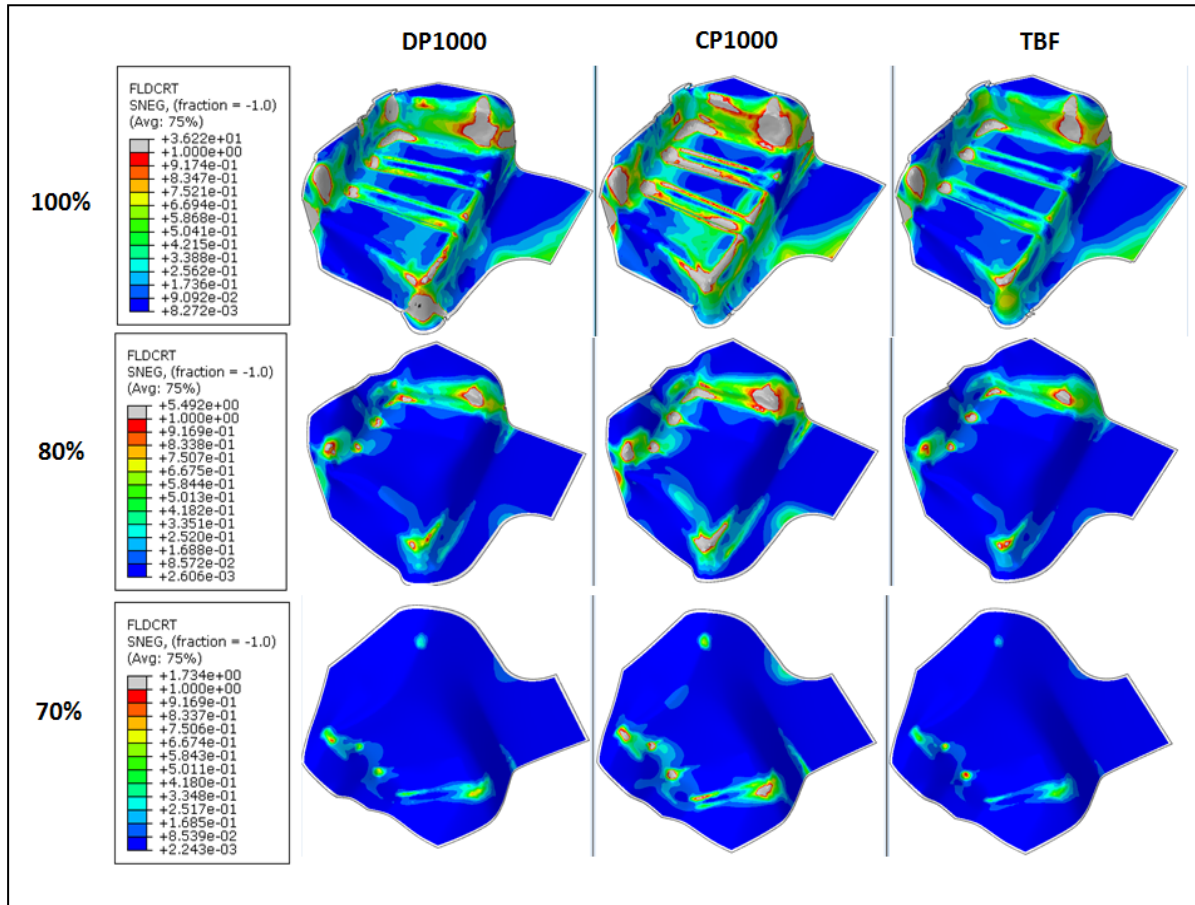


Figure 171. The steps of the forming simulation of the three materials.

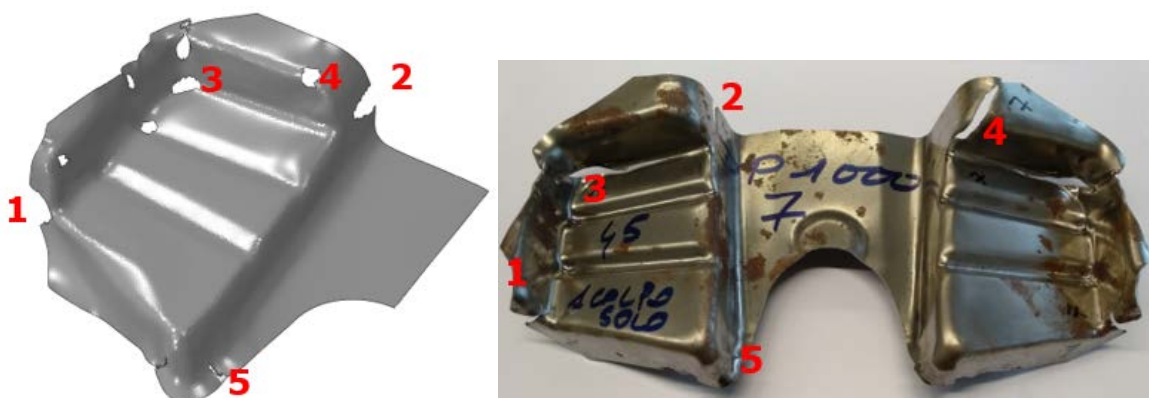


Figure 172. Simulation (left) and experimental (right) forming of a component manufactured with DP1000.

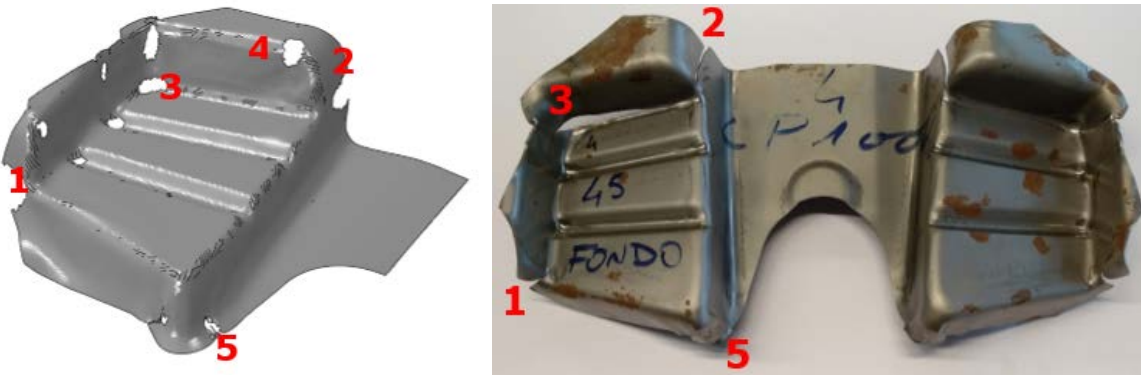


Figure 173. Simulation (left) and experimental (right) forming of the CP1000.

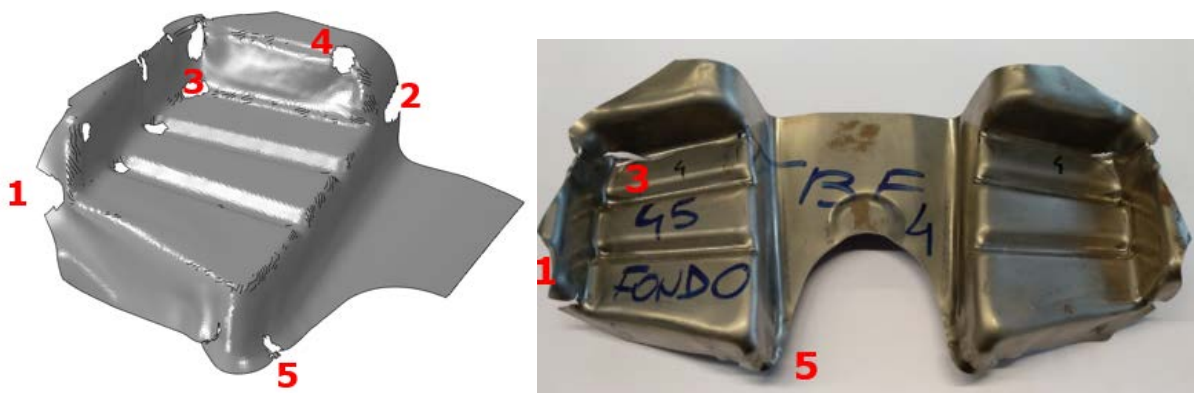


Figure 174. Simulation (left) and experimental (right) forming of the TBF.

The sheet metal forming simulations were able to detect many of the failures of the real parts, especially in DP1000 and CP1000. The application of two types of damage (FLD in the interior and EWF in the exterior edges) improved significantly the correlation between simulations and experimental tests. Results showed that a EWF-based damage evolution model could be included in finite elements software, as Abaqus, to properly described edge cracking in cold forming of AHSS.

2.2.8. WP8. Management, dissemination and reporting

The objectives of WP8 were to plan and coordinate between all the partners the tasks performed in the different work packages, and to follow up the project outcomes vs the plans. The coordinator of the project, CTM, was the responsible for the project management. CTM as the coordinator of Toughsheet, ensured that all milestones and deliverables were accomplished and that all reports were performed in agreement with the contractual requirements and defined dead-lines.

Dissemination tasks were carried out aimed at spreading the knowledge gathered in the project to a wider audience and to facilitate the industrial use of the project outcome.

Table 30. Tasks of WP8.

Task	Name of the task
Task 8.1	Coordination, management, reporting and meetings
Task 8.2	Dissemination, including website, workshops and publications

Task 8.1 Coordination, management, reporting and meetings

CTM was the responsible to ensure the accomplishment of the defined milestones and deliverables as agreed in the proposal and also of the financial administration of the project. The project progress was closely followed by periodic technical progress meetings. Eight progress meetings were held

along the project: 3 online and 5 face-to-face meetings. The meetings were hosted by each partner in turn. The kick-off meeting and the final meeting were held in CTM.

The minutes of the meetings were written and uploaded to the project homepage. The coordinator of the project participated in all the meetings and supervised that all the milestones and deliverables were accomplished within the deadlines.

The collection and compilation of the results of each work package was done by the respective work package leader. The information, once completed and revised, was submitted to the project coordinator. The coordinator was responsible of gather all the information and write the technical periodic reports.

Task 8.2 Dissemination, including website, workshops and publications

A project website (<http://toughsheet.ctm.com.es/>) was created to facilitate the exchange of information between all the partners, the organization of meetings and to keep all the participants updated with the latest project's news. The dissemination of the results obtained in the project was carried out by the participation of the partners in diverse conferences and the publication of papers in scientific journals. A list of contributions presented in conferences and published papers is detailed in section 5.5.

2.3 Conclusions

This section describes the main conclusions obtained in Tough-sheet project, task per task.

WP1

Task 1.1 Materials and samples preparation:

Nine industrially produced AHSS grades were investigated in the project. Eight grades were supplied by voestalpine and one grade by CRF:

- 3 commercially available first generation AHSS cold forming grades (DP1000, CP1000 and CP1200)
- 3 new developments of 3rd generation AHSS: 1 TBF steel (bainitic ferrite matrix with retained austenite), 1 Q&P steel (tempered martensite matrix with retained austenite), and 1 mixed TBF/Q&P microstructure.
- 2 microstructures of hot stamped boron steel: one in the press hardened condition (strength of about 1500 MPa) and the other with an additional tempering treatment (strength of about 1000 MPa).
- 1 TWIP (Twining Induced Plasticity) steel with a fully austenitic microstructure.

Task 1.2 Mechanical characterization:

- Elongation at fracture from conventional tensile tests, usually used to define the material ductility, strongly underestimates the post uniform local ductility potential of the material. This property cannot be used to predict edge cracking resistance or crashworthiness.
- DIC-assisted tests are very useful to evaluate local ductility and post necking deformation levels. The fracture strains obtained with these tests better define the local ductility of the material. Therefore materials with high elongation at fracture can show poorer local ductility and vice versa.
- The levels of deformation found in biaxial bulge tests are very similar to the local strains observed in DIC-assisted tensile tests.

Task 1.3. Laboratory impact resistance tests

- The use of the CI, defined according to an overall crack length, has shown to be suitable to assess the crash resistance of AHSS grades.
- A new parameter to describe the evolution of damage in axial and impact resistance tests has been introduced, the Crash Index Decreasing Rate (CIDR), which is determined by the slope defined by the decrease of the CI in function of the intrusion level. CIDR describes the resistance to crack growth in crash tests.
- The CIDR has been very useful to rank the crashworthiness of the different AHSS grades in axial impact tests. However, no significant differences have been found in CIDR in bending impact resistance tests.

- In general, all the investigated steel grades have shown low effect of strain rate on tensile properties up to 50 s^{-1} . A slight hardening effect and increase of mechanical properties has been observed at 500 s^{-1} .

Task 1.4. Laboratory forming tests

- The FLC obtained for the different AHSS grades has been similar in most cases, except for TWIP steel, which has shown much greater formability than the other steel gradees. In general, it has been oberved that steels containing retained austenite (TBF, Mixed and Q&P) shows superior formability than equivalent 1st generation AHSS grades (DP1000, CP1000, CP1200).
- All the steel grades have shown a little sensitivity to the strain paths, indicated by the lower FLC strain values obtained with Marciniak punch.
- FLC are suitable to evaluate AHSS formability under determined deformation modes. However, FLC and tensile properties fail to predict edge cracking or stretch-flangeability.
- HET have shown to be suitable to assess the edge cracking sensitivity of the investigated AHSS grades.
- Great differences have been observed in HER among the different steels. In general, CP-like (CP1000, CP1200, Mixed,Q&P) steel showed greater HER than DP-like (DP1000, TBF). The tempering treatment performed in PHS showed a positive effect on edge cracking resistance.

WP2

Task 2.1 Evaluation of EWF in AHSS

- The EWF methodology has shown to be reliable experimental tool to assess the fracture toughness of thin AHSS sheets.
- The notch radius has a large influence on fracture toughness results. Thus, when considering the fracture toughness as a material property,it is recommended to use the lowest possible radius. Cracks propagated by fatigue from the machined notches are recomnded to obtain the fracture toughness of AHSS.
- The EWF values at crack initiation (w_e) are equivalent to the elastoplastic fracture mechanics toughness value, J_c . In contrast, the EWF for the whole fracture (w_e) has an energetic contribution from crack propagation and it is a good measure of the energy dissipated during the ductile tearing process. This parameter, w_e , can be compared to the J_{max} obtained in J-R curves.

Task 2.2 Simulation of EWF tests

- The simulation of DENT specimens have shown a good correlation with experimental test only up to fracture initiation. Thus, the value of w_e' or J_c can be obtained by FEM. It has not been possible to simulate the EWF for the final fracture.
- The application of *J-integral* calculation in Abaqus software has shown a reasonable good correlation with the experimental works of fracture obtained in experimental tests.

WP3

Task 3.1 Material selection according to impact and EWF results

- According to the cracking behaviour observed in laboratory impact resistance tests performed in WP1, 3 AHSS grades were selected in this task to perform the corresponding investigations: DP1000, TBF and Q&P. The three steels presented significant cracking during axial and bending impact tests, which was essential to investigate the evolution of crack propagation during crash and correlate it with fracture toughness results. All the investigations carried out in WP3 were focused in these 3 steels.

Task 3.2 Effect of strain rate on EWF in AHSS

- It has been observed that, in general, the EWF tends to increase with strain rate. A slight increase of EWF was observed at medium strain rate. Such increase was more significant at high strain rates. Results were in good agreement with dynamic tensile tests.
- The experimental difficulties on the determination of the exact instant of fracture can affect significantly the results and compromise the reliability of EWF values at high loading rates.

Task 3.3 Simulation of laboratory impact resistance tests

- After the evaluation of the capabilities of the constitutive models in the LS-Dyna material formulations, it was concluded that there is not any constitutive model considering the effects that can be relevant in the impact-related simulations:
 - Strain-rate related effect
 - Inclusion of a failure envelope
 - Definition of complex damage evolution laws.
 - Implementation of the smeared methodology, in order to reduce the dependency of the results with the mesh-refinement.
- Application of fracture toughness as a failure criterion has shown that EWF values are valid for the magnitude of energy dissipated during the damage evolution in the material, but not to be accurate enough for the prediction of the damage initiation and propagation for all the different loading cases studied.

Task 3.4 Correlation of fracture toughness evaluated by means of EWF with crash resistance

- Fracture toughness, measured in terms of EWF, has shown to be a suitable material property to assess AHSS crashworthiness. Such results highlight the important role of fracture toughness on AHSS crashworthiness
 - A direct correlation was found between EWF values and CIDR and energy absorbed in axial impact resistance tests.
 - A threshold EWF value was observed in bending impact resistance tests, from which no cracks appeared in impact tested specimens.
- An EWF-based damage evolution law has been developed aimed at improving the accuracy of crash simulations. The law describes the evolution of damage after the onset of the fracture.

WP4

Task 4.1. Material selection according to the formability and EWF results

- 3 materials were selected for the formability investigations in WP4, according to the results of WP1 and WP2:
 - 1 bending grade: CP1000. This grade presents high fracture toughness, stretch flangeability and bendability, which makes it suitable for bending operations with small bending radii. On the other hand, the deep drawing of this steel is moderate.
 - 2 deep-drawing grades: TBF and DP1000. These two steel grades, show lower fracture toughness and stretch flangeability, but their high n-value and elongation make them more suitable for deep-drawing operations.

Task 4.2. Effect of pre-straining on EWF in AHSS

- It has been observed that the EWF is not significantly influenced by pre-straining conditions.

Task 4.3. Fracture origin characteristics in cold forming

- It has been observed that sheet fracture under general deformation modes (uniaxial strain, plane strain, biaxial strain) is driven by strain localization and, thus, fracture takes place after significant necking.
- On the other hand, edge cracking is governed by the edge quality and the material resistance against the propagation of cracks, i.e. the fracture toughness. The damage induced during shearing or punching (voids, microcracks, etc.) is the origin of fracture in subsequent forming operations.
- The effect of edge quality on edge cracking has been examined in a industrial component.

Task 4.4. Simulations of forming tests

- In general, a good correlation between experimental and modelling results was observed.

Task 4.5. Correlation of fracture toughness evaluated by means of EWF with sheet forming tests

- The correlation between EWF and HER shows that fracture toughness is useful to rationalize AHSS edge cracking resistance and prove again the importance of fracture toughness on stretch-flangeability.
- A damage evolution model similar to the obtained in task 3.4 has been developed, aimed at implementing it in forming simulations.

WP5

Task 5.1. Effect of sheet thickness on EWF

- Under plane stress conditions, the fracture toughness is thickness dependent. In the range of thickness investigated 1-2.2 mm the fracture toughness increased linearly with the sheet thickness in a CP steel.

Task 5.2. Effect of plastic anisotropy on EWF

- No large anisotropic effects on fracture toughness have been found in fine-grained and microstructurally homogeneous steels, as CP-like. The EWF is very similar in 0°, 45° and 90° with respect to the rolling direction. It follows the same trend observed in tensile tests
- Some anisotropy effect on the EWF values were found for DP-like steel, with no fine or homogeneous microstructure. The EWF values are higher in the 0° orientation respect to rolling direction and lower in the 45° one for DP1000. This effect was also observed in the tensile tests.

Task 5.3. Evaluation of microstructural features

- A general relation between microstructure and fracture toughness was observed: DP-like steel grades (mixture of soft-hard microstructural components), such as DP1000 and TBF, exhibited poorer toughness values than CP-like grades (homogeneous bainite/martensite matrix).
- The influence of TRIP-effect on crack propagation resistance was evaluated in three steel grades with different amounts of retained austenite. EBSD investigations showed the evolution of martensitic transformation with the deformation. However, EBSD measurements resulted not accurate enough to quantify the retained austenite content of the investigated specimens. The large discrepancy observed between EBSD and magnetic measurements on retained austenite content was probably caused by either transformation of retained austenite to martensite at the sample surface during preparation (bcc instead of fcc is measured by EBSD), or due to low band contrast of the austenitic areas (leading to zero solutions in the EBSD measurement). Thus, local investigation of retained austenite transformation by EBSD measurements could only be used to draw a qualitative comparison between the states examined.
- Investigations showed that most of the retained austenite was transformed before or shortly after crack initiation. However, after crack initiation, it was observed a larger amount of retained austenite in the plastic zone between the cracks than in the crack tip, which allows speculating that TRIP contribution might have some influence on crack propagation resistance. Further investigations are suggested to discern the role of TRIP-effect on crack propagation.

WP6

Task 6.1 Design and fabrication of crash subsystems

- An anti-intrusion door beam was used as a crash demonstrator. The component was manufactured with DP1000, CP1000 and TBF.

Task 6.2 Crash tests and comparisons with simulations

- Three experimental setups were proposed, aimed at investigating the damage induced in the component under different load crash scenarios.
- In general, the results of the simulation over the different materials showed a similar behaviour. The first part of the test showed a good level of correlation when taking into account the damage of the material introduced as a GIISMO model using MAT_ADD_EROSION as described in WP3 (considering the failure envelope). However, the experimental acceleration values showed a softer evolution after their maximum point.

Task 6.2 Improvement of crash simulations accuracy by means of EWF

- The results with the proposed EWF-based damage evolution law developed in Abaqus offer a better correlation in both axial and side impact crash cases when it is scaled taking into account the mesh influence.

WP7

Task 7.1 Material selection according to the components and forming requirements

- The materials chosen for this WP were the steel grades selected in WP4 for formability investigations: DP1000, CP1000 and TBF. The manufactured component was the side sill internal reinforcement of the Alfa Romeo Stelvio model, which in serial production is made from low alloyed steel: LAC340 with 1.5mm of thickness.

Task 7.2 Forming processes and comparison with simulations

- Two different cutting conditions were used, in order to evaluate the role of edge quality in AHSS cold forming: laser cutting and hard cutting.
- Laser cutting provides a high edge quality. The fractures in laser cut blanks cracks appeared after high levels of deformation. Such fractures were caused by strain localization and not by edge damage. TBF, showed better formability than DP1000 and CP1000.
- Fracture in components manufactured from hard cut blanks, showed fracture at much lower deformation levels. In this case, the fractures were highly influenced by edge conditions. A poor level of necking was observed near the fractures. In this case, the tougher material CP, show the best behaviour.
- A good relation has been found between EWF parameters and edge cracking:
 - Crack initiation is governed by the EWF at crack initiation, w_e^I
 - Crack propagation during forming is governed by the total EWF, w_e
- Computer simulations performed with conventional FLC failure criteria predicted accurately the zones of fracture apparition.

Task 7.3 Improvement of forming simulations accuracy by means of EWF

- The application of a damage evolution model based on EWF in forming simulations in combination with conventional FLC criteria showed an improvement of simulation accuracy.
- Preliminary results with the EWF-FLC criteria predict the location of edge cracks.
- Further work is necessary to implement an energy based fracture criterion in crash simulation, able to take into account the energy dissipated in crack propagation.

WP8

Task 8.1 Coordination, management, reporting and meetings

- The project progress was closely followed by periodic technical progress meetings. Eight progress meetings were held along the project: 3 online and 5 face-to-face meetings.
- The coordinator of the project participated in all the meetings and supervised that all the milestones and deliverables were accomplished within the deadlines.
- A project website was created to facilitate the exchange of information between all the partners, the organization of meetings and to keep all the participants updated with the latest project's news.
- The dissemination of the results obtained in the project was carried out by the participation of the partners in different conferences (5 contributions) and the publication of papers in peer-reviewed scientific journals (1).

2.4 Exploitation and impact of the research results

The results obtained in Tough-sheet project highlight the high potential of fracture toughness, evaluated by means of the EWF methodology, to predict edge cracking and crashworthiness in AHSS sheets. EWF tests are proposed as useful tool for steel products developers and carmakers to not only select commercially available steel grades with superior crashworthiness and edge cracking resistance but also to help in the development of new AHSS with enhanced fracture resistance. The methodology may be implemented at industrial level, as an additional material property for forming and crash applications at affordable costs.

The results of impact tests simulations showed the need to introduce new damage criteria, aimed at exploiting the full energy absorption potential of AHSS. The EWF-based damage evolution model developed can help to improve the accuracy of crash simulations taking into account energy dissipated in crack propagation. However, further investigations are necessary to properly implement this fracture criterion in FEM simulations. Such damage model will also help to improve the accuracy of forming simulations, especially in areas where FLCs fail to predict the fracture, such as stretched edges, expanded holes, etc.

Some of the main results obtained in the project were presented in important conferences of the automotive and steel sector:

- D. Frómeta, M.Tedesco, J.Calvo, A.Lara, S.Molas and D.Casellas, Assessing edge cracking resistance in AHSS automotive parts by the Essential Work of Fracture methodology. 36th IDDRG Conference, Munich (Germany), July 2-6, 2017
- D. Frómeta, A. Lara, S. Molas, D. Casellas, J. Rehrl, C. Suppan, P. Larour, Evaluation of crash resistance by means of fracture toughness measurements in advanced high strength steels. 5th International Conference on Steels in Cars and Trucks (SCT), June 18-22, 2017, Amsterdam (The Netherlands)
- D. Casellas, D. Frómeta, A. Lara, S. Molas, P. Jonsén, S. Golling, M. Oldenburg, A fracture mechanics approach to develop high crash resistant microstructures by press hardening. 6th International Conference on hot Sheet Metal Forming of High-Performance Steel, June 4-7, 2017, Atlanta (USA).
- D. Frómeta, A. Lara, D. Casellas, S. Molas, J. Rehrl and C. Suppan, Fracture toughness evaluation of AHSS sheets and relation to stretch-flangeability, COMAT 2016, November 2016, Pilsen (Czech Republic)
- A. Lara, D. Frometa, S. Molas, J. Rehrl, C. Suppan, D. Casellas, Relation between Stretch-Flangeability and Fracture Toughness in Advanced High Strength Steels. 35th International Deep Drawing Research Group (IDDRG), June 12-15, 2016, Linz (Austria).

Additionally, one paper was published in the scientific journal Metallurgical Materials Transactions:

- D. Casellas, A. Lara, D. Frómeta, D. Gutiérrez, S. Molas, Ll. López, J. Rehrl, C. Suppan, Fracture Toughness to Understand Stretch-Flangeability and Edge Cracking Resistance in AHSS. Met Mat Trans A 86-94 (2017), 48

3. LIST OF FIGURES

Figure 1. Distribution of project Work Packages	5
Figure 2. SEM microstructure of CP1000, CP1200 and DP1000 grade	17
Figure 3. SEM microstructure of TBF, Q&P and TBF/Q&P grade	17
Figure 4. SEM microstructure of PHS1500, PHS100 and TWIP grade	17
Figure 5. Uniaxial tensile curves of CP1000, DP1000, CP1200, TBF, Q&P, mixed, PHS1500 and PHS1000 grade transverse to rolling direction	18
Figure 6. Uniaxial tensile curve of TWIP grade transverse to rolling direction	18
Figure 7. Local engineering stress-strain curves obtained from DIC	19
Figure 8. Flow curves of the investigated steel grades from bulge tests	20
Figure 9. a) geometry of axial (length=300 mm) and b) bending (length=900 mm) crash samples	20
Figure 10. Crash index vs. Intrusion at axial impact tests for investigated steel grades	21
Figure 11. Crash index vs. intrusion at axial impact tests for investigated steel grades	21
Figure 12. Crash index vs. intrusion at axial impact tests for TWIP steel	22
Figure 13. Crash index vs. intrusion for TWIP steel	22
Figure 14. Crash index vs. intrusion at bending impact tests for investigated steel grades	23
Figure 15. Crash index vs. intrusion at bending impact tests for investigated steel grades	23
Figure 16. Crash index vs. intrusion at bending impact tests for investigated steel grades	23
Figure 17. Schematic representation of the MHB machine (top) and image of the MHB machine at CRF	24
Figure 18. True stress-strain curves from dynamic tensile tests for CP1000, DP1000, PHS1000, TBF, TBF/Q&P and CP1200	25
Figure 19. True stress-strain curves from dynamic tensile tests for Q&P, PHS1500 and TWIP	26
Figure 20. Nakajima test	27
Figure 21. Nakajima and Marciniak sample geometries	27
Figure 22. FLCs obtained from Nakajima tests for CP1000, DP1000, CP1200 and TBF	28
Figure 23. FLCs obtained from Nakajima tests for Q&P, TBF/Q&P and TWIP	28
Figure 24. Marciniak test (left) and image of the carrier blank (right)	29
Figure 25. Results of Marciniak tests compared to the FLCs obtained with Nakajima tests	30
Figure 26. Hole punching procedure	31
Figure 27. Hole expansion procedure	32
Figure 28. Tool setup with DIC system	32
Figure 29. Definition of the Fracture Process Zone, FPZ	33
Figure 30. Schematic representation of the EWF experimental procedure	34
Figure 31. a) DENT geometry and detail of the ligament area. b) Notch radius of 150 μm and c) Notch radius of 0.1 μm (fatigue pre-crack)	35
Figure 32. Images taken from the DIC system for the PHS1500 steel	35
Figure 33. Checking of Mises strain at P_{max} before fracture initiation in the shortest (left) and the largest ligament (right). Measurements in PHS1500 specimens	36
Figure 34. NP specimens. w_f values in function of the ligament length for CP1000, DP1000, CP1200 and TBF steel grades	36
Figure 35. NP specimens. w_f values in function of the ligament length for Q&P, Mixed, PHS1500, PHS1000 and TWIP steel grades	37
Figure 36. EWF results for NP specimens	38
Figure 37. P specimens. w_f values in function of the ligament length for CP1000, DP1000, CP1200 and TBF	38
Figure 38. P specimens. w_f values in function of the ligament length for Q&P, Mixed, PHS1500, PHS1000 and TWIP steel grades	39
Figure 39. EWF results for specimens with fatigue pre-cracked specimens	40
Figure 40. Determination of the work for fracture initiation (w_f^i)	40
Figure 41. NP specimens. Summary of w_e^i and w_e values for the investigated AHSS grades	41
Figure 42. P specimens. Summary of w_e^i and w_e values for the investigated AHSS grades	42
Figure 43. Geometry of the CT specimen used for J-integral measurements	43
Figure 44. Experimental setup of J-integral measurements	43
Figure 45. J determination through partial unloadings following the compliance method. Area A_{pl} for the evaluation of J. Curve A is the real $P-\delta$ curve registered. Curve B is an hypothetic curve for a crack length = a_5	44
Figure 46. J values against crack extension for the J-R curve determination	45
Figure 47. J-R curve for CP1000 obtained by the elastic compliance method	45
Figure 48. J-R curve for PHS1500 obtained by the elastic compliance method	46
Figure 49. Measurement of the CTOD by means of DIC and J_c value obtained for CP1000	46
Figure 50. Measurement of the CTOD by means of DIC and J_c value obtained for PHS1500	47
Figure 51. Comparison between experimental and simulation force-displacement curves for some ligaments of DP1000	47
Figure 52. Comparison between experimental and FEM analysis results with different mesh size	48
Figure 53. Comparison between different mesh type analyses	48
Figure 54. Simulation model and mesh of the DENT specimen	49
Figure 55. Correlation between experimental tension test and simulation	50

Figure 56. Correlation between experimental values of w_f and <i>J-Integral</i> values of simulation.....	50
Figure 57. EWF results at low strain rate	52
Figure 58. EWF results at medium strain rate.....	52
Figure 59. Specimen geometry for high strain rate EWF tests	53
Figure 60. EWF tests at high strain rate	53
Figure 61. Summary of EWF results at different stain rates.....	54
Figure 62. DP1000 with linear (upper) and bilinear (lower) damage definition, G_c 138 kJ/m ²	55
Figure 63. Force-displacement curves for QP linear axial impact at 30.1 km/h (left) and side impact at 27.8 km/h (right)	56
Figure 64. Force-displacement curves for QP bilinear axial impact at 30.1 km/h (left) and side impact at 27.8 km/h (right)	56
Figure 65. DP1000 mat 24 and MAT_ADD_EROSION, G_c 297 kJ/m ²	57
Figure 66. Force-displacement curves for QP mat 24 axial impact at 30.1 km/h (upper) and side impact at 27.8 km/h (lower)	57
Figure 67. Force vs impactor displacement curves for two axial impact tests with DP1000	58
Figure 68. Variation of Crash Index (CI) in function of the intrusion and energy absorbed in axial impact tests for the studied steels. The slopes define the crash resistance of the material.....	59
Figure 69. Correlation between w_e and axial CIDR	59
Figure 70. Correlation between w_e and bending CIDR.....	60
Figure 71. Correlation between w_e and energy absorbed at maximum intrusion in axial crash tests	60
Figure 72. Correlation between w_e and energy absorbed at maximum intrusion in bending crash tests	61
Figure 73. DP1000 1 element tensile test comparing damage inputs.....	62
Figure 74. Comparison Implicit vs Explicit solver. Ligament length (LL) = 15 mm	62
Figure 75. Mesh influence. Ligament length (LL) = 5 mm	63
Figure 76. DP1000 EWF test with different damage evolution values.....	63
Figure 77. Failure processes modelling.....	64
Figure 78. EWF quasistatic DP1000 NP with two new damage laws	64
Figure 79. EWF energy with the last two damage laws	65
Figure 80. Schematic representation of uniaxial, biaxial and plane pre-straining conditions for fracture toughness measurements.....	66
Figure 81. Rectangular specimens extracted from pre-strained samples.	67
Figure 82. Results of EWF with plane and biaxial pre-strained NP-type specimens. EWF results with no pre-strained NP-type specimens are also shown for comparison.....	67
Figure 83. Results of EWF with uniaxial pre-strained P-type specimens. EWF results with no pre-strained P-type specimens are also shown for comparison.....	67
Figure 84. DP1000. SEM images of the fracture surfaces of Marcinick test specimens at plane and biaxial deformation modes.....	68
Figure 85. TBF. SEM images of the fracture surfaces of Marcinick test specimens at uniaxial and biaxial deformation modes.....	69
Figure 86. Characteristics of sheared fracture surface	69
Figure 87. CP1000. Fracture surface of punched area. Top left: General view of the fracture surface at 45x. a) Detail of burnished area (100x), b) Detail of fracture zone (350x) and c) detail of fracture zone (500x).....	70
Figure 88. DP1000. Fracture surface of punched area. Top left: General view of the fracture surface at 45x. a) Detail of burnished area (500x), b) Detail of transition burnished-fracture zone (2000x) and c) detail of fracture zone (1000x)	70
Figure 89. TBF. Fracture surface of punched area. Top left: General view of the fracture surface at 45x. a) Detail of transition burnished-fracture area (350x), b) Detail of transition burnished-fracture zone (350x) and c) detail of fracture zone (350x)	71
Figure 90. Inner sill side reinforcement.....	71
Figure 91. First crack appearance (red circles) in components manufactured with laser cut blanks of DP1000, CP1000 and TBF.....	72
Figure 92. DP1000 SEM analysis. Laser cut blank	72
Figure 93. CP1000 SEM analysis. Laser cut blank	73
Figure 94. TBF SEM analysis. Laser cut blank	73
Figure 95. First crack appearance (red circle) in a component manufactured with DP1000 sheared blank.	73
Figure 96. First crack appearance (red circle) in a component manufactured with CP1000 sheared blank	74
Figure 97. First crack appearance (red circle) in a component manufactured with TBF sheared blank	74
Figure 98. DP1000 SEM analysis. Sheared blank	74
Figure 99. CP1000 SEM analysis. Sheared blank.....	75
Figure 100. TBF SEM analysis. Sheared blank	75
Figure 101. Geometry of experimental FLD specimens and modelled specimens.....	76
Figure 102. Mesh of the 60 mm specimen.	76
Figure 103. Maximum principal plastic strain in the specimen of 20mm with mirror extended in its symmetry.....	76

Figure 104. FLC from experimental and simulation results and estimated fracture energy for DP1000	77
Figure 105. FLC from experimental and simulation results and estimated fracture energy for CP1000.	77
Figure 106. FLC from experimental and simulation results and estimated fracture energy for TBF....	77
Figure 107. Stress-strain curve with progressive damage degradation and hypothesis about the relationship between the EWF and the evolution of the damage.	78
Figure 108. Displacement-damage of TBF.....	78
Figure 109. Force-displacement and EWF of DP1000.....	79
Figure 110. Force-displacement and EWF of CP1000.	79
Figure 111. Force-displacement and EWF of TBF.	79
Figure 112. Correlation between w_e and HER.	80
Figure 113. Hardness profiles measured at punched specimens. Note the high increase in hardness for TWIP steel in the sheared area, compared to the moderate increase of the other AHSS grades.	81
Figure 114. Correlation between w_e and HER with the corrected behaviour of TWIP, considering the 'local' fracture toughness due to the twinning transformation around the punched hole (this effect is much lower for other AHSS grades and has minor effect on EWF-HER relationship).	81
Figure 115. Effect of specimen thickness on toughness	82
Figure 116. CP1000. EWF values obtained from sheets with different thicknesses.....	82
Figure 117. Variation of EWF with sheet thickness for CP1000 steel grade. EWF values obtained from No Propagated specimens.	83
Figure 118. CP1000. EWF values at different orientations respect to the rolling direction.....	84
Figure 119. DP1000. EWF values at different orientations respect to the rolling direction.....	84
Figure 120. Tensile tests for CP1000 and DP1000 at different rolling directions	84
Figure 121. Sections on samples used for LOM. Section 1 is in the upper third and section 2 in the center line of the sample. Circle 3 shows the area for investigations on crack surface appearance.	85
Figure 122. Stress situation on the surface and crack propagation for side impact test samples.....	86
Figure 123. Fracture surfaces generated during the side impact test.	86
Figure 124. The observed four areas at the fracture zone at EWF samples.	87
Figure 125. Ductile fracture behaviour in zone III.	87
Figure 126. Ductile fracture behaviour in zone IV.....	88
Figure 127. EBSD-mapping at state 4 in the plastic zone between the cracks. (a) TBF grade. (b) Q&P grade. Blue = bcc, red = fcc, white = zero solution.	89
Figure 128. Component chosen for subsystem evaluation.....	90
Figure 129. Subsystem test first setup.....	90
Figure 130. Damage value in first subsystem configuration, impacting with 20kg at 40 km/h.....	90
Figure 131. Second experimental setup: pendulum impact.....	91
Figure 132. LS-Dyna model for the second setup.....	91
Figure 133. Proposal for the third setup	92
Figure 134. Subsystem first setup correlation for: (a) TBF, (b) DP1000, (c) CP1000	93
Figure 135. Subsystem second setup correlation for: (a) TBF, (b) DP1000, (c) CP1000.....	94
Figure 136. (a) TBF subsystem third setup correlation at 10km/h. (b) DP1000 subsystem third setup correlation at 8km/h. (c) CP1000 subsystem third setup correlation at 10km/h.....	95
Figure 137. Tensile one-element test in Abaqus and comparison with LS-Dyna.....	95
Figure 138. Von Mises Stress [GPa] for DP1000 axial impact at 23.4 km/h in Abaqus with 3mm mesh	96
Figure 139. Von Mises Stress [GPa] for DP1000 side impact at 27.4 km/h in Abaqus with 3mm mesh	96
Figure 140. Von Mises Stress [GPa] for DP1000 crash subsystem impact setup#1 at 40 km/h in Abaqus with 3mm mesh.....	97
Figure 141. Von Mises Stress [GPa] for DP1000 crash subsystem. Impact setup#2 at 21 km/h in Abaqus with 3mm mesh.....	97
Figure 142. Von Mises Stress [GPa] for DP1000 crash subsystem impact setup#3 at 8 km/h in Abaqus with 3mm mesh	97
Figure 143. Hydraulic press for side sill internal reinforcement of Alfa Romeo Stelvio model production	99
Figure 144. Cracks in DP1000 steel grade (45mm stroke)	100
Figure 145. Cracks in DP1000 steel grade (50mm stroke)	100
Figure 146. Cracks in Dual Phase 1000 steel grade (60mm stroke).....	100
Figure 147. Cracks in CP1000 grade (45mm stroke)	101
Figure 148. Cracks in CP1000 grade (50 mm stroke)	101
Figure 149. Cracks in CP1000 grade (60 mm stroke)	101
Figure 150. Cracks in TBF grade (50 mm stroke).....	102
Figure 151. Cracks in TBF grade (55 mm stroke).....	102
Figure 152. Cracks in TBF grade (60 mm stroke).....	102
Figure 153. Hard cut area in Stelvio component	103
Figure 154. Crack in DP1000 at 38mm	103
Figure 155. Crack in CP1000 at 39mm.....	104
Figure 156. Crack in TBF1000 at 37mm	104

Figure 157. Part geometry provided (left) and model designed for simulations in Abaqus (right).....	105
Figure 158. Mesh on the sheet blank.	105
Figure 159. DP1000. Simulations with FLC criterion in Abaqus software. Maximum principal strain..	106
Figure 160. DP1000. Simulations with FLC criterion in Abaqus software. Minimum principal strain ..	106
Figure 161. DP1000 FLC with the points of the simulation	106
Figure 162. DP1000. Forming simulations with FLC failure criterion at first crack initiation (45 mm of stroke) and 100% (60 mm of stroke) of the forming process.....	107
Figure 163. DP1000. Industrial formed component at 60 mm of stroke	107
Figure 164. CP1000. Simulations with FLC criterion in Abaqus software. Maximum principal strain..	107
Figure 165. CP1000. Simulations with FLC criterion in Abaqus software. Maximum principal strain..	108
Figure 166. FLC with the points of the simulation for CP1000 steel.	108
Figure 167. TBF. Simulations with FLC criterion in Abaqus software. Maximum principal strain.	108
Figure 168. TBF. Simulations with FLC criterion in Abaqus software. Maximum principal strain.	109
Figure 169. FLC with the points of the simulation for TBF steel.....	109
Figure 170. Model for forming simulation.....	109
Figure 171. The steps of the forming simulation of the three materials.....	110
Figure 172. Simulation (left) and experimental (right) forming of a component manufactured with DP1000.....	110
Figure 173. Simulation (left) and experimental (right) forming of the CP1000.....	111
Figure 174. Simulation (left) and experimental (right) forming of the TBF.	111

4. LIST OF TABLES

Table 1. Tasks of the WP1	15
Table 2. Steels investigated. UC=uncoated, Z=zinc coated.....	15
Table 3. Chemical composition of the industrial produced grades [mass%]	16
Table 4. Characterized steel grades, main constituents of microstructure and retained austenite content	16
Table 5. Tensile parameters of grades transverse to rolling direction	18
Table 6. Local strain at fracture values obtained from DIC-assisted tensile tests.....	19
Table 7. Definition of the CI [LAR10]	21
Table 8. Equipment parameters for Nakajima test	27
Table 9. FLC ₀ for each steel grade in Nakajima test.	29
Table 10. Equipment parameters for Marciniak test	29
Table 11. FLC ₀ for each steel grade in Marciniak test.	31
Table 12. Hole Expansion Ratio for the investigated steels.....	32
Table 13. Tasks of WP2.....	33
Table 14. EWF results for NP specimens	37
Table 15. EWF results for fatigue pre-cracked specimens.....	39
Table 16. EWF at crack initiation for NP specimens	41
Table 17. EWF at crack initiation for fatigue pre-cracked specimens.....	42
Table 18. Tasks of WP 3	51
Table 19. w _e ⁱ values at LSR and HSR.....	54
Table 20. Tasks of WP4	65
Table 21. Tasks of WP5.....	81
Table 22. Content of bcc, fcc and zero-solutions for the grades and states investigated.....	88
Table 23. Tasks of WP6	89
Table 24. Level of correlation in crash simulations with different damage models	98
Table 25. Tasks of WP7	98
Table 26. Summary of press stroke levels for manufactured components with laser trimmed edge. In red the stroke level at what the first crack is detected.	99
Table 27. Different strokes for DP1000, CP1000 and TBF1000 hard cut blanks. In red the stroke level at what the first crack is detected.....	103
Table 28. Values of stroke at first crack appearance and crack initiation toughness, w _e ⁱ	104
Table 29. Crack growth for different press strokes and w _e values for the investigated steels.	105
Table 30. Tasks of WP8.....	111

5. LIST OF ACRONYMS AND ABBREVIATIONS

AHSS	Advanced High Strength Steel
AR	Annual Report
CAL	Continuous annealing line
CP	Complex phase grade
CR	Centro Ricerche Fiat (BEN3)
CT	Coiling temperature
CT specimen	compact tension specimen
CTM	Fundació CTM Centre Tecnològic (CO1)
CTOD	Crack Tip Opening Displacement
DENT	Double Edge Notched Tensile
DIC	Digital Image Correlation
DP	Dual phase grade
E	Young's Modulus
EDM	Electric Discharge Machining
EPFM	Elastic-Plastic Fracture Mechanics
EWF	Essential Work of Fracture
FEM	Finite element method
FLD	Forming Limit Diagram
FLC	Forming Limit Curve
FPZ	Fracture Process Zone
HDGL	Hot dip galvanizing line
HER	Hole Expansion Ratio
HET	Hole Expansion Test
HSR	High strain rate
IDIADA	IDIADA Automotive Technology (BEN4)
Jc	Critical J value for crack initiation
K	stress intensity factor
K _{IC}	Linear Elastic Fracture Toughness
<i>l</i> : ligament	<i>l</i> : ligament
LEFM	Linear Elastic Fracture Mechanics
LSR	Low strain rate
PHS	Press hardened steel
Q&P	Tempered martensite matrix with retained austenite
β	shape factor
δ _c	The critical CTOD
σ _{ys}	yield strength
W _e	Specific essential work of fracture
W _e ^l	Specific work for fracture initiation
W _f	Specific work of fracture
W _f	Total work of fracture

6. REFERENCES

- [CAS15] D. Casellas et al., Fracture resistance of tailor tempered microstructures obtained by different Press Hardening conditions. Proc. of the 5th Int. Conf. on Hot Sheet Metal Forming of High-Performance Steel (Toronto, Canada) 2015
- [CAS17] D. Casellas et al. Fracture Toughness to Understand Stretch-Flangeability and Edge Cracking Resistance in AHSS. Met Mat Trans A 86-94 (2017), 48
- [CHE12] X. Chen et al., *Simulation Technique for Pre-forming of AHSS Edge Stretching*. 12th International LS-DYNA® Users Conference (Michigan, USA, June 03-05)
- [CLU03] Clutton, E. 2003 ESIS EWF Protocol: Essential work of fracture and cohesive zone fracture toughness. Moore DR
- [COT77] B. Cotterell, J.K. Reddel. The Essential Work of Plane Stress Ductile Fracture, Int. J. Fract., 1977, vol. 13, pp. 267-277.
- [DIE61] G.E. Dieter. Mechanical Metallurgy. International Student Edition. Mc Graw-Hill, 1961.
- [FER99] D. Ferrer-Balas and M. L. et al. Maspoch. On the essential work of fracture method: Energy partitioning of the fracture process in iPP _lms. Polymer Bulletin, 42:101-108, 1999
- [FON11] N. Fonstein et al., Effect of Bainite on Mechanical Properties of Multiphase Ferrite-Bainite-Martensite Steels *Proceedings from the Materials Science & Technology Conference (October 16-20, 2011, Columbus, Ohio)*
- [FRO17] D. Frómeta et al., Evaluation of crash resistance by means of fracture toughness measurements in Advanced High Strength Steels. 5th Int. Conf. on Steel in Cars and Trucks (SCT17), Amsterdam (The Nederlands). 2017
- [GLA14] T. Gläsner et al., Methods to decrease cut edge sensitivity of high strength steels Key Engineering Materials 611-612 (2014) 1294-1307
- [GUT12] D. Gutiérrez, et al., Toughness evaluation of high strength steels sheets by means of the essential work of fracture. 19th European Conference on Fracture: Fracture Mechanics for Durability, Reliability and Safety, ECF 2012
- [GUT13] D. Gutiérrez et al., *The influence of fracture toughness in stretch-flangeability in advanced high strength steels sheets*. Proceedings of the IDDRG 2013 (Zurich, Switzerland, June 02-05)
- [KAR97] J. Karger-Kocsis and E. J. Moskala. Relationships between molecular and plane-stress essential work of fracture parameters in amorphous copolymers. Polymer Bulletin, 39:503-510, 1997.
- [LAC08] G. Lacroix et al., *The fracture toughness of TRIP-assisted multiphase steels* Acta Materialia (2008) 3900-3913.
- [LAR10] P. Larour et al., Influence of post uniform tensile and bending properties on the crash behaviour of AHSS and press-hardening steel grades. Proc. of the IDDRG2010, Graz, Austria, 2010
- [LAR11] P. Larour et al., *Alternative stretch flangeability characterization methods for AHSS steel grades*. Proceedings of the IDDRG2011 (Bilbao, Spain, June 05-08)
- [LAR15] P. Larour et al., "Side impact crash behaviour of press-hardened steels-correlation with mechanical properties". Conference: CHS2 2015, 5th International Conference on Hot Sheet Metal Forming of High-Performance Steel, Toronto, Ont., Canada, Volume: pp. 281-290
- [MAI86] Y.W. Mai and B. Cotterell. On the essential work of ductile fracture in polymers. International Journal of Fracture, 32:105-125, 1986.
- [MAR96a] Y. Marchal et al., Influence of the test parameters on the measurement of the essential work of fracture of zinc sheets. International Journal of Fracture, 1996, 295-310.
- [MAR96b] Y. Marchal et al., Comparison methods for the measurement of fracture toughness of thin sheets: (ECF 11) Mechanisms and Mechanics of Damage and Failure, 1996, 2259-2265.
- [PAR99] Pardoén, T. et al. Thickness dependence of cracking resistance in thin aluminium plates. J. of Mech. Sol. (1999) 2093-2123.
- [RIC73] Rice JR, Paris PC, Merkle JG. Some further results of *J-integral* analysis and estimates. Progress in Flaw Growth and Fracture Toughness testing, ASTM SPT 536. Philadelphia: American Society for Testing and Materials; 1973. p. 231-45.

[TAK09] Y. Takahashi et al., Fracture Mechanical Study on Edge Flange-ability of High Tensile-strength Steel Sheets *MS&T 2009: Proceedings from the Materials Science & Technology Conference (October 25-29, 2009, Pittsburgh, Pennsylvania)* pp 1317-1328.

[TAK12] Y. Takahashi et al., *Fracture Mechanical Study on Stretch Flange-Ability of Hot-Rolled High Tensile Strength Steel Sheets*. Proceedings of Asia Steel International Conference 2012

[THO13] D. Thomas, *Understanding the Effects of Mechanical and Laser Cut-Edges to Prevent Formability Ruptures During Automotive Manufacturing*. J Fail. Anal. And Preven. 13 (2013) 451-462

[WU12] X. Wu X et al., Characterization of mechanically sheared edges of dual phase steels *J. Mat. Proc. Tech.*(2012) 212 1209-1224

[YOO16] Yoon J I, Jung J , Joo S H, Song T J, Chin K G, Seo M H, Kim S J, Lee S and Kim H S 2016 Correlation between fracture toughness and stretch-flangeability of advanced high strength steels *Matter.Lett.* 180 322-326

Getting in touch with the EU

In person

All over the European Union there are hundreds of Europe Direct information centres. You can find the address of the centre nearest you at: https://europa.eu/european-union/contact_en

On the phone or by email

Europe Direct is a service that answers your questions about the European Union. You can contact this service:

- by freephone: 00 800 6 7 8 9 10 11 (certain operators may charge for these calls),
- at the following standard number: +32 22999696 or
- by email via: https://europa.eu/european-union/contact_en

Finding information about the EU

Online

Information about the European Union in all the official languages of the EU is available on the Europa website

at: https://europa.eu/european-union/index_en

EU publications

You can download or order free and priced EU publications at:

<https://publications.europa.eu/en/publications>. Multiple copies of free publications may be obtained by contacting Europe Direct or your local information centre (see https://europa.eu/european-union/contact_en).

EU law and related documents

For access to legal information from the EU, including all EU law since 1952 in all the official language versions,

go to EUR-Lex at: <http://eur-lex.europa.eu>

Open data from the EU

The EU Open Data Portal (<http://data.europa.eu/euodp/en>) provides access to datasets from the EU. Data can be downloaded and reused for free, for both commercial and non-commercial purposes.

The development of new Advanced High Strength Steel (AHSS) grades with increasing strength has introduced new challenges to carmakers and part producers. The limited ductility of these steels often lead to the appearance of cracks during forming or crash situations. These, increasingly common, cracking problems make necessary the application of new approaches to characterize the fracture resistance of AHSS, since conventional fracture criteria are not suitable to predict this kind of fractures.

In Tough-sheet project, the fracture toughness, from a fracture mechanics point of view, is proposed as a property to predict and rationalize cracking related phenomena in AHSS sheets. The Essential Work of Fracture (EWF) methodology has been successfully applied to evaluate the fracture toughness of different 1st, 2nd and 3rd generation AHSS (1000-1500 MPa UTS). The methodology has shown to be robust and suitable to readily measure the fracture toughness of thin AHSS sheets.

Furthermore, fracture toughness values, in terms of EWF, have shown to be useful to classify edge cracking resistance and crashworthiness of AHSS. It has been observed that toughness values show a direct correlation with laboratory forming and impact tests results; the tougher the material the greater edge cracking resistance and better crash behaviour. Thus, the fracture toughness is consolidated as a material property to select materials with enhanced formability and crash performance.

The EWF has also been used to develop a new damage evolution model to be implemented in forming and crash situations. First results, show promising accuracy improvements respect to conventional damage criteria.

Studies and reports

